Characterisation of Sub-Resolution Porosity in Sedimentary Rocks by X-ray Computed Tomography

Juan Carlos Roa Pérez

Supervisor: Prof. Ronny Pini

Department of Chemical Engineering

Imperial College London

United Kingdom

A thesis submitted in fulfillment of the requirements for the degree of Doctor of Philosophy of Imperial College London

2025

Statement of Originality

I hereby declare that the PhD thesis, entitled: Characterisation of Sub-Resolution Porosity in Sedimentary Rocks by X-ray Computed Tomography is entirely my own work and is performed under the supervision of Prof. Ronny Pini at the Department of Chemical Engineering, Imperial College London. Any published works presented in this thesis are given full acknowledgements, as stated at the beginning of each chapter.

Copyright Declaration

The copyright of this thesis rests with the author. Unless otherwise indicated, its contents are licensed under a Creative Commons Attribution-Non Commercial 4.0 International Licence (CC BY-NC). Under this licence, you may copy and redistribute the material in any medium or format. You may also create and distribute modified versions of the work. This is on the condition that: you credit the author and do not use it, or any derivative works, for a commercial purpose. When reusing or sharing this work, ensure you make the licence terms clear to others by naming the licence and linking to the licence text. Where a work has been adapted, you should indicate that the work has been changed and describe those changes.

Please seek permission from the copyright holder for uses of this work that are not included in this licence or permitted under UK Copyright Law.

Abstract

Accurate porosity characterisation is critical for understanding fluid flow in geological porous media, yet existing methods face significant limitations in capturing multi-scale pore systems in sedimentary rocks. This thesis develops and validates a novel dual-resolution X-ray computed tomography (CT) methodology that integrates medical CT and micro CT imaging to provide three-dimensional porosity quantification across multiple length scales. The dual-resolution approach addresses the fundamental trade-off between spatial resolution and field of view in conventional CT methods. Medical CT provides large-scale effective porosity maps with complete sample coverage, while micro CT resolves individual pore structures at microscale for the same domain. Integration of these complementary datasets enables quantification of effective, resolved, and unresolved porosity components within a unified framework, providing important insight into hierarchical pore system organisation. A key innovation involves using radio-opaque gases, specifically krypton, as saturating fluids for differential imaging. This advancement extends applicability to low permeability samples where conventional liquid saturants cannot penetrate adequately, overcoming a major limitation in tight rock characterisation. The methodology was validated on four representative sedimentary rocks: Bentheimer sandstone, Ketton limestone, Nugget sandstone, and Silurian dolomite, encompassing both simple and complex porosity systems. Validation against established techniques including helium pycnometry, mercury intrusion, and Archimedes methods demonstrates excellent agreement, with porosity values typically within 2-3% of reference measurements. The method successfully generates detailed 3D porosity maps revealing spatial heterogeneity and connectivity patterns. The approach enables enhanced parametrization through sub-resolution porosity mapping in numerical modelling applications, showing important differences in transport behaviours when heterogeneous sub-resolution porosity is applied, representing significant advancement over traditional homogenised approaches. This work addresses critical needs in reservoir

characterisation, carbon sequestration, and geothermal applications. The dual-resolution methodology provides enhanced tools for characterising complex porous media and establishes new opportunities for porosity quantification in digital rock physics.

Keywords: X-ray computed tomography, porosity quantification, digital rock physics, multi-scale analysis.

Acknowledgements

Firstly, I would like to thank my academic supervisor, Professor Ronny Pini for his invaluable support and guidance in shaping this project. His technical expertise, academic curiosity and thoughtful advice were instrumental in helping me accomplish this project while always striving for quality and excellence, traits that I will carry with me and for which I will be forever thankful.

To the industrial supervisors, Steffen Berg, Ali Fadili, and Conxita Taberner from Shell Global Solutions International B.V. for their valuable technical input in all the discussions and meetings we had during this project, which were critical for achieving outstanding research. I would also like to thank the Shell Digital Rocks 2 programme for the funding of the project and everyone involved: Shell directors, programme leaders from Imperial College, Professor Sam Krevor, Professor Martin Blunt, Professor Martin Trusler, Postdocs and fellow PhD students for their academic support and constant motivation. Special thanks to experimental officer Mr. Vincenzo Cunsolo and Dr. Takeshi Kurotori for their indispensable help associated to the required experimental work in the CT imaging lab. To the project managers, Bhavna Patel and Asheeka Padhiar, always friendly and helpful for administrative arrangements when needed.

To my colleagues in the Multiphase Systems Lab research group, in no particular order: Lucy Barton, Hassan Azzan, Amarjot Singh Bhullar, Andrea Rovelli, Anna Maria Eckel, Adam Ward, Kleio Zervidi, Carsten Wedler, Killian Gmyrek, David Büchner, Tristan Spreng, Kristen He, with whom I shared this exciting period of my life. Thank you for helping me balance academic life, and for creating long-lasting friendships.

To my partner, Sara Helm Knudsen, an unconditional source of motivation, encouragement, and support throughout this journey. I am deeply grateful to have you by my side. Jeg elsker dig.

To my friends, Valeria Arboleda, César Chacón, Giancarlo Marini, Gianpiero Marini, Ornella Di Marzo, Leonardo Sanchez, Fiorella Marchetti, Sara Erviti, José Soto, Alfredo Méndez, Ernesto Méndez, Tinne Nissen, Frederik Barsøe and Julie Nielsen who were always present and rooting for me.

A mis padres, Ramón Yovani y Sabina Aurora, el motor y la fuente de inspiración para completar mis objetivos. Éste logro es en gran parte gracias a ustedes; valoro mucho su esfuerzo y dedicación. Los quiero.

Thanks to all. Gracias totales.

Contents

Abstract **6**

Acknowledgements **8**

List of Figures **25**

List of Tables **26**

1 Introduction **32**

1.1 Thesis Outline 34

1.2 Objectives 35

Nomenclature **32**

2 Literature Review and Background Information **36**

2.1 Fundamental Concepts in Porous Media 36

2.1.1 Hierarchical Porosity in Geological Porous Media 38

2.2 Petrophysical Properties: Definitions and Equations 40

2.2.1 Porosity 40

2.2.2 Permeability 42

2.2.3 Saturation 42

2.3 Standard Bulk Porosity Quantification Methods 43

2.3.1 Caliper 43

2.3.2 Vacuum Saturation - Archimedes Method 44

2.3.3 Helium Pycnometry 45
2.3.4 Mercury Injection Capillary Pressure 47
2.4 Imaging Methods for Porosity Characterisation 48
2.4.1 X-ray Computed Tomography 50
2.5 Digital Rocks Physics and Applications 52
2.6 X-ray Imaging Methods for Sub-Resolution Porosity Characterisation . . . 55
3 Rock Samples: Geological Context and Petrophysical Properties 60
3.1 Bentheimer Sandstone 60
3.2 Ketton Limestone 62
3.3 Nugget Sandstone 63
3.4 Silurian Dolomite 64
3.5 Bulk Porosity Characterisation 66
3.5.1 Vacuum Saturation (Archimedes Method) 66
3.5.2 Helium Pycnometry 68
3.5.3 Mercury Intrusion Capillary Pressure 74
3.6 Concluding Remarks 78
4 The Dual-Resolution X-ray CT Method for Porosity Quantification 79
4.1 Methodology Description 80
4.1.1 Effective Porosity Calculation from Medical CT Imaging 80
4.1.2 Resolved Porosity Calculation from Micro CT Imaging 82
4.1.3 Methodology Sensitivity 85
4.2 Experimental Workflow 87

4.2.1 Experimental Apparatus 87

4.3 Image Acquisition 90

4.4 Image Processing 93

4.4.1 Medical CT Data Analysis 93

4.4.2 Micro CT Data Analysis 101

4.5 Sub-Resolution Porosity Mapping 106

4.6 Concluding Remarks 108

5 Use of Radio-Opaque Gas in the Dual-Resolution X-ray CT Method for Low Permeability Samples 110

5.1 Rationale for the Use of a Radio-Opaque Gas as a Saturating Fluid 110

5.2 Calibration Experiments 111

5.3 Revised Workflow for Image Acquisition with Krypton 113

5.4 Porosity Maps Derived from Differential Imaging Using Krypton as Saturating Fluid 119

5.5 Concluding Remarks 124

6 3D Porosity Mapping in Sedimentary Rocks 125

6.1 Simple Porosity Systems: Bentheimer Sandstone and Ketton Limestone . . 127

6.1.1 Effective Porosity Maps in 2D and 3D 127

6.1.2 Resolved Porosity Map from Micro CT Image Segmentation 133

6.1.3 Calculation of Unresolved Porosity Map by Integrating Effective and Resolved Porosity Maps 139

6.2 Complex Porosity Systems: Nugget Sandstone and Silurian Dolomite. . . . 144

6.2.1 Effective Porosity Maps in 2D and 3D 145

6.2.2 Resolved Porosity Map from Micro CT Image Segmentation 150

6.2.3 Calculation of Unresolved Porosity Map by Integrating Effective and Resolved Porosity Maps 155

6.3 Comparison of Pore Size Distribution with MICP Measurements 160

6.4 Bulk Porosity Comparison 165

6.5 Concluding Remarks 166

7 Numerical Studies Using Image-Based Porosity Maps 168

7.1 Simulation Set-Up 169

7.2 Model Validation 174

7.3 Model Parametrization 179

7.4 Flow and Transport Simulation in Ketton Limestone 183

7.5 Concluding Remarks 192

8 Conclusions and Future Work 195

8.1 Conclusions 195

8.2 Suggested Future Work 196

List of Figures

2.1 Porosity types in carbonate rocks - Choquete-Pray Classification (Choquette and Pray 1970). 38

2.2 Porosity heterogeneity found in a carbonate rock including microporosity (Keelan and Marschall 1979). 39

2.3 Micro CT 2D slice of a Estaillades limestone, highlighting the typical porosity heterogeneity in carbonates (Bultreys, Van Hoorebeke, and Cnudde 2015). 40

2.4 Figure 6. Schematic of apparatus used for Archimedes' method (API 1998). 45

2.5 Schematic of Double cell pycnometry porosimeter (API 1998). 47

2.6 Segmentation approach using differential imaging by injecting high salinity brine. Top: differential image (brine at 5% concentration - dry). Middle: differential image (brine at 30% concentration - dry). Bottom: Threshold selection (red lines) for phases segmentation (Lin et al. 2016). 56

2.7 Top: Histogram of the different phases after segmentation. Bottom: Slice image showing the resulted phases segmentation (a. solid grain in red, b. micropores in orange, c. macropores in blue) (Gao et al. 2019). 57

2.8 Top: Linear attenuation profile of xenon and quartz over different x-ray energy levels. Bottom left: Image of sample saturated with xenon at 34 KeV. Bottom center: Image of sample saturated with xenon at 35 KeV. Bottom right: Xenon distribution map after application of image subtraction representing porosity (Mayo et al. 2015). 58

3.1 Photograph of the Bentheimer Sandstone cylindrical core sample and micro CT image showing the homogeneous internal pore structure. Dimensions: Diameter = 1.2 cm and Length = 4.8 cm. 61

3.2 Photograph of the Ketton Limestone cylindrical core sample and micro CT image showing only the resolvable intergranular pore space. Dimensions: Diameter = 1.2 cm and Length = 3.7 cm. 62

3.3 Photograph of the Nugget sandstone cylindrical core sample and micro CT image showing the layering system in the sample. Dimensions: Diameter = 1.2 cm and Length = 4.3 cm. 63

3.4 Photograph of the Silurian Dolomite cylindrical core sample and micro CT image showing the complex porosity heterogeneoty. Dimensions: Diameter = 1 cm and Length = 4.6 cm. 64

3.5 Experimental set-up for the Vacuum saturation-Archimedes' method for bulk porosity measurements. a. Vacuum saturation set-up showing the samples in the flask connected to the vacuum pump and saturation fluid. b. Dry samples. c. Samples during saturation step. d. Saturated sample placed in the basket. e. and f. Samples submerged applying the buoyancy method. 67

3.6 Diagram of the custom built helium pycnometer. 69

3.7 Compressibility factor (Z) for helium extracted from the CERN Library Catalogue (Van Sciver, Timmerhaus, and Clark 2012). The red line denotes the compressibility factor Z=1 and the red lines the experimental operating temperature and pressures. 71

3.8 Pressure and temperature reading for the calibration step of the helium pycnometer. 72

3.9 Histogram of reference- and sample cell volume estimation. 73

3.10 Pore throat size distributions obtained from mercury intrusion porosimetry for the four rock samples. 75

4.1 Calibration step showing CT values of pure fluids (air and water) scanned under identical conditions to the core samples, used for porosity calculation via differential imaging 82

4.2 Graphical description of the proposed methodology to quantify unresolved porosity spatially using dual-imaging methods. 84

4.3 Schematic of the custom-designed core holder used for X-ray CT scanning of rock samples. Adapted from (RS-Systems 2021). 88

4.4 Schematic of the experimental setup, illustrating the mounted core holder and flowline connections to hydraulic pumps used for applying confining pressure and for fluid injection during sample saturation. 89

4.5 Bentheimer image comparison test highlighting the differences of protocol selection for optimal medical CT image acquisition. FC04 and FC13 denotes reconstruction function for scanning "body" and FC30, FC81 for "bone". ORG is the scanning option with no filter, where UE0 denotes "enhancement filter" and Q06 for " quantum denoising filter". 92

4.6 Difference in the resolution of three Ketton slices at dry and saturated stage scanned in a medical CT (voxel size = 27x27x500 µm^3), a raw dry scan in the micro CT (voxel size = 7x7x7 µm^3) and an upscaled micro CT to medical CT resolution for comparison. Note that the image output for medical CT images are in Hounsfield Units and micro CT shows a 8-bit greyscale image with values from 0 to 256. 93

4.7 Procedure for determining image center coordinates and diameter to apply a circular mask across slices. 95

4.8 3D porosity map and corresponding slice-averaged porosity of the Ketton sample. Left: Volume rendering of the porosity field, averaged dry and saturated scans were used, the diameter comprises 250 voxels in the x and y axis and 68 slices. Right: Average porosity values for each cross-sectional slice. Voxel size is representative of the original resolution of 40x40x500 µm^3. 96

4.9 CT noise correlation analysis across different voxel sizes and averaging schemes. Scatter plots of CT number differences between adjacent voxels for various coarsening factors and subtraction scenarios. Smaller voxel sizes (left) show tighter correlation and lower noise variance compared to larger voxel sizes (right), demonstrating the trade-off between spatial resolution and noise characteristics in CT imaging. 97

4.10 Noise maps and histograms of grey value differences from subtraction of two single scans, two sets of two averaged scans, and two sets of three averaged scans, resolution (0.04 x 0.04 x 0.5) mm^3. Dashed lines mark the mean and one standard deviation (σ_{Δ_1}, σ_{Δ_2}, σ_{Δ_3}). The fitted Gaussian curves (right) show that averaging scans prior to subtraction reduces noise. 99

4.11 CT noise and porosity uncertainty as a function of repeated scans across voxel sizes. The CT noise, $\sigma_{\Delta n}$ (left axis), and corresponding porosity uncertainty, σ_{ϕ_n} (right axis), are plotted against the inverse square root of the number of repeated scans ($1/\sqrt{n}$), for voxel sizes of (0.04 x 0.04 x 0.5) mm^3, (1 x 1 x 1) mm^3, and (2 x 2 x 2) mm^3. Noise decreases linearly with scan averaging. Similarly, voxel averaging exhibit lower inherent noise. Vertical dashed lines indicate the number of averaged scans. The red cross denotes the value obtained for the current study as 6 scans were averaged and the final voxel size was taken as (2 x 2 x 2)mm^3, resulting in a porosity uncertainty of $\pm 0.14\%$. 100

4.12 3D porosity map and corresponding average slice porosity of the Ketton sample. Left - Volume rendering of the porosity field, the volume comprises 5 voxels in the x and y axis and 17 slices. Right - Average porosity values for each cross-sectional slice. Voxel size is 2x2x2 mm^3. 101

4.13 Comparison of denoising filters applied to micro CT data. Left to right: original slice without filtering, image after Gaussian filter, and image after applying the Non-Local Means (NLM) filter. The line profiles plotted on the right display the corresponding greyscale intensity values along the marked sections in the images. The unfiltered profile (black) exhibits high noise fluctuation. In contrast, the the Gaussian filter (blue) reduces noise but blurs boundaries, while NLM filter (orange) shows superior noise suppression while preserving edge sharpness, evidenced by a steeper gradient at the phase boundary. The red horizontal line indicates the intensity threshold used inform the segmentation step. Arrows show the edge detection span for each method, highlighting the improved boundary definition. 102

4.14 Segmentation sensitivity analysis illustrating the impact of threshold selection on resolved porosity (ϕ_R). Top left: High-resolution micro CT slice of Ketton limestone with yellow profile line indicating location of intensity transect. Top row: Intensity profiles across a grain–pore boundary after non-local means filtering. Four different greyscale thresholds (horizontal red lines) are tested for pore–grain segmentation. Bottom row: Corresponding binary segmentation masks for each threshold, where white represents pore space. The resulting porosity values ϕ_R increase with higher threshold values, highlighting the influence of segmentation threshold on quantitative porosity estimates. 104

4.15 Comparison of micro CT and medical CT scans of the same end-cap section highlighting rotational misalignment. Left: Lower resolution medical CT slice showing the internal structure and the high contrast of the metal plug; Middle: Raw micro CT slice of the same sample; Right: Overlay showing the required clockwise rotation to align the sample across modalities for image registration and multi-scale analysis. 105

4.16 Image processing workflow for porosity quantification from micro-CT images. Starting from the physical Ketton core sample (top left), the micro-CT grayscale image is cropped, denoised and segmented into binary pore–grain domains. The segmented volume is rotated for alignment with medical CT data. A 3D coarsening step is then applied to compute voxel-averaged porosity over a lower-resolution grid matching the medical CT domain. The final resolved porosity map ϕ_R (bottom left) enables direct comparison to the effective porosity map. The comparison of slice-averaged porosities (bottom center) highlights the resolution-dependent discrepancy between resolved and effective porosity. 106

4.17 3D porosity maps of Ketton limestone core obtained from multi-resolution X-ray CT imaging. Left: Effective porosity map from medical CT, representing the total connected porosity at coarse resolution (ϕ_E). Center: Resolved porosity map from micro CT, capturing connected porosity features resolved at higher resolution (ϕ_R). Right: Unresolved porosity map (ϕ_U), obtained by subtracting the resolved porosity from the effective porosity indicating sub-resolution porosity. All maps are shown over the same voxel size: (2 x 2 x 2) mm^3. Bottom: Histogram and cumulative distribution of resolved and unresolved porosity per voxel in Ketton. 108

5.1 Krypton calibration for use as a gaseous contrast agent in X-ray CT imaging. Left: Density of krypton, carbon dioxide, and nitrogen as a function of pressure, showing gases incresing density under increasing pressure, (NIST Chemistry WebBook 2025). Centre: Corresponding average CT number (in Hounsfield Units, HU) for each gas at varying pressures. Krypton exhibits a strong linear CT response with pressure, unlike carbon dioxide and nitrogen, which remain close to the baseline of air. Right: Spatial consistency of krypton CT response across the length of the core-holder at different pressures. 113

5.2 Comparison of average slice porosity measurements for Ketton limestone using water-air and krypton 20 bar-air methods. Left: Before equilibration showing measurement variability and method discrepancies, and right: After equilibration demonstrating improved consistency between techniques and reduced spatial variation. 115

5.3 CT number profiles across Ketton limestone core during the improved imaging protocol with krypton. Top: Average CT numbers for each slice showing progressive increase with krypton pressure from vacuum to 20 bar, followed by vacuum evacuation and final water saturation. Air-saturated is shown as reference from a separate dataset. Bottom: Experimental timeline showing the 11-hour sequence with equilibration periods between each pressure increment. 117

5.4 Impact of sample preparation protocol on krypton-based porosity measurements for Ketton limestone. Comparison between the improved protocol with vacuum evacuation (green dotted line) and the initial protocol without vacuum evacuation (blue dotted line) against the water-air reference (red solid line). The vacuum evacuation protocol demonstrates improved accuracy and reduced systematic bias, particularly in the middle sections of the core. 118

5.5 Comparison of average slice porosity profiles for Ketton limestone using different krypton pressure combinations in differential imaging. The water-air reference method (red solid line) was compared against four krypton-based approaches: three using 5 bar as the lower pressure baseline (purple lines) and one using vacuum as baseline (green dotted line). Pressure combinations using 5 bar as the reference state show better agreement with the water-air benchmark, while the vacuum-based approach exhibits greater variability. 119

5.6 Krypton-based porosity measurements for slice 10 at varying pressure differentials (different colours denote the pressure pairs investigated in Figure 5.5) compared to water-air reference (red line with uncertainty band). Error bars represent porosity values variability at the same slice location across different krypton pressure combinations. 120

5.7 Final porosity profiles comparing averaged krypton measurements with water-air and water-vacuum reference methods, showing good agreement and validating the multi-pressure differential imaging approach. 121

5.8 Porosity maps comparison between applying differential imaging with water and krypton as saturating fluids. 122

5.9 Comparison of voxel-wise porosity distributions in Ketton limestone. The histogram shows the porosity characterised by resolved and the derived unresolved porosity using the effective porosity map obtained using krypton ($\phi_U = \phi_E - \phi_R$). The overlaid cumulative porosity curves for krypton (dashed blue) and water (solid red). 123

6.1 Longitudinal cross sections for internal inspection of porosity features. . . . 126

6.2 Left: 3D rendering of Bentheimer effective porosity map by differential imaging using water and vacuum (top row) and Krypton at 15 bar and vacuum (bottom row) as contrasting agents. Voxel size: (2 x 2 x 2) mm^3. Right: 2D planar sections (X-Z and Y-Z) revealing internal heterogeneity patterns. 128

6.3 Left: 3D rendering of Ketton effective porosity map by differential imaging using water and vacuum (top row) and Krypton at 15 bar and vacuum (bottom row) as contrasting agents. Voxel size: (2 x 2 x 2) mm^3. Right: 2D planar sections (X-Z and Y-Z) revealing internal heterogeneity patterns. 129

6.4 Overlay of voxel-wise porosity histograms for comparison of the effective porosity distribution derived from using krypton and water as saturating fluid in differential imaging for two simple porosity systems. Left: Bentheimer. Rigth: Ketton. 131

6.5 Voxel-wise comparison of effective porosity (ϕ_E) measured using krypton and water as contrast agents for Bentheimer (top left) and Ketton (top right). Each dot represents the porosity value of an individual voxel at the same location. The red dashed line indicates the 1:1 line for reference. Bentheimer shows a strong agreement with minimal scatter, consistent with its homogeneous nature. Ketton also displays a strong correlation but with greater scatter, reflecting its intrinsic heterogeneity and dual-porosity structure. Bland-Altman plot showing the difference in porosity for each voxel as a function of its average. Bentheimer (bottom left) and Ketton (bottom rigth). 132

6.6 Left: 3D rendering of Bentheimer resolved porosity map by segmentation of micro CT images. Voxel size: (2 x 2 x 2) mm^3. Right: 2D planar sections (X-Z and Y-Z) revealing internal heterogeneity patterns. 134

6.7 Porosity distribution comparison between medical CT differential imaging and micro CT segmentation for Bentheimer sandstone. 135

6.8 Average slice porosity profiles for Bentheimer sandstone core for three imaging methods highlighting the similarities in longitudinal porosity variations. 136

6.9 Left: 3D rendering of Ketton resolved porosity map by segmentation of micro CT images. Voxel size: (2 x 2 x 2) mm^3. Right: 2D planar sections (X-Z and Y-Z) revealing internal heterogeneity patterns. 137

6.10 Average slice porosity profiles for Keton sandstone core for three imaging methods highlighting the consistent effective porosity profiles derived from water-vacuum and krypton, while micro CT consistently reports lower porosity values due to its inability to capture sub-resolution microporosity. 138

6.11 Voxel-wise comparison of effective porosity (ϕ_E) obtained via water-vacuum differential imaging and resolved porosity (ϕ_R) from micro CT segmentation for Ketton limestone. Each data point represents a voxel porosity value from both methods. The dashed lines indicate the mean values of ϕ_R (blue) and ϕ_E (red). 139

6.12 Top: 3D rendering of Bentheimer unresolved porosity map. Voxel size: (2 x 2 x 2) mm^3 and 2D planar sections (X-Z and Y-Z). Bottom: histogram of unresolved porosity distribution. 141

6.13 Top: 3D rendering of Ketton unresolved porosity map. Voxel size: (2 x 2 x 2) mm^3 and 2D planar sections (X-Z and Y-Z). Middle: Average slice porosity profiles for the effective, resolved and unresolved porosity maps. Bottom: Histogram of effective porosity distribution effectively split into resolved and unresolved porosity distributions. 143

6.14 Left: Photograph of the Nugget sandstone inlet face, clearly revealing the characteristic layering. Center: Corresponding micro CT slice highlighting internal structural features. Right: Segmentation result identifying the resolvable macroporous layers, predominantly concentrated on the right side of the sample. 144

6.15 Left: Photograph of the Silurian dolomite inlet face. Center: Micro CT slice of Silurian dolomite highlighting the complex porosity heterogeneity. Right: Segmentation result with larger pores easily identified and expected zones of microporosity throughout the sample. 145

6.16 Left: 3D rendering of Nugget effective porosity map by differential imaging using water and vacuum as contrasting agents. Voxel size: (2 x 2 x 2) mm^3. Right: 2D planar sections (X-Z and Y-Z) revealing layering patterns. . . . 147

6.17 Statistical comparison of effective porosity maps in Nugget sandstone using two saturation approaches: (i) Water–Vacuum and (ii) Krypton (15 bar)–Vacuum, via differential imaging. Top left: Histogram of voxel-wise porosity distributions. Top right: Longitudinal porosity profile across slices. Bottom left: Voxel-to-voxel comparison with 1:1 line. Bottom right: Bland–Altman plot showing differences vs. the average porosity between methods. 149

6.18 Left: 3D rendering of Silurian effective porosity map by differential imaging using Krypton at 15 bar and vacuum as contrasting agents. Voxel size: (2 x 2 x 2) mm^3. Right: 2D planar sections (X-Z and Y-Z) showing high porosity heterogeneity across the sample. 150

6.19 Left: 3D rendering of Nugget resolved porosity map by segmentation of micro CT images. Voxel size: (2 x 2 x 2) mm^3. Right: 2D planar sections (X-Z and Y-Z). 151

6.20 Image processing workflow for Silurian dolomite demonstrating the importance of connectivity in low permeability systems. The workflow shows micro CT image segmentation before and after connectivity analysis, with corresponding effective porosity measured via medical CT. Right column displays the final connected porosity map. The red rectangle highlights the better agreement between resolved porosity map excluding isolated pores and effective porosity measurements. 152

6.21 3D rendering and cross sections of Silurian resolved porosity map by segmentation of micro CT images: top: Before connectivity analysis and middle: After connectivity analysis, Voxel size: (2 x 2 x 2) mm^3. Bottom: Average slice porosity profiles for Silurian dolomite core for the effective porosity map and resolved porosity map before and after connectivity analysis. 154

6.22 Top: 3D rendering of Nugget unresolved porosity map. Voxel size: (2 x 2 x 2) mm^3 and 2D planar sections (X-Z and Y-Z). Bottom: Average slice porosity profiles for Nugget core for the effective porosity map, resolved porosity map and unresolved porosity map. 156

6.23 Top: Porosity distribution analysis per layer in Nugget. Bottom: histogram of effective porosity distribution effectively split into resolved and unresolved porosity distributions. 157

6.24 Top: 3D rendering of Silurian unresolved porosity map. Voxel size: (2 x 2 x 2) mm^3 and 2D planar sections (X-Z and Y-Z). Middle: average slice porosity profiles for the effective, resolved, and unresolved porosity maps. Bottom: Histogram of effective porosity distribution and the proportion of resolved and unresolved porosity distributions. 159

6.25 Cumulative pore size distributions obtained from imaging-based porosity mapping techniques versus normalised cumulative intrusion curves from MICP measurements for Bentheimer sandstone (top row), Ketton limestone (second row), Nugget sandstone (third row) and Silurian dolomite (bottom row). 162

6.26 Comparison of Nugget sandstone samples showing heterogeneous porosity distribution. Left: Micro CT cross-section of sample used for imaging analysis. Right: Cross-section of sample used for MICP analysis. 164

6.27 Bulk porosity (ϕ_E) of Bentheimer, Ketton, Nugget, and Silurian samples measured by different methods: Mercury intrusion capillary porosimetry (MICP), vacuum saturation, helium pycnometry, and imaging approaches with both water and krypton. Error bars represent the reported measurement uncertainties. 166

7.1 3D renderings of the inputs for MODFLOW flow simulation (a), (b), (c). and solute transport simulation (d). (a): Resolved porosity map representing the system mobile domain. (b): Calculated hydraulic conductivity. (c): Head gradient imposed in the system. (d): Unresolved porosity map representing the system immobile domain. 173

7.2 Grid refinement levels used to evaluate numerical dispersion effects. Starting from the base grid of 5×5×17, each refinement level divides each voxel by a factor of 2, resulting in grids of 10×10×34, 20×20×68, and 40×40×136, respectively. All grids represent the same physical domain (1 cm diameter × 3.4 cm length). 175

7.3 Breakthrough curves for a homogeneous case with different grid resolutions: 5×5×17, 10×10×34, 20×20×68, and 40×40×136. Left: Normalised concentration as a function of pore volume injected (PVI), highlighting the impact of numerical dispersion on plume shape. Right: Normalised concentration as a function of time, with the vertical red line indicating the theoretical residence time τ_{the}. 176

7.4 Breakthrough curves from flow simulations using two refined grids. Top: 20×20×68, bottom: 40×40×136) at flow rates of 0.05, 0.1, 0.2, and 0.5 mL/min. Left panels show concentration versus injected pore volume (PVI), with the dashed red line marking 1 PVI. Right panels show concentration versus time, where the dashed vertical lines represent simulated residence time (τ_{sim}) and solid lines indicate the theoretical residence time (τ_{the}). 178

7.5 Breakthrough curves showing the impact on solute transport of the Péclet number (Left), by adjusting the flow rate, illustrating the transition from diffusion-dominated (Pe $<$ 1) to advection-dominated (Pe $>$ 10) regimes in a dual-domain transport system, and the Damköhler number (Right) at fixed Péclet number, altering the mass transfer coefficient. 181

7.6 Internal concentration profiles and breakthrough curves (C vs. PVI and C vs. time) for cases 1-3. The red vertical dashed line indicates 1 pore volume injected (PVI), while the black vertical dashed lines mark the time points at which internal profiles are extracted and shown. 185

7.7 Snapshots of the flow simulation results showing the plume evolution at selected times (t=2.6, 7.0, 15.0, 26.0, 40.0, 60.0, and 80.0 minutes) for the first three proposed cases, displayed in the XZ cross sections. 186

7.8 Internal concentration profiles and breakthrough curves (C vs. PVI and C vs. time) for cases 4-6. The red vertical dashed line indicates 1 pore volume injected (PVI), while the black vertical dashed lines mark the time points at which internal profiles are extracted and shown. 188

7.9 Snapshots of the flow simulation results showing the plume evolution at selected times (t=1.5, 3.6, 7.0, 25.0, 40.0, 60.0, and 80.0 minutes) for the last three proposed cases, displayed in cross sections XZ and YZ respectively. 190

7.10 Breakthrough curves (C vs. time) for all simulated cases. 191

List of Tables

3.1 Summary of geological and petrophysical properties of the rock samples selected on this study. 65

3.2 Summary of averaged vacuum saturation-Archimedes method measurements for the four rock samples. 68

3.3 Summary of averaged helium pycnometry measurements for the four rock samples. 74

3.4 Summary of porosity values obtained from MICP, including total porosity and the proportion of pore volume associated with pore throats below and above 1 µm. 77

4.1 Micro CT scanning parameters used for image acquisition of each rock sample. 90

6.1 Bulk porosity results for the four rock types from standard laboratory methods and effective porosity (ϕ_E) from imaging methods. 165

7.1 Summary of residence time calculated from simulation τ_{sim} and predicted theoretical residence time τ_{the}. 179

7.2 Summary of variable inputs used for MODFLOW and MT3DMS simulations. 184

Nomenclature

Abbreviations and Acronyms

ADE	Advection-Dispersion Equation
API	American Petroleum Institute
BTC	Breakthrough Curve
CO_2	Carbon Dioxide
CT	Computed Tomography
HU	Hounsfield Units
Kr	Krypton
MICP	Mercury Intrusion Capillary Pressure
MODFLOW	Modular Three-Dimensional Finite-Difference Ground-Water Flow Model
MT3DMS	Three-Dimensional Multi-Species Solute Transport Model
NIST	National Institute of Standards and Technology
NLM	Non-Local Means
PDF	Probability Density Function
PEEK	Polyetheretherketone
PNM	Pore Network Model
PVI	Pore Volume Injected
SD	Standard Deviation

SNR	Signal-to-Noise Ratio

Symbols

α	First order mass transfer coefficient [s^{-1}]
ΔP	Pressure drop [Pa]
Δ_h	Hydraulic head gradient [cm]
γ	Surface tension of mercury [N/m]
μ	Dynamic viscosity [g/cm.s]
μ	Fluid viscosity [poise]
ϕ	Porosity [-] or [%]
ϕ_E	Effective porosity [-] or [%]
ϕ_m	Mobile domain porosity [-] or [%]
ϕ_R	Resolved porosity [-] or [%]
ϕ_U	Unresolved porosity [-] or [%]
ϕ_{im}	Immobile domain porosity [-] or [%]
$\phi_{R,\mathrm{c}}$	Connected resolved porosity [-] or [%]
ρ_w	Fluid density [g/cm^3]
ρ_{cell}	Helium density in sample cell [mol/cm^3]
ρ_{eq}	Helium density after equilibration [mol/cm^3]
ρ_{ref}	Helium density in reference cell [mol/cm^3]
σ_{Δ_n}	CT noise [HU]
σ_{ϕ_n}	Porosity uncertainty [-] or [%]
σ_{vox}	noise associated to a given voxel [HU]
$\sqrt{n}$	Square root of the number of averaged scans

τ_{sim}	Residence time from simulation [min]
τ_{the}	Theoretical residence time [min]
θ	Contact angle between mercury and grain [°]
A	Cross sectional area [cm^2]
C_m	Solute concentration in mobile domain [-]
C_{im}	Solute concentration in immobile domain [-]
CT_{air}	CT number of air [HU]
$CT_{\text{Kr},hp}$	CT number of pure krypton at higher pressure [HU]
$CT_{\text{Kr},lp}$	CT number of pure krypton at lower pressure [HU]
$CT_{\text{vox},d}$	CT number of voxel at dry conditions [HU]
$CT_{\text{vox},hp}$	CT number of voxel at saturated conditions with krypton at higher pressure [HU]
$CT_{\text{vox},lp}$	CT number of voxel at saturated conditions with krypton at lower pressure [HU]
$CT_{\text{vox},s}$	CT number of voxel at saturated conditions [HU]
CT_{water}	CT number of water [HU]
D	Hydrodynamic dispersion tensor
d_{eq}	Equivalent voxel pore diameter [mm]
d_p	Pore throat diameter [µm]
g	Gravitational force [cm/s^2]
K	Hydraulic conductivity [cm/s]
k	Permeability [cm^2], [Darcy] or [mD]
L	Sample length [cm]

L_c	characteristic length [cm]
n	Number of moles
N_p	Number of voxels labelled as pore
N_s	Number of voxels labelled as solid material
P_c	Capillary pressure [Pa]
P_{cell}	Pressure in sample cell [barg]
P_{eq}	Pressure after equilibration [barg]
P_{ref}	Pressure in reference cell [barg]
Q	Flow rate [cm^3/s] or [mL/s]
r	Sample radius [cm]
S	Permeability shape factor
S	Saturation [-]
S_s	Specific storage
t	Time [s]
v	Seepage velocity vector [cm/s]
V_b	Bulk volume [cm^3]
V_g	Grain volume [cm^3]
V_p	Pore volume [cm^3]
V_{balls}	Stainless steel balls volume [cm^3]
V_{cell}	Sample cell volume [cm^3]
V_{ref}	Reference cell volume [cm^3]
W	Volumetric flux [cm/s]
W_{dry}	Dry weight [g]

W_{sat}	Saturated weight [g]
W_{sub}	Submerged weight [g]
Da	Damköhler number [-]
Pe	Péclet number [-]

Chapter 1

Introduction

Porous media systems characterisation is fundamental to numerous scientific and engineering applications, ranging from reservoir studies and groundwater flow modelling (Ghadami et al. 2015) to carbon sequestration (Xiao, T. Xu, and Pruess 2009; Al-Menhali et al. 2014) and geothermal energy extraction (Rejeki, Hadi, and Suhayati 2005). The accurate quantification of porosity is critical for predicting fluid flow behaviour, storage capacity, and transport properties in these systems. However, the heterogeneous nature of geological porous media presents significant challenges for characterisation of the full range of porosity, as pore structures typically span multiple length scales from nanometers to centimeters, particularly for upscaling purposes as the translation of pore-scale heterogeneity into continuum-scale represents a fundamental challenge in subsurface studies (Frippiat and Holeyman 2008; Ma et al. 2019; Blunt et al. 2013).

While traditional field-scale approaches rely on bulk porosity values and empirical correlations, providing valuable average properties, they fail to capture the microscopic spatial distribution and hierarchical organisation of pore systems that fundamentally control flow and transport. The emergence of high-resolution X-ray computed tomography (CT) as a non-destructive imaging technique revolutionised the field of porous media characterisation by enabling direct visualisation of three-dimensional pore structures at smaller scales (Wildenschild and Sheppard 2013; Silva et al. 2023), allowing to generate a digital analogue of the studied rocks for predictive flow simulation analysis, commonly known as Digital Rocks Physiscs (DRP). Imaging devices used to capture pore-scale properties vary on spatial resolution. The most common for the study of reservoir geological samples are: Medical grade CT ($\approx$ 50 to 100 µm), micro CT ($\approx$ 1 to 10 µm), nano CT, scanning electron microscopy (SEM) and focused ion beam-SEM (FIB-SEM) ($\approx$ 10 nm) (Moslemipour and Sadeghnejad 2021). However, current imaging

approaches face a fundamental trade-off between spatial resolution and field of view, limiting their ability to simultaneously capture both large-scale porosity features and fine-scale pore details within a single sample (Sadeghnejad, Enzmann, and Kersten 2021). Medical grade CT systems provide excellent sample coverage but lack the resolution to resolve individual pores, while micro CT systems offer high spatial resolution but are constrained to small sample volumes that may not be representative of bulk rock properties, (Cnudde and M. N. Boone 2013). This limitation is particularly pronounced in complex sedimentary rocks such as carbonates, where multi-modal pore size distributions and intricate connectivity patterns govern macroscopic properties. The inability to adequately characterise these multi-scale porosity systems has long been recognised as a critical bottleneck in predictive modelling of subsurface processes, (Ganguli and Dimri 2023).

Several approaches have been developed to mitigate the spatial resolution limitations for truly multi-scale characterisation (Pini and Madonna 2016). The integration of imaging techniques at different resolutions has been widely explored as a solution (Grader et al. 2010), by extracting smaller features at high resolution but limited physical sample size and incorporating this information into a larger domain scanned at lower resolution through stochastic upscaling (Menke, Maes, and Geiger 2021; Zhuang et al. 2022). The main problem is that this prediction, though informed, might not be a true representation of the pore heterogeneity; therefore, a high uncertainty could be included. Another restriction is how computationally expensive DRP models can be, which is why such models are often constrained to relatively small representative domains, typically in the order of a few hundred voxels per side, or physical dimensions in the sub-millimetre to millimetre range (Prodanović, Mehmani, and Sheppard 2015; Lai, Moulton, and Krevor 2015; Bijeljic, Raeini, et al. 2018).

This thesis addresses the identified limitations through the development of a dual-resolution X-ray CT methodology that integrates imaging at multiple scales to provide porosity characterisation of sedimentary rocks, especially the spatial mapping of micro CT sub-resolution porosity in meso-scale samples (1 cm in diameter and 4 to 6 cm in length), dimensions with sufficient representative heterogeneity to bridge the gap between pore scale and core scale studies. The research approach combines the

complementary strengths of medical CT and micro CT imaging systems to overcome the traditional resolution and field of view trade-off.

1.1 Thesis Outline

Chapter 2 provides a literature review covering fundamental concepts in porous media, existing characterisation techniques, and the theoretical background for X-ray CT imaging methods.

Chapter 3 describes the geological context and petrophysical properties of the rock samples used in this study, establishing the baseline characterisation through conventional bulk porosity measurement techniques.

Chapter 4 presents the core dual-resolution methodology, detailing the experimental workflow, image acquisition protocols, and data processing procedures for both medical CT and micro CT components.

Chapter 5 extends the methodology to low permeability samples through the innovative use of radio-opaque gases, addressing the limitations of conventional saturating fluids in tight rock systems.

Chapter 6 demonstrates the application of the dual-resolution method to generate 3D porosity maps for both simple and complex porosity systems, with detailed validation against established measurement techniques.

Chapter 7 presents numerical modelling studies that utilise the image-derived porosity maps for flow and transport simulations, validating the practical utility of the characterisation approach.

The thesis concludes with a synthesis of key findings, discussion of limitations, and recommendations for future research directions. Throughout, the work maintains a focus on practical applicability while advancing fundamental understanding of multi-scale porosity systems in geological materials.

1.2 Objectives

The primary research objectives are:

1. Develop an integrated dual-resolution imaging-based experimental workflow that combines medical CT and micro CT datasets to quantify the scale and extent of resolved ("macro") and unresolved ("micro") porosity of rocks with varying degree of heterogeneity, and their spatial variability.

2. Validate the approach across diverse rock types including both simple porosity systems (clean sandstones and limestones) and complex multi-scale porosity systems (heterogeneous sandstones and dolomites) and benchmark the results against bulk porosity values obtained from standard laboratory measurements.

3. Expansion of the domain of applicability of digital rock workflows by demonstrating practical integration of image-derived 3D porosity maps with numerical simulations to improve our understanding of fundamentals in flow and transport processes in systems containing microporosity.

Chapter 2

Literature Review and Background Information

This chapter provides theoretical foundations and contextual background essential for understanding the fundamental concepts, processes, and methodologies employed throughout this thesis. The literature review systematically examines the current state-of-the-art in digital rock physics, identifies established approaches for addressing key technical challenges, and highlights potential knowledge gaps that this research project aims to address. This chapter encompasses three primary sections: petrophysical concepts and characterisation methods, fluid flow and transport mechanisms in porous media, and contemporary applications of digital rock physics in reservoir characterisation.

The integration of these interdisciplinary fields forms the conceptual framework that underpins the methodological approach and analytical techniques presented in subsequent chapters. Through critical analysis of existing literature, this chapter establishes the theoretical basis for novel contributions to digital rock physics while positioning the current work within the broader context of subsurface characterisation and modelling.

2.1 Fundamental Concepts in Porous Media

A porous medium is defined as a material composed of a solid matrix and void spaces in between, referred to as as pores. In the context of geological porous media, it is important to understand how the formation of rocks affects the internal arrangement of material and porous space.

Sedimentary rocks are a major class of geological porous media, formed by the deposition of sediments over time. These sediments can include mineral particles such as clays, quartz, and silica, as well as organic matter. Once deposited, sediments undergo a series of chemical, physical, and biological transformations, collectively known as diagenesis, which progressively convert loose sediments into consolidated rock (Boggs Jr 2009).

Among sedimentary rocks, three primary types are commonly recognised based on composition and depositional processes:

1. Siliciclastic rocks are composed mainly of silicate minerals such as quartz, feldspar, and rock fragments. They form from the mechanical weathering, transport, and deposition of pre-existing rocks. Sandstones are a common example. Their porosity is largely controlled by grain size, sorting, packing, and cementation, and they generally exhibit good mechanical strength.

2. Carbonate rocks are primarily made of carbonate minerals, such as calcite ($CaCO_3$) and dolomite ($CaMg(CO_3)_2$), which largely originate from the deposition of calcareous organisms (fossils) in marine environments (Darling 2005). During diagenesis, these minerals undergo varying degrees of dissolution, producing a highly heterogeneous and irregular pore network (Mazzullo 2004). Early-stage deposition can generate fabric-selective pores, formed by the packing of sediments and interparticle voids, while later mineral dissolution during burial can create non-fabric-selective pores, which are not directly associated with the original sediment framework. As illustrated in Figure 2.1, carbonate rocks typically contain a combination of multiple pore types, resulting in a physically complex pore system whose connectivity and pore throat distribution are strongly influenced by grain size, compaction, mineral composition, and diagenetic history (Choquette and Pray 1970). This complexity makes the quantification of total and microporosity in carbonates particularly challenging.

3. Clay-rich rocks, including mudstones and shales, are dominated by fine-grained clay minerals such as kaolinite, illite, and smectite. These rocks generally have low permeability and microporous structures, making them effective seals or barriers in hydrocarbon systems. Their porosity is highly sensitive to compaction and diagenetic transformations.

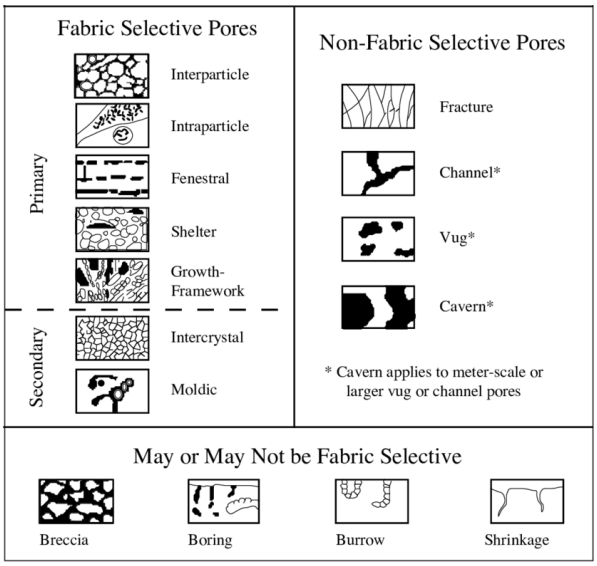


Figure 2.1: Porosity types in carbonate rocks - Choquete-Pray Classification (Choquette and Pray 1970).

.

Through diagenetic processes, the resulting pore network comprising interconnected and isolated voids plays a fundamental role in controlling the storage and movement of fluids such as water, hydrocarbons, or gases. Interconnected pores enable fluid flow, while isolated pores contribute to storage without direct transport pathways. The geometry, size distribution, and connectivity of pores, collectively referred to as pore structure, directly impact the hydraulic and petrophysical properties of rocks and are therefore key considerations in reservoir characterisation, hydrogeology, and carbon storage studies.

2.1.1 Hierarchical Porosity in Geological Porous Media

Hierarchical porous media are a subclass of porous materials distinguished by a multi-scale pore structure, in which distinct pore networks coexist across several length scales. In geological contexts, these networks are typically categorised into macropores, mesopores, and micropores, spanning dimensions from millimeters down to sub-micron levels (Nimmo 2013; Luna et al. 2016). Macropores generally refer to pores larger than 65 microns, mesopores to intermediate-sized pores, and micropores to pores smaller than 1 micron. This classification reflects the fact that pore size strongly influences fluid storage and

transport mechanisms within the rock.

The hierarchical organisation of pores has important implications for transport properties. Large-scale macropores provide the primary pathways for bulk fluid flow, while smaller-scale meso- and micropores contribute to storage, capillary retention, and diffusion-controlled transport. As a result, fluids moving through hierarchical porous media experience a combination of advection-dominated transport in larger pores and diffusion-dominated behavior in finer pores, which can significantly affect solute mixing, breakthrough times, and reactive transport. Figure 2.2 illustrates this multi-scale pore structure in a carbonate rock.

Hierarchical porosity is common in carbonate rocks, sandstones with secondary porosity, and certain diagenetically altered reservoirs, making its characterisation crucial for accurate modelling of fluid flow and reactive transport in subsurface systems. Quantifying the contribution of each pore scale often requires a combination of experimental techniques, including mercury intrusion porosimetry, helium pycnometry, and imaging-based methods such as micro CT scanning.

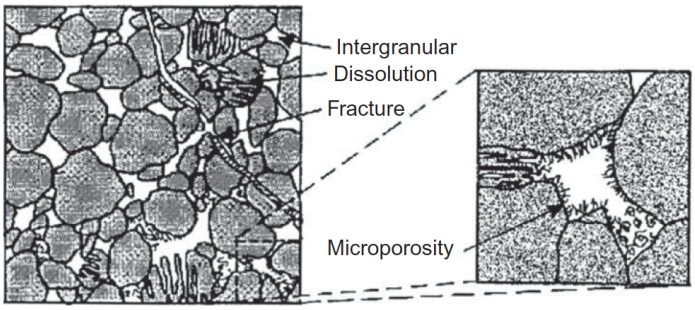


Figure 2.2: Porosity heterogeneity found in a carbonate rock including microporosity (Keelan and Marschall 1979).

.

This project aims to study the microporosity distribution in sedimentary rocks, with a particular focus on quantifying porosity features that fall below the resolution limits of conventional X-ray scanning techniques. Carbonate rocks are the primary target due to their inherently wide range of pore sizes and complex pore networks, as illustrated in

Figure 2.3. In contrast, homogeneous siliciclastic rocks (such as sandstones) are used as benchmarks because of their relatively simpler and better-connected pore systems, which allow for comparison and validation of microporosity characterisation methods. By contrasting these two rock types, the study seeks to improve understanding of sub-resolution porosity, its contribution to total storage, and its impact on fluid flow and transport properties in sedimentary reservoirs.

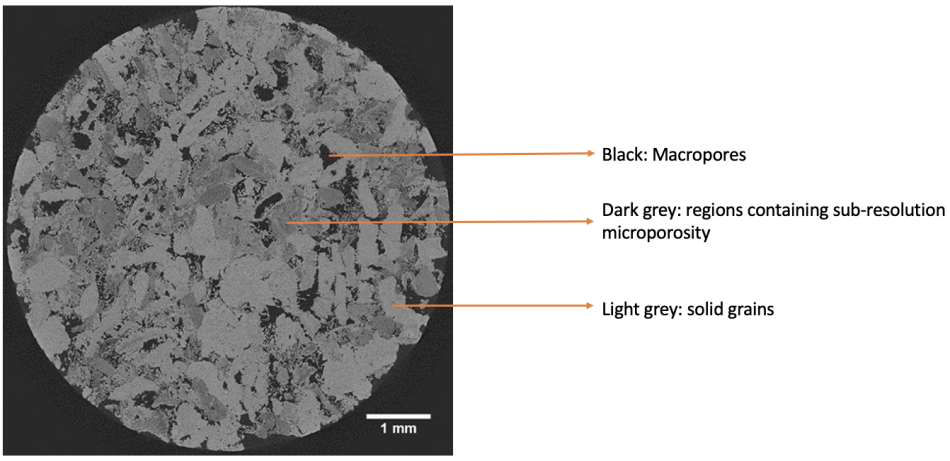


Figure 2.3: Micro CT 2D slice of a Estaillades limestone, highlighting the typical porosity heterogeneity in carbonates (Bultreys, Van Hoorebeke, and Cnudde 2015).

.

2.2 Petrophysical Properties: Definitions and Equations

2.2.1 Porosity

Rock porosity is a physical property defined as the ratio of void volume inside a rock over the total volume of the same rock. The values are reported as percentage or as a decimal fraction between 0 and 1. It can be expressed by the following equation:

$$\phi = \frac{V_b - V_g}{V_b} = \frac{V_p}{V_b} \tag{2.1}$$

where:

- ϕ is the porosity
- V_b is the bulk volume
- V_g is the grain volume
- V_p is the pore volume

Bulk volume comprises the entirety of the rock where porosity is to be calculated. Grain volume is the solid material forming the rock and the subtraction of the grain volume to the bulk volume will define the pore volume as the sum of all the void spaces.

Rock porosity varies depending on the material forming the rock, grain size, shape, and distribution. The combination of these factors define pore size and interconnection between pores. Large particles forming the rock will normally generate large pores an porosity will reduce as the grain size decreases. It is common to find different grain sizes inside the same rock and its distribution will determine the porosity heterogeneity. Rock porosity typically falls within a range between 5% and 30% for sedimentary reservoirs (Kashif et al. 2019).

Isolated pores can also be found inside the rock, meaning that there is no connection with the rest of the porous space. The sum of interconnected pores and isolated pores is defined as absolute porosity whereas the volume of interconnected pores is defined as effective porosity. Effective porosity is the rock property of interest when studying underground fluids storage and transport inside geological formations, effective porosity determines the fluids volumes and paths inside the rock that allows fluids movement.

2.2.2 Permeability

Permeability (k) quantifies the ability of a porous material to allow fluid flow. Rocks permeability is directly related to the effective porosity of the rock as fluids can only move through connected pores; other factors that influence permeability are pore size and pore distribution, cementation, orientation of the rock layers, pressure, and fractures. Absolute permeability is the term used when a single phase is flowing through the rock, in case of multi-phase flow each phase has a relative permeability, which is the ratio of the effective permeability of a given phase over the absolute permeability. Darcy's Law equation (Eq. 1) is an empirical law to calculate permeability assuming a single uncompressible phase is flowing through a homogeneous rock (Peters, Curry, and Kacewicz 2012).

$$k = \frac{Q\mu L}{A\Delta P} \tag{2.2}$$

where:

- k is the permeability
- Q is the flow rate
- μ is the fluid viscosity
- L is the length of the sample
- A is the cross sectional area
- ΔP is the pressure drop between inlet and outlet

2.2.3 Saturation

Saturation (S) is defined as the fraction of the total rock pore space occupied by a particular fluid. As rocks are typically saturated with more than one fluid (oil, water, gas), there is a saturation fraction attributed to each fluid, which sum equals 1 (S_o+S_w+S_g=1).

Saturation is closely related to the porosity geometry of a given rock, the volume of fluid occupying isolated pores that are not interconnected is not mobile, therefore having a direct impact for permeability calculations (Kantzas, Bryan, and Taheri 2012).

2.3 Standard Bulk Porosity Quantification Methods

Bulk porosity can be estimated by direct measurements with laboratory techniques on rock cores. Typically, the analysis are done in cylindrical core samples of a representative section of the formation of interest. As stated in Equation (2.1), bulk volume and grain volume or alternatively bulk volume and pore volume are needed to determine porosity. The following methods are the most commonly used to determine the above mentioned volumes.

2.3.1 Caliper

Using a caliper is the simplest method to determine the bulk volume of a cylindrical sample. The diameter and length are directly measured, and the volume is then calculated using Equation (2.3). To account for surface irregularities, it is recommended to take several measurements along the sample and use their average value (API 1998). This approach provides the volume of an ideal cylinder; however, because rock sample surfaces are often non-uniform, the resulting bulk porosity represents only an initial estimate. More accurate methods should be used to complement and refine these values.

$$V_b = \pi r^2 L \tag{2.3}$$

where:

- V_b is the bulk volume
- r is the sample radius

- L is the sanple length

2.3.2 Vacuum Saturation - Archimedes Method

The Archimedes' method is a simple technique for determining the bulk volume and pore volume of rock samples through liquid displacement. The method is grounded in Archimedes' Principle, which states that a body submerged in a fluid experiences an upward buoyant force equal to the weight of the displaced fluid. Because of its conceptual simplicity and minimal equipment requirements, this approach is particularly valuable for routine core analysis, especially when dealing with samples that possess an interconnected pore network.

In practice, the procedure begins by weighing the dry rock sample in air to obtain its dry mass. The sample is then saturated with a liquid of known density, commonly water or brine, under vacuum or pressure conditions to ensure that all interconnected pores are fully filled with fluid. Complete saturation is critical to avoid underestimation of pore volume due to trapped air. After saturation, a container filled with the same liquid is placed on a balance and tared. The saturated sample is carefully submerged into the container, and the apparent increase in balance reading corresponds to the weight of the displaced liquid. From this measurement, the bulk volume of the sample can be determined by dividing the displaced liquid weight by the density of the saturating fluid.

The pore volume is obtained by calculating the difference between the mass of the saturated sample and the mass of the dry sample, which represents the mass of the fluid occupying the pore space. Dividing this difference by the fluid density yields the pore volume. Finally, the porosity of the rock can be determined from Equation (2.1), as the ratio of pore volume to bulk volume (API 1998).

While Archimedes' method provides reliable and reproducible results for rocks with well-connected pore structures, it has certain limitations. The accuracy of the measurement depends strongly on achieving complete saturation of the pore space and minimising experimental errors such as trapped air bubbles or evaporation during weighing. Furthermore, for samples with significant closed or isolated porosity, this

method may underestimate the total pore volume. Despite these limitations, Archimede's principle remains a standard technique in petrophysical analysis due to its simplicity, robustness, and direct physical basis.

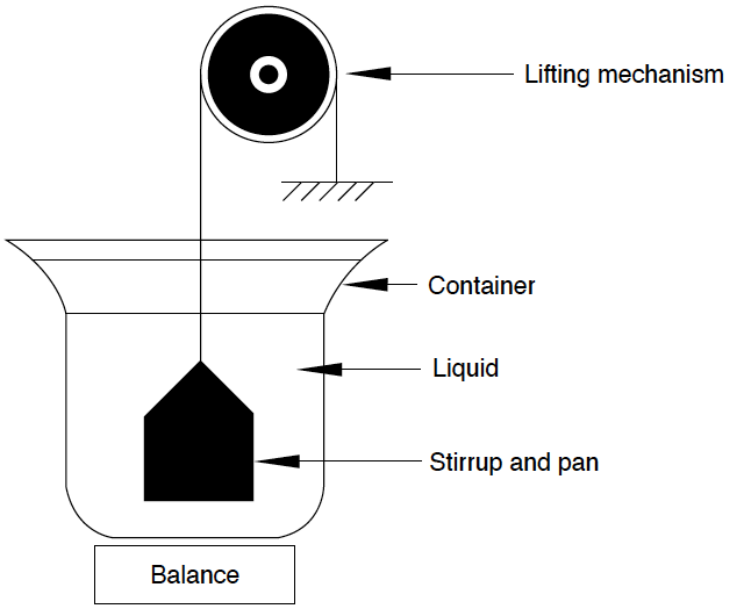


Figure 2.4: Figure 6. Schematic of apparatus used for Archimedes' method (API 1998).

.

2.3.3 Helium Pycnometry

Helium pycnometry is a non-destructive technique used to determine the grain volume of a rock sample. The method is based on Boyle's Law, which states that for a fixed amount of gas at constant temperature, the pressure exerted on the gas is inversely proportional to the volume it occupies. In practice, this means that the product of pressure and volume remains constant when temperature is stable. Helium is used as the working gas due to its inertness and extremely small atomic radius, which allows it to penetrate very fine and connected pores within the rock without reacting with the sample material.

A typical gas pycnometer consists of two connected chambers of known, fixed volume. The first chamber is empty and serves as a reference, where helium is injected and stabilised at an initial pressure P1. The second chamber contains the rock sample. Once the valve between the chambers is opened, the gas expands into the sample chamber, and the new equilibrium pressure P2 is recorded. From these pressure measurements, the free volume

in the sample chamber can be calculated using Boyle's Law. The grain volume of the sample is then obtained by subtracting this free volume from the total chamber volume, as expressed in Equation (2.4) (API 1998).

Once the grain volume is known, the pore volume can be determined by subtracting the grain volume from the bulk volume, which is usually measured independently using calipers or buoyancy methods. The ratio of pore volume to bulk volume yields the porosity of the rock sample.

Helium pycnometry is widely used in petrophysics because it provides accurate measurements with minimal sample preparation. However, the method assumes that all pores accessible to helium are interconnected. It does not account for isolated or closed porosity.

$$V_g = V_c - V_r \left(\frac{P_1}{P_2 - 1} \right) \tag{2.4}$$

where:

- V_g is the sample grain volume
- V_c is the sample chamber volume
- V_r is the reference chamber volume
- P_1 is the absolute initial reference pressure
- P_2 is the absolute expanded pressure

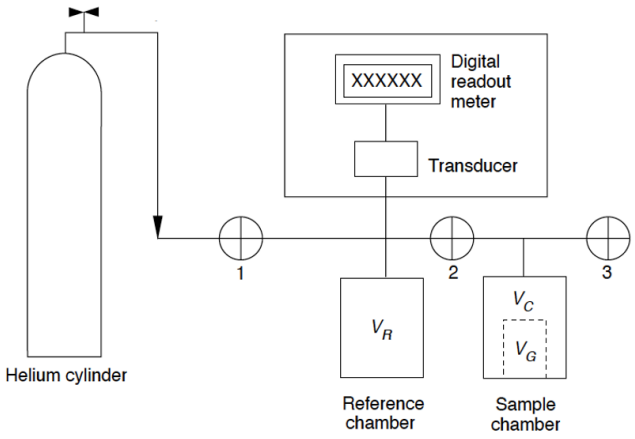


Figure 2.5: Schematic of Double cell pycnometry porosimeter (API 1998).

.

2.3.4 Mercury Injection Capillary Pressure

Mercury Injection Capillary Pressure (MICP) is a technique for determining both porosity and pore size distribution in porous materials. The method is based on the non-wetting behaviour of mercury with respect to most solid surfaces. Because mercury does not spontaneously enter pores due to its high surface tension and large contact angle with mineral surfaces, an external pressure must be applied to force mercury into the pore network.

The measurement is performed using a mercury porosimeter, which typically consists of a sample cell that holds the rock specimen and a connected stem through which mercury is introduced. The process begins with the evacuation of the sample chamber to remove air, after which mercury is injected progressively under controlled pressure. At low pressures, mercury intrudes into the largest pores, where entry requires overcoming only relatively low capillary resistance. As the applied pressure increases, mercury progressively fills smaller and smaller pores, since higher pressures are required to overcome the greater capillary entry pressures associated with narrower pore throats. This relationship is governed by the Washburn equation, which links the applied pressure to the corresponding pore throat radius, allowing the calculation of the pore size distribution.

The in-house MICP instrument (Micromeritics AutoPore IV) operate over a pressure range from vacuum up to 400 MPa, corresponding to an accessible pore throat diameter range of about 3–400 µm at low pressures down to 3–4 nm at high pressures. This wide range allows the technique to provide sufficient detailed information on pore throat size distribution to capture the full range of pore structures typically encountered in rock samples (Kantzas, Bryan, and Taheri 2012).

Despite its accuracy and wide adoption, MICP has notable limitations. The technique requires only small sample sizes, which may not always be representative of bulk rock properties. Moreover, because the high pressures used during mercury intrusion can physically damage the rock structure or alter pore geometry, the method is inherently destructive, and samples cannot be recovered for further testing. With its ability to provide quantitative and high-resolution pore structure information, MICP serves as a valuable reference for the classification of pore types in the studied samples, complementing other characterisation methods employed in this study.

2.4 Imaging Methods for Porosity Characterisation

Imaging techniques are widely used in porous media research to characterise the internal structure and pore networks of rock samples. Common methods include optical microscopy, scanning electron microscopy (SEM), nuclear magnetic resonance (NMR) imaging, and X-ray computed tomography.

Whitin imaging techniques, microscopy-based methods provide direct visualization of pore structures at multiple scales, offering complementary information about pore geometry, connectivity, and distribution. Optical microscopy of thin sections represents one of the oldest yet still valuable approaches for porosity characterisation. Thin sections, typically 30 µm thick, are prepared by impregnating rock samples with colored epoxy resin before polishing, allowing pores to be distinguished from the mineral matrix under transmitted or reflected light. This technique enables qualitative assessment of pore types (intergranular, intragranular, fracture porosity) and their spatial relationships to mineralogy and diagenetic features. While thin section analysis provides excellent

context for understanding pore genesis and distribution patterns, it is limited by its two-dimensional nature and relatively modest resolution (typically 1-5 µm), which prevents detection of micropores that may contribute significantly to total porosity in tight formations (Iscan and Kok 2009).

Scanning electron microscopy (SEM) extends the resolution capabilities to the nanometer scale, revealing fine-scale pore structures invisible to optical methods. SEM imaging of freshly fractured or ion-milled rock surfaces can resolve pores down to approximately 10-20 nm, making it particularly valuable for characterising tight sandstones, shales, and carbonate mudstones where microporosity dominates. Secondary electron imaging highlights topographic features and pore throats, while backscattered electron imaging provides compositional contrast that aids in distinguishing organic matter porosity from mineral-hosted pores. However, SEM analysis faces challenges in quantitative porosity estimation due to surface preparation artifacts, the two-dimensional nature of images, and difficulties in distinguishing true pores from surface roughness or plucked grains. Additionally, the high vacuum requirements can alter clay structures and cause desiccation artifacts in samples containing expandable clay minerals (Tang and Gratchev 2023).

Transmission electron microscopy (TEM) represents the highest resolution microscopy technique applicable to rock samples, capable of resolving individual pores down to 1 nm and providing crystallographic information through electron diffraction. TEM has proven especially valuable for characterizing nanopores in organic-rich shales, where pores within kerogen and clay platelets can be directly imaged at molecular scales. The technique requires preparation of electron-transparent sections (typically $<$100 nm thick) using focused ion beam (FIB) milling or ultramicrotomy, which allows investigation of specific features identified at lower magnifications. Despite its exceptional resolution, TEM analysis is extremely time-consuming, samples only minute volumes (typically $<$10 µm^3), and requires sophisticated sample preparation that may introduce artifacts. Consequently, TEM is best employed as a targeted technique to investigate specific pore types or validate interpretations from other methods rather than as a primary porosity characterization tool (Prior et al. 1999).

Nuclear magnetic resonance (NMR) provides a non-destructive method for quantifying porosity and characterising pore size distributions through measurement of hydrogen

atoms in pore fluids. When placed in a magnetic field, hydrogen nuclei in water or hydrocarbons align with the field and, upon application of radiofrequency pulses, produce measurable relaxation signals whose decay rates (T_1 and T_2 relaxation times) correlate with pore sizes. The technique exploits the principle that fluids in smaller pores relax faster due to increased surface-to-volume ratios and interactions with pore walls, allowing the T_2 distribution to be inverted into a pore size distribution. NMR offers several advantages over imaging methods: it samples bulk volumes (typically 1-100 cm^3), directly measures fluid-filled porosity without assumptions about pore geometry, and can distinguish between bound and free fluids, providing insights into permeability and fluid mobility. The method is widely used in both laboratory core analysis and well-logging applications, though it requires calibration against other porosity measurements and can be influenced by paramagnetic minerals, clay content, and the presence of multiple fluid phases that complicate signal interpretation (N. Zhang et al. 2021).

While each technique offers unique advantages in terms of resolution and contrast, the focus of this study is on X-ray CT imaging, which provides non-destructive, three-dimensional visualisation of pore structures at micrometer to millimeter scales, enabling detailed analysis of porosity distribution and connectivity in sedimentary rocks.

2.4.1 X-ray Computed Tomography

X-ray CT is a non-destructive imaging technique that reconstructs the internal structure of a sample in three dimensions based on the fundamental principle of X-ray photons attenuation as they pass through matter. This attenuation follows Beer's Law (Equation 2.5), which describes the exponential decay of X-ray intensity.

$$I = I_0 \cdot e^{-\int \mu(s)\, ds} \tag{2.5}$$

where:

- I is the transmitted X-ray intensity
- I_0 is the incident X-ray intensity

- $\mu(s)$ is the linear attenuation coefficient along the path s

During scanning, an X-ray source emits a beam that passes through the sample, and a detector measures the intensity of transmitted X-rays at multiple angular positions as the sample rotates. Materials with different densities and compositions attenuate X-rays to varying degrees, producing contrast in the recorded projections. Using computational reconstruction algorithms, these projections are combined to generate a three-dimensional grayscale volume composed of discrete volume elements (voxels), where each voxel represents the local X-ray attenuation coefficient define as CT value and expressed in Hounsfield Units (HU), and their size determines the spatial resolution of the scan. The spatial resolution of X-ray CT is determined by the detector pixel size, the geometric magnification, and the characteristics of the reconstruction filter. In porous media, regions of high attenuation in X-ray CT images correspond to the solid matrix, while low-attenuation regions represent pores or voids, enabling detailed visualisation and quantification of porosity, pore connectivity, and internal heterogeneity. However, when the characteristic size of pores or grains is smaller than the voxel dimension, a single voxel may contain a mixture of both solid and pore space, yielding an average of their attenuation CT values. This pore fraction which cannot be directly imaged is referred to as sub-resolution porosity (Cnudde and M. N. Boone 2013).

X-ray computed tomography techniques can be broadly categorised into medical CT, industrial CT, micro CT, nano CT and synchrotron-based CT, each offering distinct trade-offs between resolution and sample size. Medical CT is optimised for imaging large objects, typically achieving spatial resolutions of 50 to 100 µm for sample sizes up to tens of centimeters, making it suitable for large-scale structural characterisation but not fine pore-scale analysis. Industrial CT spans a wider range, with resolutions from tens of micrometers to a few millimeters, accommodating relatively large and dense samples such as engineering components and core plugs. Micro CT provides much higher resolutions, typically in the range of 1 to 10 µm voxel size, but with smaller sample sizes, generally a few millimeters to a few centimeters in diameter. Finally, synchrotron X-ray CT exploits the high brilliance and coherence of synchrotron radiation to achieve sub-micron to nanometer-scale resolution. However, it is restricted to very small samples, often less than a few millimeters and requires access to large-scale synchrotron facilities.

Nano-CT extends this capability further, reaching voxel sizes in the tens of nanometers, but is limited to extremely small samples, typically below 100–200 µm in diameter. Together, these CT modalities cover a broad spectrum of imaging needs, where the choice of technique is dictated by the balance between sample size and the resolution required to resolve the pore structures of interest (Philip J Withers et al. 2021).

In addition to the limitations of X-ray CT regarding the trade-off between spatial resolution and sample size, image artifacts can further complicate analysis. Beam hardening occurs when lower-energy X-rays are preferentially absorbed as they pass through the sample, producing non-uniform attenuation and streaks in the reconstructed image. Ring artifacts arise from imperfect detector calibration, appearing as circular bands that can obscure fine details. Material phase contrast can cause similar-attenuation phases to blend, making it difficult to distinguish between minerals or pore-filling materials. Noise, from both the X-ray source and detector electronics, reduces image clarity and can interfere with segmentation, especially at high resolution or in low-density regions (Boas, Fleischmann, et al. 2012; Wildenschild and Sheppard 2013). Finally, CT imaging is generally time- and data-intensive, requiring substantial computational resources for reconstruction and analysis, particularly for high-resolution scans that generate large datasets. Careful image processing and analysis procedures, including beam-hardening correction, ring artifact removal, noise filtering, and phase segmentation techniques, must be applied to mitigate these artifacts and ensure accurate quantitative interpretation of CT data (Iassonov, Gebrenegus, and Tuller 2009). Detailed information about these procedures are presented in Chapter 4.

2.5 Digital Rocks Physics and Applications

Digital rock physics (DRP) is an approach to understand subsurface reservoir properties by creating high-resolution three-dimensional digital representations of rock samples using X-ray CT imaging. These digital twins capture the complex pore geometries, mineral distributions, and structural heterogeneities at the pore scale (Sadeghnejad, Enzmann, and Kersten 2021; Dvorkin et al. 2011). By applying computational fluid dynamics, finite element methods, and statistical physics directly to these digital rock structures.

This approach allows to simulate fluid flow and transport (Bultreys, M. A. Boone, et al. 2016; Fusseis et al. 2014; Karlsons et al. 2022; Bijeljic, Mostaghimi, and Blunt 2013; Kurotori, Zahasky, Sally M Benson, et al. 2020), predict permeability and capillary pressure curves (Tanino and Blunt 2012; Patmonoaji et al. 2025), model single and multiphase flow behaviour (Blunt et al. 2013), elastic properties (Andrä et al. 2013b; Maire and Philip John Withers 2014), and enables rapid property prediction (C. F. Berg, O. Lopez, and Berland 2017), sensitivity analysis, and the investigation of scenarios that would be difficult or impossible to replicate in physical laboratory conditions.

The cornerstone of digital rock physics (DRP) models is the voxel-based discretization of high-resolution X-ray CT images into solid matrix and pore space, typically achieved through a segmentation process. This step is the primary source of uncertainty in DRP workflows, as it directly influences the accuracy of derived porosity, connectivity, and permeability. Segmentation is often user-dependent, relying on threshold selection or image-processing parameters (Andrä et al. 2013a; Schlüter et al. 2014; Alatrash and Velledits 2024), and the absence of a definitive ground truth makes it challenging to establish a single "correct" segmentation (S. Berg et al. 2018). Consequently, careful validation, sensitivity analysis, and, where possible, complementary experimental measurements are essential to ensure the reliability of DRP-based predictions.

After segmentation, the 3D binary volume can be used for direct quantification of porosity, pore size distribution and specific surface area with the caveat of a limited sample size. It also supports morphological analyses such as pore connectivity, tortuosity, and percolation pathways. Beyond direct measurements, binary images serve as computational domains for numerical simulations that predict petrophysical properties directly from pore-scale structures. Several numerical approaches are commonly employed, each with distinct advantages depending on the physical processes of interest and computational constraints, the following are among the most commonly deployed in DRP:

Finite Element Methods (FEM) excel at solving complex boundary value problems with irregular geometries. FEM applications include elastic property prediction, thermal conductivity calculation, and coupled flow-geomechanics problems. The flexibility of the method enables the incorporation of complex constitutive relationships and boundary conditions (W.-j. Xu, Yue, and Hu 2008; Y.-F. Yang et al. 2021).

Finite Difference Methods (FDM) provide computationally efficient solutions for regular grid geometries. Applications include steady-state flow simulation for permeability prediction and diffusion problems for formation factor calculation (Menke, Gao, et al. 2022; Qajar, Mohammadi, and Aghaei 2021; Alpak, Samardžić, and Frank 2018).

Lattice Boltzmann Methods (LBM) offer particular advantages for fluid flow simulation through their natural handling of complex boundaries and multi-phase systems. LBM enables simulation of transient flow phenomena, non-Newtonian fluids, and coupled transport processes (Y. Yang et al. 2018; Zahid and Cunningham 2025; Q. Liao et al. 2023).

Pore Network Models (PNM) provide simplified representations of pore structure through networks of pores connected by throats. While less detailed than direct simulation methods, PNM enables rapid property prediction and offers physical insights into controlling mechanisms (Shah et al. 2016; Moslemipour and Sadeghnejad 2021; Alyafei, Mckay, and Solling 2016; H. Zhang et al. 2021).

While these numerical approaches differ in formulation and level of detail, they all serve the purpose of simulating fundamental processes governing fluid and solute behaviour in porous media. Fluid flow through porous media involves complex interactions between viscous, capillary, and gravitational forces, with flow behaviour governed by fundamental physical principles that operate across multiple scales. To this end, it is important to understand the fundamental flow and transport processes occurring within porous media, including advection, the bulk fluid motion through connected pores driven by pressure gradients; diffusion, the molecular-scale spreading of solutes due to concentration gradients; and dispersion, the spreading of solute plumes caused by velocity heterogeneities at the pore scale, while sorption and chemical interactions at mineral surfaces can further influence transport (Vafai 2015). Together, these processes determine how fluids and solutes migrate through porous rock, and they form the foundation for the pore-scale simulations carried out in this study. (For the purpose of the present study, FDM will be deployed, extended details on method selection and application in Chapter 7).

2.6 X-ray Imaging Methods for Sub-Resolution Porosity Characterisation

Imaging methods have been developed to address the challenge of microporosity characterisation in geological samples. (Lin et al. 2016) introduced a differential imaging approach to resolve sub-resolution porosity in micro CT images of a carbonate sample (4.8 mm in diameter and 10 mm in length) by injecting high-salinity brine, thereby enhancing phase contrast between a brine-saturated scan and a corresponding dry scan. The two scans were accurately registered to align voxel positions and subsequently subtracted voxel by voxel, producing a differential image (Figure 2.6). This approach expanded the grey-value range, as reflected in the differential histogram, making it easier to define threshold values for segmenting solid, macro-, and micro-porosity. Two segmentation strategies were evaluated: (i) a histogram-based method relying on intensity gradients to distinguish phases (Otsu 1979; P.-S. Liao, Chen, Chung, et al. 2001), and (ii) a seed-growing method (Andrew, Bijeljic, and Blunt 2014). Following segmentation, histograms of each phase were analysed, with the peak of each distribution taken as the representative CT value for that phase, which was then used to estimate average sub-resolution porosity.

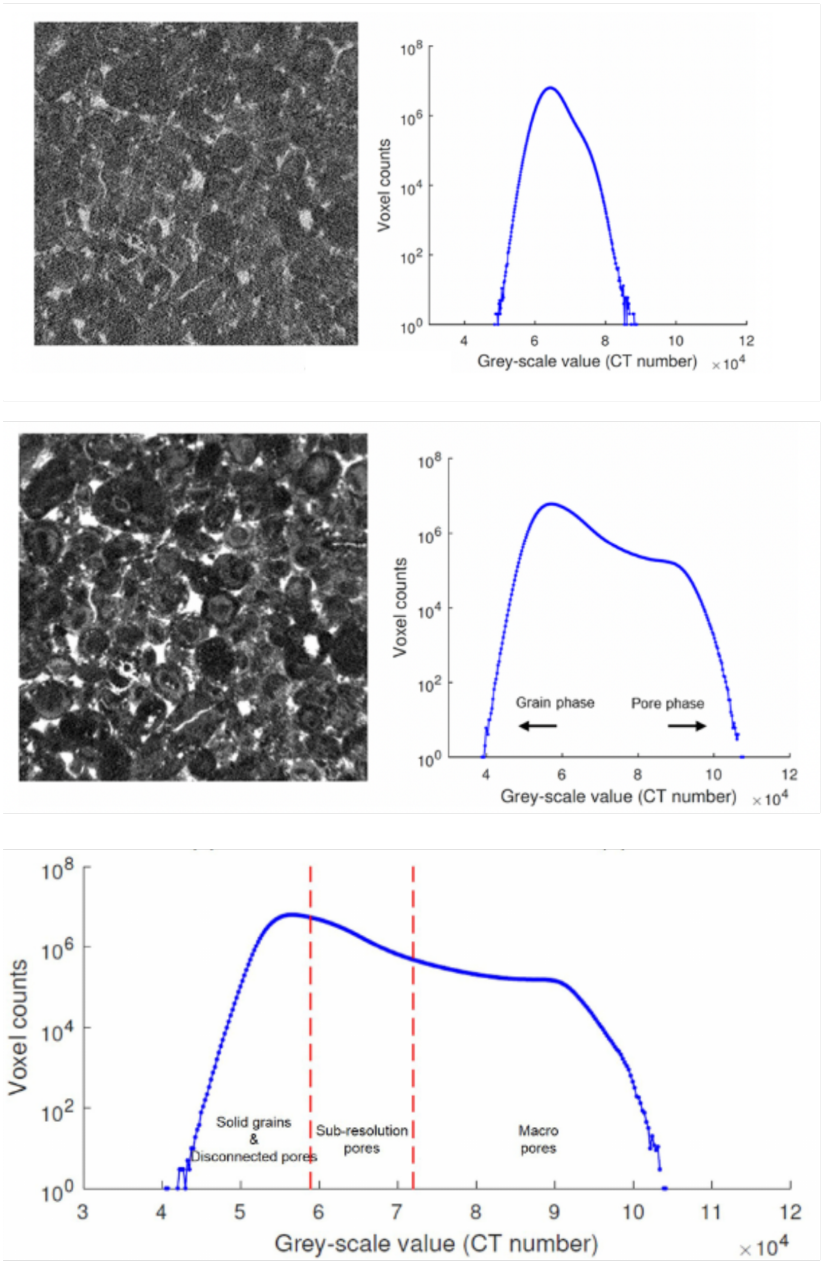


Figure 2.6: Segmentation approach using differential imaging by injecting high salinity brine. Top: differential image (brine at 5% concentration - dry). Middle: differential image (brine at 30% concentration - dry). Bottom: Threshold selection (red lines) for phases segmentation (Lin et al. 2016).

Another differential imaging approach using high-salinity brine injection to resolve sub-resolution porosity was presented by (Gao et al. 2019). Brine was injected into a heterogeneous carbonate sample (6 mm in diameter and 51 mm in length), where most of the porosity was associated with micropores, at incremental flow rates. By analysing the changes in grey-value intensity, solid material and macropores could be identified

as regions where grey values remained unchanged, while intermediate grey values that varied during brine injection were interpreted as microporous regions invaded by brine (Figure 2.7). The total porosity estimated from image analysis was 28.4%, of which 21.5% was attributed to microporosity. These results were lower than helium pycnometry measurements on the same sample (30.3%), suggesting that segmentation inaccuracies and unresolved porosity contributed to underestimation.

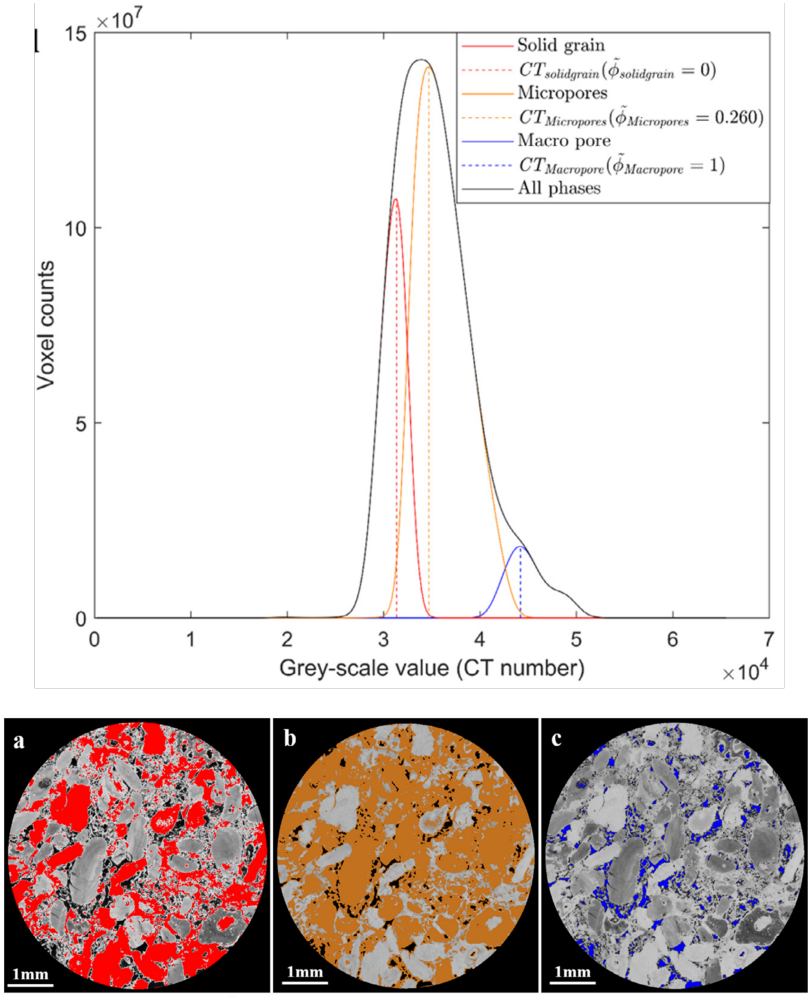


Figure 2.7: Top: Histogram of the different phases after segmentation. Bottom: Slice image showing the resulted phases segmentation (a. solid grain in red, b. micropores in orange, c. macropores in blue) (Gao et al. 2019).

(Mayo et al. 2015) proposed an approach to quantify sub-micron porosity using xenon as a contrasting agent in combination with an image subtraction segmentation method. Gases are advantageous over liquids as contrast agents because they can penetrate micropores

that may be inaccessible to liquids due to higher surface tension and capillary forces. The method exploits the X-ray absorption properties of gases, specifically the sharp change in their linear attenuation at characteristic absorption edges (34.55 keV for xenon) (Figure 2.8). Instead of scanning the sample before and after gas injection, the experiment involved acquiring two scans of the xenon-saturated sample (4 mm in diameter) at energies just below and just above the absorption edge, a capability made possible by synchrotron-based X-ray CT. Subtracting these two images highlighted regions invaded by xenon, producing a binary map of its distribution. Voxels containing both solid material and xenon-filled pores were distinguished from zero-xenon voxels representing the rock matrix, while the surrounding area reflected the attenuation of 100% xenon.

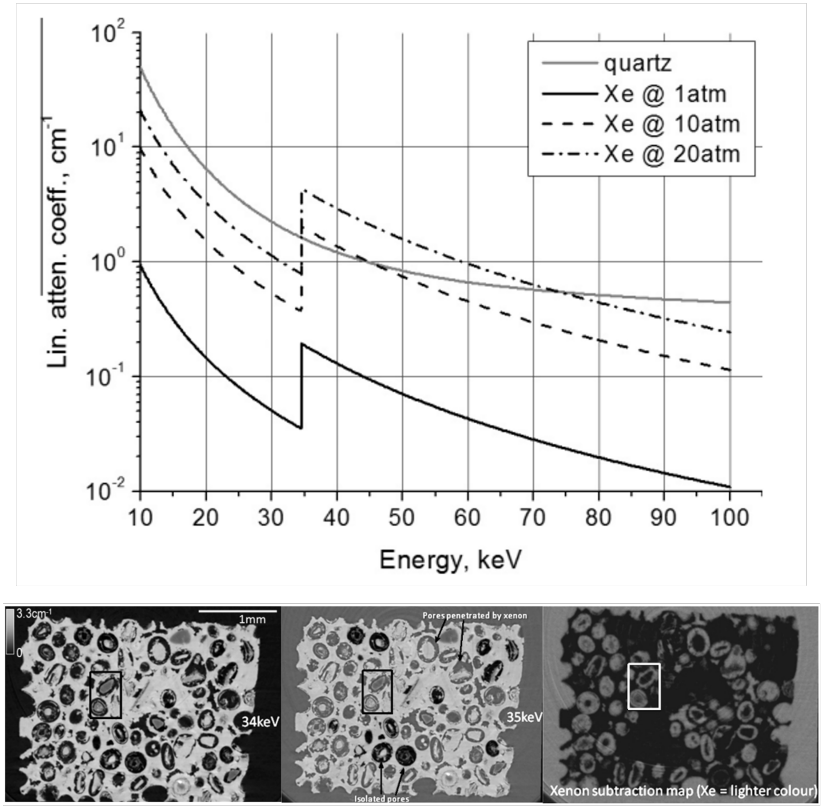


Figure 2.8: Top: Linear attenuation profile of xenon and quartz over different x-ray energy levels. Bottom left: Image of sample saturated with xenon at 34 KeV. Bottom center: Image of sample saturated with xenon at 35 KeV. Bottom right: Xenon distribution map after application of image subtraction representing porosity (Mayo et al. 2015).

While differential imaging methods show strong potential for resolving sub-resolution porosity, significant challenges remain for accurate quantification. Moreover, these

approaches are typically applied to very small samples suitable for micro CT imaging, analysing sub-volumes which may fail to capture porosity heterogeneity at larger scales. In this study, the objective is to characterise the multi-scale porosity of a representative heterogeneous sample. The selected specimens (1 cm in diameter and 4 to 6 cm in length) fall within the size range suitable for both medical CT and micro CT, as defined in Section 2.4.1. This dual applicability allows the extraction of different porosity types with each imaging modality, using image-based porosity quantification methods described in detail in Chapter 4.

The literature review highlights several knowledge gaps and research opportunities that this thesis aims to address. First, integration challenges remain in combining multi-scale characterisation data from different techniques, since no single imaging method covers the full range of relevant scales, and robust registration and correlation across scales are still underdeveloped. Second, improved workflows that link digital rock physics with conventional laboratory measurements are required to enhance characterisation reliability and better address the resolution–sample size trade-off. Third, validation remains limited, with a need for more systematic comparisons between digital rock predictions and experimental measurements. Fourth, advances in computational efficiency are necessary to enable the routine application of digital rock physics to larger, more representative sample volumes while keeping computational costs manageable. Finally, uncertainty quantification approaches require further development to provide meaningful confidence intervals for digital rock predictions and to support informed decision-making in reservoir management applications.

Chapter 3

Rock Samples: Geological Context and Petrophysical Properties

This chapter provides a detailed overview of the four rock samples that have been used throughout this study: Bentheimer Sandstone, Ketton Limestone, Nugget Sandstone, and Silurian Dolomite. These samples were strategically selected to represent a progression of increasing complexity in pore structure, ranging from relatively homogeneous, well-connected networks to heterogeneous dual-porosity systems commonly encountered in reservoir rocks.

The chapter is structured to provide: (1) geological descriptions establishing the petrophysical context of each sample, and (2) laboratory measurements of bulk porosity, which serve as a reference for evaluating and validating porosity estimates derived from image-based methods.

Sample sourcing: Bentheimer Sandstone, Ketton Limestone, and Nugget Sandstone were obtained from Kocurek Industries INC. (USA), while Silurian Dolomite was provided by Shell Global Solutions International B.V. (The Netherlands).

3.1 Bentheimer Sandstone

Bentheimer Sandstone is a Lower Cretaceous rock consisting predominantly of well-sorted, fine to medium-grained quartz grains (grain size range of 100-300 µm in diameter) with $<$3% clay content. The rock exhibits a relatively simple mineralogical composition, displays excellent sorting, and rounded grain morphology (Figure 3.1).

From a petrophysical perspective, Bentheimer Sandstone is characterised by high porosity (typically 20-26%) and permeability values in the range of 1-3 Darcy. The pore structure is predominantly intergranular with good connectivity, resulting in relatively homogeneous flow properties.

Its clean composition and well-understood pore geometry make it a benchmark material (Peksa, Wolf, and Zitha 2015) frequently used in digital rock physics studies (Wetzel, Kempka, and Kühn 2020) aimed at validating numerical methods, testing upscaling techniques (D. Zhang et al. 2025), and studying fundamental relationships between microstructure and transport properties due to its reproducible characteristics and availability of extensive experimental datasets (Anna L Herring et al. 2014; Blunt et al. 2013; Andersson et al. 2013; A. Herring et al. 2021).

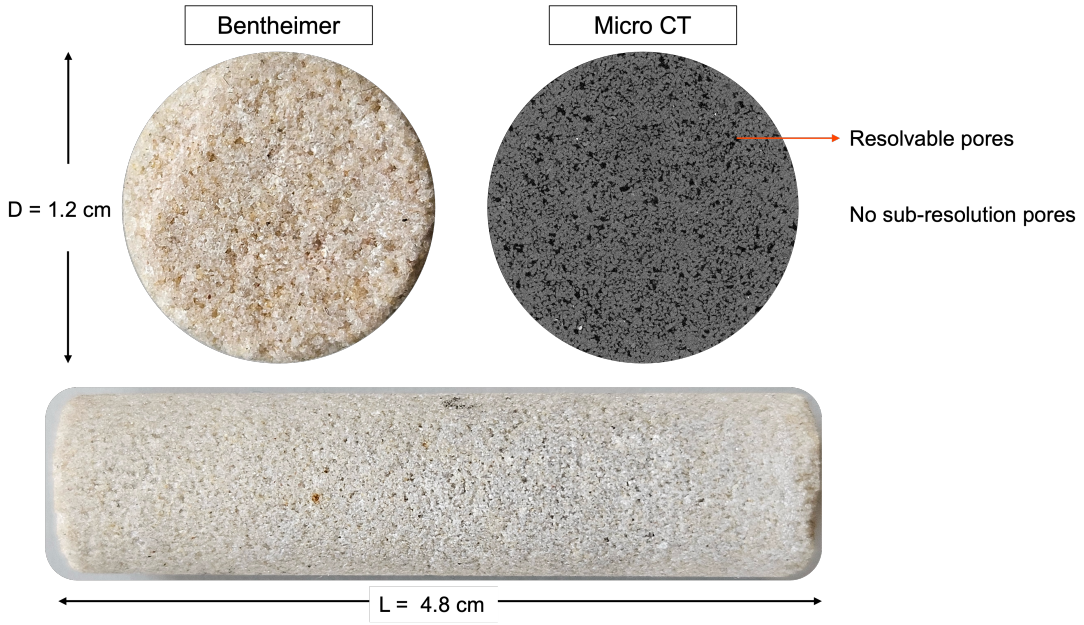


Figure 3.1: Photograph of the Bentheimer Sandstone cylindrical core sample and micro CT image showing the homogeneous internal pore structure. Dimensions: Diameter = 1.2 cm and Length = 4.8 cm.

3.2 Ketton Limestone

Ketton Limestone is an oolitic limestone from the Jurassic period. This carbonate rock is composed primarily of calcium carbonate in the form of well-developed spherical grains (Flügel and Munnecke 2010) predominantly ranging from 400-800 µm in diameter, cemented together in a relatively clean matrix (Figure 3.2). Ketton limestone displays moderate to high porosity (18-28%) with complex pore networks that include both intergranular and intragranular porosity within the ooids themselves. Permeability values typically range from 0.5-2 Darcy, with significant heterogeneity due to the dual-porosity nature of the rock. The limestone serves as an excellent model system for studying carbonate reservoir rocks in digital rock physics applications. Its distinctive dual-porosity structure, availability of high-resolution imaging data, and representation of important reservoir rock types make it valuable for testing pore-scale modeling approaches (Rücker et al. 2020), investigating multiphase flow behavior (Singh et al. 2017), chemical transport (Kurotori, Zahasky, Sally M Benson, et al. 2020), and understanding the relationship between geological processes and petrophysical properties in carbonate systems.

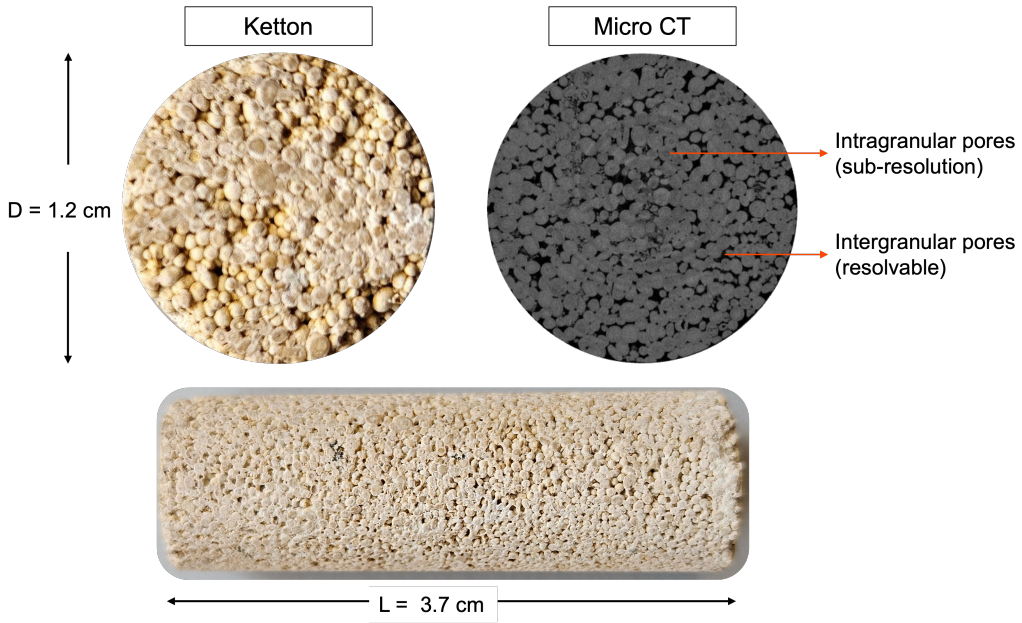


Figure 3.2: Photograph of the Ketton Limestone cylindrical core sample and micro CT image showing only the resolvable intergranular pore space. Dimensions: Diameter = 1.2 cm and Length = 3.7 cm.

3.3 Nugget Sandstone

Nugget Sandstone is a Late Triassic sandstone formation found across the western United States, particularly well-exposed in Utah, Wyoming, and Colorado. This formation represents ancient desert dune deposits and is characterised by large-scale cross-bedding, well-rounded fine to medium-grained sand and excellent sorting (Figure 3.3). It is composed almost entirely of quartz grains with trace amounts of feldspar and heavy minerals. The petrophysical properties of Nugget Sandstone are highly variable due to its stratified nature that results in porosity anisotropy. Porosity ranges from less than 5% to over 20%, while permeability varies from microdarcy to several hundred millidarcies, depending on the degree of quartz cementation and compaction. The sandstone commonly exhibits complex pore systems with both primary intergranular porosity and secondary porosity from partial dissolution of quartz cement (Lindquist 1988). In digital rock studies, Nugget Sandstone provides insights into the effects of diagenesis on reservoir quality (Keele and Evans 2008) and has been used to test flow distribution in compacted pore geometries (Dalton, Crandall, and Goodman 2020).

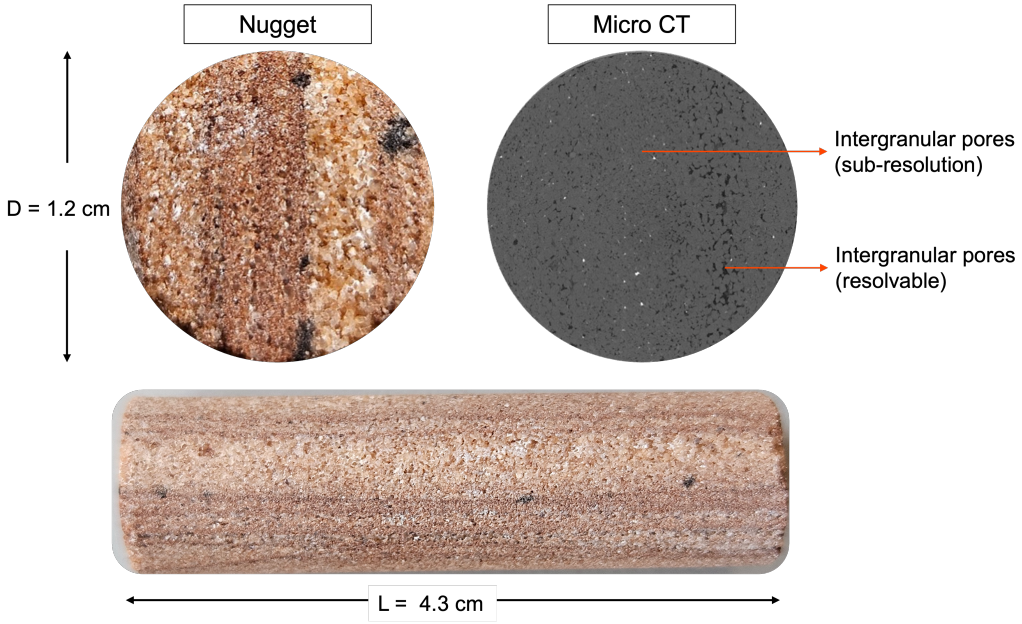


Figure 3.3: Photograph of the Nugget sandstone cylindrical core sample and micro CT image showing the layering system in the sample. Dimensions: Diameter = 1.2 cm and Length = 4.3 cm.

3.4 Silurian Dolomite

Silurian Dolomites are carbonate rocks originally deposited as shallow marine limestones during the Silurian period and later transformed through dolomitisation, a diagenetic process in which calcium carbonate is replaced by calcium-magnesium carbonate. The dolomitisation process often preserves original sedimentary structures while modifying the mineralogy and pore structure. Silurian Dolomites commonly exhibit fine crystalline (micritic) textures characteristic of dolomite (Figure 3.4). Silurian Dolomites display highly variable properties depending on the extent and style of dolomitisation. Porosity can range from less than 2% in tight, completely dolomitised sections to over 30% in zones where dolomitisation created significant secondary porosity through mineral replacement and dissolution. Permeability is similarly heterogeneous, from nanodarcies to several Darcies, often controlled by the connectivity of the dolomite crystal network and the presence of fractures or vugs. The complex pore systems in dolomites make them challenging subjects for digital rock analysis. These rocks are particularly valuable in digital rock studies for developing new imaging and modeling techniques capable of handling multi-scale heterogeneity in carbonate reservoir rocks.

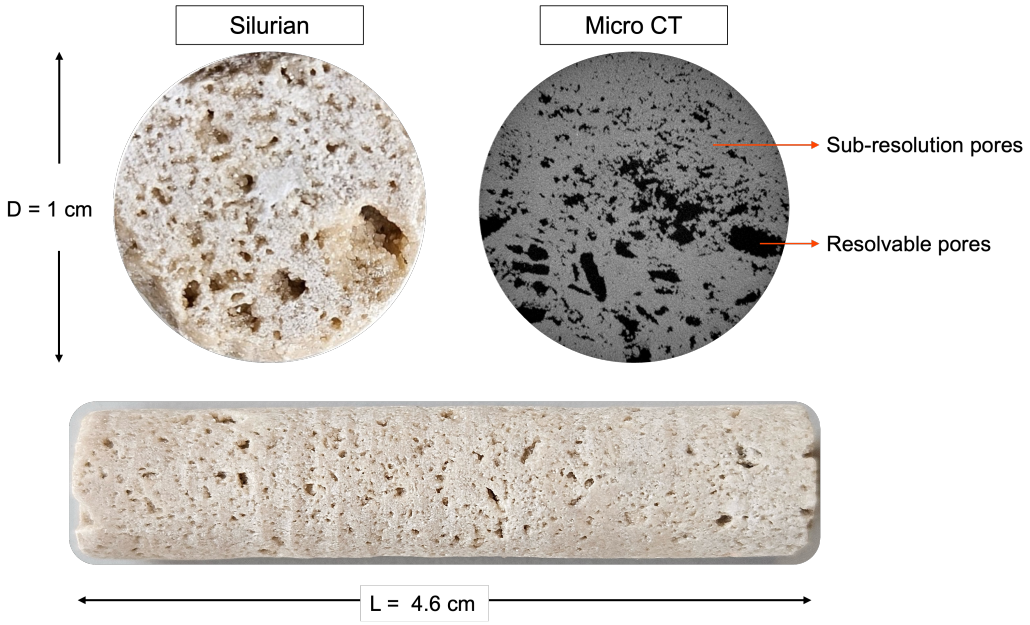


Figure 3.4: Photograph of the Silurian Dolomite cylindrical core sample and micro CT image showing the complex porosity heterogeneoty. Dimensions: Diameter = 1 cm and Length = 4.6 cm.

Table 3.1 provides a comprehensive overview of the key petrophysical properties of the four rock samples investigated in this study. The listed parameters include porosity, permeability, mineral composition, and characteristic grain textures, as reported in the literature. Collectively, these descriptors define the structural and petrophysical nature of each sample. The compiled values offer essential baseline data and serve as reference points for validating bulk porosity estimation methods. This systematic comparison highlights the geological diversity of the selected samples, ranging from simple intergranular pore structures to more complex dual-porosity systems.

	Bentheimer Sandstone	**Ketton Limestone**
Age	Early Cretaceous	Middle Jurassic
Composition	Quartz (>90%)	Calcite (>90%)
Porosity	20–26%	18–28%
Permeability	1–3 Darcy	0.5–2 Darcy
Texture	Well-sorted, quartz	Oolitic to micritic
Depositional Environment	Fluvial to shallow marine	Shallow marine carbonate platform
	Nugget Sandstone	**Silurian Dolomite**
Age	Late Triassic	Silurian
Composition	Quartz (>95%)	Dolomite ($CaMg(CO_3)_2$)
Porosity	5–25%	5–20%
Permeability	10 mD–1 Darcy	1 mD–1 Darcy
Texture	Cross-bedded, fine to medium grain	Crystalline, vuggy, moldic
Depositional Environment	Eolian and fluvial	Shallow marine, dolomitised

Table 3.1: Summary of geological and petrophysical properties of the rock samples selected on this study.

3.5 Bulk Porosity Characterisation

This section outlines the standard laboratory methods used to measure bulk porosity of the rock samples and presents the corresponding porosity values obtained from each technique. Multiple independent measurements were employed to ensure reliability and provide comprehensive characterisation of the pore systems. The different methods offer complementary information about pore connectivity, while their comparison enables assessment of measurement uncertainty and identification of potential pore system complexities.

3.5.1 Vacuum Saturation (Archimedes Method)

Sample Preparation: Samples were initially dried in an oven at 80°C for 24 hours to remove residual moisture from the pore space. The dry weight of each sample (W_{dry}) was recorded using an analytical balance.

Vacuum Saturation Set-up: Samples were placed in a two-neck Erlenmeyer flask connected to a vacuum saturation apparatus. The side-arm port was connected to a vacuum pump, while the main neck was fitted with tubing leading to a container of de-ionised water, Density (ρ_w) at room temperature was defined at 0.998 g/cm^3. A valve in the water line was initially kept closed to perform an initial evacuation step, (see Figure 3.5).

Evacuation and Saturation Process: The vacuum pump was activated to remove air from the flask and sample pores for six hours, achieving complete degassing. Following evacuation, the water container valve was carefully opened, allowing de-ionised water to slowly fill the flask until samples were completely covered, and then the valve was closed. Samples remained under vacuum saturation for a minimum of twelve hours to ensure complete pore filling, particularly for low-permeability samples.

Saturated Weight Measurement: Upon completion of saturation, samples were removed and gently rolled on paper towels to achieve a saturated surface-dry condition,

removing excess surface water while maintaining full pore saturation. The saturated weight (W_{sat}) was immediately recorded. Pore volume (V_p) was calculated using:

$$V_p = \frac{W_{sat} - W_{dry}}{\rho_w} \tag{3.1}$$

Bulk Volume Determination: Bulk volume was measured using the buoyancy method. A beaker filled with deionised water was placed on an analytical balance, with an aluminum wire basket suspended from a stand positioned above the beaker. The empty basket was submerged to a predetermined depth, the balance was zeroed, and the immersion depth was marked for consistency. Each sample was placed in the basket, lowered to the marked depth, and the submerged weight (W_{sub}) corresponding to the displaced fluid was recorded (see Figure 3.5). Bulk volume (V_b) was calculated as:

$$V_b = \frac{W_{sub}}{\rho_w} \tag{3.2}$$

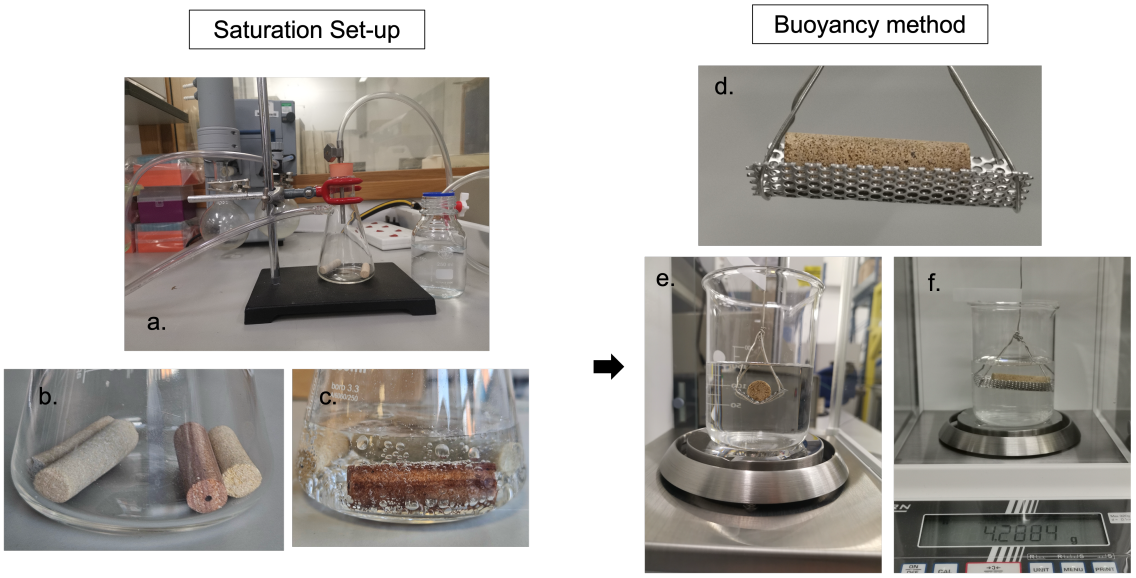


Figure 3.5: Experimental set-up for the Vacuum saturation-Archimedes' method for bulk porosity measurements. a. Vacuum saturation set-up showing the samples in the flask connected to the vacuum pump and saturation fluid. b. Dry samples. c. Samples during saturation step. d. Saturated sample placed in the basket. e. and f. Samples submerged applying the buoyancy method.

Porosity Calculation: Porosity was determined using $\phi = \frac{V_p}{V_b}$. To assess measurement precision and account for experimental uncertainty, the entire procedure was repeated twenty times for each sample, and the mean bulk porosity value with standard deviation was calculated as shown in Table 3.2

Sample	$\overline{W_{dry}}$ **(g)**	$\overline{W_{sat}}$ **(g)**	$\overline{W_{sub}}$ **(g)**	$\overline{V_p}$ **(cm³)**	$\overline{V_b}$ **(cm³)**	$\overline{\phi}$ **(-)**
Bentheimer Sandstone	10.716	11.926	5.112	1.213	5.122	$\mathbf{0.237 \pm 0.004}$
Ketton Limestone	8.069	8.962	3.707	0.895	3.714	$\mathbf{0.241 \pm 0.007}$
Nugget Sandstone	11.006	11.559	4.332	0.554	4.340	$\mathbf{0.127 \pm 0.004}$
Silurian Dolomite	8.011	8.419	3.419	0.408	3.426	$\mathbf{0.119 \pm 0.005}$

Table 3.2: Summary of averaged vacuum saturation-Archimedes method measurements for the four rock samples.

3.5.2 Helium Pycnometry

A custom helium pycnometer was built to accommodate the specific sample dimensions, enabling porosity measurements on intact samples without the need for sub-sampling or cutting. The set-up also allowed for vacuum evacuation and operating at high pressures. Figure 3.6 presents both the schematic diagram and photograph of the pycnometer apparatus.

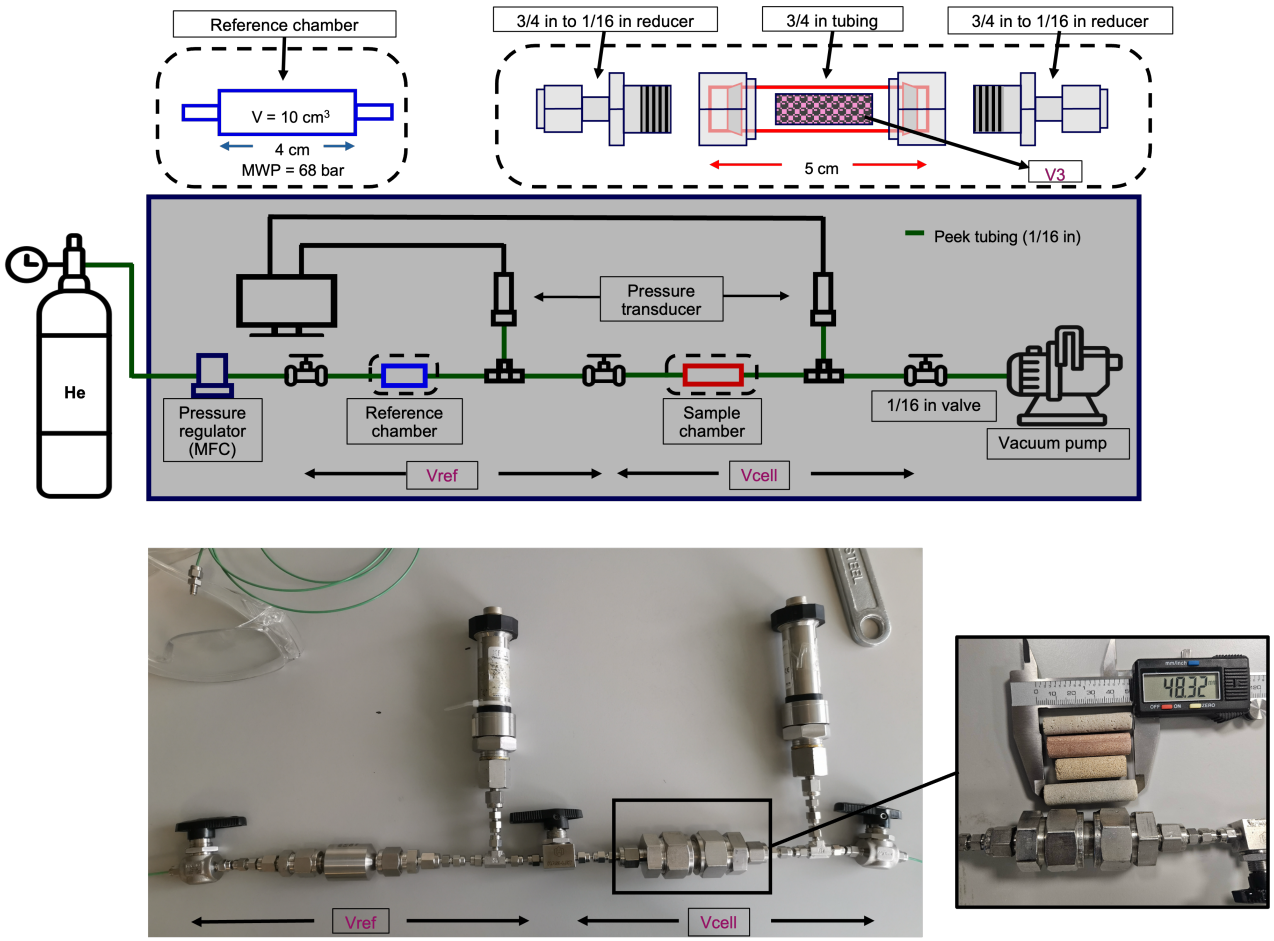


Figure 3.6: Diagram of the custom built helium pycnometer.

Calibration Procedure: The pycnometer operates on the principle of gas expansion from a reference cell to the sample chamber. Prior to sample analysis, a calibration procedure was required to determine the reference cell volume (V_{ref}) and sample cell volume (V_{cell}), including all connecting fittings. Since both volumes were unknown, two mole balance equations were established and rearranged in terms of density and volume using the relationship $n = \rho \cdot V$. The first equation was derived with an empty sample cell, while the second incorporated a known reference volume. The second term on the left-hand side of both equations is zero, as the sample cell is initially under vacuum with no gas moles present.

Empty sample cell:

$$\rho_{ref1}V_{ref} + \cancel{\rho_{cell}V_{cell}} = \rho_{eq1}(V_{ref} + V_{cell}) \tag{3.3}$$

Steel balls in sample cell:

$$\rho_{ref2}V_{ref} + \cancel{\rho_{cell}V_{cell}} = \rho_{eq2}(V_{ref} + V_{cell} - V_{balls}) \tag{3.4}$$

where:

ρ_{ref1} = *Reference cell initial gas density in measurements with empty sample cell, mol/cm³*

V_{ref} = *Reference cell volume, cm³*

ρ_{cell} = *Sample cell initial gas density in measurements with empty sample cell, mol/cm³*

V_{cell} = *Sample cell volume, cm³*

ρ_{eq1} = *Gas density after equilibration in measurements with empty sample cell, mol/cm³*

ρ_{ref2} = *Reference cell initial gas density in measurements with steel balls in sample cell, mol/cm³*

ρ_{eq2} = *Gas density after equilibration in measurements with steel balls in sample cell, mol/cm³*

V_{balls} = *Stainless steel volume, cm³*

For calibration, fifteen stainless steel spheres with 0.8 cm diameter were employed, providing a total known volume of 3.992 cm^3 (V_{balls}). To minimise temperature fluctuations associated with pressure changes, the entire apparatus was immersed in an ice bath throughout the calibration process.

Gas densities were determined by inputting the experimentally measured pressures (P_{ref} and P_{eq}) and temperatures from the calibration experiments into the NIST Thermophysical Properties WebBook assuming ideal gas relationship $\rho = P/(ZRT)$. For helium, under the experimental conditions of 40–50 barg (4–5 MPa) and 2–3 °C (275–276 K), the deviation from ideal-gas behaviour is small but non-negligible. At these pressures and temperatures, helium exhibits Z1.005, corresponding to a deviation of approximately 0.5% from ideality. This deviation was therefore included in the overall volume uncertainty analysis.

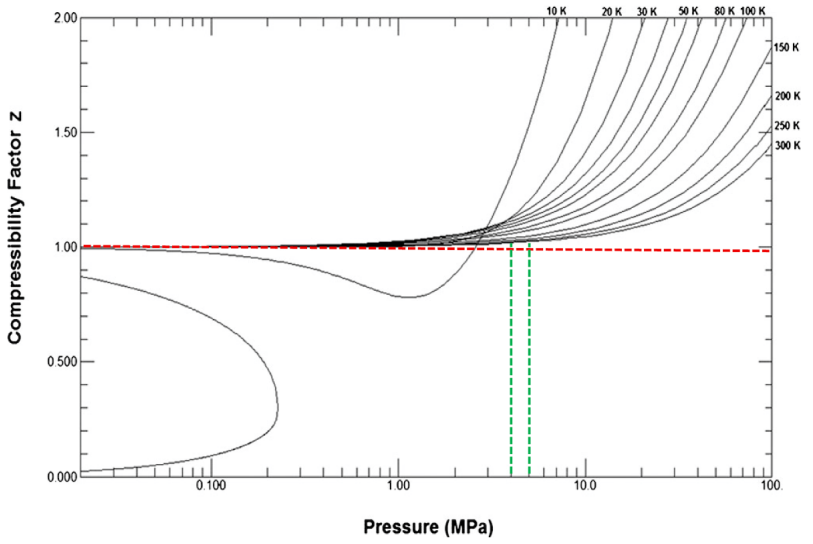


Figure 3.7: Compressibility factor (Z) for helium extracted from the CERN Library Catalogue (Van Sciver, Timmerhaus, and Clark 2012). The red line denotes the compressibility factor Z=1 and the red lines the experimental operating temperature and pressures.

The experimental procedure to obtain the required pressures followed a systematic valve operation sequence. Initially, the left valve (LV) was closed while the middle valve (MV) and right valve (RV) remained open to the vacuum pump, evacuating the entire system. Upon achieving stable vacuum conditions, MV was closed and LV was opened to introduce high-purity helium into the reference cell at a predetermined pressure (P_{ref}). For the calibration step, four measurements were taken at 50 barg and four at 40 barg. LV was then closed, isolating a known quantity of gas moles within V_{ref}. After P_{ref} stabilised, RV was closed and MV was opened, allowing gas expansion into V_{cell} and resulting in a lower equilibrium pressure (P_{eq}). Results are shown in Figure 3.8, notice the higher P_{eq}

when the steel balls are introduces and the temperature fluctuation was kept between 0.5°C and 1°C, respectively.

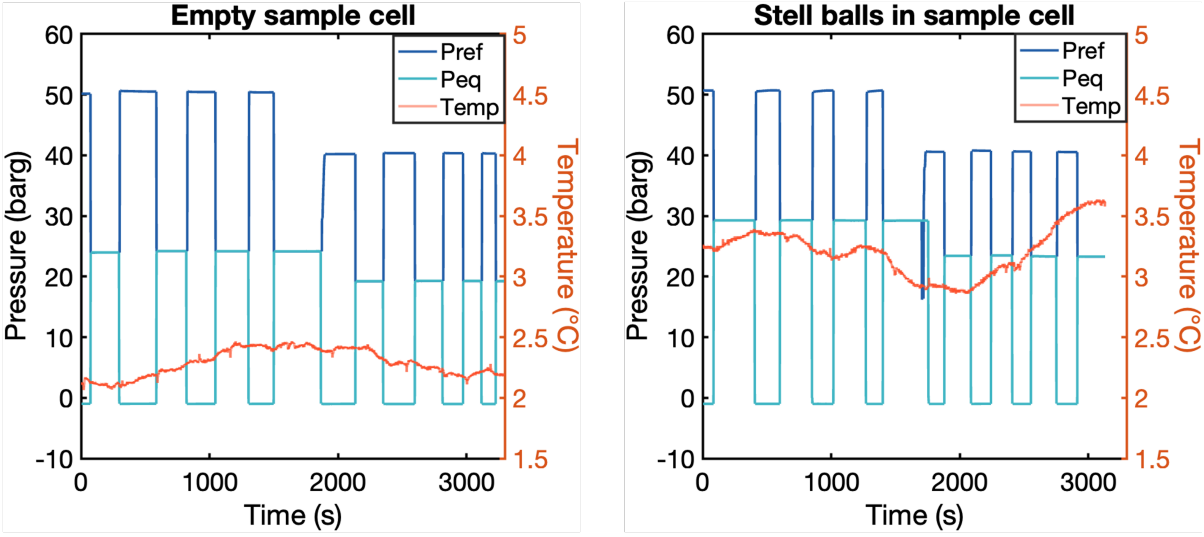


Figure 3.8: Pressure and temperature reading for the calibration step of the helium pycnometer.

Equations (3.3) and (3.4) were solved simultaneously to determine V_{ref} and V_{cell}. Eight measurements at each calibration stage enabled a comprehensive uncertainty analysis through permutation of the measurement combinations, with results presented in Figure 3.9. The reference cell volume (V_{ref}) was determined to be 12.213 ± 0.174 cm^3, while the sample cell volume (V_{cell}) was 12.436 ± 0.146 cm^3. These uncertainties include both the measurement-derived variability and the additional uncertainty arising from the non-ideality of helium, incorporated through root-sum-square propagation of the deviation of the compressibility factor Z from unity.

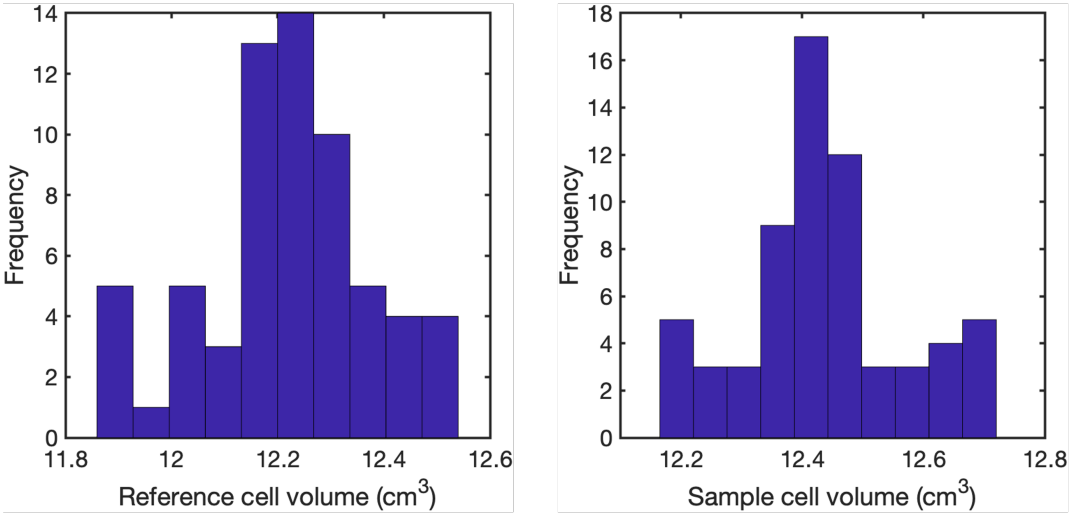


Figure 3.9: Histogram of reference- and sample cell volume estimation.

Porosity Calculation: Once the cell volumes were determined, grain volume measurements (V_g) were conducted for each sample following the same experimental protocol described above. Prior to measurement, samples were oven-dried at 80°C for 24 hours and then placed into the sample cell. Pressure and temperature readings were recorded before and after gas equilibration to determine the corresponding gas densities. In this case, V_{balls} in Equation (3.4) was replaced with the unknown grain volume V_g. Solving this modified equation for V_g yields Equation (3.5). Porosity was then calculated using $\phi = \frac{V_b - V_g}{V_b}$, employing the bulk volume (V_b) previously obtained from the vacuum saturation-Archimedes method. Porosity values for the four samples are shown in Table 3.3

$$V_g = \frac{\rho_{eq}(V_{ref} - V_{cell}) - \rho_{ref} V_{ref}}{\rho_{eq}} \tag{3.5}$$

Sample	$\overline{\rho_{ref,50barg}}$ $(\frac{mol}{cm^3})$	$\overline{\rho_{eq,50barg}}$ $(\frac{mol}{cm^3})$	$\overline{\rho_{ref,40barg}}$ $(\frac{mol}{cm^3})$	$\overline{\rho_{eq,40barg}}$ $(\frac{mol}{cm^3})$	$\overline{V_g}$ $(\mathbf{cm^3})$	$\overline{V_b}$ $(\mathbf{cm^3})$	$\overline{\phi}$ (-)
Bentheimer	2191.6	1290.8	1779.3	1048.5	3.915	5.122	$\mathbf{0.236 \pm 0.006}$
Ketton	2191.8	1225.9	1773.2	991.8	2.813	3.714	$\mathbf{0.242 \pm 0.008}$
Nugget	2216.9	1298.4	1785.7	1045.9	3.796	4.340	$\mathbf{0.125 \pm 0.008}$
Silurian	2196.0	1235.1	1749.7	984.1	2.934	3.426	$\mathbf{0.143 \pm 0.009}$

Table 3.3: Summary of averaged helium pycnometry measurements for the four rock samples.

3.5.3 Mercury Intrusion Capillary Pressure

While the previous methods were performed on samples designated for X-ray CT imaging, pore throat size distributions were obtained using mercury intrusion porosimetry (Micromeritics AutoPore IV) on separate, smaller cylindrical plugs approximately 1.2 cm in diameter and 1.2 cm in length. Six Bentheimer Sandstone samples, seven Ketton Limestone samples, two Nugget Sandstone samples, and six Silurian Dolomite samples were analysed. Although this approach provides valuable insights into pore throat size distributions, the results should be considered complementary rather than directly comparative to the X-ray CT samples, as variations in pore morphology may exist between different plugs, particularly in heterogeneous samples such as Nugget Sandstone and Silurian Dolomite.

Mercury intrusion porosimetry (MICP) operates on the principle that mercury, being a non-wetting fluid with high surface tension, requires external pressure to overcome the capillary forces at pore throat entrances. It relates the applied pressure to the diameter of pore throats accessible at that pressure. During the measurement, mercury was progressively injected into the samples under increasing pressure ranging from 0.03 to 2275 bar, with the corresponding volume of mercury intrusion recorded at each pressure step. Since mercury preferentially enters larger pores at lower pressures and progressively smaller pores as pressure increases, the pressure-volume relationship provides information about the pore throat size distribution.

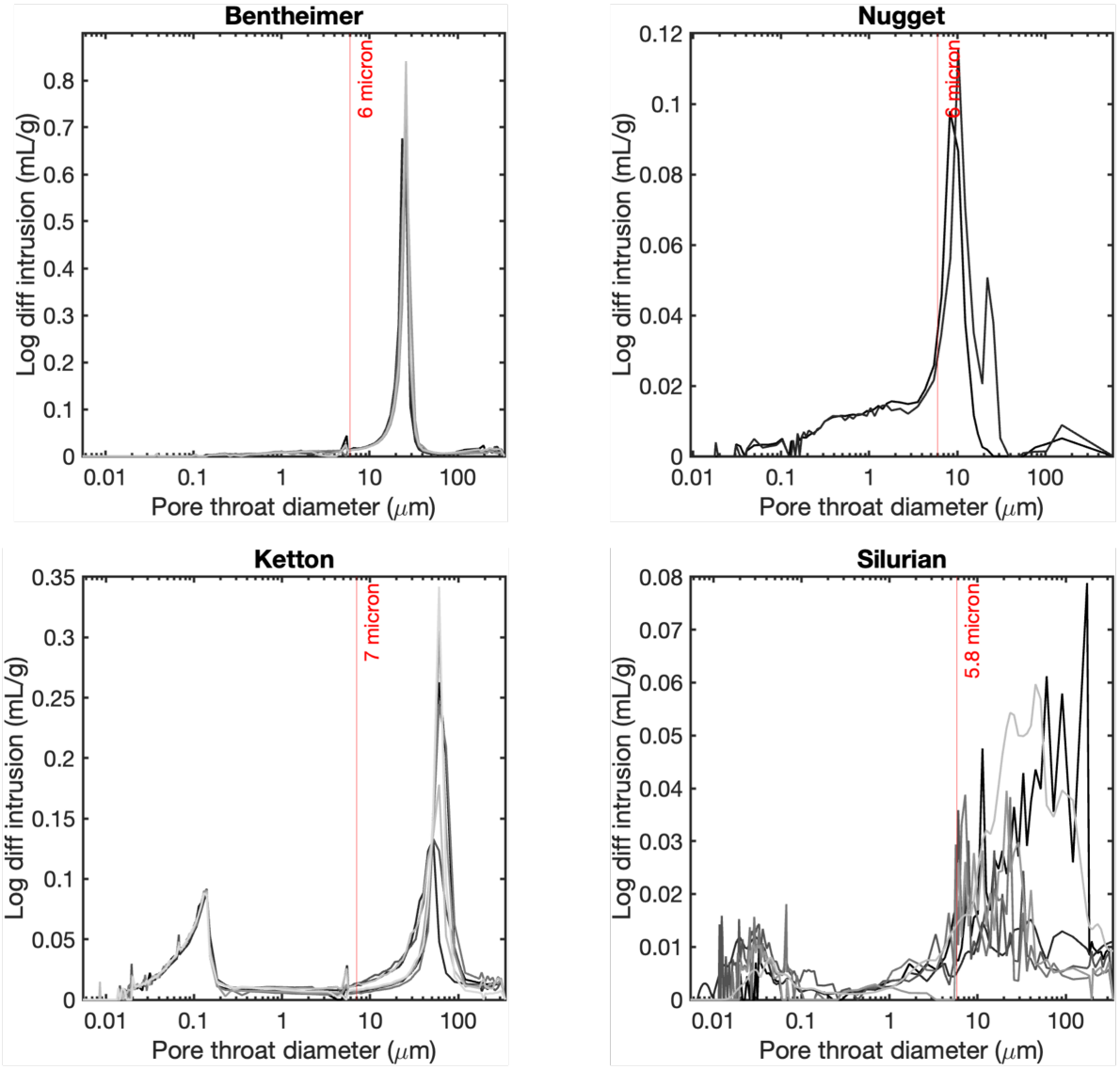


Figure 3.10: Pore throat size distributions obtained from mercury intrusion porosimetry for the four rock samples.

Figure 3.10 presents the pore throat size distribution characteristics for each rock type, the red vertical line serves as a reference for the X-ray CT resolution limit which for the high resolution micro CT could range between 1 and 10 µm depending on sample size and scanning parameters, the values correspond to the acquired resolution of each sample. This suggests that the pores to the right of the red line are potentially resolvable by micro CT imaging, while the pores to the left of the red line correspond to sub-resolution pores.

Bentheimer Sandstone exhibits a relatively homogeneous, unimodal distribution with

a narrow peak centered around 20 µm, indicating a well-connected and uniform pore network. Ketton Limestone displays a bimodal distribution with two sets of throat sizes. The smaller peak likely represents sub-resolution porosity within ooids grains (intragranular porosity) ranging from 0.01 to 0.2 µm, while the larger peak corresponds to pore throats between ooids (intergranular porosity) from 10 to 100 µm. Nugget Sandstone shows a broader distribution with a main peak around 5 µm likely representing larger pores layers, and a significant population of smaller pores ranging from 0.01 to 2 µm. Silurian Dolomite exhibits the most complex and heterogeneous pore throat distribution with each sample displaying multiple peaks at different sizes, reflecting the intricate pore structure created by dolomitisation processes. Overall, most samples exhibit a substantial portion of pore throats exceeding 1 µm reaching sizes over 100 µm, and a subset of smaller sub-micron pore throats ranging from 0.01 to 0.3 µm.

A proportion of the porosity above and below the 1 µm threshold was estimated by integrating the area under the pore throat distribution curve on either side of the 1 µm reference point. These values represent the fraction of pore volume associated with resolvable and sub-resolution pores, respectively. The results are presented in Table 3.4, along with total porosity values derived from MICP by dividing the cumulative volume of mercury intruded into the sample by its independently measured bulk volume.

Sample	$\phi_{<1m}$ (%)	$\phi_{>1m}$ (%)	ϕ (-)
Bentheimer Sandstone	2.42	97.58	0.242
	3.34	96.66	0.239
	2.33	97.67	0.228
	2.77	97.23	0.233
	3.10	96.90	0.236
	2.43	97.57	0.231
Average	**2.73**	**97.27**	$\mathbf{0.235 \pm 0.005}$
Ketton Limestone	34.64	65.36	0.222
	39.88	60.12	0.244
	36.36	63.64	0.249
	33.93	66.07	0.248
	34.35	65.65	0.246
	36.27	63.73	0.244
	37.27	62.73	0.242
Average	**36.10**	**63.90**	$\mathbf{0.242 \pm 0.009}$
Nugget Sandstone	25.09	74.91	0.121
	20.42	79.58	0.143
Average	**22.76**	**77.24**	$\mathbf{0.132 \pm 0.016}$
Silurian Dolomite	4.49	95.51	0.165
	27.47	72.53	0.081
	29.99	70.01	0.077
	20.00	80.00	0.084
	15.23	84.77	0.081
	7.00	93.00	0.145
Average	**17.36**	**82.37**	$\mathbf{0.106 \pm 0.039}$

Table 3.4: Summary of porosity values obtained from MICP, including total porosity and the proportion of pore volume associated with pore throats below and above 1 µm.

3.6 Concluding Remarks

This chapter presented a comprehensive overview of the geological characteristics and porosity architecture of four rock types: Bentheimer Sandstone, Ketton Limestone, Nugget Sandstone, and Silurian Dolomite. The selected samples represent a systematic progression of increasing pore system complexity, ranging from well-sorted sandstones with predominantly intergranular porosity to heterogeneous carbonates exhibiting multi-scale pore networks with vuggy and microporous characteristics.

Porosity quantification using three independent methods (vacuum saturation-Archimedes, helium pycnometry, and mercury intrusion porosimetry) demonstrated excellent agreement for homogeneous samples such as Bentheimer Sandstone, while significant discrepancies emerged for heterogeneous rocks, particularly Silurian Dolomite. These variations reflect the complex pore connectivity and spatial heterogeneity inherent in diagenetically altered carbonates. Mercury intrusion porosimetry provided detailed pore throat size distributions that revealed distinct patterns across lithologies and enabled quantitative distinction between resolvable (>1 µm) and sub-resolution (<1 µm) pore contributions.

Together, the geological descriptions and bulk porosity measurements obtained through independent laboratory methods provide a solid foundation for understanding pore structure heterogeneity and its impact on fluid flow and transport in the studied rocks. These insights are essential for validating the porosity characterisation derived from the image-based methodology proposed in this study.

Chapter 4

The Dual-Resolution X-ray CT Method for Porosity Quantification

This chapter presents the experimental methodology used to characterise the internal structure and properties of rock samples, with a particular emphasis on extracting sub-resolution features of the pore space.

The experimental workflow was designed to meet the specific research objectives of quantifying the scale and extent of the resolved ('macro') and unresolved ('micro') porosity of rocks using digital rocks analysis techniques. It covers procedures for sample preparation, scanning protocols, image reconstruction, and quantitative image analysis.

The methodology is presented in a structured manner, beginning with the selection and preparation of rock samples, followed by details on the scanning techniques and parameters employed, and concluding with post-processing and analysis of the resulting data.

To capture the full spectrum of pore sizes present in the rock samples, a combined imaging approach was implemented using medical X-ray computed tomography (medical CT) and high-resolution X-ray micro-computed tomography (micro CT). This dual-modality approach enables a multi-scale characterisation of the samples, facilitating both macroscopic analysis of large-scale features such as: fractures, vugs, bedding structures, and microscopic examination of fine pore networks that govern fluid flow and solute transport. By integrating data across these spatial scales, the methodology provides a more comprehensive representation of the internal architecture of the rock, linking structural heterogeneity at the core scale with averaged pore-scale geometries that influence transport processes.

Each imaging technique offers distinct advantages for characterising the pore space. The operational differences between scanners provide complementary pathways for accurate porosity quantification.

4.1 Methodology Description

4.1.1 Effective Porosity Calculation from Medical CT Imaging

Medical CT is a fast acquisition imaging technique (on the order of seconds) that allows the sample to be scanned multiple times, quickly implement changes to scan under different conditions, and avoid external disruption of the experimental set-up that could compromise outcomes. Fast scanning consistency and repeatability ensures a reliable image output. The downside of this scanning technique is the maximum spatial resolution it is capable of generating. As detailed in Chapter 2 (equipment scanning conditions) and Chapter 3 (sample dimensions), the maximum achieved voxel resolution was 27 µm in x and y coordinates of the slices plane and the slice thickness denotes the voxel depth which was 500 µm. At this resolution, features smaller than the voxel such as fine pores or grains cannot be individually resolved. Instead, the CT number (voxel greyscale value) represents the average X-ray attenuation across all materials within the voxel, influenced by both the amount of solid material and void space, as well as density variations.

Despite this resolution limit, medical CT has proven effective for porosity characterisation through the widely used "differential imaging" technique (Jeandey et al. 1990). In this method, the same rock sample is scanned while saturated with two fluids of different densities, leading to changes in the CT number that correlate with the fluid-filled pore volume. Pure fluids exhibit distinct linear attenuation coefficients that translate into theoretical CT numbers (e.g., air $\approx$ 1000 HU, water $\approx$ 0 HU). Because the density of the rock matrix remains constant, shifts in the CT number between the dry and saturated states reveal the pore space occupied by the fluid in each voxel. To ensure complete saturation, the wetting fluid was introduced in the sample at high pressure during the image acquisition (40 bar), which is higher than the capillary pressure needed to ensure

complete saturation of all the pore space based on the rearranged Young-Laplace equation which relates pore radius to pressure difference and surface tension (Equation 4.1). For a saturating pressure of 40 bar the pore throat radius is 36 nm, sufficient to saturate the sample based on the pore throat radius of the samples obtained by MICP and the pore connectivity of the samples.

$$r = \frac{20\gamma \cos\theta}{\Delta P} \tag{4.1}$$

where:

- r is the pore throat radius, µm
- γ is the water-air surface tension, 0.072 N/m
- θ is the contact angle, samples are water-wet θ<30°, assume $\cos\theta$ 1
- ΔP is the saturating pressure, bar

This technique allows the construction of a 3D porosity map. The porosity obtained represents all the connected pores in the sample where the saturating fluid was able to penetrate and it is defined as the total effective porosity (ϕ_E).

Effective porosity (ϕ_E) is calculated using the following expression:

$$\phi_E = \frac{CT_{\text{vox},s} - CT_{\text{vox},d}}{CT_{\text{water}} - CT_{\text{air}}} \tag{4.2}$$

where:

- ϕ_E is the effective porosity (–)
- $CT_{\text{vox},s}$ is the CT number of the saturated voxel (HU)
- $CT_{\text{vox},d}$ is the CT number of the dry voxel (HU)
- CT_{water} is the CT number of water (typically 0 HU)

- CT_{air} is the CT number of air (typically –1000 HU)

An additional calibration step was performed to accurately determine the CT values of the pure fluids—air and the saturating fluid (water)—which are essential for computing porosity using Equation 4.2. These values are used in the denominator of the differential imaging equation and must reflect the actual scanner response under the experimental conditions. To obtain them, two vials filled respectively with water and air were scanned under the same medical CT set-up and using identical scanning parameters to those applied to the core samples. This ensured consistency in image acquisition and minimized scanner-induced variability.

The measured CT values slightly deviated from the theoretical expectations, with water yielding $CT_{\text{water}} = 39$ (HU) and air yielding $CT_{\text{air}} = -1024$ HU. These deviations are attributed to scanner calibration and imaging artifacts but were consistent across measurements, making them reliable for use in porosity calculations. The results of this calibration are illustrated in Figure 4.1.

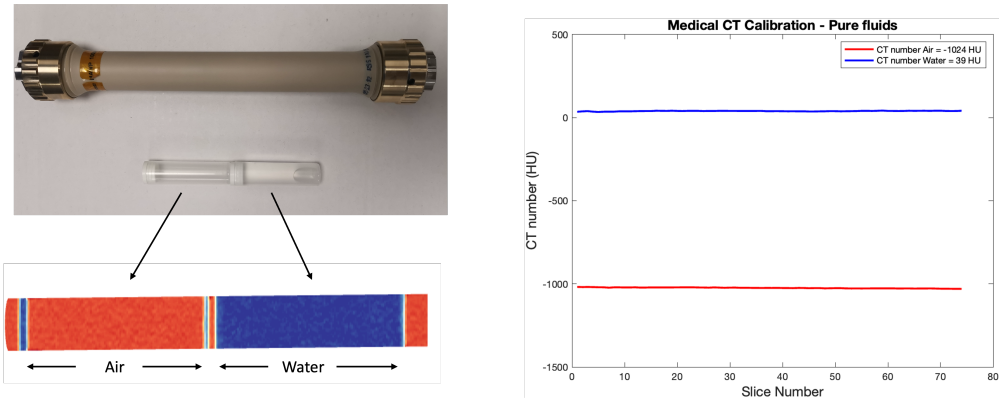


Figure 4.1: Calibration step showing CT values of pure fluids (air and water) scanned under identical conditions to the core samples, used for porosity calculation via differential imaging

4.1.2 Resolved Porosity Calculation from Micro CT Imaging

Micro CT is an X-ray technique which generates images of higher resolution (voxel size = 1–10 μm^3), allowing the inspection of smaller features within the rock and a more

direct porosity calculation. Despite the benefits on resolution, significant longer scanning time (hours) is the main disadvantage because it relates to a number of problems such as: inconsistency in the greyscale level at different points across the length of the sample or blurring issues due to movement of the sample or set-up during scanning (motion artifacts).

The preferred method to measure porosity from the greyscale images is a segmentation process, which consists of defining voxels corresponding to solid material and pore space according to the gray values across the image. Porosity can then be calculated by the following equation.

$$\phi_R = \frac{N_p}{N_p + N_s} \tag{4.3}$$

where:

- ϕ_R is the resolved porosity (–)
- N_p is the number of voxel representing pore space after segmentation
- N_s is the number of voxels representing solid material after segmentation

The combined use of medical CT and micro CT imaging was essential for characterising the full range of porosity heterogeneity in the rock samples. This approach enabled the classification of porosity into resolved porosity (ϕ_R), corresponding to "macropores", and unresolved porosity (ϕ_U), corresponding to "micropores". For the purposes of this thesis, microporosity is arbitrarily defined as pore space below the resolution limit of the micro CT scanner (<7µm). Resolved porosity encompasses pore structures and features that directly influence macroscopic flow behavior. In contrast, unresolved porosity represents sub-resolution pore networks that are not captured in conventional imaging but play a critical role in transport processes, largely governed by capillary forces and diffusive transport mechanisms.

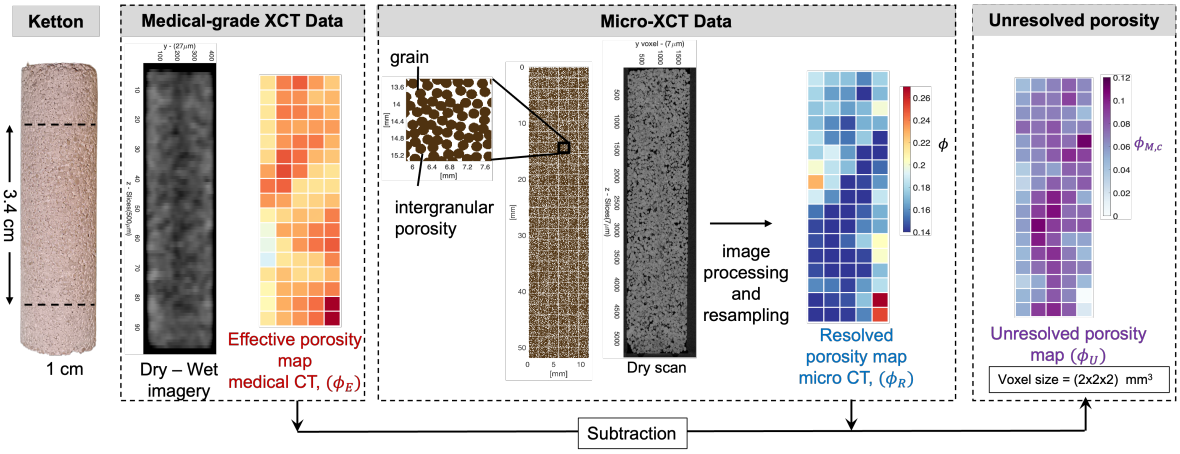


Figure 4.2: Graphical description of the proposed methodology to quantify unresolved porosity spatially using dual-imaging methods.

Figure 4.2 presents a graphical overview of the dual-imaging methodology used to quantify and spatially resolve unresolved porosity in porous rock samples.

Starting from the left, a photograph of a cylindrical Ketton limestone sample is shown, annotated with its meso-scale dimensions (1 cm diameter and 5.6 cm length). The dashed region indicates the selected section for quantitative analysis, this was selected for comparison across the four samples given they have diverse lengths.

In the next panel, medical grade CT data are displayed. A sample of the tomographic cross-section of the rock which was used to apply the differential imaging method. Since medical CT has a relatively low resolution, individual pore spaces are not resolved at the grain scale. However, the difference in attenuation between the dry and saturated states (highlighted as a "Dry – Wet" intensity difference) enables the derivation of effective porosity maps through differential imaging. The resulting map, labelled as "Effective porosity map" ϕ_E, provides volumetric porosity values encompassing both resolved and unresolved pore regions.

The central panel focuses on micro CT data, which provide significantly higher spatial resolution, sufficient to resolve intergranular porosity at the grain scale. A representative zoom-in illustrates the microstructure, showing clearly defined solid grains and interstitial pore spaces. A dry scan of the entire core section is then processed to generate a resolved porosity map ϕ_R through direct segmentation of the pore space based on grayscale thresholds. This detailed imaging permits quantification of the porosity that is directly visible within the micro CT resolution limits.

The "Subtraction" arrow indicates the key computational step in the methodology. By subtracting the resolved porosity map ϕ_R obtained from micro CT from the effective porosity map ϕ_E obtained from medical CT, one can derive the unresolved porosity ϕ_U. This component accounts for porosity not visible at the micro CT resolution, such as submicron-scale pores or microporous textures within grains or cementing material.

The rightmost panel summarises this outcome by presenting a spatial map of unresolved porosity ϕ_U, calculated as the difference between the total and resolved porosity maps voxel by voxel. This step spatially localises the microporosity within the sample volume and enables quantification of its distribution along the sample length.

In conclusion, the figure illustrates a robust workflow that leverages multi-scale imaging to decompose total porosity into resolved and unresolved components, enabling a more comprehensive characterisation of the pore structure in heterogeneous geological materials.

4.1.3 Methodology Sensitivity

The accuracy of the multi-scale porosity characterisation presented in this work depends critically on three key image processing steps: registration, noise removal, and segmentation. Each of these steps introduces potential uncertainties that can propagate through the analysis and affect the final porosity maps and flow simulations.

Image registration: Image registration is essential for aligning multi-scale X-ray datasets acquired at different resolutions and for correcting sample movement during scanning. Misalignment between high-resolution microporosity scans and lower-resolution macroporosity datasets can lead to spatial inconsistencies in the integrated porosity maps. Registration assumes no deformation between scans, which may be an incorrect assumption if the sample experienced compression or thermal expansion between acquisitions. Tests performed on repeated scans of the same sample region showed registration errors typically below 2-3 voxels (equivalent to 10-15 µm at high resolution), but these errors can accumulate when integrating data across multiple scales. In regions with limited textural contrast or homogeneous mineral composition, registration

algorithms may converge to local minima, producing systematic spatial offsets. To assess this sensitivity, registration were performed using multiple initial conditions and evaluated the consistency of porosity distributions in overlapping regions. Variations in total porosity estimates due to registration uncertainty were found to be less than 0.5%, though local variations could reach 1-3% in highly heterogeneous zones.

Noise treatment: X-ray micro-CT data inherently contains noise from various sources including photon counting statistics, detector artifacts, beam hardening, and ring artifacts from detector element variations. The choice of noise filtering approach significantly impacts the preservation of small pores while suppressing spurious features. Aggressive filtering using large kernel sizes or strong edge-preserving filters effectively reduces noise but can blur pore boundaries and eliminate genuine microporosity, leading to underestimation of porosity and altered pore size distributions. Conversely, insufficient noise removal results in false identification of noise as pores during segmentation, inflating porosity values and introducing artificial heterogeneity. Multiple filtering approaches were tested including Gaussian filtering, median filtering, and NLM filtering with varying parameters. Results showed that porosity estimates could vary by 5-12% depending on filter selection, with the largest sensitivity observed in the micropore fraction where pores approach the resolution limit. The optimal filtering parameters were determined by visual inspection of known pore structures and validation against independent measurements, selecting parameters that preserved edges while achieving favourable signal-to-noise ratios in homogeneous regions.

Segmentation: The partitioning of grayscale images into distinct phases (pore vs. matrix)—represents perhaps the most critical and subjective step in the workflow. The choice of segmentation method and threshold values directly determines which voxels are classified as pores, fundamentally affecting all subsequent analyses. Global thresholding methods assume uniform imaging conditions throughout the sample, which is often erroneous due to beam hardening, scatter, or variations in local mineral composition. Local adaptive thresholding can account for spatial variations in grayscale values but introduces additional parameters requiring optimization. More sophisticated approaches such as watershed segmentation, machine learning-based classification, or indicator kriging offer improved accuracy but require training data or significant computational resources.

We evaluated segmentation sensitivity by varying threshold values by ±5% around the optimal threshold determined from histogram analysis and porosity calibration. This threshold variation produced porosity changes of 3-8%, with the largest sensitivity in regions containing partial volume effects or pores near the resolution limit. The segmentation uncertainty also affects pore connectivity and tortuosity calculations, which are highly sensitive to the presence or absence of narrow pore throats that may fall below the imaging resolution. To mitigate these effects, we employed a combination of grayscale-based segmentation with morphological operations (opening/closing) to remove isolated noise voxels while preserving genuine pore connectivity. Validation against independent measurements (MICP) and visual inspection of segmented results in representative sub-volumes provided confidence that the chosen segmentation approach captured the essential pore structure.

4.2 Experimental Workflow

4.2.1 Experimental Apparatus

A custom-designed core holder was commissioned from RS-Systems (Norway) to accommodate meso-scale rock samples (schematic shown in Figure 4.3). The body of the core holder is made of PEEK, a material preferred for X-ray imaging due to its excellent radiolucency and high mechanical strength. These properties enable clear X-ray visualisation while maintaining the structural integrity required for pressurised experiments. The ring nuts and end cap stems are made of aluminum; however, these components were located outside the scanning field of view and did not interfere with image quality.

The core holder supports samples up to 12.5 mm in diameter and 120 mm in length. It is rated for a maximum working pressure of 100 bar, allowing high confining pressure to ensure full saturation of the rock sample.

The sample was placed between two PEEK end caps and wrapped in a Viton sleeve, which

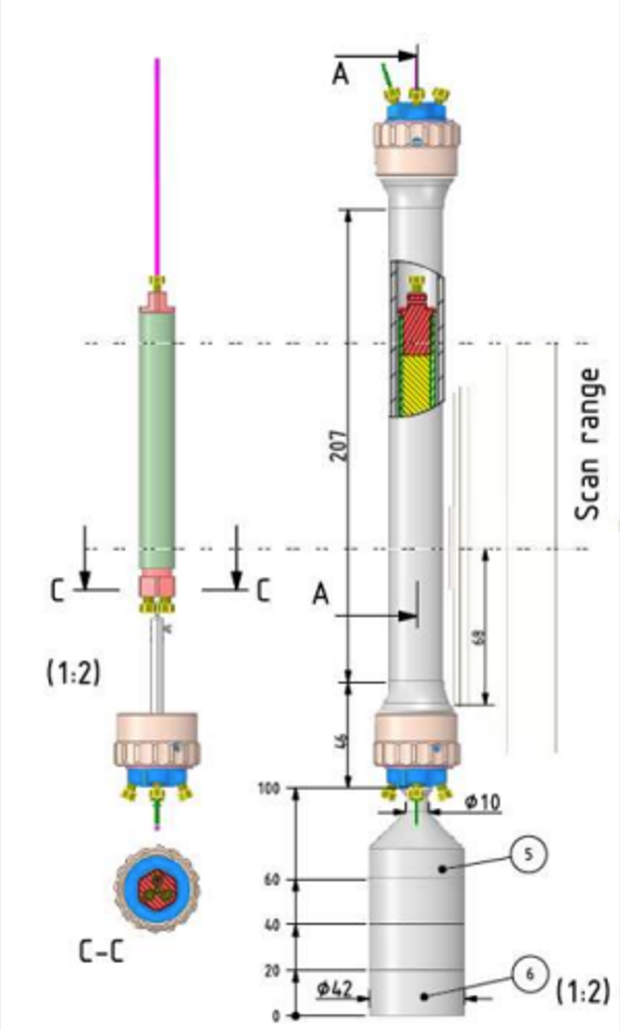


Figure 4.3: Schematic of the custom-designed core holder used for X-ray CT scanning of rock samples. Adapted from (RS-Systems 2021).

also covered the outer surfaces of the end caps. Each end cap is equipped with three $^1/_{16}$ inch ports for fluid handling. One port on each end cap was used for fluid injection and withdrawal. A second port on each end was connected to pressure transducers to monitor the pressure differential across the sample. The remaining ports were sealed with blind plugs.

The sample and end caps were assembled inside the core holder, and the ring nuts were tightened at both ends. Each ring nut has four $^1/_{16}$ inch ports. At the inlet side, three ports were used: two for flow lines connected to the end cap, and a third for injecting confining pressure fluid into the annular space between the Viton sleeve and the inner wall of the core holder. At the outlet side, two ports were used to connect to the outlet end cap.

The same set-up was used to scan the samples sequentially, first in the micro CT scanner and then in the medical CT scanner. Once the sample was placed inside the core holder and the apparatus fully assembled, the next step involved applying the confining pressure. The dedicated flowline (blue line in Figure 4.4) was connected to a piston-driven syringe pump (Teledyne ISCO, model 1000D). During this step, a blind plug on the outlet ring nut was removed to allow air to escape. Water was then pumped into the core holder to fill the annular space between the sample and the inner wall of the core holder. Once water began to overflow through the opening, the blind plug was reinserted, and the confining pressure was gradually increased to 30 bar.

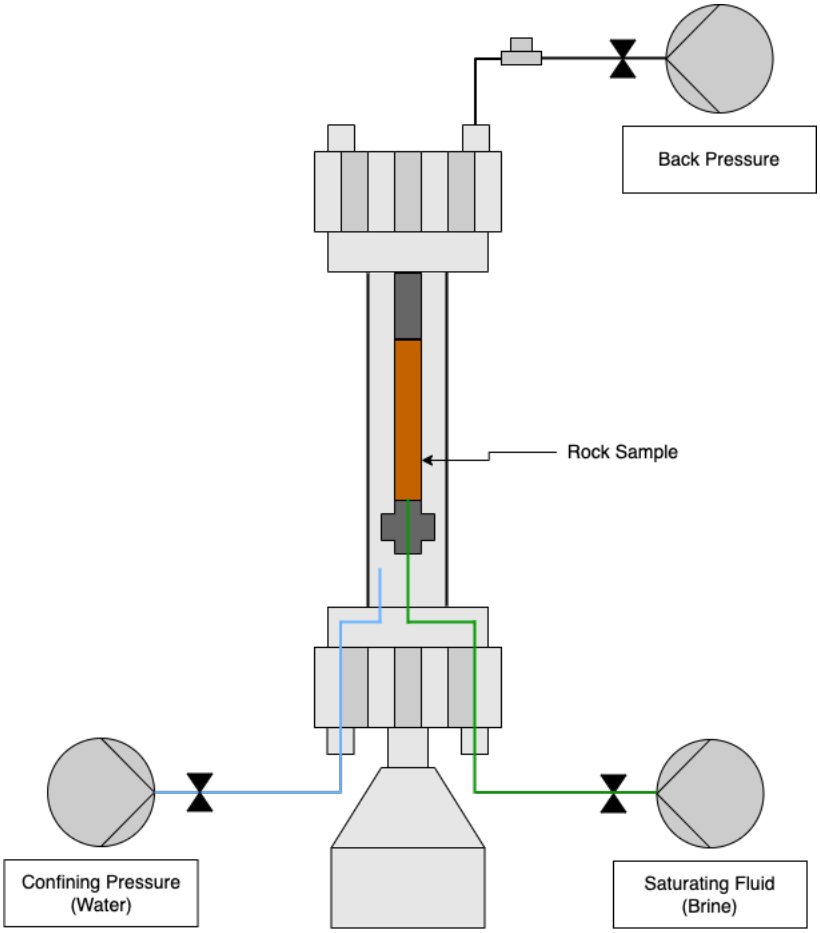


Figure 4.4: Schematic of the experimental setup, illustrating the mounted core holder and flowline connections to hydraulic pumps used for applying confining pressure and for fluid injection during sample saturation.

4.3 Image Acquisition

After assembly, the mounted set-up was transferred to the micro CT scanner (Skyscan 1273, Bruker) for scanning under dry conditions. To minimise motion artifacts and ensure consistent image quality, the core-holder was securely fixed on the rotational stage, held tightly in place by metal screw clamps attached to the stage base and positioned as close as possible to the X-ray source to achieve the highest spatial resolution, as this distance directly affects the resulting voxel size. The scan length was chosen to ensure that the image field of view included part of the PEEK end-caps, allowing future co-registration with images obtained from the medical CT scanner.

The scanning parameters were optimised individually for each rock type based on density and desired resolution. Table 4.1 summarises the scanning conditions used for each sample.

Parameter	**Bentheimer**	**Ketton**	**Nugget**	**Silurian**
Rotation step angle (deg)	0.2	0.2	0.15	0.15
Source voltage (kV)	90	110	90	100
Source current (µA)	88	72	88	80
Source spot size	Small	Small	Small	Small
Frame averaging	2	3	2	2
Distance to source (mm)	53.5	40.2	40.1	38.9
Filter	Al 1 mm	Cu 0.3 mm	Al 1 mm	Al 1 mm + Cu 0.3 mm
Voxel size (µm)	6.0	7.0	6.0	5.8
Scan duration (h:mm)	35:35	14:24	30:00	59:45

Table 4.1: Micro CT scanning parameters used for image acquisition of each rock sample.

The preprocessing of the raw projections included flat-field correction and dark-field subtraction to reduce noise and eliminate detector anomalies. Image reconstruction was performed using the software *NRecon* (Skyscan 1273, version 2.1.0.1). The reconstruction settings included a beam hardening correction coefficient of 60% and ring artifact correction set to level 20.

While the scanning protocol provided high-resolution images of internal pore structures, limitations such as beam hardening in highly dense regions and long scan durations in some samples posed practical constraints. These issues were mitigated by careful parameter tuning and post-reconstruction quality treatments. ; the choice of filters for each sample was guided by the need to reduce beam hardening while preserving sufficient contrast in low-attenuation pore regions. Higher-density or compositionally heterogeneous rocks, such as Ketton and Silurian dolomite, required the inclusion of a Cu filter (alone or in combination with Al) to harden the X-ray spectrum and minimise streaking artifacts. In contrast, lower-density sandstones such as Bentheimer and Nugget achieved optimal contrast-to-noise ratios with a 1 mm Al filter, which provided adequate attenuation of low-energy photons without excessively reducing signal intensity.

After completion of micro CT scanning, the same core-holder assembly was carefully transferred and placed horizontally onto the medical CT scanner bed (Toshiba Aquilion 64 - TSX-101A). The scanning protocol was selected on the basis of the optimal greyscale distribution to enhance contrast between phases (prior test results are shown in Figure 4.5). The preferred reconstruction kernel was the “bone” setting, which applies a high-frequency filter optimised for sharpness and fine-detail detection in high-density materials. An additional enhancing filter (FC30-UE0) was applied to further improve edge definition. The scanning mode was set to "helical", and parameters were kept constant across all samples: source voltage = 120 kV, source current = 200 mA, and slice thickness = 0.5 mm.

Following a procedural scanner warm-up, the field of view was configured to encompass the entire length of the core sample, including both inlet and outlet end caps. Particular attention was paid to aligning the sample longitudinally along the scanner axis to minimise

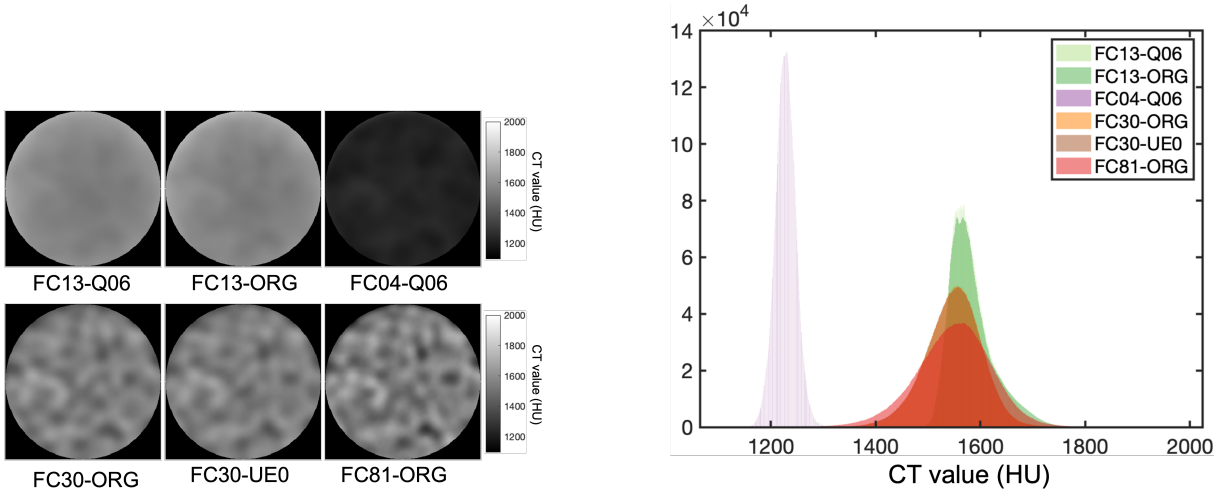


Figure 4.5: Bentheimer image comparison test highlighting the differences of protocol selection for optimal medical CT image acquisition. FC04 and FC13 denotes reconstruction function for scanning "body" and FC30, FC81 for "bone". ORG is the scanning option with no filter, where UE0 denotes "enhancement filter" and Q06 for " quantum denoising filter".

any angular deviation or positional offset. To ensure repeatability and capture potential variability, six consecutive scans were acquired under dry conditions, with the core-holder assembly remaining fixed in position throughout the scanning sequence.

The sample saturation procedure involved an initial flushing with gaseous CO_2 to displace air from the pore space and facilitate subsequent water infiltration. This was followed by the injection of the saturating fluid (deionised water) at a constant flow rate of 2 mL/min. Throughout the injection, the pressure drop across the sample was closely monitored, while also maintaining pressure offset between the sample and the confining pressure at $\Delta P = 30$ bar. The pore pressure was gradually increased until it reached 40 bar, at which point full saturation of the pore space was assumed based on stabilisation of the pressure response and pore entry pressure of 10 bar for well sorted sandstones and 30 bar for Ketton. A limitation on saturation pressure exists as the maximum working pressure of the core-holder cell is 100 bar. A second set of six consecutive scans was acquired under saturated conditions, with the core-holder remaining in place to preserve alignment with the dry scans.

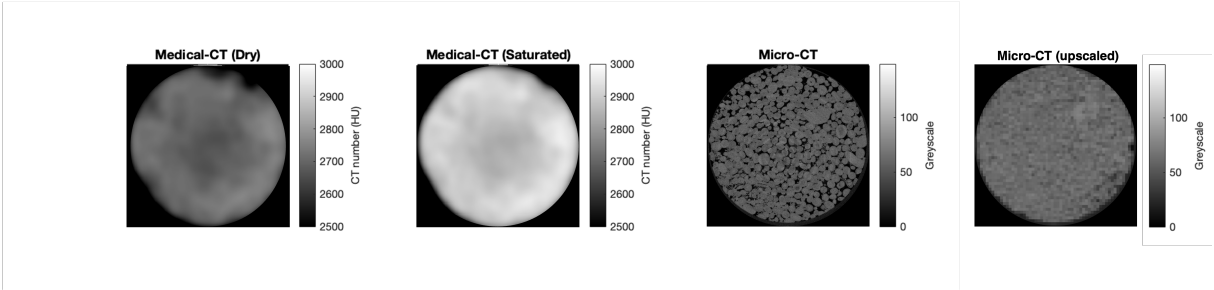


Figure 4.6: Difference in the resolution of three Ketton slices at dry and saturated stage scanned in a medical CT (voxel size = 27x27x500 µm^3), a raw dry scan in the micro CT (voxel size = 7x7x7 µm^3) and an upscaled micro CT to medical CT resolution for comparison. Note that the image output for medical CT images are in Hounsfield Units and micro CT shows a 8-bit greyscale image with values from 0 to 256.

4.4 Image Processing

With both dry and saturated scans acquired, the next phase involved detailed image data analysis. This stage included differential imaging of the medical CT data, segmentation of pore and solid domains from micro CT images, and uncertainty analysis to assess the robustness and reproducibility of the measurements. For consistency and comparison purposes across samples, data analysis and porosity map generation were performed over the same axial length of $L = 3.4$ cm.

The reconstructed image datasets were as follows:

- Medical CT: For each sample, 6 consecutive scans consisting of 68 slices each under two different saturation conditions (dry and saturated).
- Micro CT: 5666 slices (Bentheimer), 4864 slices (Ketton), 5930 slices (Silurian), 5670 slices (Nugget).

4.4.1 Medical CT Data Analysis

Medical CT images were processed using MATLAB (MathWorks). The first step involved cropping each tomogram to isolate the rock sample from surrounding components. Since the samples were cylindrical, the masking process required locating the central axis of the core and defining a circular region of interest. This was done by manually identifying

the center coordinates at the inlet and outlet slices, denoted as (x_i, y_i) and (x_o, y_o), respectively.

Due to slight misalignments during scanning, the center of the sample may not remain fixed along the scan length. To compensate for this, the center of the mask was linearly interpolated across slices using the following equations:

$$x_n = \left(\frac{x_o - x_i}{n}\right) x + x_i \quad \text{and} \quad y_n = \left(\frac{y_o - y_i}{n}\right) x + y_i$$

where:

- x_n, y_n are the center coordinates at slice x
- x_i, y_i are the center coordinates at the inlet slice
- x_o, y_o are the center coordinates at the outlet slice
- n is the total number of slices
- x is the slice index along the axial direction

The sample diameter was determined by analysing grayscale transitions across each slice to identify the interface between the rock and the surrounding sleeve as seen in Figure 4.8. This diameter was matched across both image sets. This approach ensured consistent masking across the scan length, improving the reliability of subsequent differential imaging analysis.

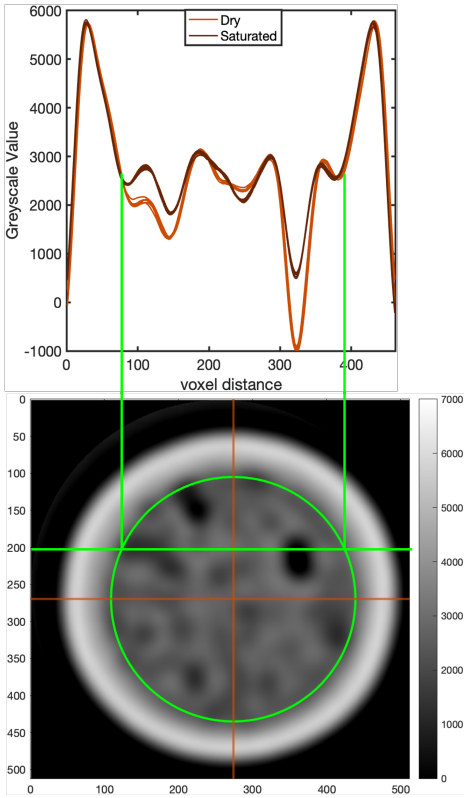


Figure 4.7: Procedure for determining image center coordinates and diameter to apply a circular mask across slices.

Once the 3D volumes of the scanned samples have been acquired, aligned, and registered in both dry and saturated conditions, ensuring that the corresponding voxel locations in both sets of images correspond to the same physical space, the six scans at each state are averaged and the differential imaging method can be applied using Equation 4.2. The differential imaging method involved voxel-wise subtraction of the dry state image from the saturated image, normalised by the contrast between the CT values of pure water and air. Figure 4.8 shows the resulting porosity map revealing the spatial distribution of fluid-accessible pores within the sample at the original voxel size.

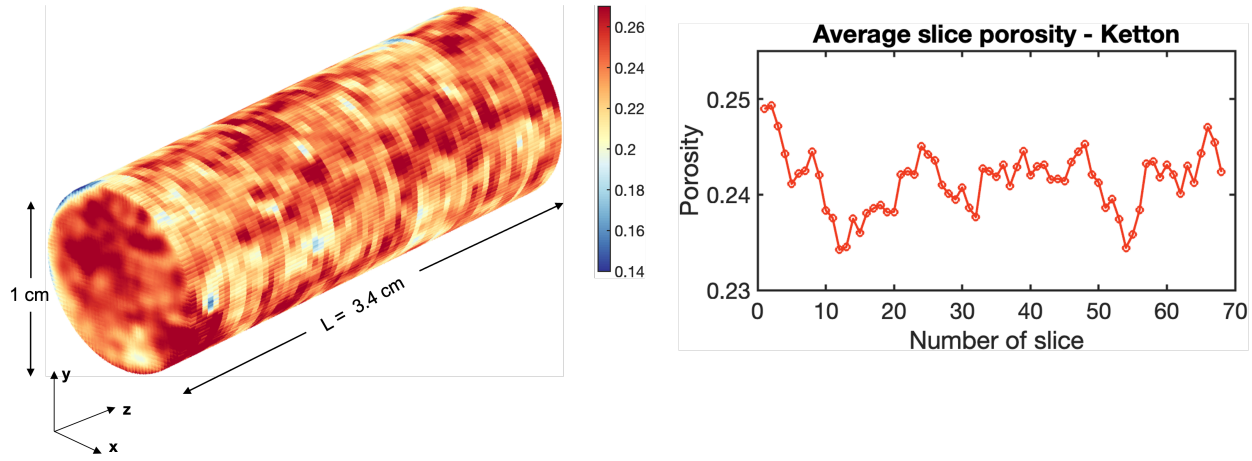


Figure 4.8: 3D porosity map and corresponding slice-averaged porosity of the Ketton sample. Left: Volume rendering of the porosity field, averaged dry and saturated scans were used, the diameter comprises 250 voxels in the x and y axis and 68 slices. Right: Average porosity values for each cross-sectional slice. Voxel size is representative of the original resolution of 40x40x500 μm^3.

Experimental noise is unavoidable in medical X-ray CT imaging. To assess whether this noise is truly random and uncorrelated across space, a lag-plot analysis was conducted. This method tests whether neighbouring voxels show systematic similarity in their values, which would indicate spatially correlated noise. After subtracting two scans acquired under identical conditions, each voxel $vox_{i,j}$ was compared against all immediately adjacent voxels $vox_{i+\delta_i, j+\delta_j}$, where $\delta_i, \delta_j \in \{-1, 0, 1\}$ and $(\delta_i, \delta_j) \neq (0, 0)$. This set of neighbours corresponds to the eight surrounding voxels in the 2D plane. For each voxel–neighbour pair, the first voxel value was plotted against the neighbour value to construct the lag plot.

Figure 4.9 presents the voxel comparison in the x-axis direction (δ_i=1), though analysis was performed for all neighboring directions. It shows that the raw images (coarsening factor = 1) exhibit a noticeable linear correlation, indicating highly spatially correlated noise. This correlation decreases progressively when voxel averaging is applied, approaching a random (uncorrelated) distribution when the data are resampled to a voxel size of (0.46×0.46) mm^2. This resolution is therefore considered the minimum voxel size at which reliable, spatially independent porosity maps can be produced.

Comparable trends were observed for voxel comparisons in all other directions, confirming that the correlation is isotropic in the image plane and no systematic directional bias exists

in the noise structure. The same analysis was performed subtracting averaged scans rather than individual scans, similar results were observed, though tighter clustering indicates that averaging scans further reduces noise magnitude but preserves correlation patterns. The combination of temporal averaging (to reduce noise magnitude) and spatial coarsening (to achieve statistical independence) provides an optimal strategy for noise reduction while maintaining measurement reliability.

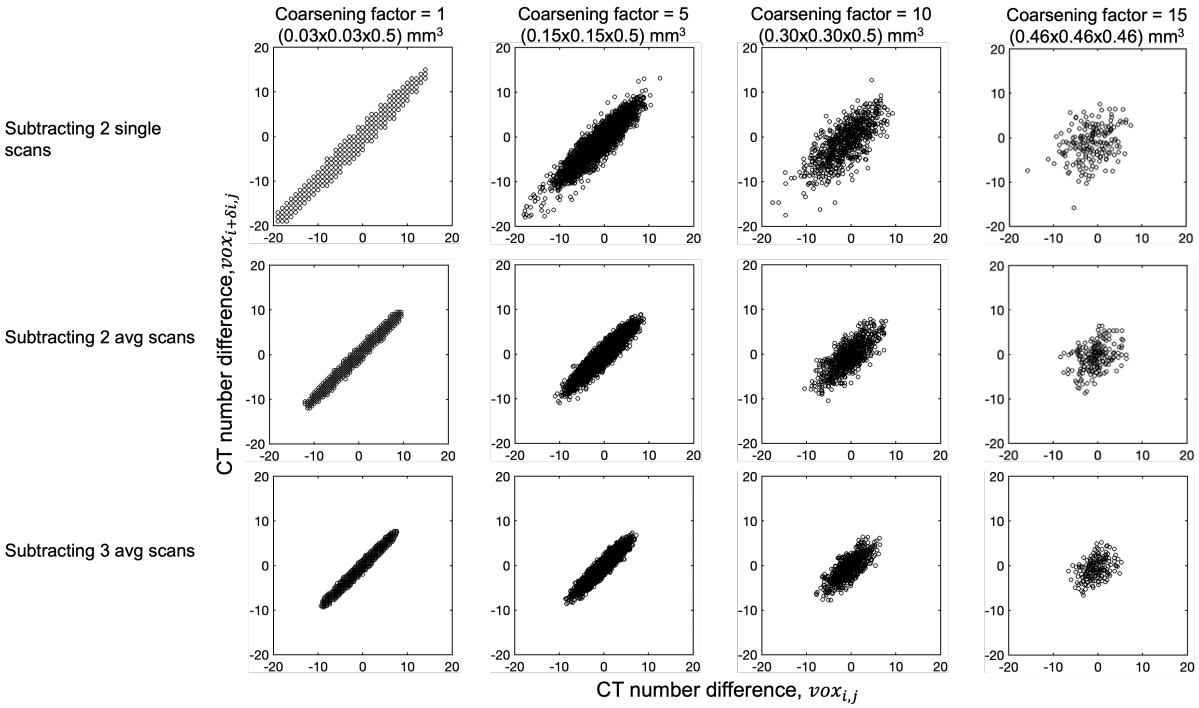


Figure 4.9: CT noise correlation analysis across different voxel sizes and averaging schemes. Scatter plots of CT number differences between adjacent voxels for various coarsening factors and subtraction scenarios. Smaller voxel sizes (left) show tighter correlation and lower noise variance compared to larger voxel sizes (right), demonstrating the trade-off between spatial resolution and noise characteristics in CT imaging.

CT noise can be quantified using the standard rules of error propagation. Assuming that each scan is equally affected by random Gaussian noise, the voxel-wise standard deviation across repeated scans can be estimated as outlined in Equation 4.4. Similarly, the uncertainty in porosity is calculated using Equation 4.5. (Pini and Madonna 2016)

$$\sigma_{\Delta_n} = \sqrt{2} \cdot \frac{\sigma_{\text{vox}}}{\sqrt{n}} \tag{4.4}$$

where:

- $\sigma_{\Delta n}$ is the standard deviation when two n-averaged scans are subtracted
- σ_{vox} is the noise associated to each voxel
- n are the number of averaged scans

$$\sigma_{\phi_n} = \frac{\sqrt{2}\,\sigma_{\text{vox}}}{\sqrt{n}(CT_w - CT_a)} \approx \frac{\sigma_{\Delta_n}}{1000} \tag{4.5}$$

where:

- σ_{ϕ_n} is the porosity uncertainty
- σ_{vox} is the noise associated to each voxel
- CT_w, CT_a are the CT values of the pure fluids used for calibration

To mitigate the influence of inherent experimental noise, six consecutive scans were acquired for each state (dry and saturated). The uncertainty associated with CT noise was quantified by calculating the standard deviation (σ_{Δ_n}) of the difference between pairs of scans. Figure 4.10 illustrates noise maps obtained by subtracting: i. two single scans, ii. two sets of two averaged scans and iii. two sets of three averaged scans for the original voxel resolution of (0.04 x 0.04 x 0.5)mm^3. The second row shows histograms of the noise distributions, which are centered around zero, the panel on the right shows an overlay of their corresponding fitted Gaussian probability density functions (PDFs) for direct comparison. The associated standard deviations (σ_{Δ_1}, σ_{Δ_2}, and σ_{Δ_3}) demonstrate that noise is progressively reduced when multiple scans are averaged prior to subtraction. The observed reduction follows the expected statistical trend, decreasing approximately with the inverse square root of the number of scans, $\sigma \propto 1/\sqrt{N}$.

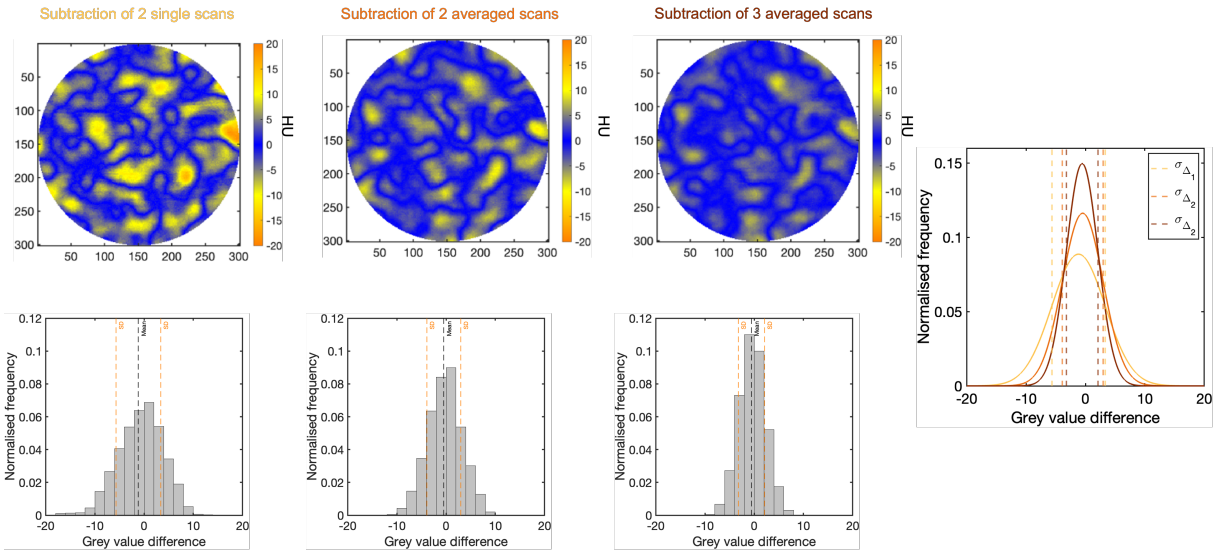


Figure 4.10: Noise maps and histograms of grey value differences from subtraction of two single scans, two sets of two averaged scans, and two sets of three averaged scans, resolution (0.04 x 0.04 x 0.5) mm³. Dashed lines mark the mean and one standard deviation (σ_{Δ_1}, σ_{Δ_2}, σ_{Δ_3}). The fitted Gaussian curves (right) show that averaging scans prior to subtraction reduces noise.

A similar analysis was performed for voxel-averaged datasets (coarsening) at three voxel sizes: (0.04 × 0.04 × 0.5) mm³, (1 × 1 × 1) mm³, and (2 × 2 × 2) mm³. The results (Figure 4.11) show that CT noise decreases through two main mechanisms: (i) averaging a larger number of scans prior to subtraction, and (ii) increasing voxel size via spatial averaging. Voxel-wise averaging was applied to each scanning condition to generate representative volumes, which enhanced image stability and ensured consistency in greyscale contrast across the dataset. This procedure also helped account for residual variability arising from minor reconstruction artifacts, thereby reducing overall uncertainty.

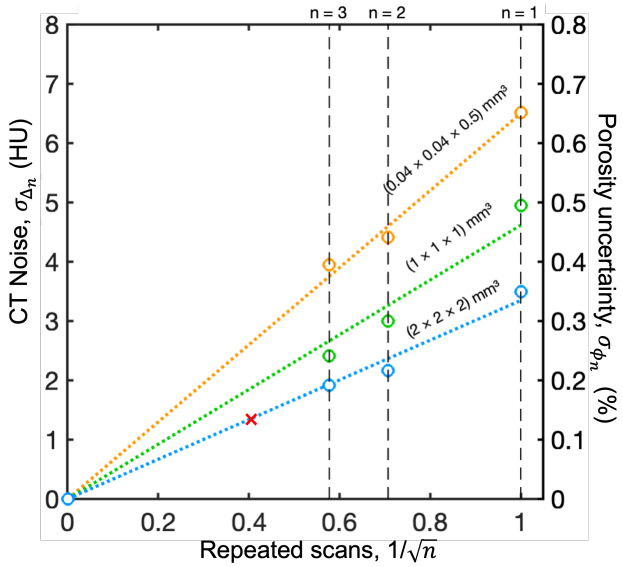


Figure 4.11: CT noise and porosity uncertainty as a function of repeated scans across voxel sizes. The CT noise, $\sigma_{\Delta n}$ (left axis), and corresponding porosity uncertainty, σ_{ϕ_n} (right axis), are plotted against the inverse square root of the number of repeated scans ($1/\sqrt{n}$), for voxel sizes of (0.04 x 0.04 x 0.5) mm^3, (1 x 1 x 1) mm^3, and (2 x 2 x 2) mm^3. Noise decreases linearly with scan averaging. Similarly, voxel averaging exhibit lower inherent noise. Vertical dashed lines indicate the number of averaged scans. The red cross denotes the value obtained for the current study as 6 scans were averaged and the final voxel size was taken as (2 x 2 x 2)mm^3, resulting in a porosity uncertainty of ±0.14%.

Following these analyses, the minimum reliable voxel size for porosity quantification was determined to be (2 x 2 x 2)mm^3. This resolution ensured a balance between spatial detail and signal-to-noise ratio across the scanned volumes. The scans and voxel averaging procedure significantly reduced random fluctuations, yielding a voxel-wise uncertainty in effective porosity estimation of approximately ±0.14%.

Figure 4.12 presents the final effective porosity map, denoted as ϕ_E, computed via differential imaging between dry and saturated conditions. The resulting map captures spatial variations in pore structure across the core, offering a robust representation of connected porosity at the medical CT scale.

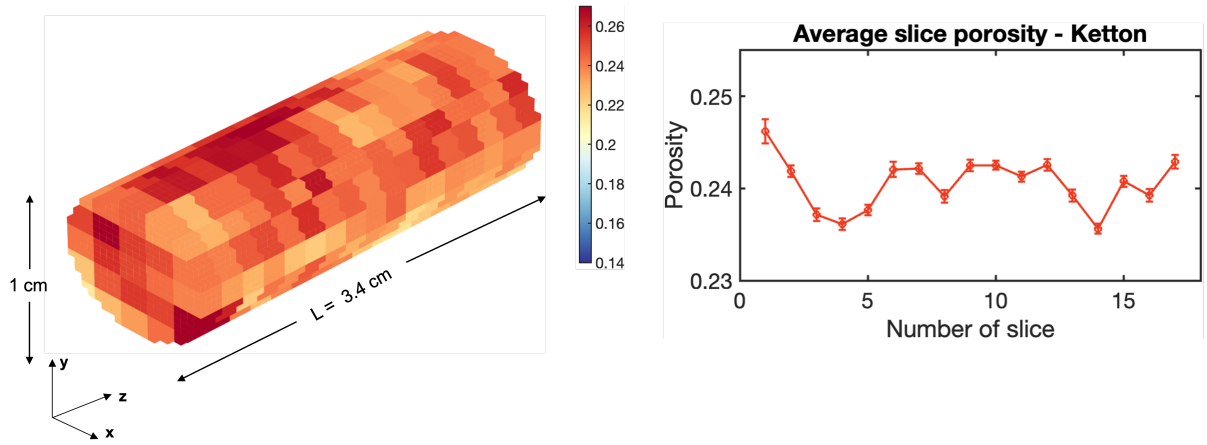


Figure 4.12: 3D porosity map and corresponding average slice porosity of the Ketton sample. Left - Volume rendering of the porosity field, the volume comprises 5 voxels in the x and y axis and 17 slices. Right - Average porosity values for each cross-sectional slice. Voxel size is 2x2x2 mm^3.

4.4.2 Micro CT Data Analysis

Micro CT image data were processed using a combination of Avizo (Thermo Fisher Scientific) for image pre-processing and segmentation, and MATLAB for the generation of spatially resolved porosity maps. Raw X-ray CT datasets are inherently subject to multiple forms of noise and artifacts introduced during the acquisition and reconstruction processes, potentially worsening image clarity and the reliability of subsequent analysis. If left uncorrected, this noise could negatively impact true phase boundaries, generate invalid features during segmentation, and widen the uncertainty of porosity quantification. Consequently, the first step of the workflow involved applying a noise-reduction filter to the reconstructed image volumes. Particular attention was given to the transition zones between solid grains and pore spaces, as voxels in these regions are most susceptible to misclassification, potentially leading to significant errors in subsequent segmentation and porosity calculations.

Several denoising filters were evaluated. The selection criteria prioritised both effective noise suppression and preservation of edge definition. Classical filters such as Gaussian or median kernels improve signal-to-noise ratio (SNR) but do so at the expense of edge

blurring. Based on this assessment, the Non-Local Means (NLM) filter was chosen because of its superior ability to reduce noise while maintaining sharp phase boundaries. This filtering step ensured that pore–grain interfaces were accurately preserved. NLM filter operates on the principle that image features tend to repeat throughout the volume, even if they are not spatially adjacent instead of operating exclusively in neighboring voxels. The idea is to replace the intensity of each voxel with a weighted average of similar patches found throughout the image. In this study, the NLM filter was implemented using Avizo's built-in module, with parameters tuned to balance noise reduction and feature preservation.

The intensity of every voxel $I(v_i)$ is replaced by the weighted average $w(i,j)$ within a set search window S_i. The weights satisfy $\sum_j w(i,j) = 1$. The denoised intensity is computed as:

$$I(v_i) = \sum_{j \in S_i} w(i,j)\, I(v_j) \tag{4.6}$$

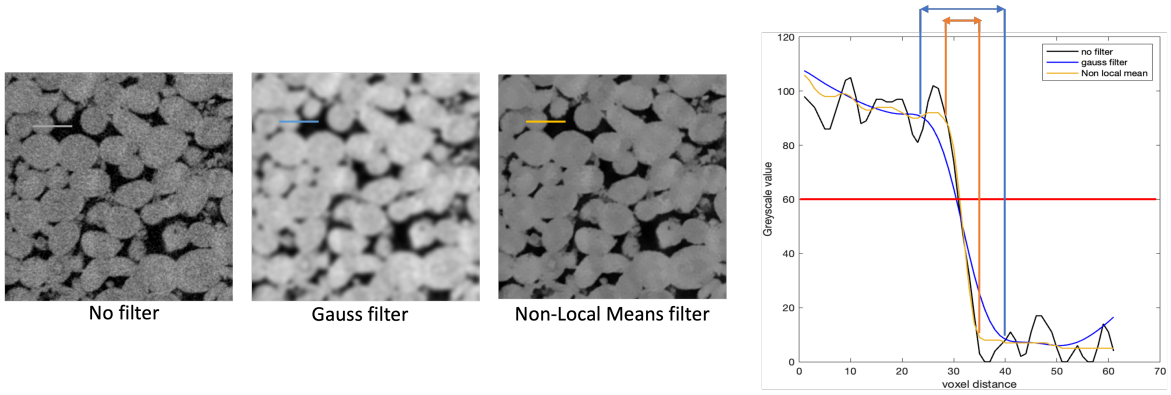


Figure 4.13: Comparison of denoising filters applied to micro CT data. Left to right: original slice without filtering, image after Gaussian filter, and image after applying the Non-Local Means (NLM) filter. The line profiles plotted on the right display the corresponding greyscale intensity values along the marked sections in the images. The unfiltered profile (black) exhibits high noise fluctuation. In contrast, the the Gaussian filter (blue) reduces noise but blurs boundaries, while NLM filter (orange) shows superior noise suppression while preserving edge sharpness, evidenced by a steeper gradient at the phase boundary. The red horizontal line indicates the intensity threshold used inform the segmentation step. Arrows show the edge detection span for each method, highlighting the improved boundary definition.

Following the denoising step, the next task was to isolate the sample from surrounding voxels corresponding to the Viton sleeve. This was accomplished through a segmentation

procedure that exploited the contrast in X-ray attenuation between the rock and the highly attenuating sleeve material. Once the sample volume was successfully cropped, a second segmentation was carried out to distinguish between the pore space and the solid grain matrix.

For this purpose, a watershed segmentation algorithm was used. This method interprets the greyscale image as a topographic surface, where voxel intensity corresponds to elevation. Seed points were manually defined to mark voxels confidently classified as either grain or pore, this selection was aided by the threshold definition during the denoising step. The watershed method then simulates a flooding process from the seed locations, progressively assigning intermediate voxels of intermediate intensity to one of the two phases. Boundaries are formed where these growing regions meet, allowing for accurate delineation of pore and grain labels based on local intensity gradients.

One key source of uncertainty in porosity quantification originates from the thresholding used during segmentation. Since pore and grain phases are distinguished based on voxel intensity, factors such as image noise, partial volume effects, and overlapping intensity distributions make the selection of an optimal threshold non-trivial. Even small variations in the threshold can significantly alter the number of voxels classified as pores, particularly near the pore–grain interface. As porosity is defined as the ratio of pore voxels to total voxels within the segmented region, this threshold sensitivity directly affects the calculated porosity.

To quantify and minimise this uncertainty, a sensitivity analysis was conducted in which a range of plausible thresholds were tested. This analysis identified a greyscale interval where the computed porosity remains within an acceptable range, allowing upper and lower bounds to be established. These bounds were also used to define the placement of watershed seeds. The porosity obtained through this method is consistent with the macroporosity fraction estimated from mercury intrusion capillary pressure (MICP) data for Ketton limestone. The estimated uncertainty in the resolved porosity using this approach is $\pm 0.214\%$, as shown in Figure 4.14.

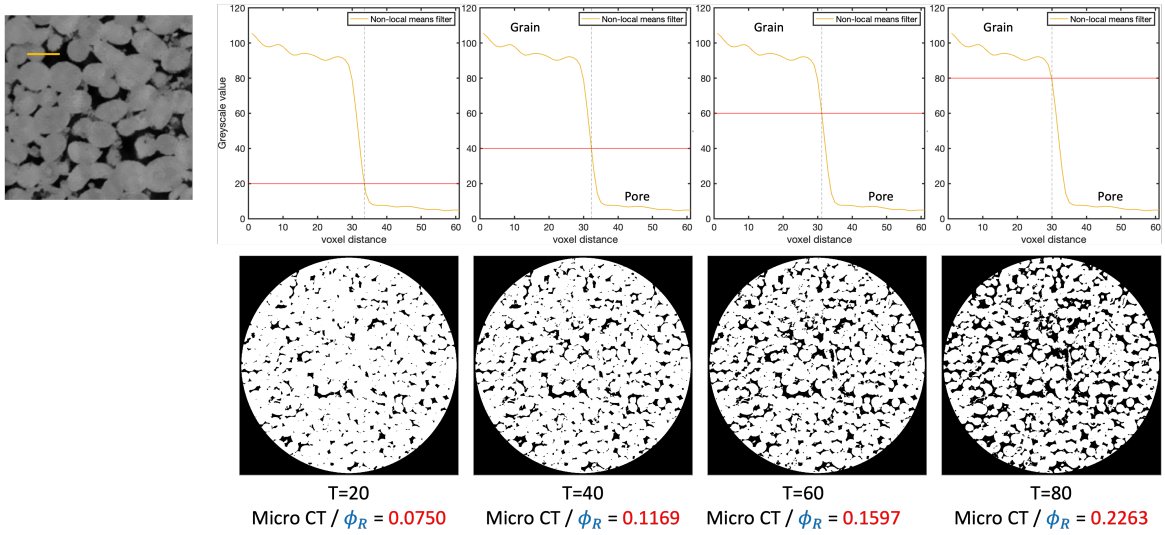


Figure 4.14: Segmentation sensitivity analysis illustrating the impact of threshold selection on resolved porosity (ϕ_R). Top left: High-resolution micro CT slice of Ketton limestone with yellow profile line indicating location of intensity transect. Top row: Intensity profiles across a grain–pore boundary after non-local means filtering. Four different greyscale thresholds (horizontal red lines) are tested for pore–grain segmentation. Bottom row: Corresponding binary segmentation masks for each threshold, where white represents pore space. The resulting porosity values ϕ_R increase with higher threshold values, highlighting the influence of segmentation threshold on quantitative porosity estimates.

Once the binary images were obtained, the volume had to be rotated to achieve registration between the medical CT and micro CT datasets. This alignment was performed by visually comparing distinct features within the sample, with particular emphasis on the metal plugs embedded in the core-holder end caps. Due to their high density, these metal plugs produce strong contrast in both imaging modalities, making them clearly identifiable. Their consistent visibility across scans provides reliable reference points for estimating and applying the necessary rotational transformation for accurate alignment. The transformation was applied using the "Nearest Neighbor Interpolation" algorithm in MATLAB, which preserved the binary nature of the segmented images without altering voxel structure. This ensured that the porosity calculation remained consistent before and after rotation, something not achieved with other interpolation methods tested.

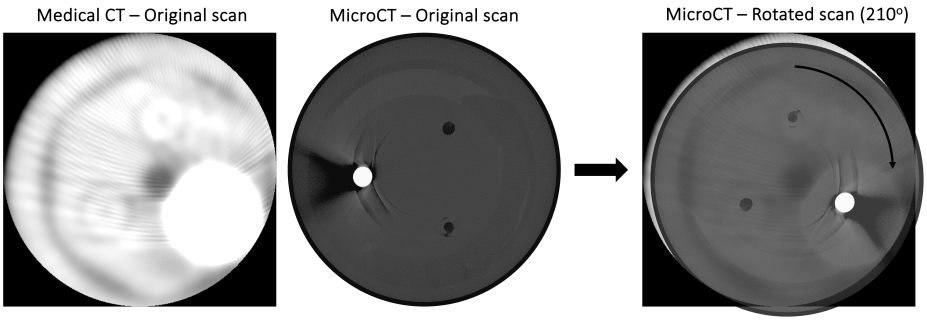


Figure 4.15: Comparison of micro CT and medical CT scans of the same end-cap section highlighting rotational misalignment. Left: Lower resolution medical CT slice showing the internal structure and the high contrast of the metal plug; Middle: Raw micro CT slice of the same sample; Right: Overlay showing the required clockwise rotation to align the sample across modalities for image registration and multi-scale analysis.

The final step in the micro CT data processing was to generate the resolved porosity map at the same spatial resolution as the effective porosity map derived from the medical CT image analysis. This required downscaling the original micro CT volume from its full resolution of (1700 x 1700 x 4864) voxels to an upscaled volume of (5 x 5 x 17). To achieve this, a coarsening procedure was applied: the upscaled 3D matrix was defined, and for each voxel in the upscaled grid, the corresponding subvolume in the high-resolution binary image was averaged. Because the binary image consists of pore (value = 1) and grain (value = 0) voxels, this averaging directly yields the porosity value for each upscaled voxel, as defined in Equation 4.3.

Figure 4.16 illustrates the complete micro CT image analysis workflow, culminating in the generation of the resolved porosity map (ϕ_R) at a resolution comparable to the effective porosity map (ϕ_E) derived from the medical CT data. The resulting resolved porosity map (ϕ_R) is visualised as a voxel-wise porosity distribution across the core, and its correspondence with the effective porosity (ϕ_E) is shown in the porosity profile plot, confirming the sub-resolution features captured at different scales.

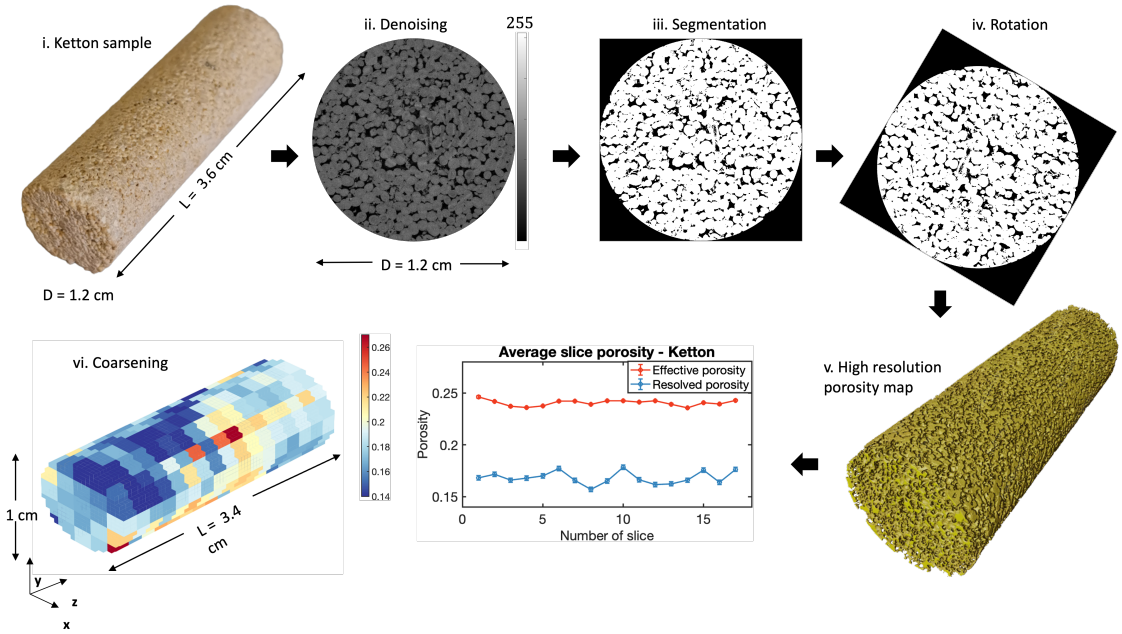


Figure 4.16: Image processing workflow for porosity quantification from micro-CT images. Starting from the physical Ketton core sample (top left), the micro-CT grayscale image is cropped, denoised and segmented into binary pore–grain domains. The segmented volume is rotated for alignment with medical CT data. A 3D coarsening step is then applied to compute voxel-averaged porosity over a lower-resolution grid matching the medical CT domain. The final resolved porosity map ϕ_R (bottom left) enables direct comparison to the effective porosity map. The comparison of slice-averaged porosities (bottom center) highlights the resolution-dependent discrepancy between resolved and effective porosity.

4.5 Sub-Resolution Porosity Mapping

As outlined in Section 4.1, the primary goal of this methodology is to quantify and spatially map micro-pores that fall below the resolution limit of the imaging system and therefore remain unresolved in high-resolution micro CT scans. By integrating both imaging modalities, we can differentiate between the pore structures captured at each scale. Up to this point, we have produced two complementary porosity maps: the effective porosity map (ϕ_E), derived from medical CT data, which captures all connected pore spaces regardless of size (left panel in Figure 4.17); and the resolved porosity map (ϕ_R), obtained from micro CT analysis, which includes only those pores that exceed the resolution threshold of the scanner (center panel in Figure 4.17).

To bridge the resolution gap and isolate the contribution of sub-resolution pore structures,

we compute a third porosity map, the unresolved porosity map (ϕ_U) by subtracting the resolved porosity map from the effective porosity map on a voxel-by-voxel basis (rigth panel in Figure 4.17). Mathematically, this can simply be expressed as:

$$\phi_U = \phi_E - \phi_R \tag{4.7}$$

This operation provides a spatially distributed estimate of the microporosity within the sample, highlighting zones where unresolved pores contribute significantly to overall storage or flow properties. The resulting microporosity map serves as a key link between the two imaging scales and offers a more complete petrophysical characterisation of the rock. Additionally, a histogram and cumulative distribution of both ϕ_R and ϕ_U is shown in Figure 4.17, The bimodal distribution supports the dual-porosity character of Ketton, with microporosity and macroporosity occurring in distinct voxel populations. This observation is consistent with independent Mercury Injection Capillary Pressure (MICP) measurements, which typically reveal two distinct pore throat sizes in Ketton.

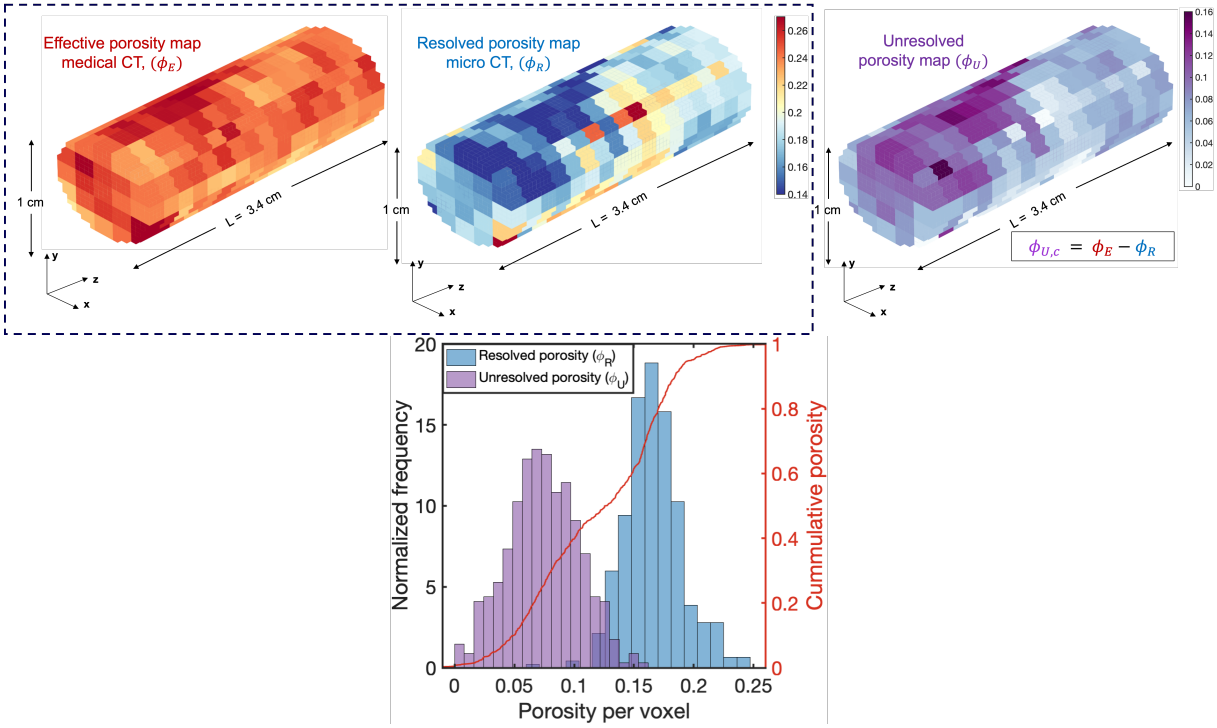


Figure 4.17: 3D porosity maps of Ketton limestone core obtained from multi-resolution X-ray CT imaging. Left: Effective porosity map from medical CT, representing the total connected porosity at coarse resolution (ϕ_E). Center: Resolved porosity map from micro CT, capturing connected porosity features resolved at higher resolution (ϕ_R). Right: Unresolved porosity map (ϕ_U), obtained by subtracting the resolved porosity from the effective porosity indicating sub-resolution porosity. All maps are shown over the same voxel size: (2 x 2 x 2) mm^3. Bottom: Histogram and cumulative distribution of resolved and unresolved porosity per voxel in Ketton.

4.6 Concluding Remarks

This chapter has outlined the full methodology developed to quantify and analyse porosity across scales, integrating medical CT and micro CT imaging. The experimental setup and imaging procedures have been described in detail for both medical CT and micro CT modalities, establishing standardised protocols that ensure reproducibility and comparability across different samples and imaging conditions. The data processing strategies implemented for each modality were specifically tailored to optimise the extraction of porosity information while accounting for the inherent limitations and noise characteristics of each imaging technique.

Effective porosity was calculated from medical CT analysis, while micro CT image segmentation provided a direct quantification of the resolved pore space. Uncertainty analysis in medical CT analysis demonstrated the influence of experimental noise and highlighted the benefits of scan averaging and voxel coarsening in reducing variability. For the micro CT uncertainty analysis, a systematic evaluation of segmentation sensitivity, threshold selection criteria, and the impact of partial volume effects were explored. This rigorous approach ensures that confidence intervals associated with porosity measurements are both realistic and accurate.

Finally, the integration of medical CT–derived effective porosity with micro CT–resolved porosity enabled the derivation of sub-resolution porosity maps. This innovative approach effectively bridges the resolution gap between imaging techniques, enabling the characterisation of pore features that exist below the resolution limit of medical CT while maintaining the spatial context provided by the larger field of view. The sub-resolution porosity maps represent a novel petrophysical data that captures the heterogeneous distribution of fine-scale porosity within the broader sample volume, providing unprecedented insight into the multi-scale nature of pore structure.

Overall, this workflow provides a robust and reproducible framework for characterising pore structure, capturing both the macroscopic effective response and the microscopic pore architecture, while quantifying the uncertainty associated with each step. This methodological foundation sets the stage for subsequent analyses, including the interpretation of flow and transport processes in complex porous systems.

Chapter 5

Use of Radio-Opaque Gas in the Dual-Resolution X-ray CT Method for Low Permeability Samples

While the dual-resolution X-ray CT approach enables a detailed quantification of pore structures across scales, its application to low-permeability samples presents additional challenges. One of the primary difficulties lies in the incomplete saturation of the pore space with liquid-phase contrast agents when applying the differential imaging method. To overcome this limitation, a radio-opaque gas was introduced as a contrasting fluid during imaging. Due to the extremely small pore throat sizes and poor connectivity in such rocks, full saturation is often not achievable, leading to underestimation of porosity and connectivity in regions where fluid penetration is limited. This section outlines the implementation of radio-opaque gas approach within the dual-resolution CT framework and demonstrates its effectiveness in revealing subtle transport features in tight porous media.

5.1 Rationale for the Use of a Radio-Opaque Gas as a Saturating Fluid

The use of a radio-opaque gas as a saturating medium in CT imaging of low-permeability rocks offers several key advantages over conventional liquid-phase contrast agents. In rocks with ultra-tight porosity features, the capillary entry pressures are high and pore

throats diameters are often too small to allow uniform liquid infiltration. Under such conditions, even applying elevated pressure may not be sufficient to achieve full saturation with liquids, leading to partial saturation and spatially biased porosity maps when relying on liquid contrast agents alone.

In contrast, gaseous contrast agents offer much more favourable transport properties for such tight porous systems, due to their lower viscosities, gases can penetrate finer pore structures more readily and achieve a more uniform distribution, even in poorly connected networks. This improved access allows for a more representative imaging (Vega, Dutta, and Kovscek 2014).

Additionally, when implementing gases with high atomic number (e.g., xenon, krypton), such gases produce sufficient X-ray attenuation contrast. Importantly, their CT number response increases with pressure, allowing to apply differential imaging using only the gas. Krypton, in particular, has been successfully applied in the characterisation of pore structures in coal and shale samples (Vega, Dutta, and Kovscek 2014), demonstrating its suitability for imaging in low-permeability materials (Mayo et al. 2015).

In this context, the adoption of a radio-opaque gas not only addresses the practical limitations of liquid saturation but also expands the capabilities of the dual-resolution X-ray CT workflow. It enables the reliable detection of sub-resolution porosity and low-connectivity features that are otherwise neglected, thus improving the completeness and accuracy of pore space characterisation in tight rocks.

5.2 Calibration Experiments

Applying differential imaging with krypton as a saturating fluid requires a modification of Equation 4.2 where the denominator changes from the CT number of water and air to the CT number of krypton at different pressures where the contrast is high enough to quantify porosity. Equation 5.1 was employed to generate porosity maps when using krypton as a saturating fluid.

$$\phi_E = \frac{CT_{\text{vox},hp} - CT_{\text{vox},lp}}{CT_{\text{Kr},hp} - CT_{\text{Kr},lp}} \tag{5.1}$$

where:

- ϕ_E is the effective porosity (–)
- $CT_{\text{vox},hp}$ is the CT number of the voxel when scanned with krypton at the higher pressure (HU)
- $CT_{\text{vox},lp}$ is the CT number of the voxel when scanned with krypton at the lower pressure (HU)
- $CT_{\text{Kr},hp}$ is the CT number of pure krypton at the higher pressure
- $CT_{\text{Kr},lp}$ is the CT number of pure krypton at the lower pressure

To validate the suitability of krypton as a gaseous contrast agent for differential CT imaging, a calibration experiment was performed over a range of pressures (vacuum to 34 bar in increments of 5 bar). As shown in Figure 5.1, krypton displays a clear linear increase in both density and CT number (HU) with pressure, in contrast to nitrogen and carbon dioxide which exhibit minimal attenuation variation. This behavior confirms the capacity of krypton to produce measurable contrast for CT-based porosity quantification. In addition, the rightmost panel demonstrates the spatial uniformity of the CT signal along the core-holder length, indicating consistency and minimal axial variation, which are essential for accurate and reproducible imaging in low-permeability rocks.

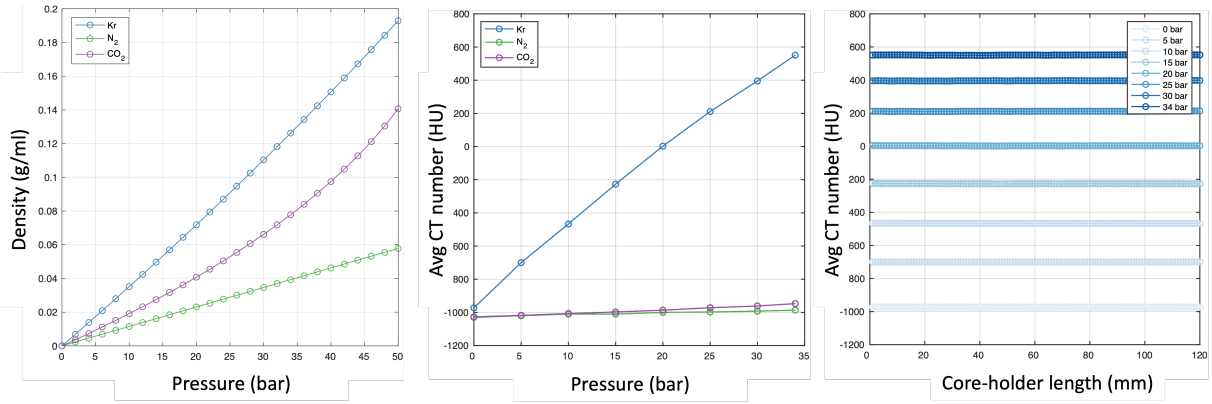


Figure 5.1: Krypton calibration for use as a gaseous contrast agent in X-ray CT imaging. Left: Density of krypton, carbon dioxide, and nitrogen as a function of pressure, showing gases incresing density under increasing pressure, (NIST Chemistry WebBook 2025). Centre: Corresponding average CT number (in Hounsfield Units, HU) for each gas at varying pressures. Krypton exhibits a strong linear CT response with pressure, unlike carbon dioxide and nitrogen, which remain close to the baseline of air. Right: Spatial consistency of krypton CT response across the length of the core-holder at different pressures.

The imaging data processing steps used for the krypton-based scans followed the same procedure described in Section 5.4.1, with the exception that krypton-specific attenuation values were applied via Equation 5.1. To validate the performance of krypton as a contrast agent, Ketton limestone sample was selected as a benchmark due to its high permeability and dual porosity. These characteristics allow the rock to be effectively saturated with both liquid and gaseous contrast agents, making it an ideal candidate for comparative imaging.

5.3 Revised Workflow for Image Acquisition with Krypton

Once the CT attenuation values for pure krypton were calibrated, a modified imaging workflow was developed to enable effective porosity mapping using krypton as the contrast medium. The experimental setup described previously in Section 5.2.1 including sample preparation, core-holder assembly, confining pressure, initial CO_2 flushing and ports dedicated for pressure control was retained. The key changes involved modifications

to the gas injection and evacuation system to accommodate the properties and handling requirements of krypton gas. In the revised setup, the inlet flow line was connected to a high-purity krypton gas cylinder (N5.0 purity grade, 100 lt, Max. pressure: 44 bar, BOC) via a digital electronic pressure regulator (Model: EPR 500, Equilibar), which was used to establish and monitor the injection pressure.

An initial imaging experiment using krypton gas was conducted by scanning the samples first under ambient conditions, with a pore pressure of 1 bar. Subsequently, krypton was injected into the sample until an internal pressure of 20 bar was reached. These pressure conditions were selected to replicate the differential imaging strategy typically employed in water–air experiments, where a CT number difference of approximately 1000 HU is commonly observed. The goal was to achieve a similar X-ray attenuation contrast using krypton, as supported by the calibration data shown in Figure 5.1, which illustrates the CT number response to krypton at various pressures.

The second CT scan, conducted at elevated pressure, was acquired immediately after pressure readings stabilised at both the inlet and outlet, under the assumption that the sample had reached full krypton saturation. However, the resulting porosity profile, shown in the left plot in Figure 5.2, while generally following the same trend as the reference water–air experiment, displays a notable underestimation of slice porosity in the second half of the core (downstream relative to the injection direction).

A plausible explanation for this discrepancy is the limited equilibration time between krypton injection and imaging. While the intergranular pore space may have rapidly equilibrated, as suggested by the stabilised pressure sensors, diffusion into smaller intragranular microporous regions likely continued during and after scanning. Given that krypton was introduced from the left side of the core, incomplete saturation in the later slices (towards the right end) can be attributed to slower diffusive transport into these less accessible pores. Similarly, the first slice shows an overestimation of the porosity due to the higher concentration of krypton, resulting in a larger attenuation difference between the scans.

To address this limitation and minimise saturation artifacts in the CT-derived porosity maps, a saturation equilibration period following krypton injection and prior to scanning was implemented, allowing sufficient time for the gas to diffuse throughout the entire

pore network, including micropores. This approach ensures a more accurate estimation of porosity by reducing the contrast bias introduced by partial gas occupancy and incomplete density equilibration.

The right-hand plot in Figure 5.2 presents the porosity profile obtained after incorporating an equilibration period prior to scanning. This profile shows an improved agreement in trend with the porosity distribution derived from the reference water–air experiment, with the elimination of the declining trend observed in the pre-equilibration data. However, a consistent underestimation of approximately 0.6% porosity is observed across the core length. This discrepancy is attributed to the reduced density of the Kr–CO_2 gas mixture, which leads to a diminished X-ray attenuation contrast. Specifically, the attenuation difference in the numerator of Equation 5.1 is lowered, resulting in underestimated porosity values when applying the differential imaging method.

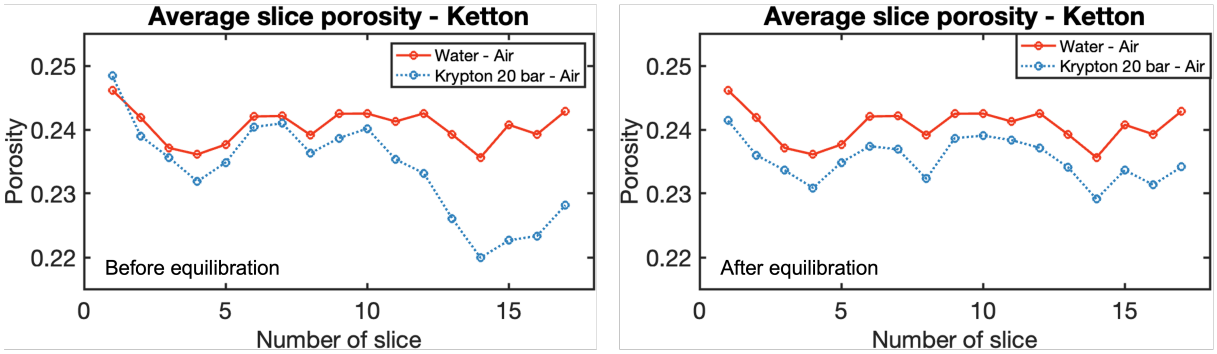


Figure 5.2: Comparison of average slice porosity measurements for Ketton limestone using water-air and krypton 20 bar-air methods. Left: Before equilibration showing measurement variability and method discrepancies, and right: After equilibration demonstrating improved consistency between techniques and reduced spatial variation.

Building on these observations, a second imaging campaign was designed to address the limitations encountered in the initial experiment. In particular, the introduction of CO_2 (a standard practice in water-based differential imaging due to its solubility) was recognised as detrimental when using noble gases like krypton. To eliminate residual air and minimise gas mixing within the pore space, an additional evacuation step was introduced prior to krypton injection, ensuring that the imaging reflected only the distribution of krypton.

To achieve effective removal of residual gases and improve the reliability of krypton-based

porosity measurements, an outlet flow line was connected to a vacuum pump to evacuate ambient air and any remaining gas from the pore space of the core sample. After assembling the core holder, the vacuum pump was activated, reducing the internal pressure to near-vacuum conditions. Once a stable vacuum was reached and maintained, the outlet valve was closed to seal the system, and an initial CT scan was performed under vacuum conditions to serve as the baseline for subsequent differential imaging.

Following this, krypton gas was injected through the inlet at a pressure of 5 bar. After allowing a two-hour equilibration period (intended to ensure full saturation, particularly of micropores) a second CT scan was acquired. This process was repeated at pressures of 10, 15, and 20 bar, with an equilibration step preceding each scan to ensure consistent saturation throughout the core at each pressure increment.

As the final step after the 20 bar scan, krypton was removed from the sample by re-opening the outlet valve and reactivating the vacuum pump, drawing the internal pressure down to near-vacuum levels once again. While maintaining these low pressure conditions, the inlet was connected to a syringe pump filled with deionised water. Water was then injected into the evacuated core to achieve full saturation under controlled flow conditions. A final CT scan was taken with the sample in a fully water-saturated state. This dataset was used as a comparison with previous water-air experiments, enabling a comprehensive evaluation of the accuracy and reproducibility of the imaging protocol.

To validate the experimental protocol and assess the quality of krypton saturation at each pressure level, CT numbers were monitored across all slices throughout the experiment. Figure 5.3 shows the resulting CT number profiles, illustrating the systematic response to pressure changes and the effectiveness of the equilibration periods.

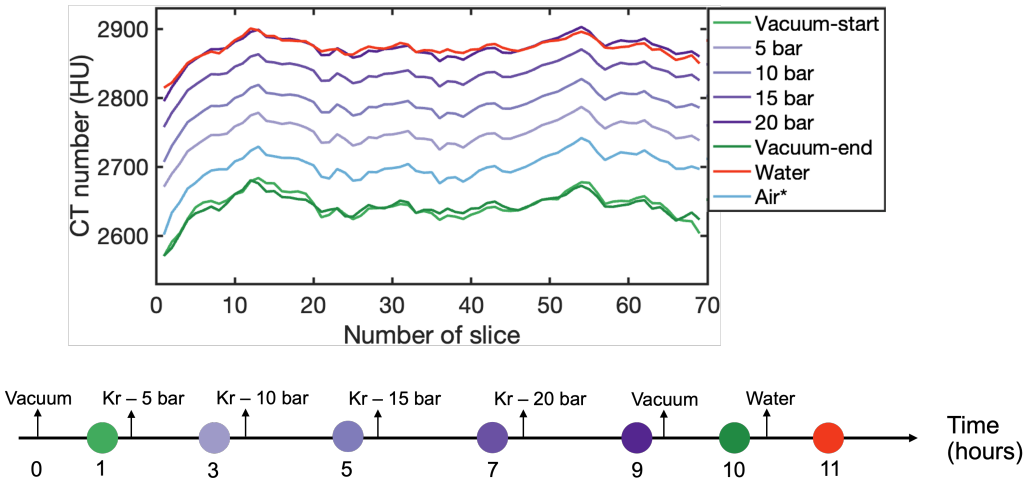


Figure 5.3: CT number profiles across Ketton limestone core during the improved imaging protocol with krypton. Top: Average CT numbers for each slice showing progressive increase with krypton pressure from vacuum to 20 bar, followed by vacuum evacuation and final water saturation. Air-saturated is shown as reference from a separate dataset. Bottom: Experimental timeline showing the 11-hour sequence with equilibration periods between each pressure increment.

The resulting krypton-based porosity profiles are shown in Figure 5.4, demonstrating a notable improvement in measurement accuracy. The profiles exhibit greater alignment with those obtained using the traditional water–air approach, indicating that the revised saturation protocol and exclusion of CO_2 effectively enhanced the reliability of krypton-based porosity imaging.

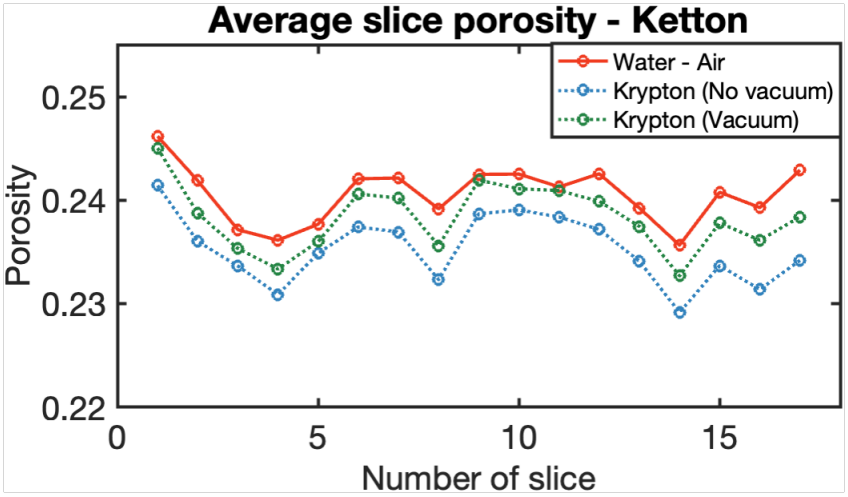


Figure 5.4: Impact of sample preparation protocol on krypton-based porosity measurements for Ketton limestone. Comparison between the improved protocol with vacuum evacuation (green dotted line) and the initial protocol without vacuum evacuation (blue dotted line) against the water-air reference (red solid line). The vacuum evacuation protocol demonstrates improved accuracy and reduced systematic bias, particularly in the middle sections of the core.

A key advantage of using krypton gas for imaging over the conventional water–air approach (where only two discrete conditions -dry and fully saturated- are typically available) is the ability to acquire multiple datasets at varying pressure levels within a single experimental campaign. As demonstrated in the krypton calibration experiments (Figure 5.1), each pressure increment produces a distinct CT number due to the pressure-dependent variation in krypton density and corresponding X-ray attenuation. This enables the application of differential imaging across a range of pressure pairs, rather than being limited to a single baseline and saturation condition.

This flexibility opens up new opportunities for validating the robustness of porosity estimations by performing differential imaging using multiple combinations of pressure pairs. The next stage of the study focused on assessing the consistency and reliability of the derived porosity profiles when using these different dataset pairs. By comparing the porosity outcomes from various pressure combinations, it was possible to evaluate the sensitivity of the differential imaging method to pressure selection and determine the optimal pressure intervals that yield the most stable and accurate porosity measurements. This approach also serves as a diagnostic tool to identify potential non-uniform saturation or imaging artifacts across the core.

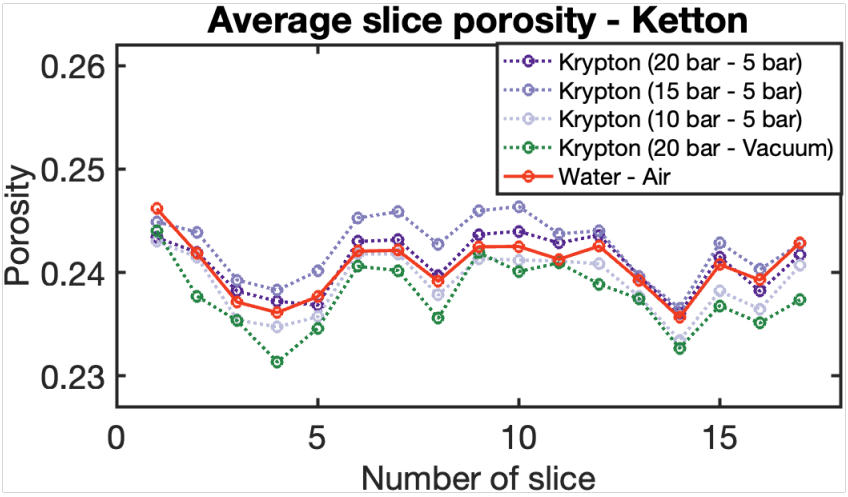


Figure 5.5: Comparison of average slice porosity profiles for Ketton limestone using different krypton pressure combinations in differential imaging. The water-air reference method (red solid line) was compared against four krypton-based approaches: three using 5 bar as the lower pressure baseline (purple lines) and one using vacuum as baseline (green dotted line). Pressure combinations using 5 bar as the reference state show better agreement with the water-air benchmark, while the vacuum-based approach exhibits greater variability.

5.4 Porosity Maps Derived from Differential Imaging Using Krypton as Saturating Fluid

Figure 5.5 presents the porosity profiles obtained from four selected combinations of krypton pressure pairs, chosen from a broader set of possible differential imaging configurations. These combinations illustrate how varying the lower and higher pressure affects the accuracy and consistency of porosity estimation. Notably, the porosity values obtained using 5 bar krypton as the lower pressure baseline yielded results that were closer to the benchmark water–air profile, compared to those derived using the vacuum dataset as the reference state.

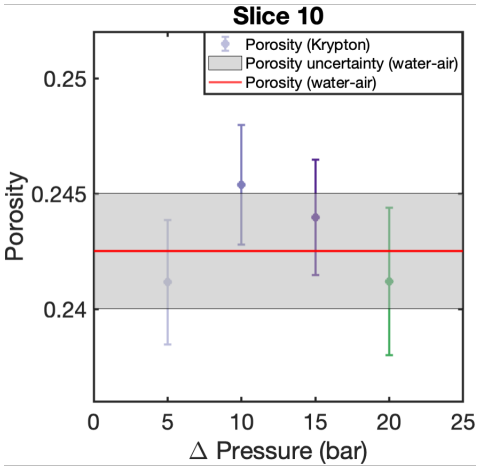


Figure 5.6: Krypton-based porosity measurements for slice 10 at varying pressure differentials (different colours denote the pressure pairs investigated in Figure 5.5) compared to water-air reference (red line with uncertainty band). Error bars represent porosity values variability at the same slice location across different krypton pressure combinations.

Porosity uncertainties were calculated by obtaining the mean and standard deviation of the porosity values in the same slice. As Figure 5.6 suggests, the vacuum scan introduces greater uncertainties, potentially due to reduced contrast or more accurate CT number readings for Krypton, whereas scans using 5 bar as the lower pressure provide a more stable and reproducible baseline. Additionally, it was observed that the increase in porosity with rising pressure was not directly proportional to the pressure increment, indicating that the relationship between krypton pressure and CT attenuation is not strictly linear in this range. This non-systematic variation suggests that other factors such as gas compressibility, incomplete equilibration or krypton density changes at higher pressures may influence the measured attenuation and, consequently, the derived porosity values. These findings reinforce the importance of calibration and pressure selection in gas-based differential imaging workflows.

The availability of multiple pressure levels allows for a statistical approach to the estimation of a porosity, where each possible pressure combination contributed to the final result. Individual porosity maps were calculated for all viable pressure pairs, and the set of results was averaged to generate the final composite porosity map. This approach improved spatial resolution and reduced measurement uncertainty compared to any single pressure pair result.

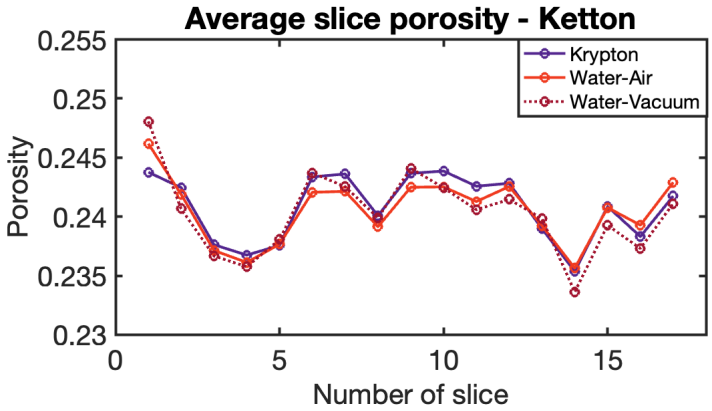


Figure 5.7: Final porosity profiles comparing averaged krypton measurements with water-air and water-vacuum reference methods, showing good agreement and validating the multi-pressure differential imaging approach.

Figure 5.7 presents the final porosity profile obtained by combining multiple krypton pressure pairs, compared against two reference measurements: water-air differential imaging and a water-vacuum combination using the water-saturated scan acquired at the end of the improved protocol. The three profiles demonstrate strong overall agreement in both shape and magnitude (core average porosity for i. water-air = 0.2405, ii. krypton = 0.2407, iii. water-vacuum = 0.2403), with an average uncertainty of less than 0.002 across the core length, indicating that the krypton-based imaging protocol yields porosity estimations comparable to those obtained via the conventional water–air method when combined with vacuum preconditioning and sufficient equilibration. Small variations among the three profiles are noted, likely arising from experimental noise, local heterogeneities, or minor image registration mismatches. These differences underscore the sensitivity of CT-based porosity analysis. However, the results highlight the reproducibility of the porosity estimation across different approaches and that consistent porosity measurements can be achieved with acceptable uncertainty.

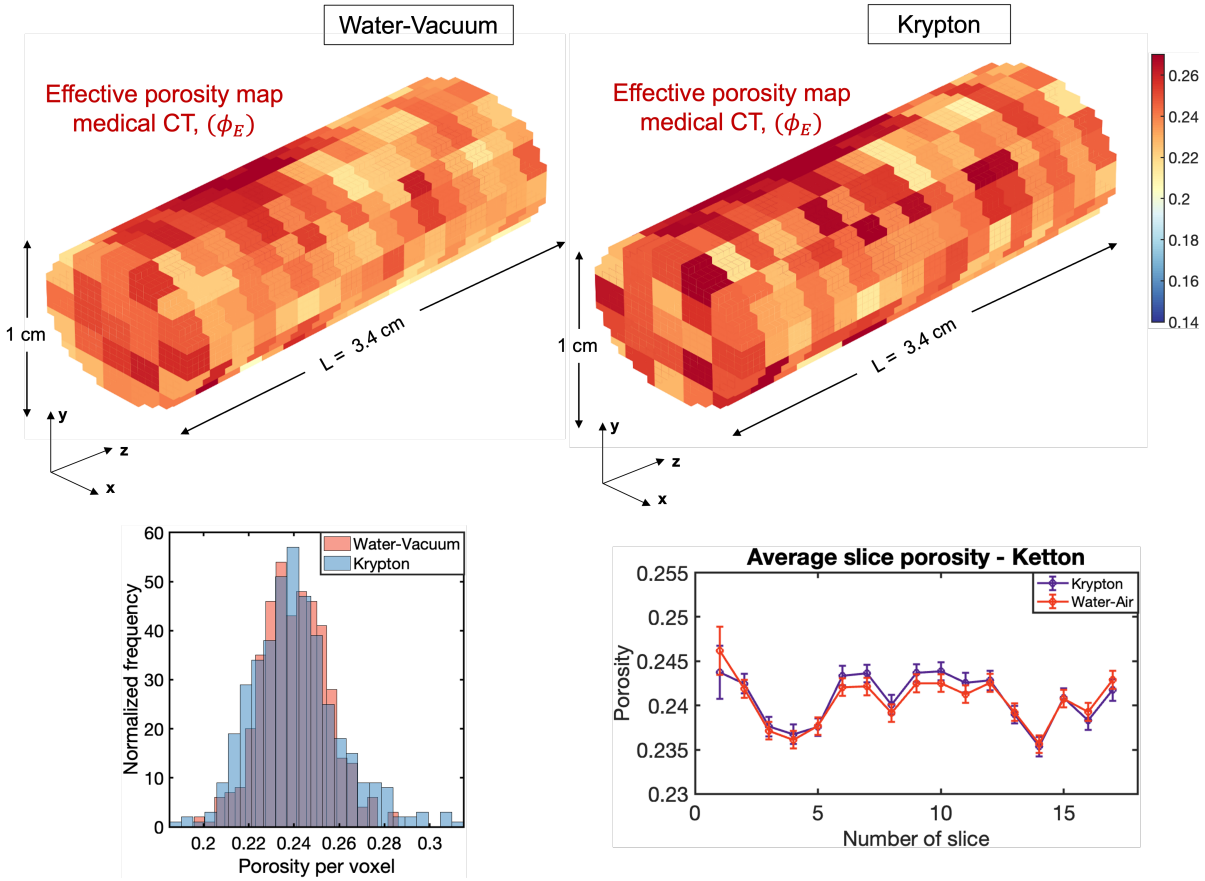


Figure 5.8: Porosity maps comparison between applying differential imaging with water and krypton as saturating fluids.

Figure 5.8 presents a side-by-side comparison of porosity maps obtained using water and krypton as saturating fluids. The accompanying histogram overlays illustrate strong agreement in voxel-wise porosity distributions between the two methods, confirming that krypton can effectively resolve the pore space in samples with sufficient connectivity.

Furthermore, the line plot shows the slice-averaged porosity along the length of the core. Both fluids yield comparable profiles, with consistent porosity trends and spatial variations. Notably, a slight increase in porosity is observed in the midsection of the krypton-based map. This subtle difference may be attributed to microporosity that remained unsaturated during the water-based scan due to the higher capillary entry pressures associated with liquid infiltration, as well as minor inconsistencies in the cropping protocol or registration process. The ability of krypton to penetrate such regions underscores its utility in identifying otherwise undetectable microporous features.

The effective porosity map obtained using krypton as a contrast agent can be directly applied in the final step of the microporosity mapping workflow described in Section 5.5, using the same resolved porosity map generated through micro CT segmentation.

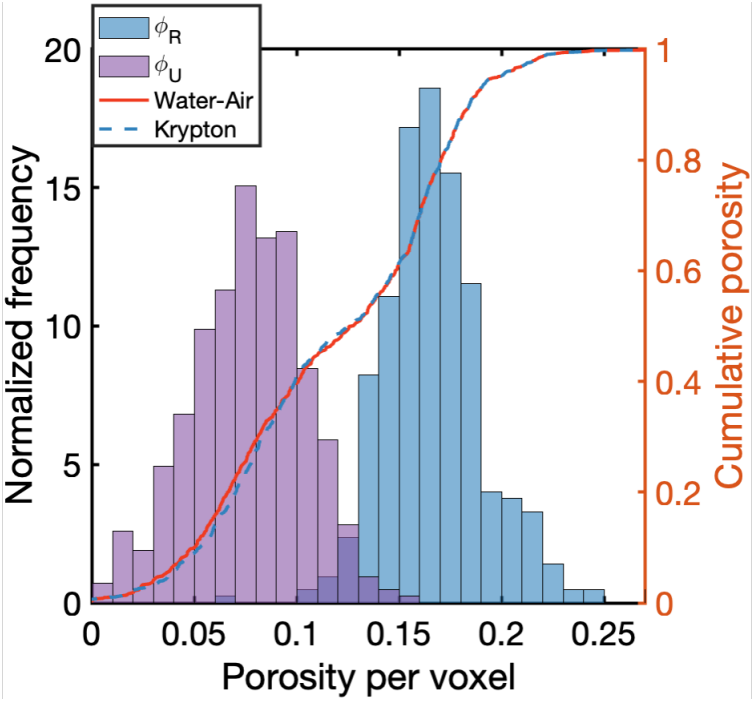


Figure 5.9: Comparison of voxel-wise porosity distributions in Ketton limestone. The histogram shows the porosity characterised by resolved and the derived unresolved porosity using the effective porosity map obtained using krypton ($\phi_U = \phi_E - \phi_R$). The overlaid cumulative porosity curves for krypton (dashed blue) and water (solid red).

The resulting voxel-wise porosity distribution for the krypton-based approach is shown in Figure 5.9. A comparison with the cumulative distribution derived from the water-based method reveals a strong agreement across the full porosity range. This consistency confirms the suitability of krypton for quantifying effective porosity, validating its use in place of traditional liquid-phase contrast agents. The histogram also highlights the distinct contributions of the resolved and unresolved porosity, reinforcing the capacity of this dual-modality approach to capture pore structures across scales.

5.5 Concluding Remarks

This chapter presented a comprehensive experimental framework for estimating porosity in rock samples using krypton gas as a contrast agent in CT imaging. The approach was developed as a robust alternative to traditional water–air methods, particularly for low-permeability rocks where achieving full water saturation can be challenging due to limited pore connectivity and long equilibration times. The method leveraged the high atomic number and radiodensity of krypton to generate sufficient contrast in CT scans, allowing for differential imaging at multiple pressure points.

A key component of the protocol involved calibrating the CT number response of krypton at various pressures, followed by the implementation of a rigorous injection and scanning procedure. This included vacuum evacuation of the sample to remove residual air and other gases, as well as extended equilibration periods at each pressure step to ensure full saturation, particularly of microporous regions. The resulting porosity profiles showed improved consistency and spatial resolution across the sample.

Comparison with conventional water–air porosity measurements revealed a strong agreement between methods, validating krypton-based imaging as a reliable alternative. Notably, the use of multiple pressure datasets introduced additional flexibility, enabling differential imaging using a variety of scan pairs to assess reproducibility and quantify uncertainties. The study also identified and addressed critical challenges such as the effects of gas diffusion limitations, impact of residual gases, and the sensitivity of CT attenuation to gas density.

These challenges were mitigated through iterative refinement of the workflow, optimizing saturation workflow, pressure control, and image acquisition, the methodology achieved accurate and repeatable porosity estimates. Overall, the findings confirm that krypton CT imaging is a viable, non-invasive, and versatile technique for digital rock analysis, particularly well-suited to low-permeability systems where fluid-based contrast agents may be less effective.

Chapter 6

3D Porosity Mapping in Sedimentary Rocks

In the following chapter, the porosity maps for the selected samples using the imaging methodology developed throughout this study are presented. A combination of image processing, segmentation, and contrast agent based differential imaging was used to obtain both resolvable and effective porosity distributions in three dimensions. The analysis aim to assess the ability of the method to quantify porosity across different scales, particularly sub-resolution porosity, in rocks with varying degrees of porosity heterogeneity and connectivity.

In addition to visualising the full 3D porosity distributions, representative cross-sectional slices along orthogonal planes are shown for each core to highlight internal features and heterogeneities as represented in Figure 6.1. Statistical analyses of porosity distributions, such as voxel-wise histograms, cumulative distributions, and cross-plot comparisons are also presented to compare the outcomes of different imaging techniques and to evaluate the robustness and accuracy of the methodology.

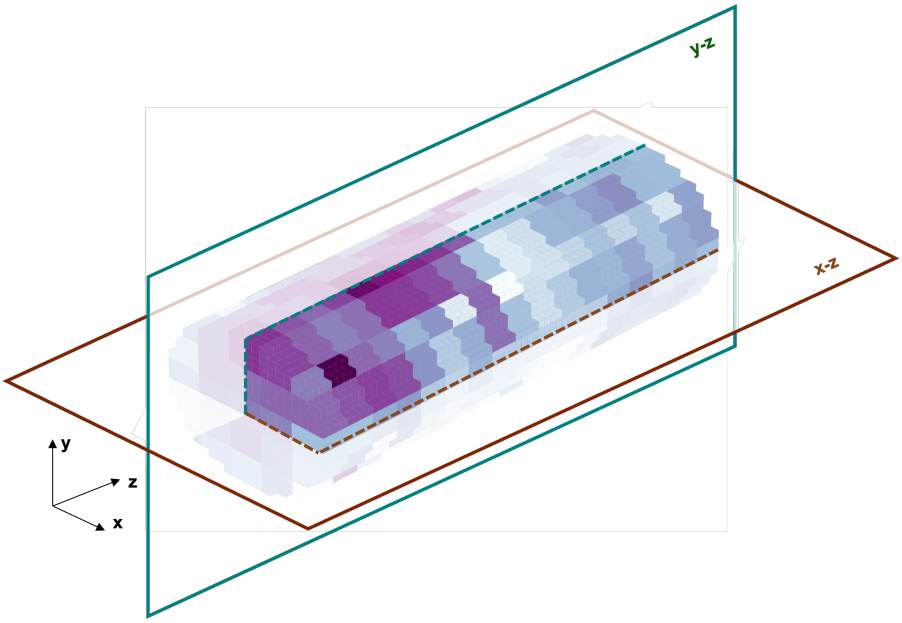


Figure 6.1: Longitudinal cross sections for internal inspection of porosity features.

The chapter is divided into two distinct sections, categorising the rock samples according to their respective petrophysical characteristics. In the first section, Bentheimer sandstone and Ketton limestone are grouped together based on their well-connected pore networks, high permeability, and extensively documented petrophysical properties. Their structural simplicity and predictable behavior make them ideal benchmarks for evaluating and comparing different porosity mapping techniques. They serve as a reference for validating both the water-based and gas-based imaging protocols developed in this study. Ketton limestone, in particular, provides an optimal test case for the dual-resolution imaging approach, as it enables comprehensive characterisation of the complete porosity spectrum by distinguishing resolved macroporosity from sub-resolution microporosity.

The second section focuses on samples with complex pore architectures: Nugget sandstone and Silurian dolomite. These samples exhibit heterogeneous pore systems with variable connectivity patterns that challenge conventional imaging and analysis approaches. Nugget sandstone displays a dual-porosity structure comprising well-connected macroporous layers and poorly connected microporous zones. Silurian dolomite presents a highly heterogeneous, low-permeability system with spatially variable connectivity, thereby testing the limits of applicability for the developed methodologies.

6.1 Simple Porosity Systems: Bentheimer Sandstone and Ketton Limestone

As described in Section 3.1.1, Bentheimer is characterised by well-connected, intergranular porosity with pore sizes mostly above the imaging resolution. The micro CT scans were performed at a voxel resolution of 6x6x6 µm which is sufficient to capture the majority of the pore structure in this sample. Results from MICP analysis showed consistent pore throat sizes in the range between 10-40 µm, indicating that virtually most of the porosity is resolvable through imaging methods. As a result, sub-resolution porosity is expected to be negligible in Bentheimer, and the majority of porosity features can be directly visualised and quantified. Furthermore, the high degree of pore connectivity facilitates the full saturation of the pore space with contrast agents, enabling accurate extraction of effective porosity values via differential imaging.

In the case of Ketton limestone, its characteristic dual-porosity structure presents an ideal scenario for testing the developed sub-resolution imaging methodology. This rock exhibits two distinctly different pore size domains: intragranular microporosity, with pore diameters ranging from approximately 0.01 to 0.2 µm (average $\approx$ 0.1 µm), and intergranular macroporosity, with pore diameters between 10 and 200 µm (average $\approx$ 55 µm), as per MICP measurements. The micro CT imaging performed for this sample achieved a voxel resolution of 7x7x7 µm, which falls between these two pore size ranges. As a result, the macropores are resolvable and can be segmented directly from the micro-CT images, whereas the micropores fall below the resolution threshold and thus remain unresolved by conventional segmentation.

6.1.1 Effective Porosity Maps in 2D and 3D

The section begins by presenting effective porosity maps derived from differential imaging using two contrasting agents: (i) water and vacuum, and (ii) pressurised krypton gas at 15 bar and vacuum. This comparison allows assessment of the consistency and reliability of the krypton-based method relative to the well-established water-vacuum technique.

The corresponding 3D porosity distributions are shown in Figure 6.2 for Bentheimer and Figure 6.3 for Ketton, respectively.

Bentheimer:

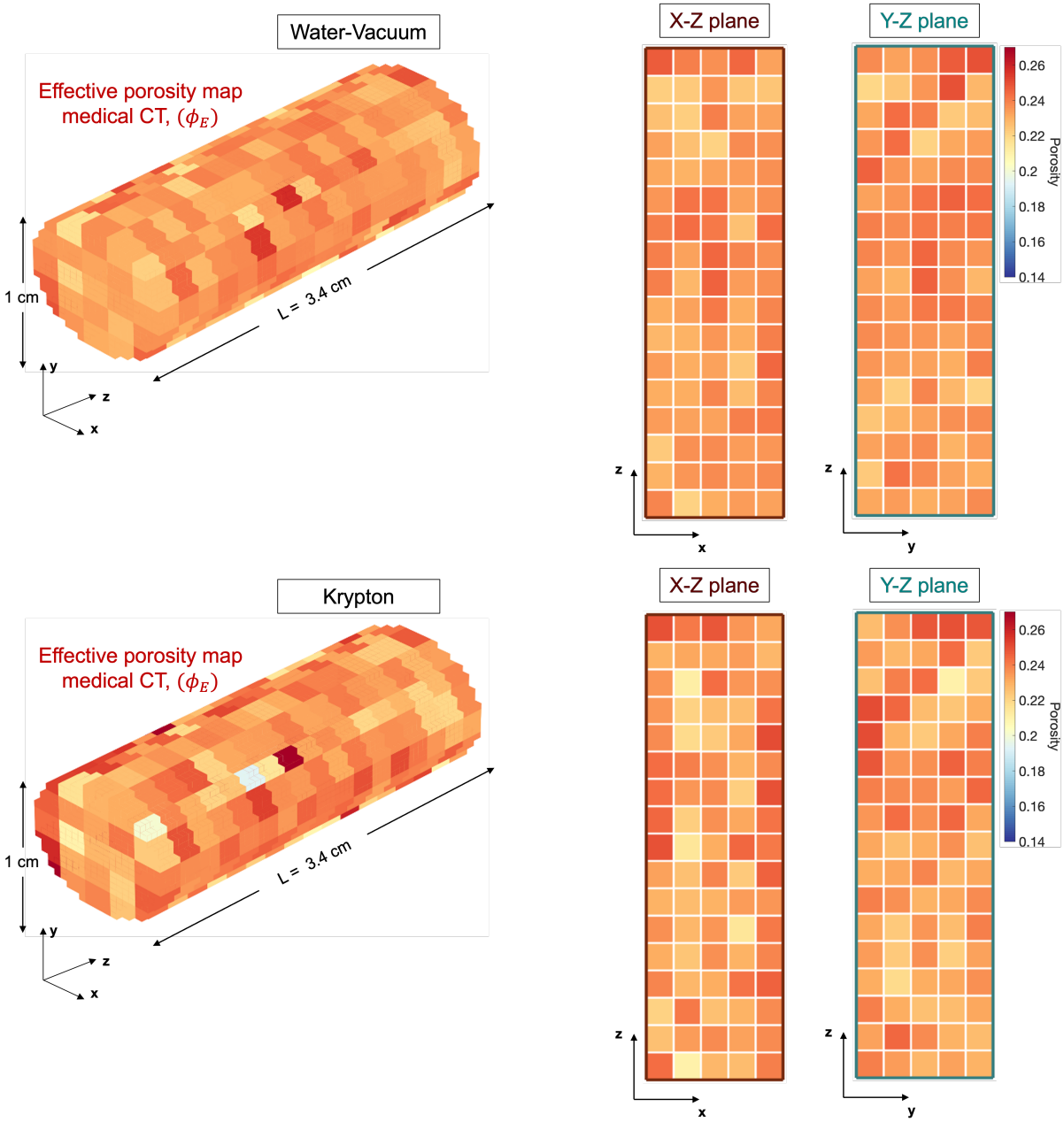


Figure 6.2: Left: 3D rendering of Bentheimer effective porosity map by differential imaging using water and vacuum (top row) and Krypton at 15 bar and vacuum (bottom row) as contrasting agents. Voxel size: (2 x 2 x 2) mm^3. Right: 2D planar sections (X-Z and Y-Z) revealing internal heterogeneity patterns.

Ketton:

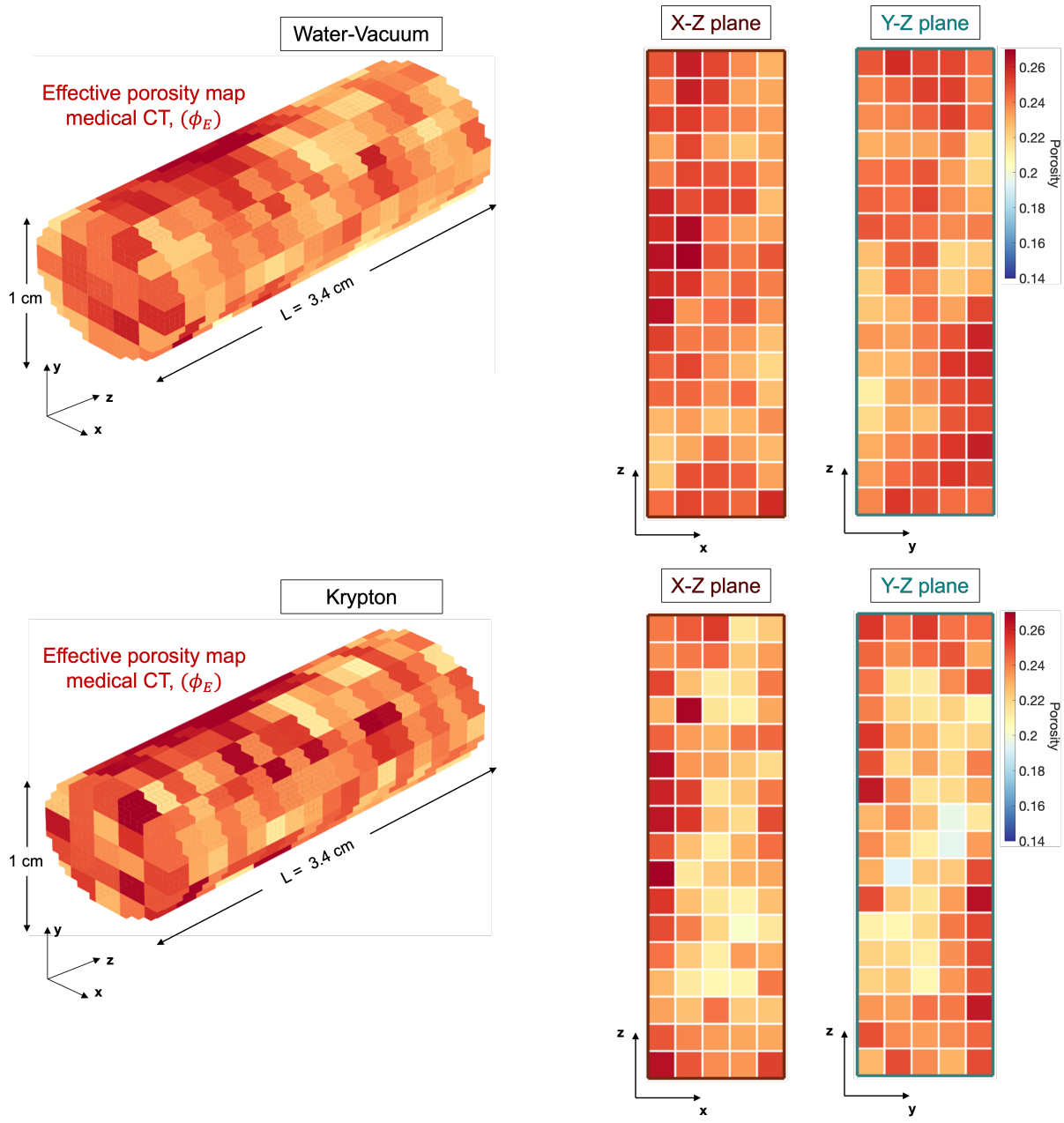


Figure 6.3: Left: 3D rendering of Ketton effective porosity map by differential imaging using water and vacuum (top row) and Krypton at 15 bar and vacuum (bottom row) as contrasting agents. Voxel size: (2 x 2 x 2) mm^3. Right: 2D planar sections (X-Z and Y-Z) revealing internal heterogeneity patterns.

Upon visual inspection, it is evident that, although both Bentheimer and Ketton are generally considered homogeneous rock types, the porosity maps derived from the two imaging methods reveal subtle but consistent patterns of heterogeneity at

the voxel scale. These patterns, while not pronounced, appear consistently in both porosity maps, indicating that they reflect genuine internal structural features rather than imaging artifacts. Bentheimer sandstone exhibits relatively homogeneous porosity distribution, displaying only minor spatial variations across both 2D planes that manifest as gentle progression rather than sharp contrasts. Conversely, Ketton limestone shows greater heterogeneity, with porosity values spanning a wider range and displaying more pronounced spatial variability, characterised by distinct high-porosity zones combined with lower-porosity areas, minor local discrepancies between the two maps are attributed to variations in the applied saturation mechanisms. Both samples demonstrate a good correlation between the two porosity maps obtained by the two saturating fluids, capturing similar spatial patterns and magnitude ranges. This qualitative assessment is further supported by quantitative analysis through voxel-wise porosity histograms.

As shown in Figure 6.4, both methods independently yield very similar overall porosity distributions, effectively capturing the same porosity range and exhibiting close agreement in mean values. The average effective porosity ($\overline{\phi_{\mathrm{E}}}$) was determined to be 0.235 for krypton and 0.234 for water in the case of Bentheimer, and 0.241 for krypton and 0.240 for water in the case of Ketton. Despite the different pore structures, the consistency across both rock types demonstrates the broad applicability and reliability of krypton as a contrasting agent.

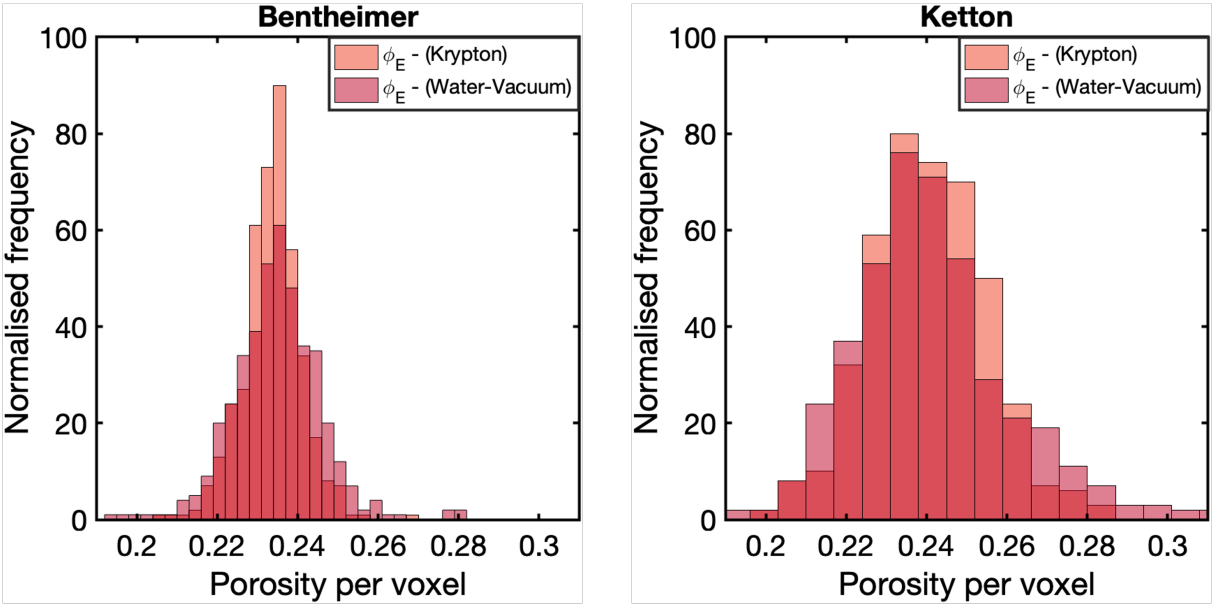


Figure 6.4: Overlay of voxel-wise porosity histograms for comparison of the effective porosity distribution derived from using krypton and water as saturating fluid in differential imaging for two simple porosity systems. Left: Bentheimer. Rigth: Ketton.

To complement the visual and statistical comparison of the voxel-wise porosity distributions, a more direct method is performed to assess the agreement between the two imaging techniques. A voxel-by-voxel comparison is shown using a one-to-one cross-plot, where each data point corresponds to the porosity value of a specific voxel location as measured by both methods. This approach enables a detailed evaluation of spatial correlation and highlights any systematic deviations or local inconsistencies between the water- and krypton-based porosity maps. The results are shown in Figure 6.5.

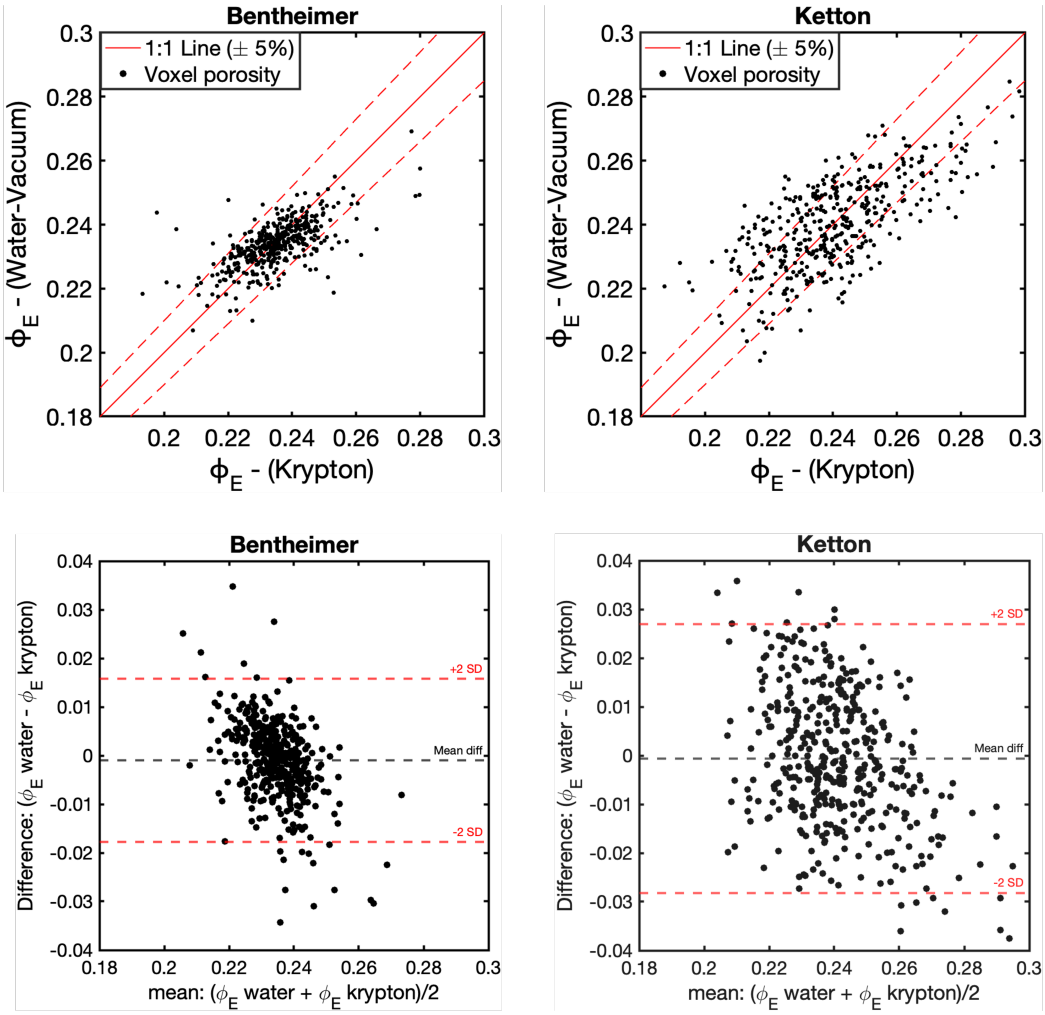


Figure 6.5: Voxel-wise comparison of effective porosity (ϕ_E) measured using krypton and water as contrast agents for Bentheimer (top left) and Ketton (top right). Each dot represents the porosity value of an individual voxel at the same location. The red dashed line indicates the 1:1 line for reference. Bentheimer shows a strong agreement with minimal scatter, consistent with its homogeneous nature. Ketton also displays a strong correlation but with greater scatter, reflecting its intrinsic heterogeneity and dual-porosity structure. Bland-Altman plot showing the difference in porosity for each voxel as a function of its average. Bentheimer (bottom left) and Ketton (bottom rigth).

In both cases, the voxel-by-voxel comparison demonstrates a strong positive correlation between the water-vacuum and krypton methods with a linear correlation coefficient of r=0.65 for Bentheimer and r=0.71 for Ketton, with data points exhibiting close alignment along the 1:1 line, (conventional interpretation thresholds $r > 0.7$ = strong, $0.5 < r \leq 0.7$ = moderate-to-strong). The relationship is predominantly linear with relatively symmetric scatter distribution. Notably, while the global porosity distributions and average values are nearly identical between methods, the corresponding R^2 values

indicate that approximately 41% (Bentheimer) and 50% (Ketton) of the variance in porosity is explained by the correlation between the two methods, with the remaining variability reflecting experimental noise, contrast sensitivity, and intrinsic heterogeneity at or below the resolution limit rather than indicating methodological limitations. This level of agreement is considered robust for natural porous systems, confirming that both imaging approaches capture the spatial distribution of porosity in an effective and complementary manner, further evidenced in the Bland-Altman plot where the mean difference between voxels at same location cluster around zero. Although variability in agreement should be expected depending on the pore structure characteristics of the specific rock type being analysed, krypton can be used with confidence for differential imaging.

6.1.2 Resolved Porosity Map from Micro CT Image Segmentation

Figure 6.6 and Figure 6.9 present the resolved porosity maps (ϕ_R) for Bentheimer and Ketton respectively, obtained by following the procedure outlined in Section 4.4.2., these porosity maps have been upscaled from their original resolution achieved in micro CT imaging to match the voxel size (2 x 2 x 2 mm^3) of the effective porosity maps obtained with medical CT differential imaging.

Bentheimer:

Bentheimer sample exhibits consistent structural features throughout, with only subtle spatial variability observed. Remarkably, the resolved porosity magnitudes closely correspond to those observed in the effective porosity maps (Figure 6.2), indicating good agreement between measurement scales.

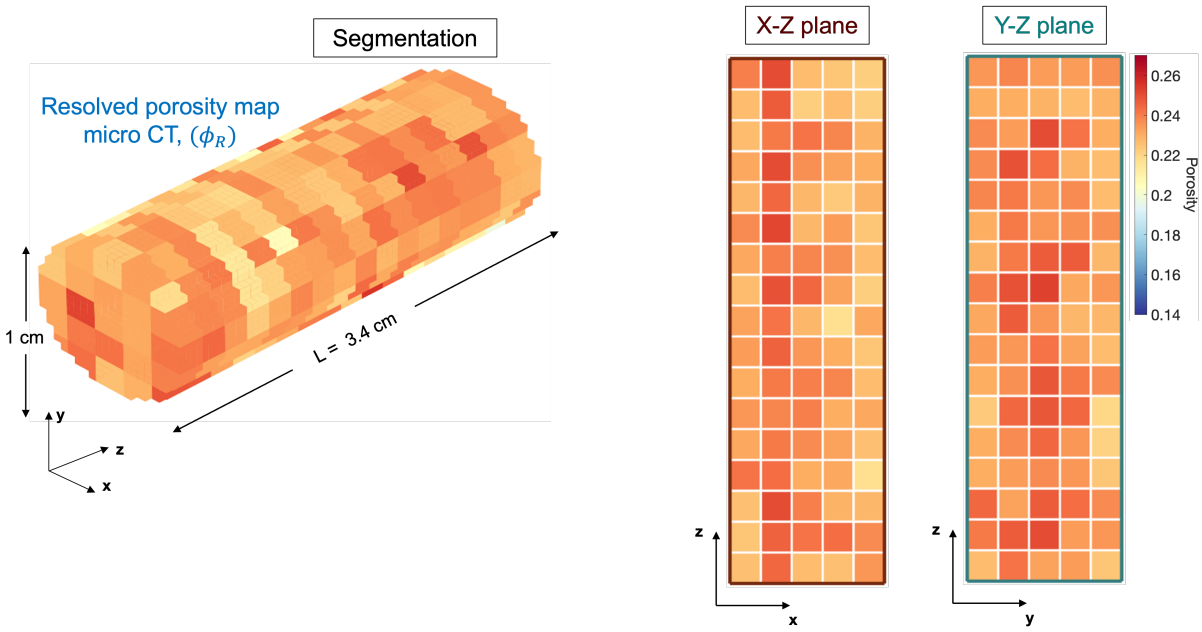


Figure 6.6: Left: 3D rendering of Bentheimer resolved porosity map by segmentation of micro CT images. Voxel size: (2 x 2 x 2) mm^3. Right: 2D planar sections (X-Z and Y-Z) revealing internal heterogeneity patterns.

To further validate the consistency between porosity derived from differential imaging using low-resolution CT data and that obtained from high-resolution micro CT segmentation, Figure 6.7 compares the porosity distributions produced by both methods. A strong agreement is observed, as expected for Bentheimer sandstone, where the majority of pores fall within the resolvable range of micro CT resolution, allowing accurate segmentation-based porosity quantification.

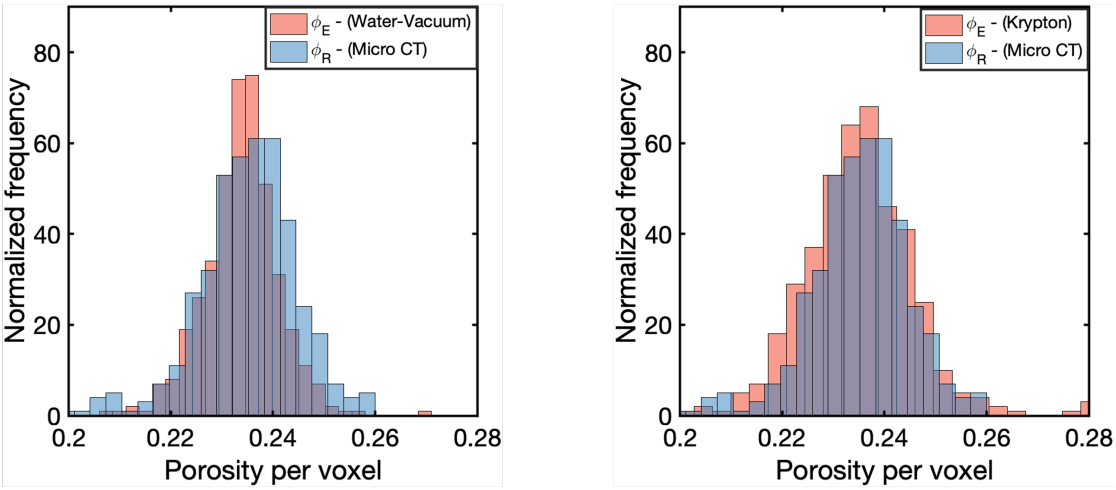


Figure 6.7: Porosity distribution comparison between medical CT differential imaging and micro CT segmentation for Bentheimer sandstone.

Figure 6.8 presents the slice-averaged porosity values as a function of longitudinal position along the core sample, providing insight into the spatial variability and methodological consistency of porosity measurements across the three imaging techniques. Each data point represents the mean porosity within individual slices, with error bars indicating the standard deviation of porosity values within each slice.

The longitudinal porosity profile reveals several key observations regarding the internal structure and methodological performance. All three methods demonstrate remarkable consistency in capturing the overall porosity trend along the core length, with slice-averaged values clustering tightly around the calculated bulk porosity of 0.235. This consistency extends to the detection of subtle longitudinal variations, such as the slight porosity reduction observed around slice 16, which is consistently captured by all three techniques. The excellent agreement observed in the slice-averaged data corroborates the voxel-by-voxel comparisons, demonstrating that the systematic offsets between methods are minimal when data are spatially averaged, providing stable and reproducible porosity estimates.

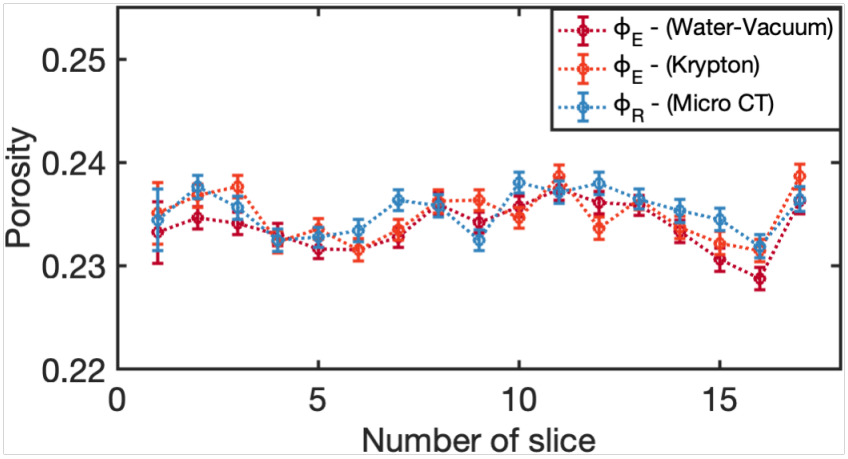


Figure 6.8: Average slice porosity profiles for Bentheimer sandstone core for three imaging methods highlighting the similarities in longitudinal porosity variations.

Ketton:

The resolved porosity map of Ketton displays notable similarities in porosity features when compared to the effective porosity map, albeit with consistently lower absolute values. For instance, a diagonal band of relatively lower porosity is observed in the middle section of the sample in the Y–Z plane, while a cluster of higher porosity is evident on the left side of the X–Z plane. These correspondences suggest that both independent imaging methods capture the same internal structural features. Since this resolved porosity map primarily reflects the intergranular pore space (estimated to account for approximately 70% of the total porosity) it can be concluded that the larger, connected macropores dominate the pore network in Ketton, and that segmentation of micro CT data is effective in capturing the macroporosity distribution in this type of dual-porosity system.

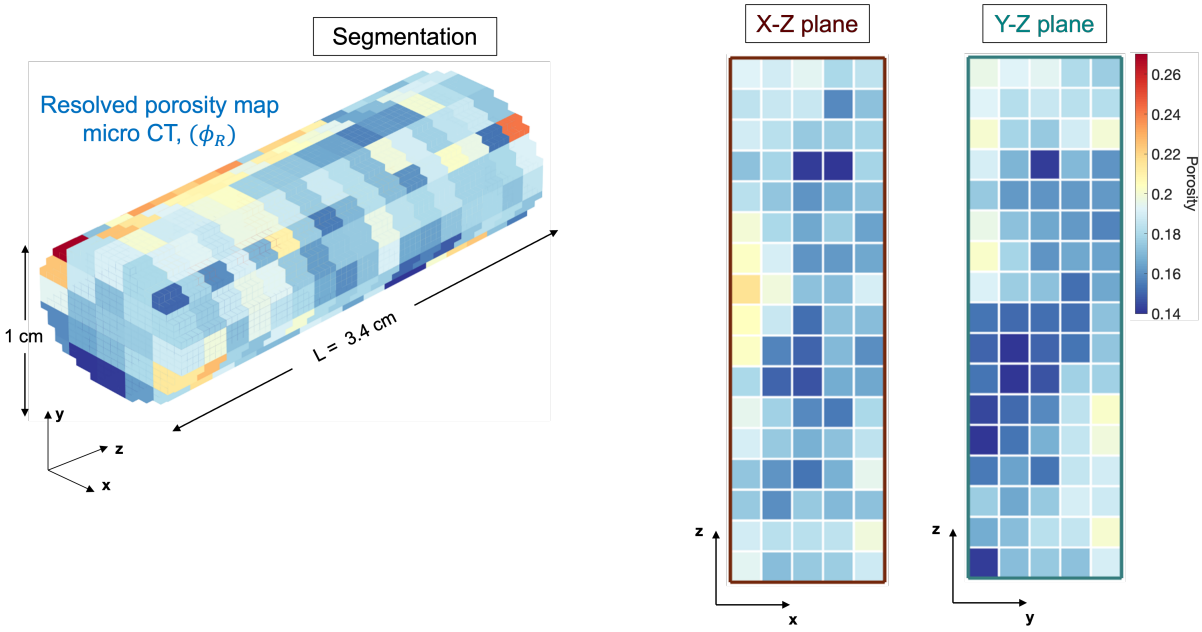


Figure 6.9: Left: 3D rendering of Ketton resolved porosity map by segmentation of micro CT images. Voxel size: (2 x 2 x 2) mm^3. Right: 2D planar sections (X-Z and Y-Z) revealing internal heterogeneity patterns.

The slice-by-slice comparison of porosity measurements reveals a systematic offset between the effective porosity values derived from differential imaging and the resolved porosity obtained from micro CT segmentation. Both krypton and water-vacuum methods yield nearly identical porosity profiles across the sample, indicating internal consistency of the differential imaging approach. In contrast, the micro CT–derived porosity remains significantly lower for all slices, reflecting its limitation in resolving sub-micron porosity. This constant gap between methods highlights the presence of a substantial sub-resolution pore network within the Ketton sample, which is captured by the contrast agents but remains hidden to conventional segmentation techniques. Furthermore, the relatively stable profile shape across slices for all three methods suggest that the sample is macroscopically homogeneous at core level, but the observed differences confirm the presence of sub-micron porosity that is spatially distributed throughout the core.

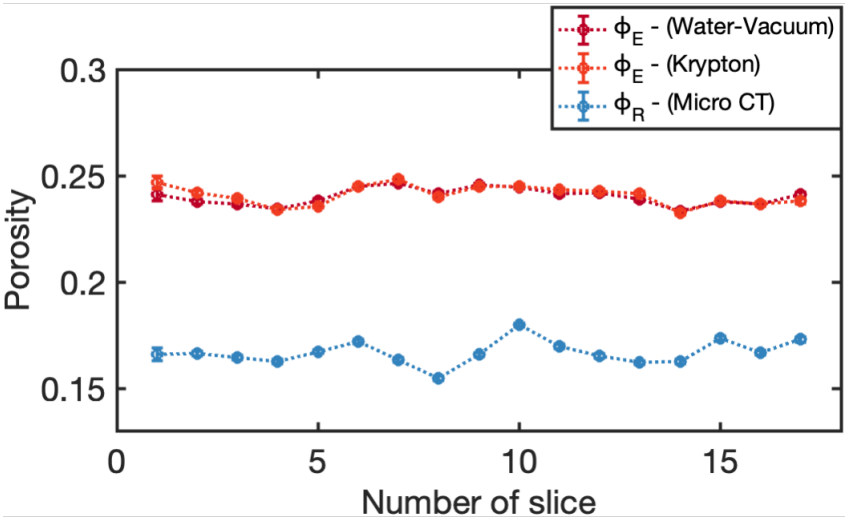


Figure 6.10: Average slice porosity profiles for Keton sandstone core for three imaging methods highlighting the consistent effective porosity profiles derived from water-vacuum and krypton, while micro CT consistently reports lower porosity values due to its inability to capture sub-resolution microporosity.

For a more detailed analysis of the voxel-scale relationship between resolved and effective porosity, Figure 6.11 shows a voxel to voxel comparison that reveals a weak correlation between the two measurements, with considerable scatter around the mean values. This observation suggests that, while both methods yield accurate average porosity, they respond differently at the voxel level. Specifically, it indicates that sub-micron porosity (present in ϕ_E but unresolved in ϕ_R) appears to be spatially heterogeneous and independent of the macropore structure. Regions with similar intergranular porosity exhibit varying levels of microporosity, reinforcing the interpretation of a spatially variable sub-resolution pore network in Ketton. This intrinsic heterogeneity cannot be directly observed with micro CT imaging alone but becomes evident when combined with differential imaging, underscoring the value of integrating multiple imaging modalities to capture the full complexity of the pore space, spatially.

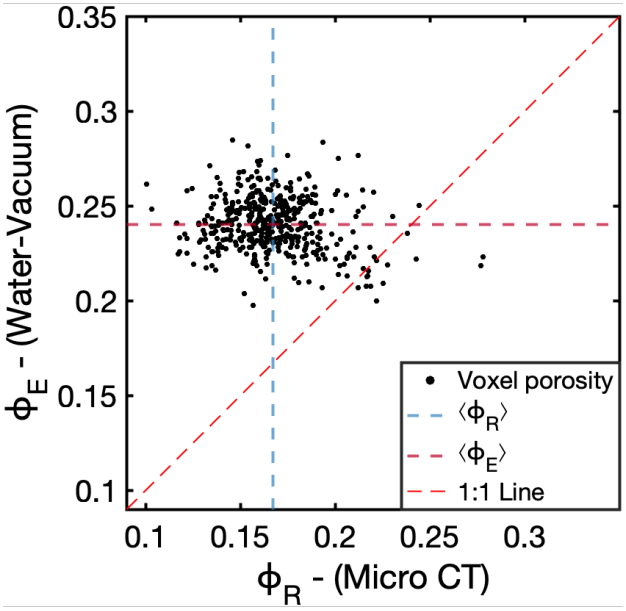


Figure 6.11: Voxel-wise comparison of effective porosity (ϕ_E) obtained via water-vacuum differential imaging and resolved porosity (ϕ_R) from micro CT segmentation for Ketton limestone. Each data point represents a voxel porosity value from both methods. The dashed lines indicate the mean values of ϕ_R (blue) and ϕ_E (red).

6.1.3 Calculation of Unresolved Porosity Map by Integrating Effective and Resolved Porosity Maps

Having validated both the effective and resolved porosity maps, the final step in the workflow involves calculating the sub-resolution porosity map (ϕ_U) using Equation 5.6. This step enables quantification of the pore volume not captured directly by high-resolution segmentation but inferred from differential imaging.

Bentheimer:

As illustrated in Figure 6.12, the resulting sub-resolution porosity distribution for Bentheimer sandstone confirms that the amount of unresolved porosity is negligible. The voxel-wise differences in porosity are minimal, with values approximately centered around zero.

This outcome aligns with the expectation that nearly all pore space in Bentheimer is

resolvable due to its relatively large and well-connected intergranular pores. The narrow spread of the unresolved porosity values further highlights the homogeneous nature of the Bentheimer sample. The computed distribution of ϕ_U exhibits a mean near zero and a standard deviation of $\pm 1.2\%$. For comparison, the propagated measurement uncertainties of the individual maps (0.14% for ϕ_E and 0.24% for ϕ_R) predict a lower expected standard deviation of $\approx 0.26\%$ for the maps subtraction. Indicating that any observed discrepancies between the effective and resolved porosity maps are likely due to the methodological differences between the techniques, slight image registration inaccuracy or segmentation sensitivity rather than systematic bias. However, the small magnitude of the observed SD is still acceptable, representing only a minor fraction of the total porosity and reinforcing the reliability of both imaging techniques for high-permeability rocks where pores fall above the resolution threshold.

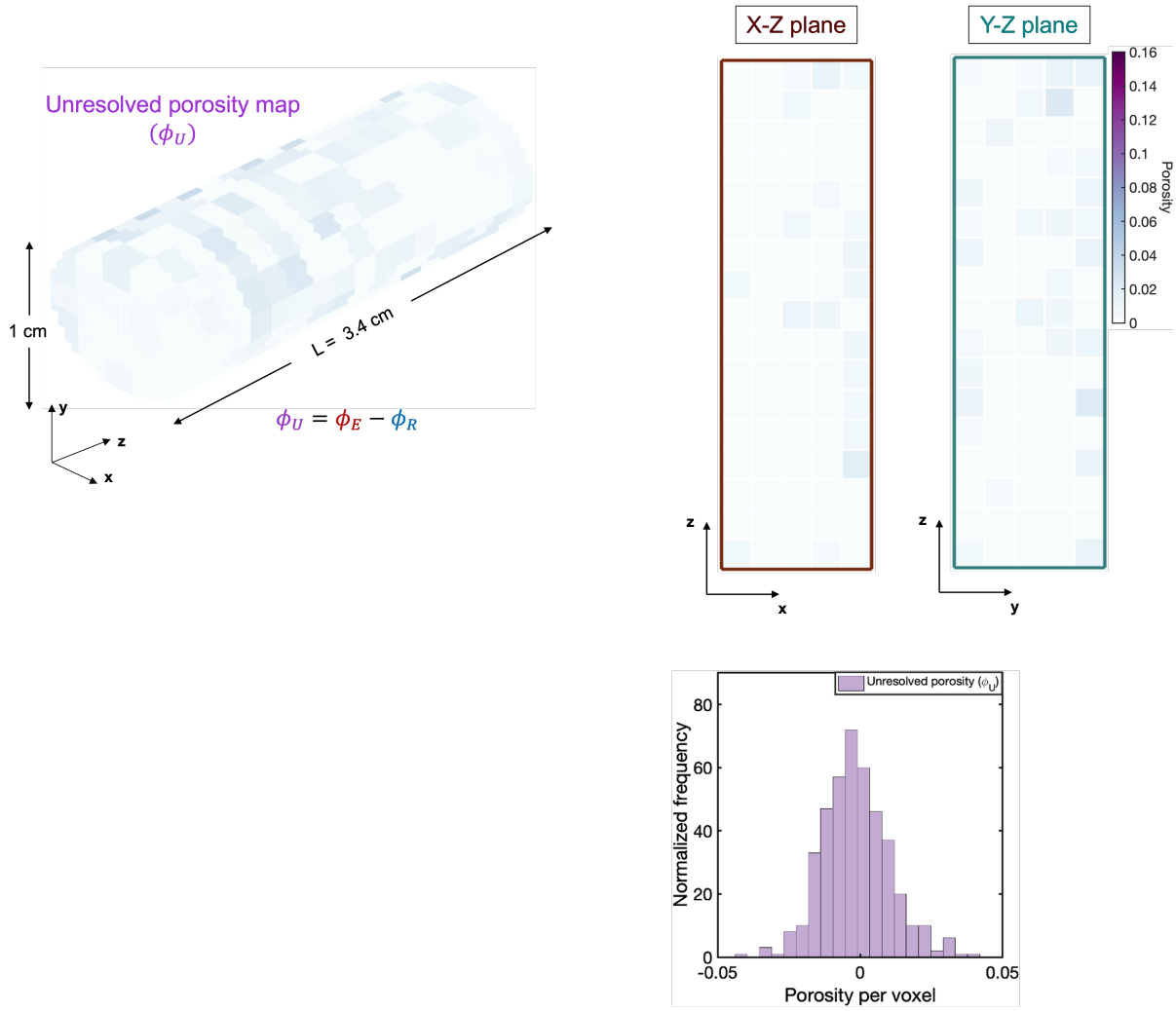


Figure 6.12: Top: 3D rendering of Bentheimer unresolved porosity map. Voxel size: (2 x 2 x 2) mm^3 and 2D planar sections (X-Z and Y-Z). Bottom: histogram of unresolved porosity distribution.

Ketton:

Figure 6.13 presents the sub-resolution porosity map of the Ketton limestone, accompanied by a statistical breakdown of how this porosity component is spatially distributed throughout the core. This map represents the portion of pore space not captured by conventional micro CT imaging but resolved through differential imaging techniques, effectively isolating the contribution of microporosity to the total porosity, offering critical insights into the fine-scale pore architecture that underpins the dual-porosity nature of Ketton.

This comprehensive analysis demonstrates the successful decomposition of total porosity

into resolved and unresolved components for Ketton limestone. The 3D unresolved porosity map reveals significant spatial heterogeneity in the microporosity distribution, with values ranging from near-zero to 0.16, confirming that sub-resolution pore space is not uniformly distributed throughout the sample. The cross-sectional views show distinct patterns of microporosity. However, the slice average shows resolved and unresolved porosity as constant fractions of the effective porosity along the sample length. The histogram analysis provides quantitative validation of this dual-porosity architecture: the effective porosity plot shows a normal distribution centered around the bulk porosity mean value of 0.241, while the decomposed histogram reveals a bimodal distribution with two independent pore systems operating at different scales, resolved porosity with mean value of 0.167 and unresolved porosity having a mean value of 0.074. These values represent 69.3% and 30.7% respectively, of the total bulk porosity, percentages that are in line with values found in the literature, (Tanino and Blunt 2012; Kurotori, Zahasky, Sally M Benson, et al. 2020).

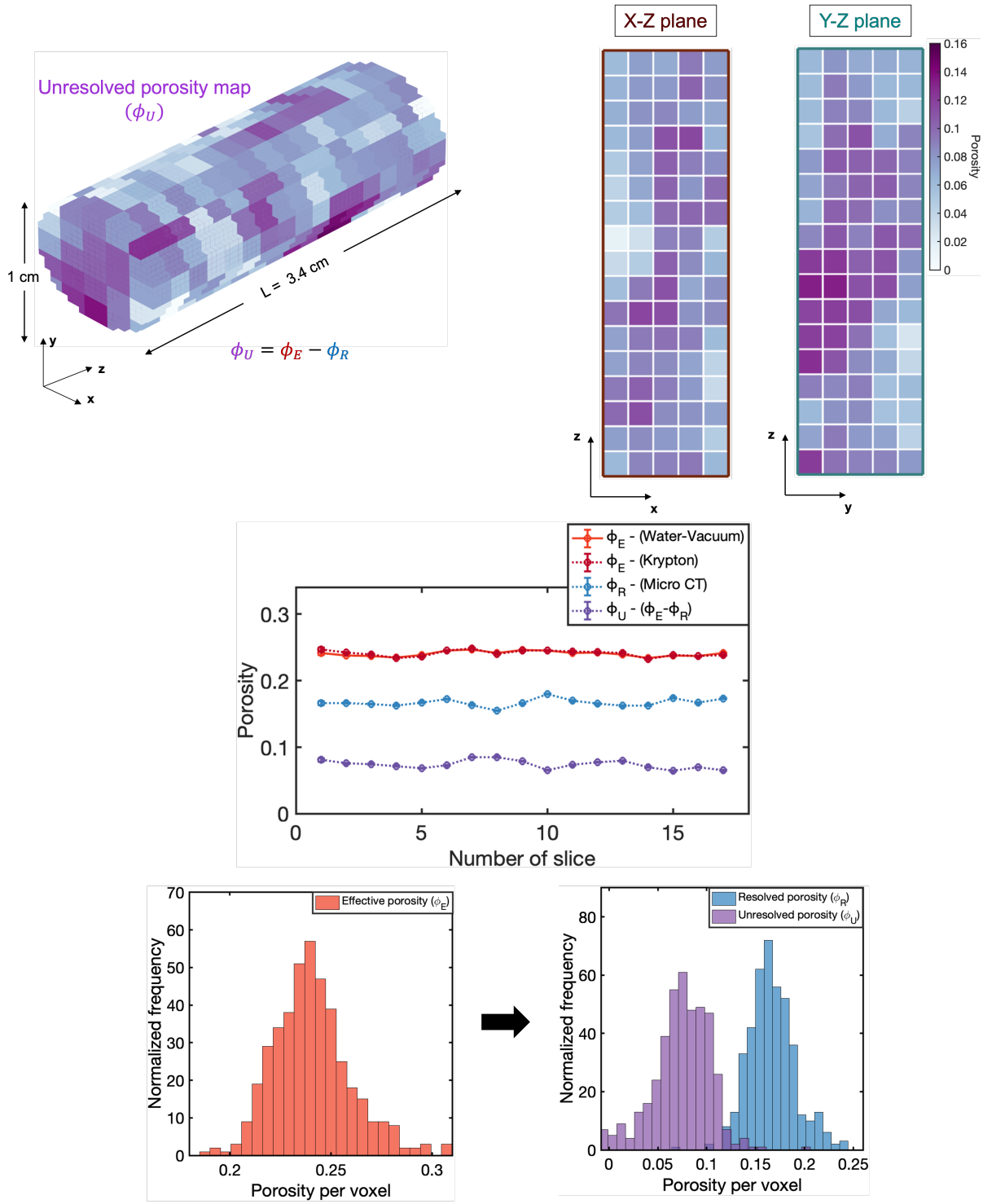


Figure 6.13: Top: 3D rendering of Ketton unresolved porosity map. Voxel size: (2 x 2 x 2) mm^3 and 2D planar sections (X-Z and Y-Z). Middle: Average slice porosity profiles for the effective, resolved and unresolved porosity maps. Bottom: Histogram of effective porosity distribution effectively split into resolved and unresolved porosity distributions.

6.2 Complex Porosity Systems: Nugget Sandstone and Silurian Dolomite.

As described in the geological description and supported by MICP data, Nugget sandstone exhibits a relatively narrow, bimodal pore size distribution with well defined stratification between high- and low-porosity layers. Unlike Ketton where microporosity is predominantly intragranular porosity, the pore space in Nugget is entirely intergranular with pore throats ranging from approximately 0.1 to 12 µm. The micro CT scans were acquired at a voxel size of 6x6x6 μm^3, enabling effective visualisation of the higher-porosity layers while the lower-porosity zones are dominated by micropores that fall below the imaging resolution threshold (Figure 6.14). This presents a challenging scenario as the bulk of the pore space contributes to sub-resolution porosity but there is also a share of sub-resolution porosity in the higher-porosity layers.

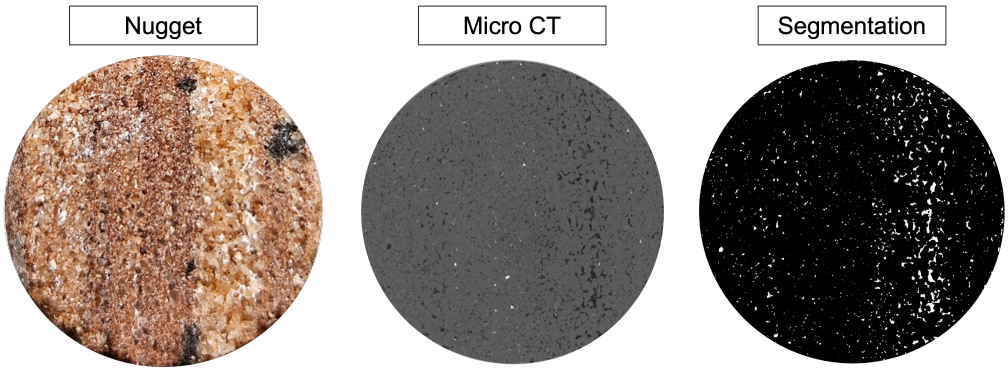


Figure 6.14: Left: Photograph of the Nugget sandstone inlet face, clearly revealing the characteristic layering. Center: Corresponding micro CT slice highlighting internal structural features. Right: Segmentation result identifying the resolvable macroporous layers, predominantly concentrated on the right side of the sample.

The Silurian dolomite presents a more complex, multi-modal pore size distribution that exemplifies the heterogeneous nature of carbonate systems. Micro CT imaging was performed at a voxel resolution of 5.8x5.8x5.8 μm^3, which falls in the intermediate range of the observed pore size spectrum. The MICP analysis reveals a broad distribution of pore sizes, ranging from sub-micron pores to vugs exceeding hundreds

of microns (Figure 6.15). While the imaging resolution is sufficient to capture the macroporous features, a substantial fraction of microporosity remains unresolved. This dual-scale porosity structure, combined with low permeability and spatially variable connectivity, produces complex saturation behavior that challenges conventional porosity quantification. As such, the Silurian dolomite serves as a valuable test case for the developed imaging methodology, particularly in assessing its capability to capture the full pore size distribution and to evaluate the use of krypton gas as a saturating agent in tight formations where water cannot effectively penetrate the pore network.

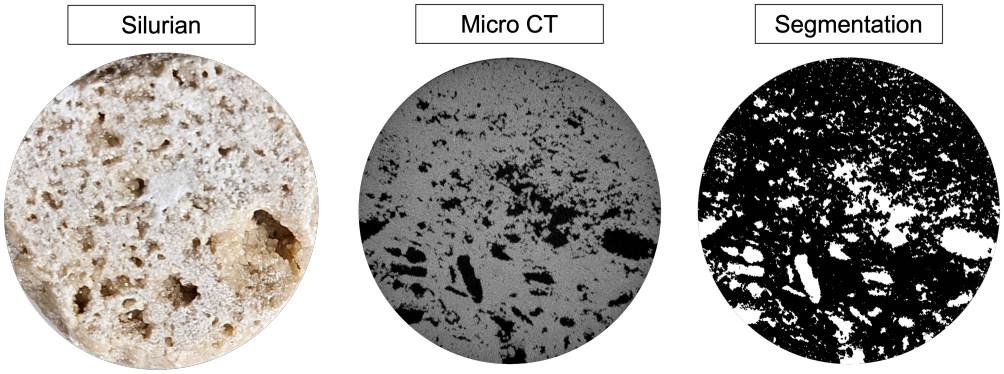


Figure 6.15: Left: Photograph of the Silurian dolomite inlet face. Center: Micro CT slice of Silurian dolomite highlighting the complex porosity heterogeneity. Right: Segmentation result with larger pores easily identified and expected zones of microporosity throughout the sample.

6.2.1 Effective Porosity Maps in 2D and 3D

Effective porosity maps for Nugget (Figure 6.16) and Silurian (Figure 6.21) are presented. For Nugget, both saturation approaches (Water-Vacuum and Krypton at 15 bar-Vacuum) were successfully applied. In contrast, due to the extremely low permeability of the Silurian dolomite, only the krypton-based saturation method could be employed.

Nugget:

The effective porosity maps of Nugget show clear representation of the layered system, where the final two layers in the X-Z plane exhibit higher porosity values (above 0.12) than the rest of the sample. In contrast, the lower porosity layers appear to represent the

majority of the total volume of the sample, with values ranging between 0.10 and 0.12. The average effective porosity for the sample is $\overline{\phi_{\mathrm{E}}}$=0.123.

An important observation from these maps comparison is the fact that both water and krypton approaches show comparable porosity values in the lower porosity layers, suggesting that, despite their smaller pore sizes, mostly sub-resolution pores, these domains are well connected and permeable enough to saturate these regions effectively, supporting the application of differential imaging with krypton in this sample. This remark is further confirmed with a statistical analysis comparing both effective porosity maps.

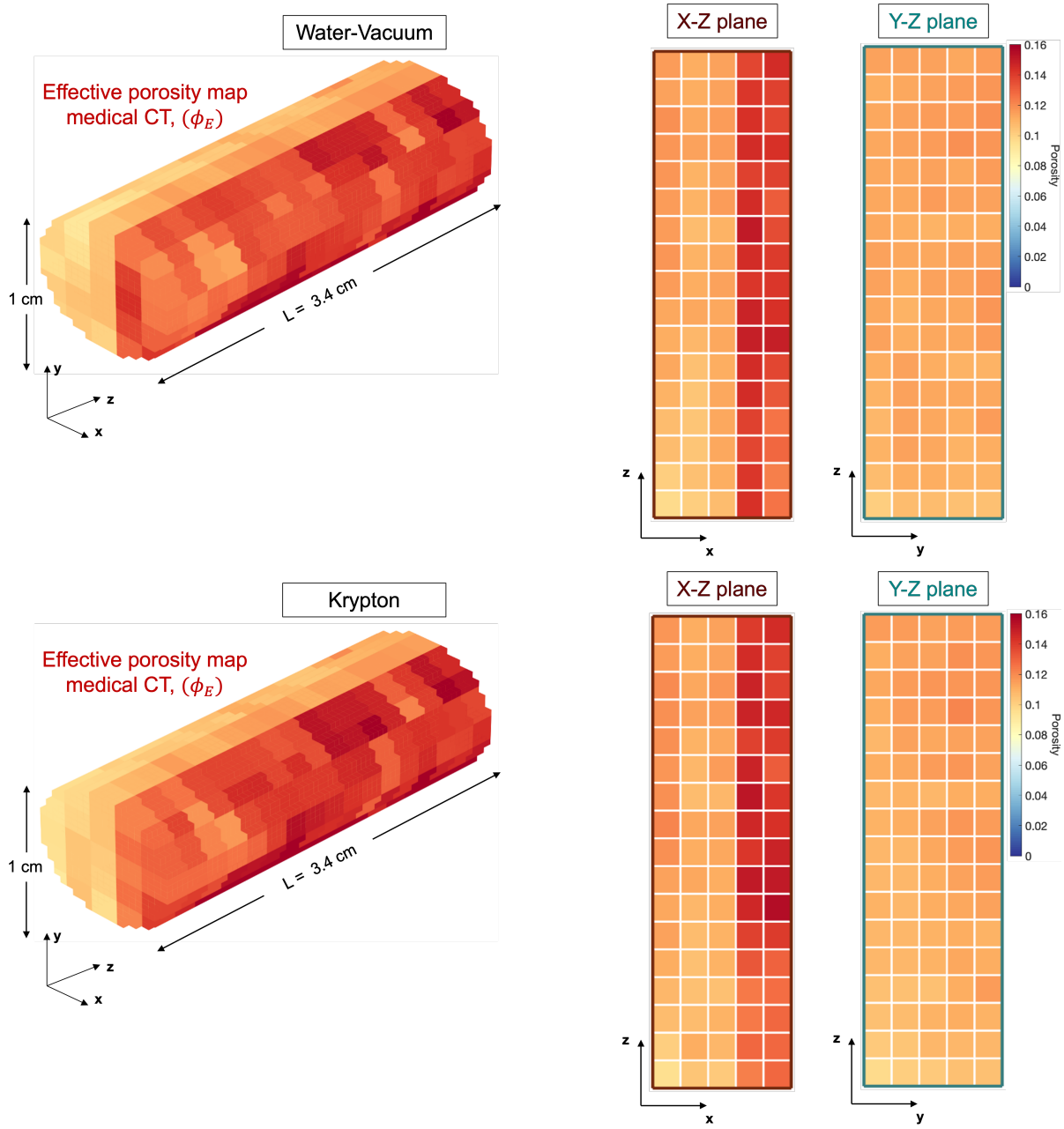


Figure 6.16: Left: 3D rendering of Nugget effective porosity map by differential imaging using water and vacuum as contrasting agents. Voxel size: (2 x 2 x 2) mm^3. Right: 2D planar sections (X-Z and Y-Z) revealing layering patterns.

The statistical analysis shown in Figure 6.17 confirms the agreement between both effective porosity maps for Nugget, reveling more accurate insights about the sample porosity distribution.

The top-left panel presents the histogram of voxel-wise porosity distributions for both methods. Both histograms show a strong agreement displaying a bimodal distribution

with a clear valley at porosity value of 0.123, separating low- and high-porosity domains, this value is reassured when looking at the correlation plot (bottom-left) where two distinct clusters are observed below and above 0.123. This threshold yields a distribution of 61.6% of the total porosity corresponding to lower porosity voxels averaging a porosity of 0.111 and 38.4 % representing higher porosity voxels with an average of 0.142.

The top-right panel shows the longitudinal porosity profile along the core slices. Both methods display a similar upward trend in porosity from inlet to outlet, indicating consistent spatial patterns. The tight overlap between the two curves and comparable error bars suggest high agreement with minimal variation between methods.

The bottom-left panel displays a voxel-to-voxel comparison of porosity values from the two approaches. The data points align closely along the 1:1 line, confirming strong correlation and overall agreement at the voxel level ($R^2 = 0.94$). However, the two distinct porosity clusters show different levels of variability, minimal deviation at lower porosity and a wider spread is observed at higher porosity values. This dual behavior in the same sample confirms the trends observed separately in Bentheimer and Ketton. Even if the values fall within the acceptable uncertainty range, it is important to know that there is correlation of increasing uncertainty with increasing pore sizes, possibly indicating greater sensitivity to more open pores.

The bottom-right panel is a Bland–Altman plot, showing the difference between the two methods plotted against their mean porosity. Most data points fall within ± 2 standard deviations, confirming that the two methods are statistically comparable. The mean difference is close to zero, suggesting minimal systematic bias. However, a slight positive trend with increasing porosity may suggest a scale-dependent deviation.

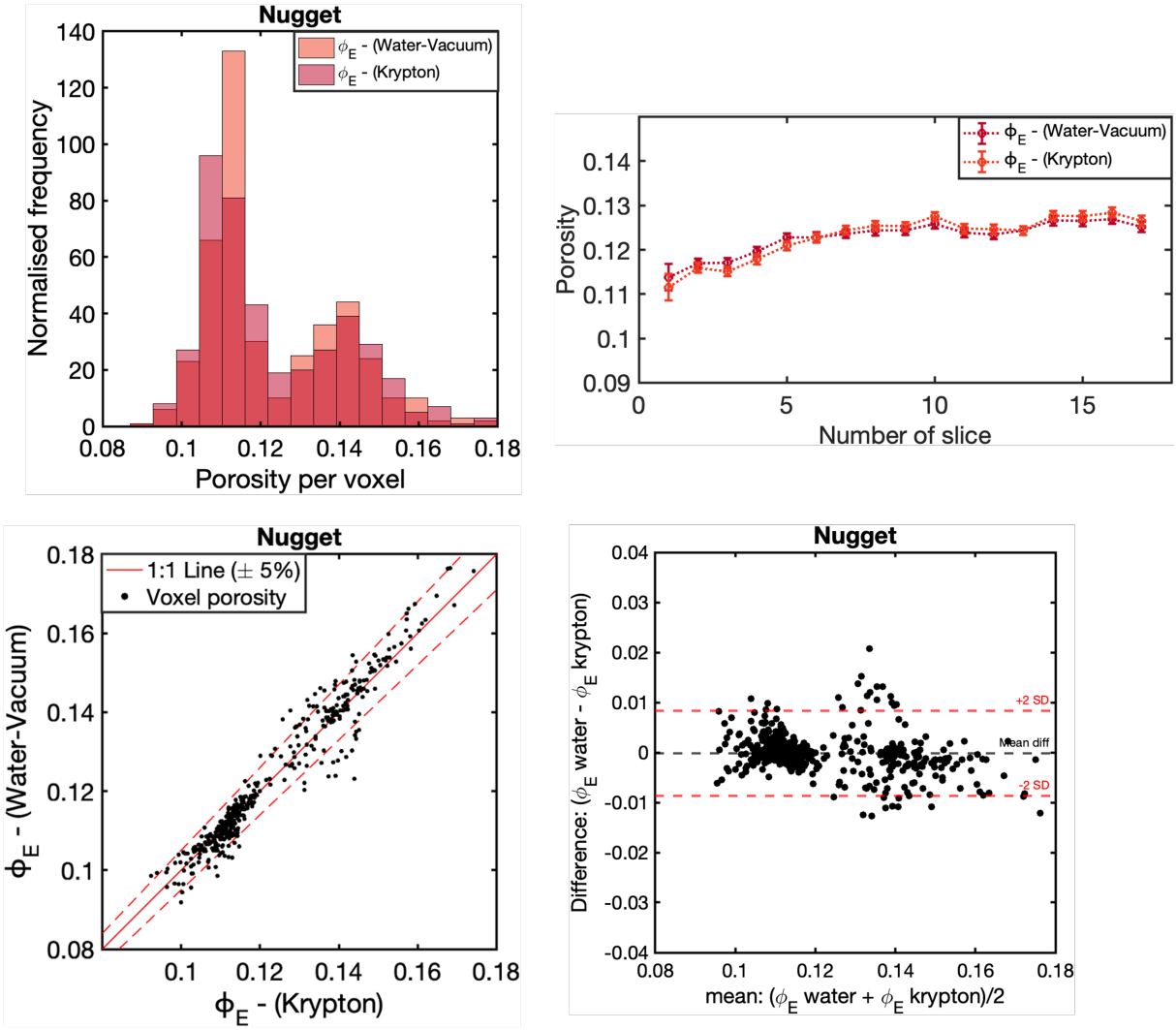


Figure 6.17: Statistical comparison of effective porosity maps in Nugget sandstone using two saturation approaches: (i) Water–Vacuum and (ii) Krypton (15 bar)–Vacuum, via differential imaging. Top left: Histogram of voxel-wise porosity distributions. Top right: Longitudinal porosity profile across slices. Bottom left: Voxel-to-voxel comparison with 1:1 line. Bottom right: Bland–Altman plot showing differences vs. the average porosity between methods.

Silurian:

Figure 6.18 presents the effective porosity map of the Silurian dolomite derived from medical CT imaging saturated with krypton. The results reveal a pronounced spatial heterogeneity in porosity distribution throughout the sample. Porosity values span a broad range, from near-zero in some regions (likely corresponding to isolated, non-connected pore spaces not reached by the saturating fluid) to values exceeding 0.3 in more connected, macroporous zones, with an average porosity of $\overline{\phi_E}$=0.144. The 3D map and orthogonal 2D planes illustrate the uneven nature of the pore network, characterised

by alternating zones of low and high porosity without a clear layering pattern.

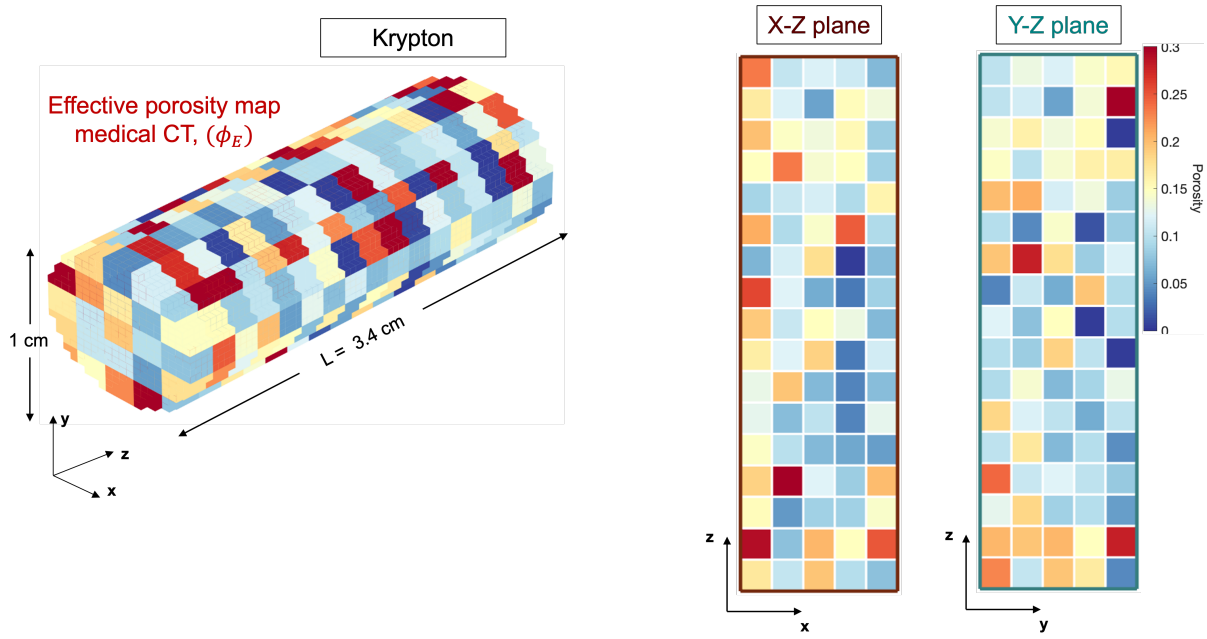


Figure 6.18: Left: 3D rendering of Silurian effective porosity map by differential imaging using Krypton at 15 bar and vacuum as contrasting agents. Voxel size: (2 x 2 x 2) mm^3. Right: 2D planar sections (X-Z and Y-Z) showing high porosity heterogeneity across the sample.

6.2.2 Resolved Porosity Map from Micro CT Image Segmentation

Figure 6.19 and Figure 6.21 present the resolved porosity maps (ϕ_R) for Nugget and Silurian, respectively, derived from micro CT image segmentation. For the Silurian sample, a connectivity analysis was applied to exclude isolated pores from the resolved porosity map. Although these pores can be segmented, their lack of connectivity suggests they are unlikely to be saturated by the contrasting agent when differential imaging is performed. Including them would result in discrepancies when comparing the resolved porosity with the corresponding effective porosity map. This approach ensures that the resolved porosity more accurately reflects the connected pore space contributing to fluid flow and saturation.

Nugget:

The resolved porosity map for Nugget (Figure 6.19) also highlights the layered structure of the sample from segmentation, with distinct variations in porosity aligned with the effective porosity maps. The low-porosity layers, which predominantly contain pores smaller than the micro CT voxel resolution, exhibit minimal segmented porosity. In contrast, the higher-porosity layers where the macropores are concentrated in this sample display significantly greater resolved porosity values, indicating that macropores within these zones are effectively captured by the imaging resolution.

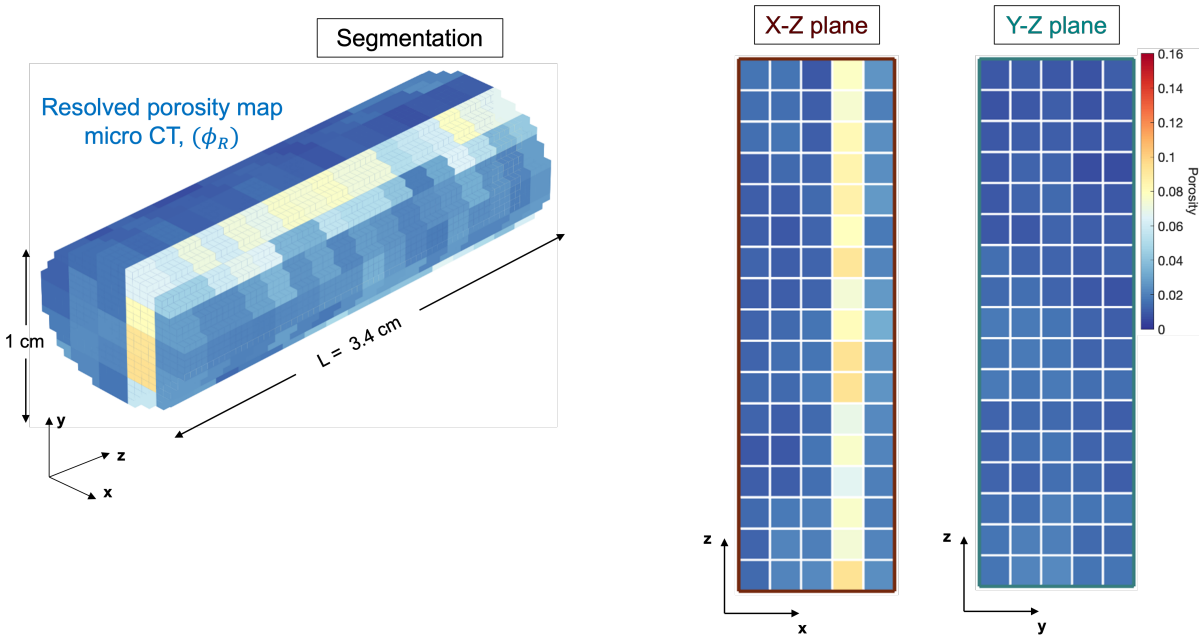


Figure 6.19: Left: 3D rendering of Nugget resolved porosity map by segmentation of micro CT images. Voxel size: (2 x 2 x 2) mm^3. Right: 2D planar sections (X-Z and Y-Z).

Silurian:

The inherently poor pore connectivity in the Silurian sample presents a key challenge for the quantification of sub-resolution porosity. The effective porosity method relies on the contrast in X-ray attenuation from a saturating agent infiltrating the connected pore space; however, isolated or poorly connected pores may not be readily saturated, leading to their exclusion from the effective porosity measurement. These same pores, could be above the segmentation threshold in micro CT imaging and therefore still be captured during

segmentation, potentially causing inconsistencies since Equation 4.7 assumes that resolved porosity is a subset of effective porosity (capturing only the macroporous fraction). It is essential to ensure that only connected pores are included in the resolved porosity calculation. A connectivity analysis, illustrated in Figure 6.20, demonstrates this process. The middle column shows regions of segmented high porosity that are not reflected in the corresponding effective porosity map, indicating disconnected pores. After applying a connectivity workflow (right column), the resolved porosity map aligns more closely with the effective porosity distribution (red rectangle), validating the need for connectivity filtering in low-permeability systems.

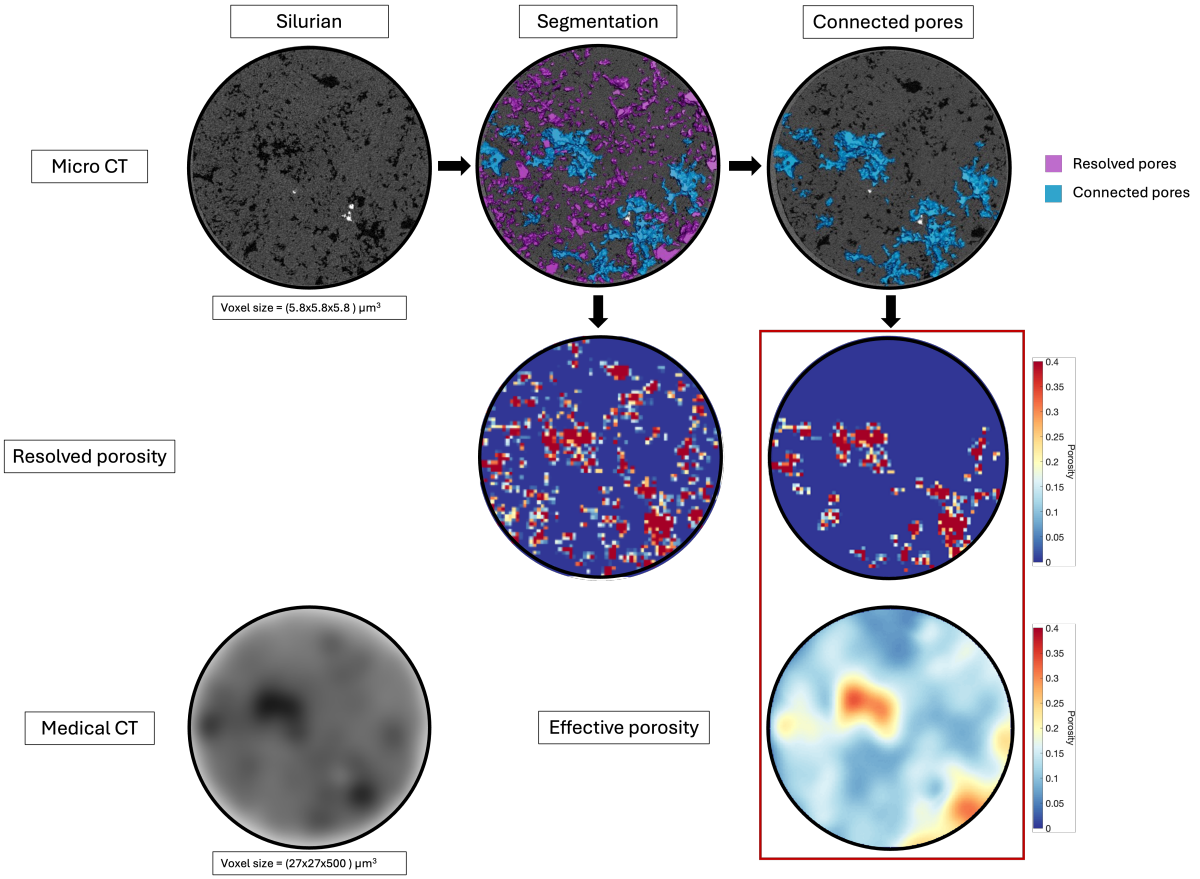


Figure 6.20: Image processing workflow for Silurian dolomite demonstrating the importance of connectivity in low permeability systems. The workflow shows micro CT image segmentation before and after connectivity analysis, with corresponding effective porosity measured via medical CT. Right column displays the final connected porosity map. The red rectangle highlights the better agreement between resolved porosity map excluding isolated pores and effective porosity measurements.

The top row of Figure 6.21 shows the resolved porosity map for the Silurian sample, including all segmented pores regardless of connectivity (ϕ_R). This map highlights the pronounced spatial heterogeneity characteristic of the sample, capturing variations in porosity across both axial and radial directions. However, many of these pores are poorly connected and likely inaccessible to fluids. The middle row presents the result after applying the connectivity workflow to exclude isolated or poorly connected pores, yielding a connected resolved porosity map ($\phi_{R,\mathrm{c}}$). The resolved porosity is significantly reduced from an average of 0.102 to 0.056. The bottom plot further emphasizes this by comparing the axial porosity profiles: effective porosity (ϕ_E) from differential imaging with krypton saturation, resolved porosity with all segmented pores (ϕ_R), and connected resolved porosity ($\phi_{R,\mathrm{c}}$).

This significant reduction highlights the dominance of isolated pores in the first half of the core, particularly between slices 4 and 6, where a large fraction of pores are either entirely unconnected or connected only through sub-resolution pathways. These findings demonstrate the importance of identifying disconnected pore regions that are not accessible to the saturating agent used in effective porosity measurements. The incorporation of connectivity filtering into segmentation workflows proves essential for heterogeneous, low-permeability carbonates such as the Silurian dolomite. Neglecting this factor may lead to systematic underestimations and unrealistic estimates of sub-resolution porosity.

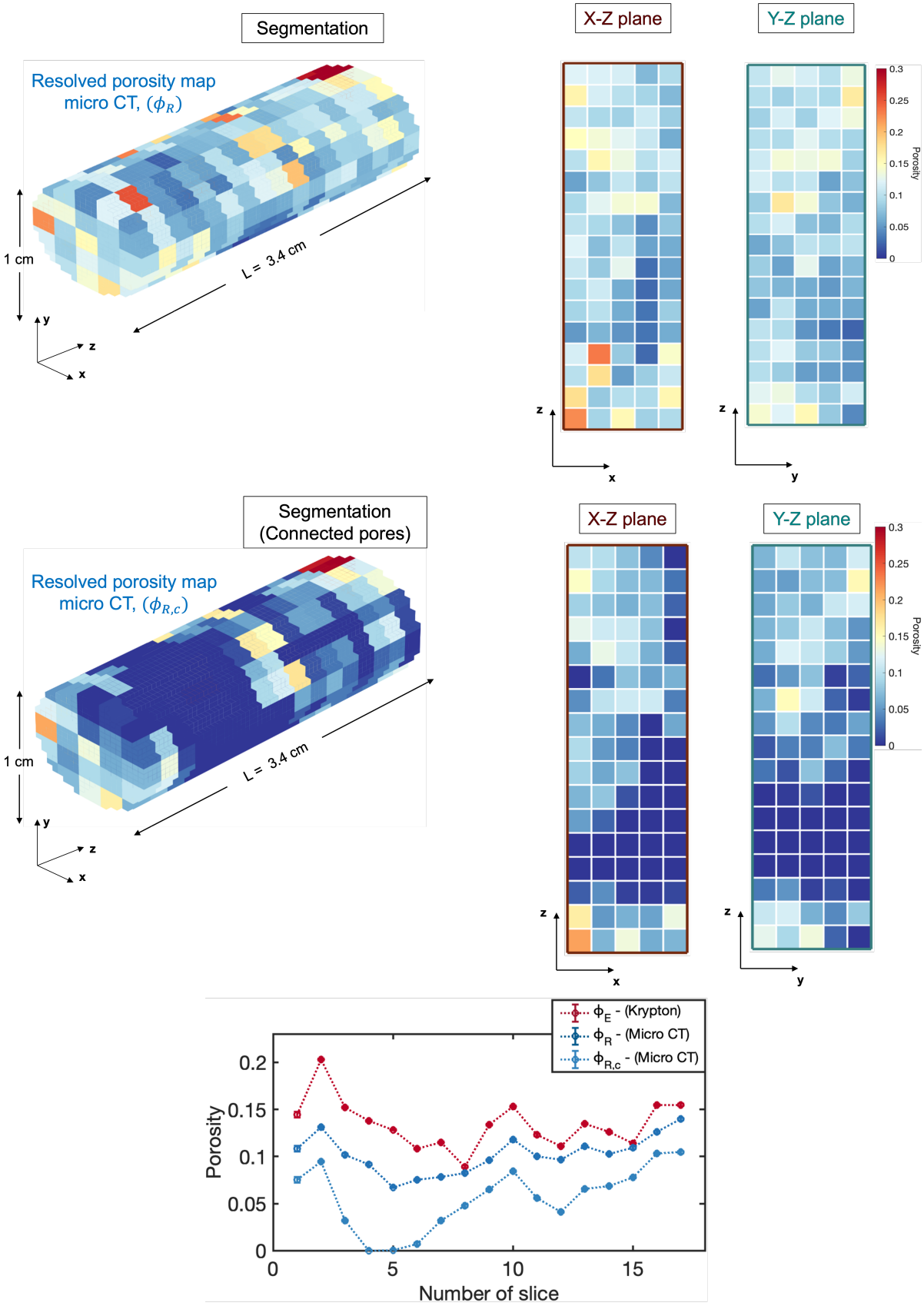


Figure 6.21: 3D rendering and cross sections of Silurian resolved porosity map by segmentation of micro CT images: top: Before connectivity analysis and middle: After connectivity analysis, Voxel size: (2 x 2 x 2) mm^3. Bottom: Average slice porosity profiles for Silurian dolomite core for the effective porosity map and resolved porosity map before and after connectivity analysis.

6.2.3 Calculation of Unresolved Porosity Map by Integrating Effective and Resolved Porosity Maps

With the effective porosity maps obtained using krypton-based differential imaging, suitable for complex low-permeable samples, and the resolved macroporosity derived from micro CT segmentation (refined through pore connectivity analysis to exclude unconnected pores) the final step involves estimating the unresolved porosity maps. These maps capture the fraction of pore volume not directly imaged but inferred from the difference between effective and connected resolved porosity. The results are presented in Figure 6.22 for Nugget and Figure 6.24 for Silurian.

Nugget:

The 3D visualisation and cross-sectional planes for Nugget displayed in Figure 6.22 clearly show uniform distribution of unresolved porosity across the core with average values of 0.094 with the exception of the high porosity layer which displays reduced unresolved porosity values of 0.066. Looking at the average porosity profile, Nugget shows consistent axial stability along the sample length.

Analysis of porosity partitioning shows that resolved porosity ($\phi_R = 0.029$) constitutes a minor fraction compared to unresolved porosity ($\phi_U = 0.094$) when evaluated against the effective porosity profile. This partitioning indicates that approximately 76.5% of the total porosity resides in the sub-resolution domain. The importance of sub-resolution porosity quantification is emphasised by the fact that, despite the apparently homogeneous bulk porosity properties, Nugget exhibits anisotropic behavior, with porosity heterogeneity patterns varying primarily between strata. This stratified variation is particularly significant because different layers exhibit distinct proportions of sub-resolution versus resolved porosity, thereby requiring layer-specific analysis for accurate characterisation.

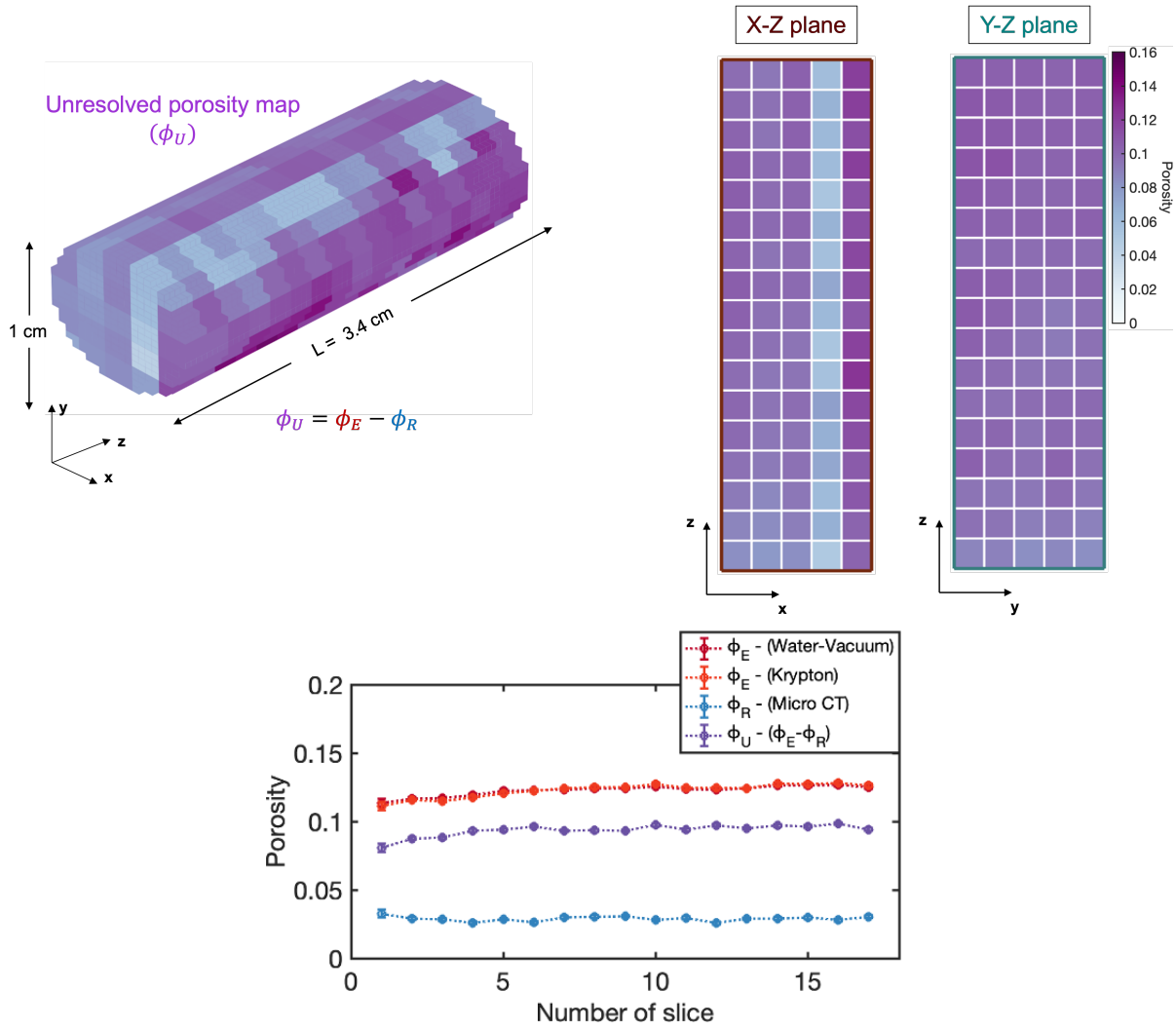


Figure 6.22: Top: 3D rendering of Nugget unresolved porosity map. Voxel size: (2 x 2 x 2) mm^3 and 2D planar sections (X-Z and Y-Z). Bottom: Average slice porosity profiles for Nugget core for the effective porosity map, resolved porosity map and unresolved porosity map.

The layer-specific analysis presented in Figure 6.23 provides deeper insights into the stratified porosity architecture of Nugget sandstone through systematic decomposition of effective, resolved, and unresolved porosity components. The bar chart analysis reveals that while layers 1, 2, and 3 exhibit similar porosity ratios, predominantly composed of unresolved porosity. In contrast, layers 4 and 5 display higher overall porosity, but with differing internal distributions: layer 4 shows a more balanced proportion from both resolved and unresolved porosity, while layer 5 remains strongly dominated by unresolved porosity. The histogram analysis further emphasises this stratified behavior, showing a bimodal distribution where effective porosity values cluster around two distinct

ranges corresponding to the high-porosity layer and matrix intervals. The resolved and unresolved porosity distributions demonstrate complementary patterns, with resolved porosity showing a narrow, low-value distribution punctuated by higher values from the macroporous layer, while unresolved porosity exhibits a broader, higher-value distribution representing the microporosity-dominated matrix. This layer-specific variation in pore size distribution underscores the need for stratified analysis for accurate rock characterisation, as bulk measurements would fail to capture the fundamental differences in pore architecture variations by layers.

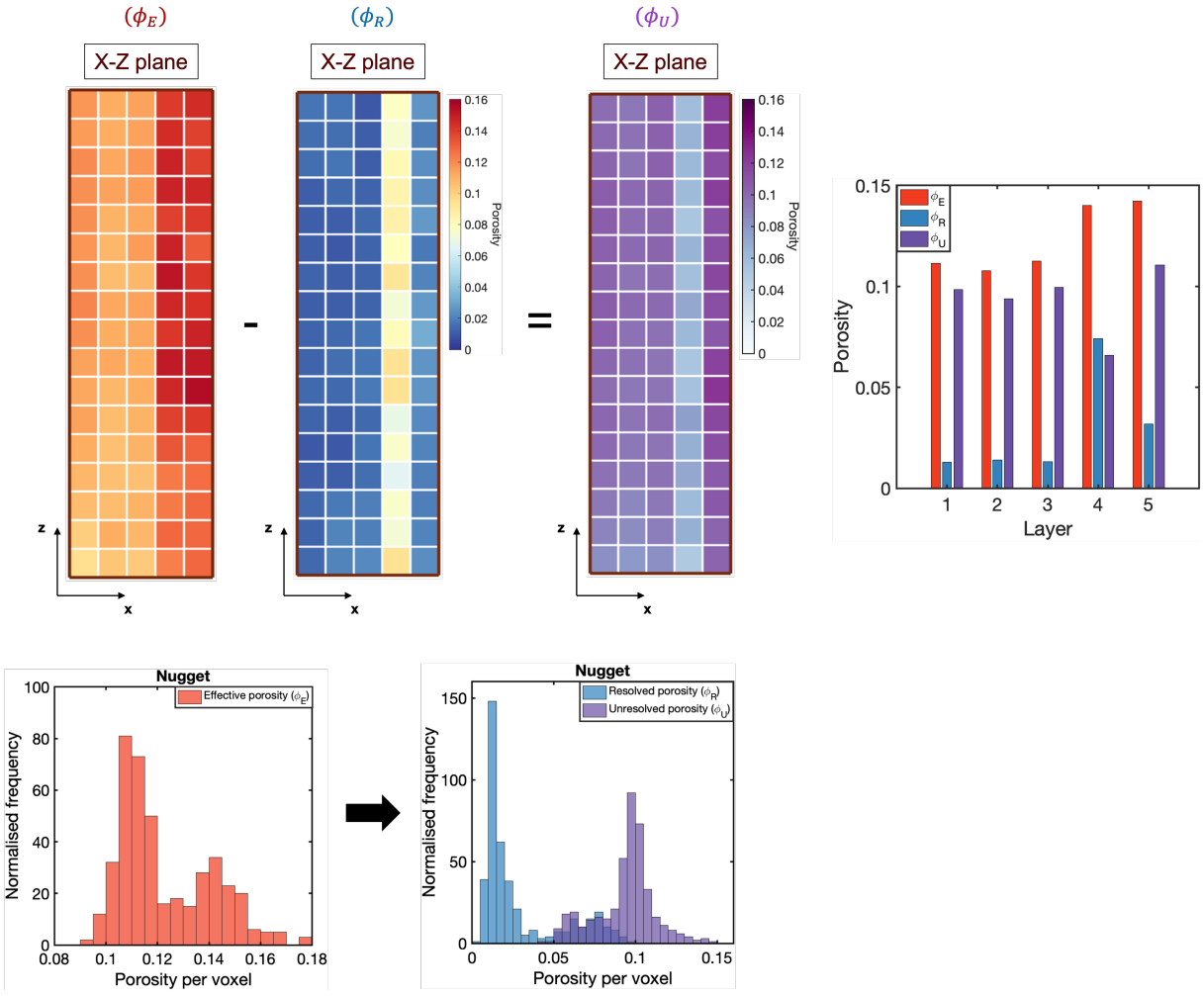


Figure 6.23: Top: Porosity distribution analysis per layer in Nugget. Bottom: histogram of effective porosity distribution effectively split into resolved and unresolved porosity distributions.

Silurian:

Figure 6.24 presents the 3D sub-resolution porosity map for the Silurian sample, revealing a highly irregular and spatially heterogeneous distribution of unresolved porosity, characteristic of complex carbonate pore systems.

The longitudinal average porosity profile demonstrates substantial fluctuations in all three porosity components, with effective porosity ranging from approximately 0.102 to 0.211. Notably, the connected resolved porosity ($\phi_{R,\mathrm{c}}$) remains consistently low throughout the sample, while unresolved porosity exhibits a larger contribution, especially in the first half of the sample.

The histogram analysis supports these observations quantitatively. Effective porosity follows a relatively narrow, unimodal distribution centered around a mean value of 0.144. In contrast, both resolved and unresolved porosity components exhibit more complex behaviors, with mean values of 0.056 and 0.088, respectively. The unresolved porosity histogram shows a broader spread with a pronounced tail toward higher values, reflecting the heterogeneous and spatially variable microporous matrix. Overall, the analysis indicates that approximately 61% of the total porosity is composed of sub-resolution features.

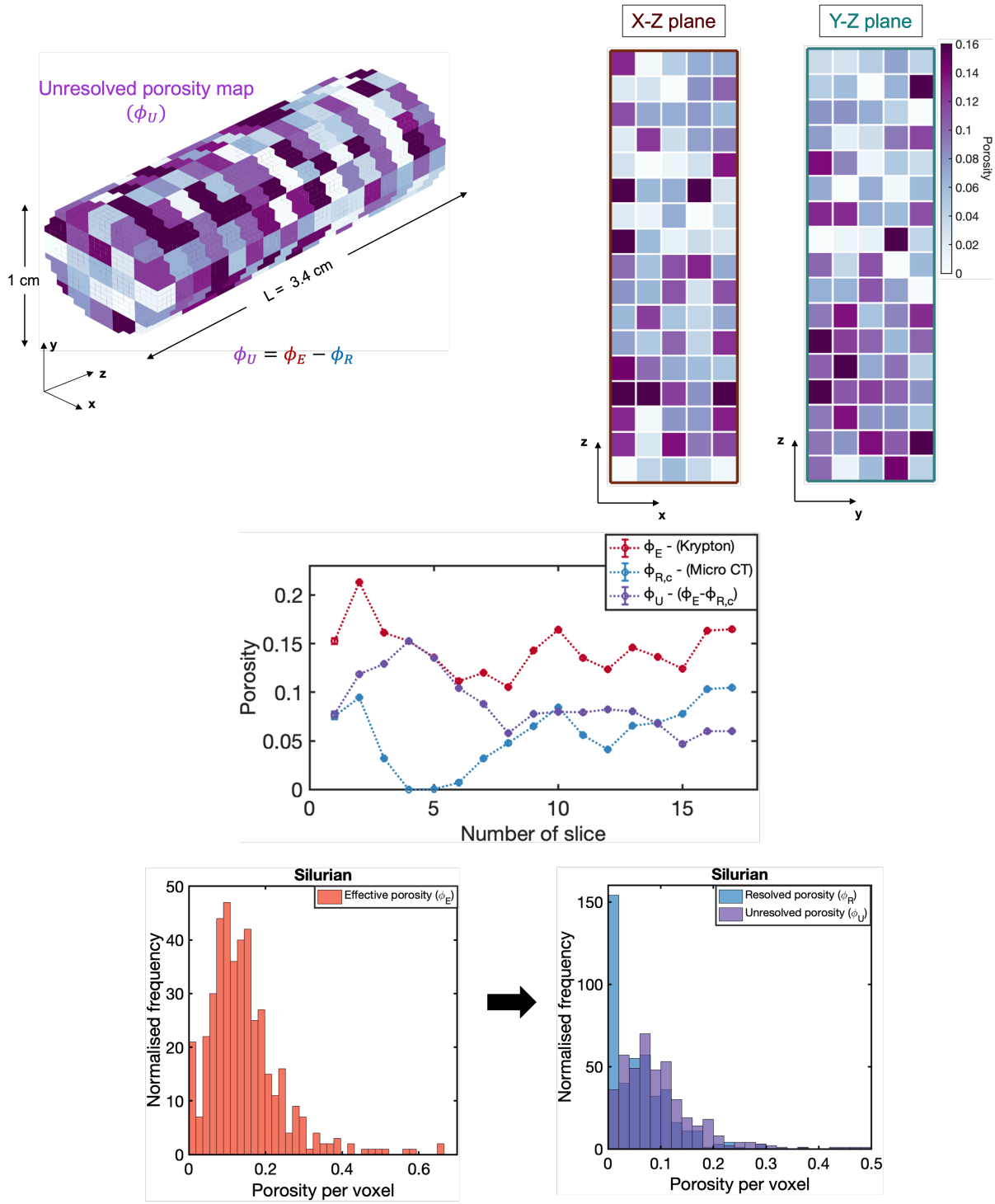


Figure 6.24: Top: 3D rendering of Silurian unresolved porosity map. Voxel size: (2 x 2 x 2) mm^3 and 2D planar sections (X-Z and Y-Z). Middle: average slice porosity profiles for the effective, resolved, and unresolved porosity maps. Bottom: Histogram of effective porosity distribution and the proportion of resolved and unresolved porosity distributions.

6.3 Comparison of Pore Size Distribution with MICP Measurements

It is instructive to carry out a qualitative comparison between the cumulative voxel porosity distributions derived from imaging methods and the cumulative pore size distribution obtained independently through MICP measurements. While these analyses were performed on different samples of the same rock types, this comparative approach focuses specifically on the characteristic curve shape rather than absolute values, as the main objective is to evaluate the ability of imaging methods to reproduce the diagnostic pore size distribution patterns that define the petrophysical signature of the rock.

To enable this comparison, equivalent pore diameters are calculated from the imaging data by converting voxel-based porosity measurements to representative pore sizes. Given the voxel volume of 6 mm^3 and the measured voxel porosity, the pore volume within each voxel is computed and subsequently converted to an equivalent spherical pore diameter using:

$$d_{ep} = \sqrt[3]{\frac{6PV}{\pi}} \tag{6.1}$$

where:

- d_{ep} is the equivalent voxel pore diameter
- PV is the voxel pore volume

Similarly, individual pore throat diameters from MICP data are determined by rearranging the Washburn equation, which relates capillary pressure to pore throat geometry:

$$d_p = -\frac{4\gamma \cos\theta}{P_c} \tag{6.2}$$

where:

- d_p is the pore throat diameter
- γ is the surface tension of mercury, 0.485 N/m
- θ is the contact angle between mercury and grains, 130°
- P_c is the capillary pressure

The fundamental distinction between these approaches lies in their physical representation, the imaging-derived equivalent diameters represent bulk pore space within discrete voxel volumes, effectively capturing the collective behavior of multiple pores, while MICP measurements characterise individual pore classes. Despite this methodological difference, the cumulative distribution shapes provide diagnostic information on the overall pore structure heterogeneity.

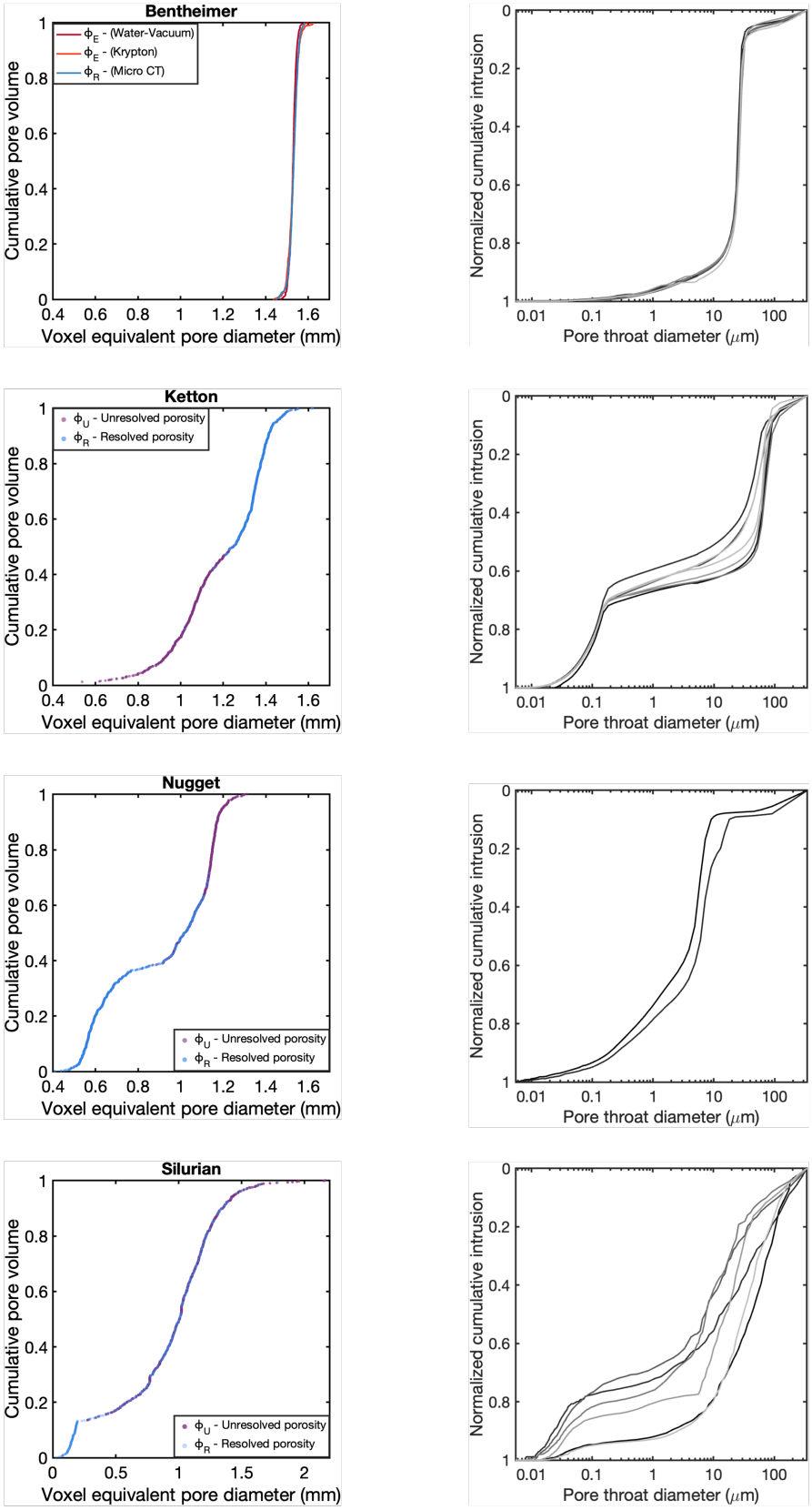


Figure 6.25: Cumulative pore size distributions obtained from imaging-based porosity mapping techniques versus normalised cumulative intrusion curves from MICP measurements for Bentheimer sandstone (top row), Ketton limestone (second row), Nugget sandstone (third row) and Silurian dolomite (bottom row).

Figure 6.25 shows the comparative analysis revealing fundamental differences in pore architecture between samples through complementary imaging and mercury intrusion techniques. Similarities in the curve shape between imaging and MICP data indicates that the imaging methods successfully capture the samples pore architecture.

Bentheimer sandstone exhibits characteristics of a unimodal pore size distribution with excellent agreement between all three porosity imaging techniques (top left panel). The cumulative pore size distribution curve shape corresponds to the MICP curve displaying a smooth, steep transition without plateaus, characteristic of a well-connected pore network with a narrow throat size distribution. This behavior confirms Bentheimer as a homogeneous, simple pore system.

Ketton limestone appears to have a bimodal pore size distribution characterised by two distinct steps in the cumulative pore volume plot (bottom left panel), confirming a dual-porosity architecture. The initial step is the contribution from the derived unresolved porosity (micropores), while the subsequent step represents the resolved porosity obtained through micro CT segmentation (macropores). This bimodal characteristic is mirrored in the MICP data, though with a critical distinction: the presence of a pronounced plateau separating the two intrusion stages. This flat region signifies a percolation gap where mercury must overcome connectivity barriers to access secondary pore networks, a feature not present in the left plot since pores are directly resolved from imaging rather than accessed through throat-controlled intrusion.

Nugget sandstone also shows a clear bimodal character with distinct contributions from unresolved and resolved porosity. Compared to Ketton and Bentheimer, the pore size distribution for Nugget is slightly shifted towards smaller diameters, reflecting its overall finer pore structure. In contrast to Ketton, where macroporosity dominates the larger pore size range, Nugget shows the opposite trend (resolved porosity is primarily associated with the smaller equivalent pore diameters, while unresolved porosity contributes more significantly to the larger range). This observation aligns with the calculated porosity ratio, where microporosity accounts for approximately 76.5% of the total porosity and macroporosity for the remaining 23.5%. The MICP-derived pore throat size distribution exhibits a steep uptake at the larger sizes with the majority of pore throats concentrated in the 1-10 µm range and fewer micropores compared to the curve obtained by imaging

techniques. This discrepancy can be explained as the layering system in Nugget is not consistent from sample to sample. Figure 6.26 illustrates how the sample used for MICP analysis exhibits a more extensive high-porosity layer compared to the sample used for the characterisation study. The black rectangular outlines highlight the relative thickness differences of the high-porosity zones between the two samples. This comparison highlights the challenge of correlating pore structure data across different analytical techniques in complex porous systems.

The Silurian sample displays a more gradual transition in the cumulative pore volume curve, with intercalated contributions from both unresolved and resolved porosity. This pattern suggests a relatively balanced distribution of micro- and macroporosity across individual voxels. A subset of voxels with smaller equivalent pore diameters appears at the lower end of the curve, representing poorly connected regions of resolved porosity identified through micro CT segmentation, a feature also reflected in the MICP data. Conversely, the upper range of the curve is dominated by voxels associated with unresolved porosity, indicating zones of high microporosity likely corresponding to those same poorly connected regions. The equivalent pore diameter range is broader for Silurian than for the previously analysed samples, as evidenced by the MICP-derived throat size distribution, which spans from sub-micron to tens of microns. The variability observed between different MICP curves highlights the inherent heterogeneity of the carbonate system, where spatial differences lead to distinct pore throat distributions. It is therefore reassuring that the imaging-based method developed in this study successfully captures the general pore structure trends observed independently by MICP analysis.

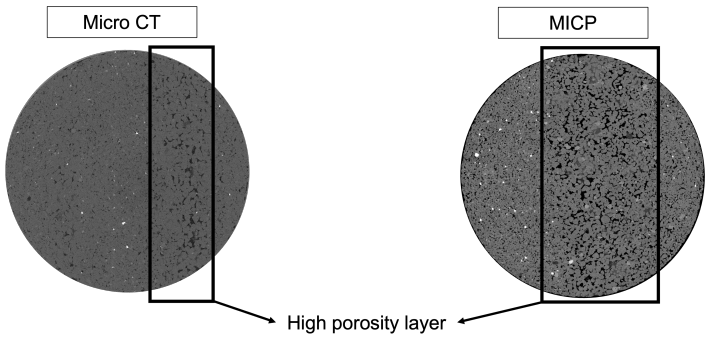


Figure 6.26: Comparison of Nugget sandstone samples showing heterogeneous porosity distribution. Left: Micro CT cross-section of sample used for imaging analysis. Right: Cross-section of sample used for MICP analysis.

6.4 Bulk Porosity Comparison

Table 6.1 summarises the bulk porosity results for all four samples, obtained using the standard laboratory methods introduced in Chapter 4, as well as imaging methods with both water and krypton approaches. All measurements were performed on the same plugs, except for the average porosity results from MICP, which were derived from different plugs of the same rock types. Consequently, the MICP results are provided for reference only and are not directly comparable with the other methods. Note that the water-based imaging value for the Silurian sample is not included, as complete water saturation could not be achieved due to the low permeability and poor pore connectivity of the rock.

Method	**Bentheimer**	**Ketton**	**Nugget**	**Silurian**
MICP	0.235 ± 0.005	0.242 ± 0.009	0.132 ± 0.016	0.106 ± 0.0039
Vacuum saturation	0.237 ± 0.004	0.241 ± 0.007	0.127 ± 0.004	0.119 ± 0.005
Helium pycnometry	0.236 ± 0.006	0.242 ± 0.008	0.125 ± 0.008	0.143 ± 0.009
Imaging (Water)	0.234 ± 0.002	0.240 ± 0.002	0.123 ± 0.002	-
Imaging (Krypton)	0.235 ± 0.002	0.241 ± 0.002	0.123 ± 0.002	0.144 ± 0.002

Table 6.1: Bulk porosity results for the four rock types from standard laboratory methods and effective porosity (ϕ_E) from imaging methods.

Figure 6.27 presents a graphical representation of the porosity data reported in Table 6.1, providing a clear visual comparison of the five measurement techniques across the four rock samples. The consistent porosity ranges obtained across different measurement techniques provide high confidence in the accuracy of the reported values for each rock type, with standard deviations typically remaining within ±0.002-0.005 porosity units for well-connected samples. However, the systematic variations observed in samples with complex pore geometry, particularly evident in Silurian, highlight the importance

of measurement method selection based on pore structure characteristics. Notably, the inability to achieve complete water saturation in tight, poorly connected rocks like the Silurian demonstrates a fundamental limitation of liquid-based methods in complex porous media. In contrast, gas-based approaches (helium pycnometry and krypton imaging) yield higher porosity values in such systems, as gases can access smaller pore throats and poorly connected pore spaces that remain inaccessible to liquids due to capillary and permeability constraints. This methodological sensitivity to pore network complexity underscores the need for complementary measurement approaches when characterising heterogeneous porous media, where the choice between liquid and gas saturation methods can significantly influence both the magnitude and spatial distribution of measured porosity values.

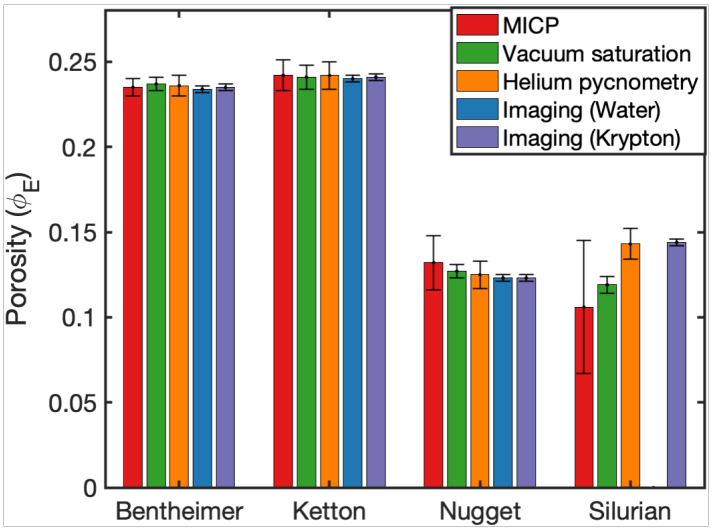


Figure 6.27: Bulk porosity (ϕ_E) of Bentheimer, Ketton, Nugget, and Silurian samples measured by different methods: Mercury intrusion capillary porosimetry (MICP), vacuum saturation, helium pycnometry, and imaging approaches with both water and krypton. Error bars represent the reported measurement uncertainties.

6.5 Concluding Remarks

The porosity mapping workflow developed in this study demonstrates a robust approach to decompose total porosity into effective, resolved, and sub-resolution components across

a variety of rock types with varying degree of porosity heterogeneity and connectivity.

The saturation strategy for differential imaging was tailored to each sample. In simple, high-permeability rocks, water proved to be an effective saturating agent, reliably enabling the generation of effective porosity maps through X-ray attenuation differences. However, in low-permeability or highly heterogeneous systems, water saturation was insufficient due to poor pore accessibility and low capillary imbibition. In such cases, krypton gas under pressure emerged as a reliable alternative for saturation, enabling the differential imaging step. The results confirmed that krypton saturation yielded consistent effective porosity maps.

In relatively homogeneous systems such as Ketton and Bentheimer, the spatial distribution of porosity components follows predictable patterns, with clear separation between macroporous and microporous domains. These systems validated the methodology under controlled pore architectures, confirming that unresolved porosity can be reliably quantified from differential imaging.

In contrast, complex porous systems such as Nugget sandstone and Silurian dolomite presented greater challenges due to their stratified or heterogeneous pore structures, low permeability, and variable connectivity. The integration of pore connectivity analysis proved essential to isolate connected porosity and avoid overestimation of resolved porosity through segmentation. Nugget exhibited a stratified dual-porosity system dominated by unresolved porosity within matrix layers and macroporosity is concentrated in distinct strata, emphasising the anisotropic nature of Nugget, while Silurian showed an irregular and multimodal pore structure requiring careful quantification of both micro- and macroporosity to accurately reflect its internal complexity.

The combined use of differential imaging, micro CT segmentation, and connectivity analysis offers a comprehensive framework to quantify porosity architecture across scales, enabling more accurate petrophysical characterisation and improved understanding of spatial microporosity variability.

Chapter 7

Numerical Studies Using Image-Based Porosity Maps

This chapter explores the practical implementation of image-based sub-resolution porosity maps in numerical flow and transport simulations, to assess their impact on transport under fully saturated conditions. The core premise of this exercise rests on the conceptual framework that pore space can be decomposed into distinct domains based on their transport characteristics. The resolved porosity maps, derived from high-resolution pore-scale image analysis, represent the interconnected pore network where flow is predominantly governed by advective processes. Conversely, the unresolved porosity component encompasses the sub-resolution scale pore space (including dead-end pores, micro-fractures, and poorly connected void spaces) where molecular diffusion becomes the dominant transport mechanism. This dual-domain concept provides a foundation for incorporating multi-scale heterogeneity into continuum-scale numerical models.

To assess the impact of sub-resolution spatial heterogeneity on solute transport behavior, the numerical simulation of tracer experiments serves as a diagnostic tool. Tracer breakthrough curves, which capture the temporal evolution of solute concentration at observation points, provide direct insight into the efficiency of mixing processes, the presence of preferential flow paths, and the magnitude of mass transfer between mobile (resolved pore space) and immobile (unresolved pore space) domains. The shape, timing, and asymmetry of these curves encode information about the underlying pore structure and its influence on transport processes across multiple scales.

The numerical framework employed in this study is built upon MODFLOW-2005, an open-source modular finite-difference groundwater flow model developed by the

US Geological Survey. This well-established platform provides robust solutions for three-dimensional groundwater flow problems and, when coupled with the MT3DMS transport package, enables comprehensive simulation of advection, dispersion, and mass transfer processes in heterogeneous porous media. The modular architecture of MODFLOW allows for the systematic investigation of different conceptual models, from single-porosity representations to complex dual-domain formulations that explicitly account for mass exchange between mobile and immobile zones.

The integration of image-derived porosity fields with numerical flow models offers the potential to bridge the gap between detailed pore-scale characterisation and the fundamental understanding of transport predictions at field-scale. Through systematic analysis of tracer breakthrough behaviour under varying heterogeneity scenarios, this chapter aims to quantify how sub-resolution porosity variations influence solute transport patterns and to establish guidelines for incorporating such detailed heterogeneity information into practical modelling workflows.

7.1 Simulation Set-Up

The two main modules employed for the numerical exercise are MODFLOW, which simulates advective flow in the mobile domain (resolved porosity map), and MT3DMS, which simulates solute transport in both the mobile and immobile domains, including advective transport in the mobile domain and diffusive mass exchange between the mobile and immobile domains (unresolved porosity map). MT3DMS uses the flow field computed by MODFLOW as input to determine the advective component of solute movement in the mobile domain, while also accounting for molecular diffusion and dispersion.

Flow Model Equations:

The general flow equation in MODFLOW is described in Equation 7.1. The left-hand side term represents the change in storage over time; however, a steady-state flow condition was assumed, which makes the term negligible, ($\frac{\partial h}{\partial t} = 0$). The right-hand side terms account for flow in the X, Y, and Z directions, although isotropic conditions were assumed ($K_x = K_y = k_z$). These hydraulic conductivity properties were allowed to vary spatially

but remaining constant within a grid cell. The source/sink term W, representing recharge, pumping, or leakage, was set to zero in this simulation (Harbaugh et al. 2000).

$$\cancel{S_s \frac{\partial h}{\partial t}} = \frac{\partial}{\partial x}\left(K_x \frac{\partial h}{\partial x}\right) + \frac{\partial}{\partial y}\left(K_y \frac{\partial h}{\partial y}\right) + \frac{\partial}{\partial z}\left(K_z \frac{\partial h}{\partial z}\right) + \cancel{W} \tag{7.1}$$

where:

- h is the hydraulic head (cm)
- K_x, K_y, K_z is the hydraulic conductivity in the x, y, z directions (cm/s)
- S_s is the specific storage
- W is the volumetric flux per unit volume

Flow is primarily driven by the direction and magnitude of the imposed hydraulic head gradient (Δh) but is locally modified by the hydraulic conductivity tensor (K), which governs how easily water moves through each cell. The inlet head boundary condition required to sustain the desired flow rate was obtained by Darcy's Law (Equation 7.2), based on the selected flow rate and the system geometry. Hydraulic conductivity was computed from cell-specific permeability values by Equation 7.3. Permeability, in turn, was estimated via the general form of the fractal geometry porosity-permeability relationship (Equation 7.4), as proposed by (Pape, Clauser, and Iffland 1999; Krause, Perrin, and SM M Benson 2011), using the resolved porosity map as input. Figure 7.1 shows the resulting spatial fields for the Ketton limestone case.

$$\Delta h = \frac{QL}{AK} \tag{7.2}$$

where:

- Δh is the head pressure (cm)
- Q is the flow rate (ml/s)
- L is the core length, 3.4 cm

- A is the cross sectional area, 0.79 cm^2
- K is the hydraulic conductivity (cm/s)

$$K = \frac{k\rho g}{\mu} \tag{7.3}$$

where:

- K is the hydraulic conductivity (cm/s)
- k is the grid cell permeability (cm^2)
- ρ is the fluid density, water = 1 g/cm^3
- g is gravitational force, 981 cm/s^2
- μ is the dynamic viscosity, 0.01 g/cm.s

$$k = S[6.2\phi + 1493\phi^2 + 58(10\phi)^{10}] \tag{7.4}$$

where:

- k is the grid cell permeability (cm^2)
- S is the permeability shape factor
- ϕ is the grid cell resolved porosity

Solute Transport Equations:

Equation 7.5 represents a specific form of the advection-dispersion equation (ADE) implemented in the MT3DMS transport module to describe solute transport within the system. In this formulation, the transport in the mobile domain is governed by advection and dispersion processes, while the immobile domain acts as a stagnant zone where transport occurs exclusively by diffusion. The two domains are coupled through

a first-order mass transfer term driven by the concentration difference between them (Equation 7.6) (Harbaugh et al. 2000; Zheng et al. 2012).

The left-hand side terms represent the temporal changes in solute concentration within the mobile and immobile pore spaces. The right-hand side captures the the physical transport processes: dispersion through the divergence of the dispersive flux vector $\nabla \cdot (\phi_m \mathbf{D} \nabla C_m)$ and advection through the divergence of the advective flux vector $-\nabla \cdot (\mathbf{v} C_m)$. Here, the hydrodynamic dispersion coefficient ($\mathbf{D}$) incorporates both mechanical dispersion and molecular diffusion, and the seepage velocity $\mathbf{v}$ is computed from the MODFLOW flow solution as $\mathbf{v} = \frac{K \nabla h}{\phi_m}$.

Notably, retardation factors for both mobile and immobile domains (R_m, R_{im}) were set to 1, indicating transport with no sorption effects. Additionally, source/sink terms and chemical reactions are neglected in this simulation, simplifying the transport to purely physical processes of advection, dispersion, and diffusion.

$$\cancel{R_m}\,\phi_m \frac{\partial C_m}{\partial t} + \cancel{R_{im}}\,\phi_{im} \frac{\partial C_{im}}{\partial t} = \nabla \cdot \left(\phi_m \mathbf{D}\, \nabla C_m\right) - \nabla \cdot \left(\mathbf{v}\, C_m\right) + \cancel{q_s C_s} + \cancel{\mathcal{R}} \tag{7.5}$$

$$\phi_{im} \frac{\partial C_{im}}{\partial t} = \alpha \left(C_m - C_{im}\right) \tag{7.6}$$

where:

- ϕ_m is the effective porosity (mobile domain)
- ϕ_{im} is the sub-resolution porosity (immobile domain)
- C_m, C_{im} are the solute relative concentrations in the mobile and immobile domains
- D is the hydrodynamic dispersion tensor
- v is the seepage velocity vector
- α first order mass transfer coefficient
- t is time

- q_s is the volumetric flow rate from sources or sinks
- C_s is the concentration of the source or sink fluid
- R_m, R_{im} are the retardation factors
- $\mathcal{R}$ are the chemical reaction terms

The flow model inputs included the domain geometry derived from the resolved porosity map, which defined the system dimensions and voxel size, as well as a constant flow rate that established the hydraulic head gradient. For the transport model, inputs consisted of the unresolved porosity map (representing the pore space available for mass exchange with the mobile domain), shown in Figure 7.1, the dispersion coefficient and the mass transfer coefficient.

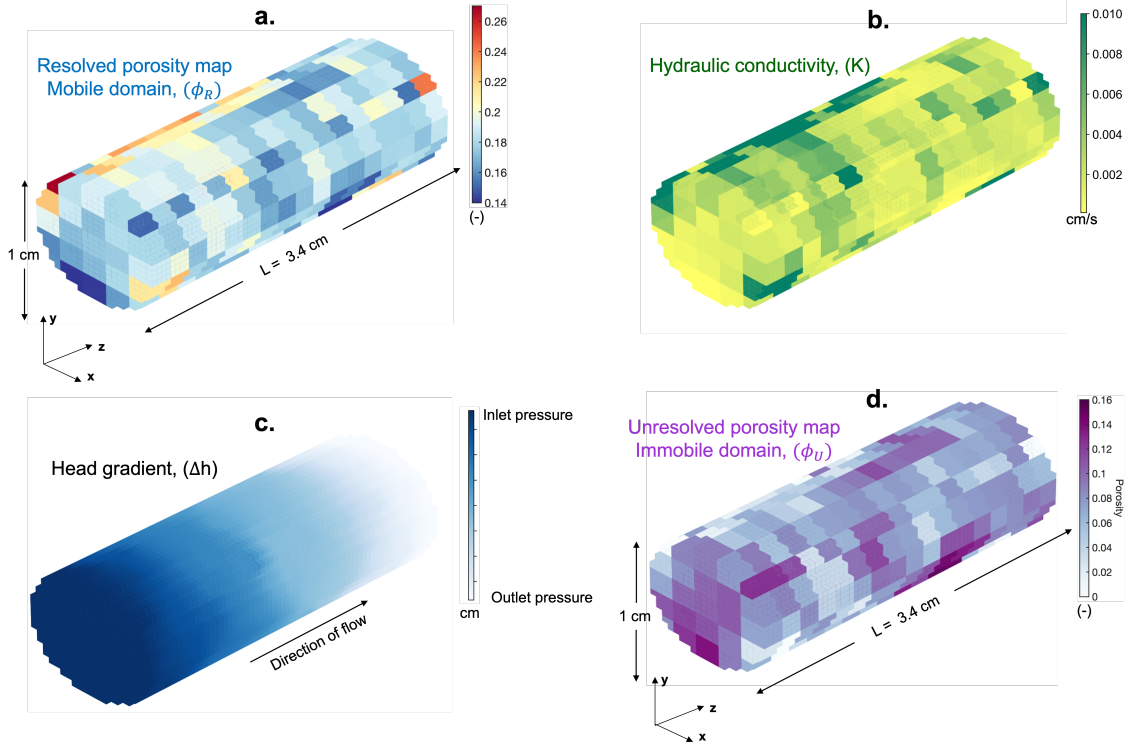


Figure 7.1: 3D renderings of the inputs for MODFLOW flow simulation (a), (b), (c). and solute transport simulation (d). (a): Resolved porosity map representing the system mobile domain. (b): Calculated hydraulic conductivity. (c): Head gradient imposed in the system. (d): Unresolved porosity map representing the system immobile domain.

7.2 Model Validation

The model was validated using a homogeneous porosity field of ϕ_m=0.25 and the same dimensions as the porosity maps obtained for the studied samples (1 cm in diameter and 3.4 cm in length). The base case used a 5x5x17 grid resulting in a voxel size of 0.2x0.2x0.2 cm^3. The objective of the first test was to assess numerical dispersion due to cell size, a common modelling error that directly affects how accurately the model can simulate sharp concentration fronts (Konikow 2011). Larger cell sizes can lead to inaccurate fronts, depending on the level of spatial discretisation. This issue can be mitigated by refining the grid to increase resolution and more accurately represent flow behavior. To evaluate this, three increasingly refined grids were tested by subdividing each voxel by factors of 2, 4 and 8 resulting in grids sizes of 10x10x34, 20x20x68 and 40x40x136 respectively, Figure 7.2.

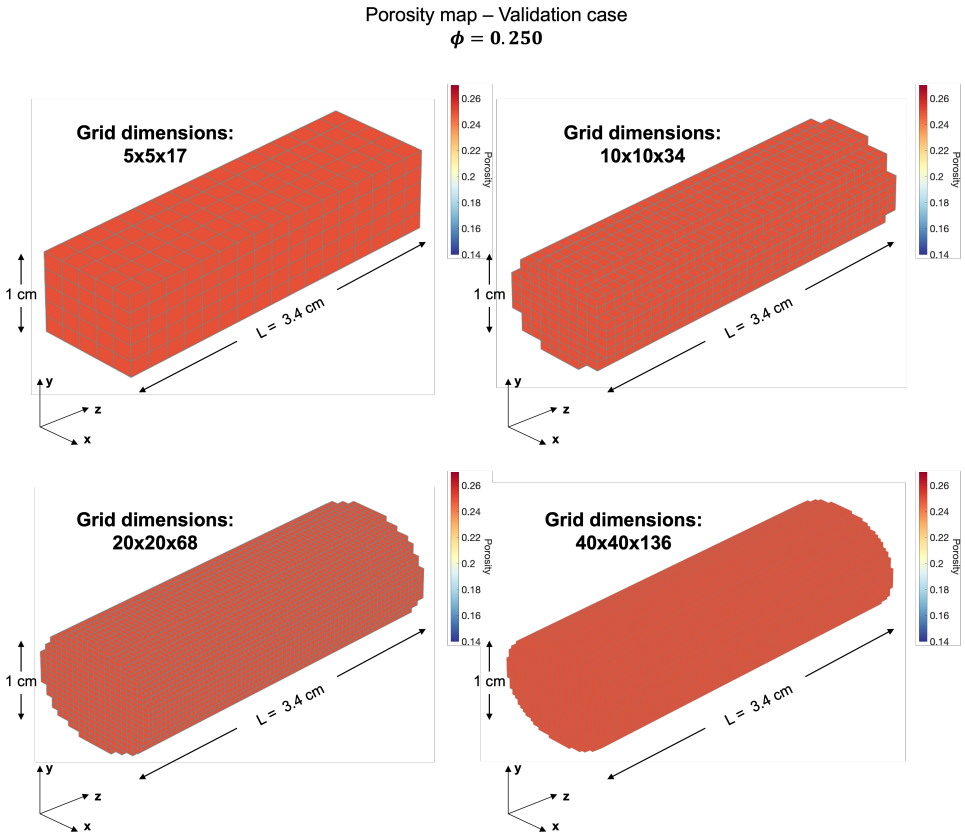


Figure 7.2: Grid refinement levels used to evaluate numerical dispersion effects. Starting from the base grid of 5×5×17, each refinement level divides each voxel by a factor of 2, resulting in grids of 10×10×34, 20×20×68, and 40×40×136, respectively. All grids represent the same physical domain (1 cm diameter × 3.4 cm length).

The conditions for this test were a constant flowrate of Q=0.1 ml/min and a tracer pulse duration of 20 seconds, corresponding to 5% of the sample pore volume ($PV = \pi r^2 L\phi$). In addition to the background flow, only advective transport was considered in the transport module, with no immobile domain included and, consequently, no mass transfer between domains. The results are presented in Figure 7.3 as breakthrough curves for each grid refinement case, plotting the concentration at the outlet against pore volume injected ($PVI = Qt/PV$). Given the homogeneous domain, the solute plume is expected to exhibit near-plug flow behavior, resulting in a Gaussian-like breakthrough curve centered around 1 PVI. When solute concentration is instead plotted against time, the simulated average residence time (Equation 7.7) can be compared to the theoretical residence time (Equation 7.8) to evaluate the accuracy of the plume travel time.

$$\tau_{\text{sim}} = \frac{\int_0^\infty t\, C_{\text{m}}(t)\, \mathrm{d}t}{\int_0^\infty C_{\text{m}}(t)\, \mathrm{d}t} \tag{7.7}$$

where:

- τ_{sim} is the average residence time obtained from the simulated breakthrough curve
- $C_{\text{m}}(t)$ is the solute concentration in the mobile domain at the outlet, expressed as a function of time
- t is the simulation time

$$\tau_{\text{the}} = \frac{PV}{Q} \tag{7.8}$$

where:

- τ_{the} is the theoretical residence time
- PV is the pore volume
- Q is the flow rate

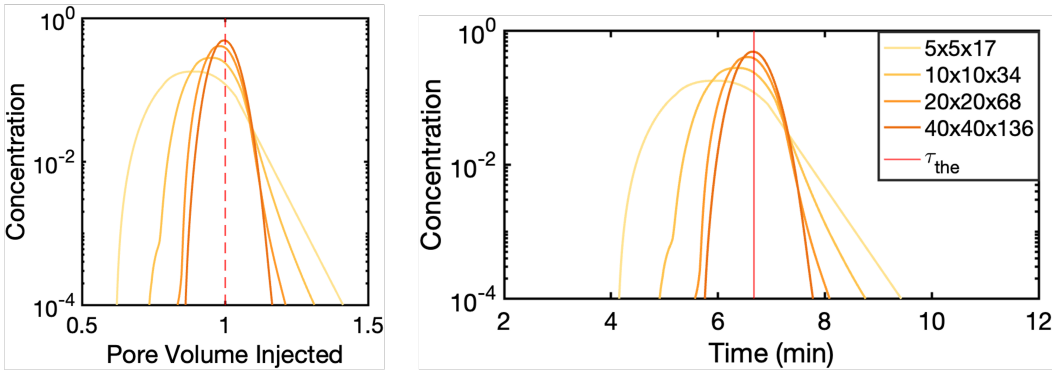


Figure 7.3: Breakthrough curves for a homogeneous case with different grid resolutions: 5×5×17, 10×10×34, 20×20×68, and 40×40×136. Left: Normalised concentration as a function of pore volume injected (PVI), highlighting the impact of numerical dispersion on plume shape. Right: Normalised concentration as a function of time, with the vertical red line indicating the theoretical residence time τ_{the}.

In the left plot it is evident that the coarse grid (5×5×17) shows an early arrival and a smeared front, evidence of numerical dispersion. As grid resolution increases, the breakthrough curves become sharper and more symmetric, and their peak shifts closer to 1 PVI, better reflecting the expected ideal plug flow behavior. In the right plot, it is clear that finer grids (40×40×136) yield average residence times much closer to the theoretical residence time, denoted by the vertical red line, while coarser grids lead to earlier plume arrival and wider tails. Overall, this demonstrates that coarser grids introduce artificial dispersion, which skews both the timing and shape of the breakthrough curve.

The two finer grids were further tested at various flowrates to evaluate the sensitivity of the model predictions to boundary conditions and input parameters, as well as to validate a suitable time step resolution. Figure 7.4 presents the results of flow simulations at flow rates of $Q = 0.05$, 0.1, 0.2 and 0.5 mL/min, the dashed vertical line represents the residence time from the simulation (τ_{sim}), while the solid vertical line marks the theoretical residence time (τ_{the}). Both grids performed well, displaying Gaussian-like breakthrough curves centered around 1 PVI, with close agreement between τ_{sim} and τ_{the} with the 20x20x68 grid, showing a slight shift to the left signifying early arrival but with minimal deviation of an acceptable error of less than 2% as shown in Table 7.1. A deviation below 2% between simulated and theoretical residence times is well within the commonly accepted tolerance of 5% for model validation in porous media transport simulations (Konikow 2011; Chunmiao Zheng, Bennett, et al. 2002). Despite these minor discrepancies, a key factor is the computing time. The 40x40x136 grid significantly increasing the elapsed simulation requiring six times longer to complete the simulation. This difference becomes more critical when modeling complex systems or including additional transport processes. Therefore, the adopted refinement protocol involved subdividing each voxel in the image-derived porosity maps by a factor of four in each direction for a final grid dimension of 20x20x68 with a voxel size of 0.05x0.05x0.05 cm^3. This approach preserves heterogeneity by retaining the porosity of each parent cell while minimising numerical dispersion.

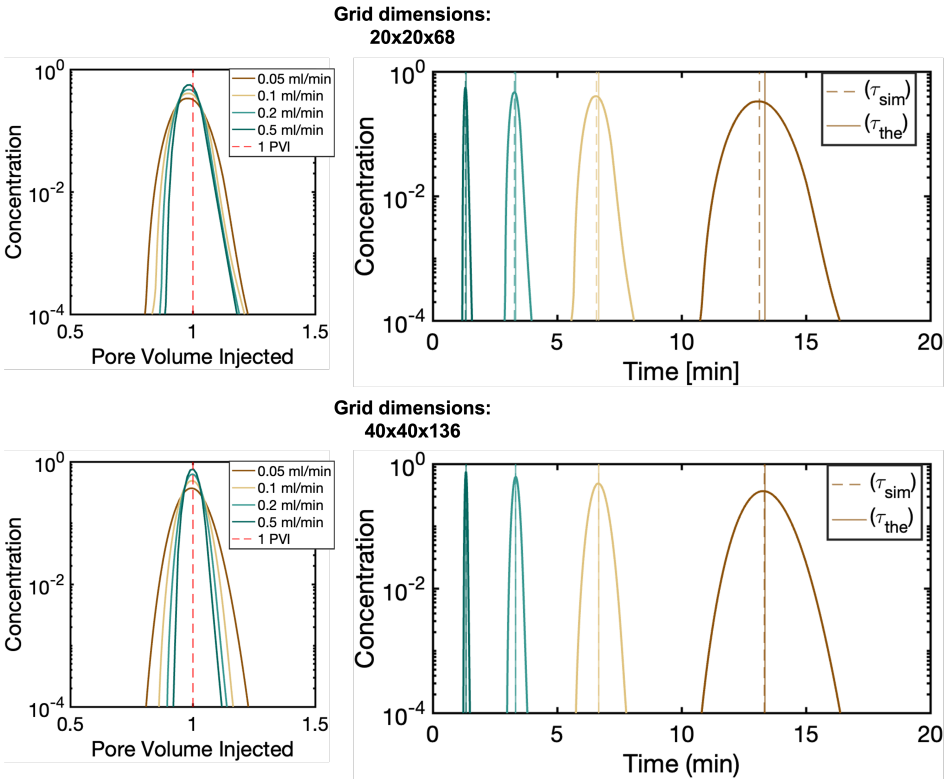


Figure 7.4: Breakthrough curves from flow simulations using two refined grids. Top: 20×20×68, bottom: 40×40×136) at flow rates of 0.05, 0.1, 0.2, and 0.5 mL/min. Left panels show concentration versus injected pore volume (PVI), with the dashed red line marking 1 PVI. Right panels show concentration versus time, where the dashed vertical lines represent simulated residence time (τ_{sim}) and solid lines indicate the theoretical residence time (τ_{the}).

Grid size	Q	τ_{sim}	τ_{the}	$deviation$
	(ml/min)	(min)	(min)	$(\%)$
20x20x68	0.05	13.13	13.35	1.66
20x20x68	0.1	6.57	6.68	1.65
20x20x68	0.2	3.29	3.34	1.49
20x20x68	0.5	1.32	1.34	1.48
40x40x136	0.05	13.33	13.35	0.15
40x40x136	0.1	6.67	6.68	0.14
40x40x136	0.2	3.34	3.34	0
40x40x136	0.5	1.34	1.34	0

Table 7.1: Summary of residence time calculated from simulation τ_{sim} and predicted theoretical residence time τ_{the}.

7.3 Model Parametrization

The inputs (flow rate, Q, and mass transfer coefficient, α) that define the flow and transport conditions for the numerical simulation in Ketton were selected based on the Péclet number (Pe) and the Damköhler number (Da), two key dimensionless parameters that characterise transport processes in porous media.

The Péclet number quantifies the relative importance of advection to diffusion, and is defined as shown in Equation 7.9. When Pe<1 diffusion dominates, and solute transport is primarily governed by molecular diffusion. Conversely, Pe>10 indicates that advection dominates, and solutes are primarily transported by the bulk movement of the fluid. Intermediate values, typically in the range of 1<Pe<10, suggest a balance between

advection and diffusion, which is desirable for studying coupled transport mechanisms and solute exchange between mobile and immobile domains,(Bear 2013).

The Damköhler number (Da), defined in Equation 7.10, compares the timescale of mass transfer between domains to the timescale of advective transport. Specifically, it reflects how quickly solute can equilibrate between regions relative to how fast it is advected through the system. For Da«0.1, tailing is effectively absent, indicating that solutes are advected faster than they can exchange with the immobile domain. When Da approaches to Da≈0.1, it corresponds to slow mass transfer relative to advection, which produces pronounced tailing as solute continues to exchange between the mobile and immobile domains long after the advective front has passed. As Da increases, mass transfer becomes faster relative to advection, reducing tailing and producing a steeper post-peak decline. For 0.1<Da<1, timescales for advective and diffusive transport are comparable, suggested by the constant decline of the BTC after peaked. A Da>1 suggests rapid equilibration with the immobile domain, potentially masking the multiple-rate mass transfer in a dual domain system and the BTC approaches the shape of a single-porosity system with minimal tailing, (Haggerty and Gorelick 1995).

$$Pe = \frac{vL_c}{D} \tag{7.9}$$

where:

- Pe is the Péclet number
- v is pore velocity, $Q/A\phi$
- L_c is the characteristic length
- D is the effective diffusion coefficient

$$Da = \frac{\alpha L_c}{v} \tag{7.10}$$

where:

- Da is the Damköhler number
- α is the first order mass transfer coefficient
- L_c is the characteristic length
- v is pore velocity, $Q/A\phi$

Figure 7.5 presents a sensitivity analysis of both Pe and Da numbers to validate that the selected parameter values place the system within the intended balanced regime. Additionally, it illustrates the impact of higher and lower Pe and Da values on breakthrough curve shapes, providing insight into the relative influence of advection, diffusion, and mass transfer. This analysis used both heterogeneous mobile and immobile porosity maps shown in Figure 7.1. In the Pe analysis, the mass transfer coefficient was kept constant and for the Da analysis, Pe was kept constant while varying the mass transfer coefficient.

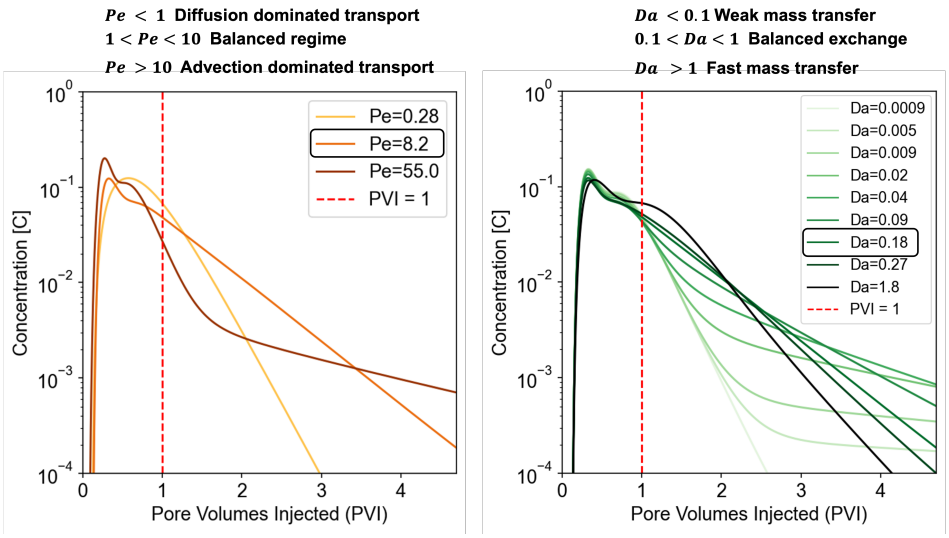


Figure 7.5: Breakthrough curves showing the impact on solute transport of the Péclet number (Left), by adjusting the flow rate, illustrating the transition from diffusion-dominated (Pe < 1) to advection-dominated (Pe > 10) regimes in a dual-domain transport system, and the Damköhler number (Right) at fixed Péclet number, altering the mass transfer coefficient.

The left panel in Figure 7.5 shows breakthrough curves (BTCs) for three simulations with different Péclet numbers (Pe), each representing a distinct transport regime. For Pe $=$

0.28 (Q = 0.001 mL/min), diffusion dominates, resulting in a more symmetric BTC. Here, solute transport occurs primarily via molecular diffusion, and the smooth peak suggests that porosity heterogeneity has minimal impact; the plume moves uniformly across both mobile and immobile domains, albeit over a longer timescale ($\tau_{\text{sim}} = 502min$).

For Pe = 8.2 (Q = 0.03 mL/min), advection and diffusion are balanced, leading to an earlier breakthrough time ($\tau_{\text{sim}} = 20min$) and longer tailing, which reflects mass exchange between mobile and immobile domains. Multiple peaks appear, a result of preferential flow paths introduced by heterogeneity in the pore structure.

At Pe = 55 (Q = 0.2 mL/min), transport is advection-dominated, with a rapid solute arrival and exit ($\tau_{\text{sim}} = 2.4min$), as shown by the narrow, steep BTC. However, instead of the expected sharp tail cutoff typical of pure advection, the curve flattens at late times, evidence that mass transfer into immobile zones still influences transport, even in highly advective systems. This behavior highlights the persistent effect of domain exchange under fast flow conditions.

This effect of mass transfer is further examined in the Damköhler number (Da) sensitivity analysis shown in the right panel. Here, Pe is held constant in the balanced regime (Pe = 8.2), and Da is varied by systematically adjusting the mass transfer coefficient. At very low Da, the timescale for mass exchange is much slower than advection, and the solute largely bypasses the immobile domain, resulting in minimal tailing, similar to transport in a purely mobile system. As Da increases, limited solute enters the immobile domain, and for Da < 0.1, tailings start to appear with advection remaining as the dominant mechanism. In the intermediate range (Da = 0.18 and Da = 0.27), a consistent post-peak decline is observed, confirming that mass transfer and advection occur on comparable timescales, and domain exchange significantly shapes the BTC.

For Da > 1, mass exchange is fast relative to advection, allowing solute to rapidly access both domains. In this regime, transport effectively occurs through an expanded mobile volume, and the BTCs become sharper. Interestingly, the curves for very low (Da = 0.0009) and very high (Da = 1.8) appear similar in shape, both reflecting primarily advective behavior, but for opposite reasons: in the former, immobile zones are effectively disconnected, while in the latter, they are fully equilibrated and act as extensions of the mobile domain.

As the objective was to assess the impact of sub-resolution porosity heterogeneity on flow and transport processes, the highlighted values ($Pe = 8.2$ and $Da = 0.18$) delineated the parameters used to carry out a numerical simulation of a tracer test in Ketton under a regime where advection and diffusion mechanisms are balanced. Using the established Pe number, the molecular diffusion coefficient of water ($D_m = 2.3 \times 10^{-5}$ cm^2/s) and the voxel size as the characteristic length (L_c=0.05), which represents the discrete volume where advection and diffusion occur. From this, the seepage velocity was calculated, and the corresponding flow rate was derived (Q=0.03 mL/min), serving as the primary input for setting the hydraulic head gradient in the model.

The Damköhler number value was selected to be in the balanced exchange rate regime (Da=0.18), where the timescales of advection and mass transfer between mobile and immobile domains are comparable. This regime is particularly sensitive to heterogeneity in the immobile domain, making it suitable for evaluating the influence of sub-resolution porosity distributions on breakthrough curves behaviour. The core length was used as the characteristic length (L_c=3.4cm) as the timescales for both processes were kept balanced across the sample, and, using the seepage velocity determined from the Pe number calculation, the corresponding mass transfer coefficient was obtained ($\alpha = 0.0002$ s^{-1}).

7.4 Flow and Transport Simulation in Ketton Limestone

Once the model was validated and flow parameters were established, a simulation was conducted to investigate the impact of sub-resolution porosity heterogeneity on flow and transport processes. This was performed using both resolved and unresolved porosity maps for Ketton limestone, representing the mobile and immobile domains, respectively. A systematic approach was adopted by defining six cases:

Case 1: Transport simulation in a homogeneous mobile domain with constant porosity equal to the average resolved porosity of the Ketton sample ($\overline{\phi_{\mathrm{m}}} = 0.167$). No immobile domain is included. This case establishes the baseline for purely advective transport through the mobile domain.

Case 2: Transport simulation using homogeneous mobile and immobile domains with constant porosity equal to the average resolved ($\overline{\phi_{\mathrm{R}}} = 0.167$) and unresolved ($\overline{\phi_{\mathrm{U}}} = 0.078$) porosity values. This case introduces dual-porosity effects with uniform domain properties.

Case 3: Transport simulation combining a homogeneous mobile domain (average resolved porosity) with a heterogeneous immobile domain using the spatially-variable unresolved porosity map (ϕ_U). This case isolates the impact of immobile domain heterogeneity.

Case 4: Transport simulation in a heterogeneous mobile domain using the image-based resolved porosity map (ϕ_R) with no immobile domain, ($\phi_U = 0$). This case examines the influence of mobile domain heterogeneity on purely advective transport.

Case 5: Transport simulation combining a heterogeneous mobile domain using the resolved porosity map (ϕ_R), with a homogeneous immobile domain (uniform unresolved porosity ($\overline{\phi_U} = 0.078$). This case explores the inclusion of diffusive transport in tighter pores assuming a constant value for sub-resolution porosity.

Case 6: Transport simulation incorporating heterogeneity in both domains: the mobile domain uses the resolved porosity field (ϕ_R), and the immobile domain uses the spatially-variable unresolved porosity field (ϕ_U). This case represents the complete heterogeneous dual-porosity system.

The simulation parameters, listed in Table 7.2, were kept constant across all six cases. The tracer pulse corresponds to 10% of the core total pore volume.

Grid size	Q	$Pulse$	$L_{c,Pe}$	D	Pe	$L_{c,Da}$	α	Da
	$(\frac{ml}{m})$	(s)	(cm)	$(\frac{cm^2}{s})$	$(-)$	(cm)	(s^{-1})	$(-)$
20x20x68	0.03	120	0.05	$2.3x10^{-5}$	8.2	3.4	0.0002	0.18

Table 7.2: Summary of variable inputs used for MODFLOW and MT3DMS simulations.

Although the simulation was conducted in 3D, results are presented as internal concentration profiles for cases 1-3 in Figure 7.6 and for cases 4-6 in Figure 7.8 and longitudinal cross-sectional views of the plume for cases 1-3 in Figure 7.7 and cases 4-6 in Figure 7.9 at selected time points highlighting key stages of plume development during the simulation.

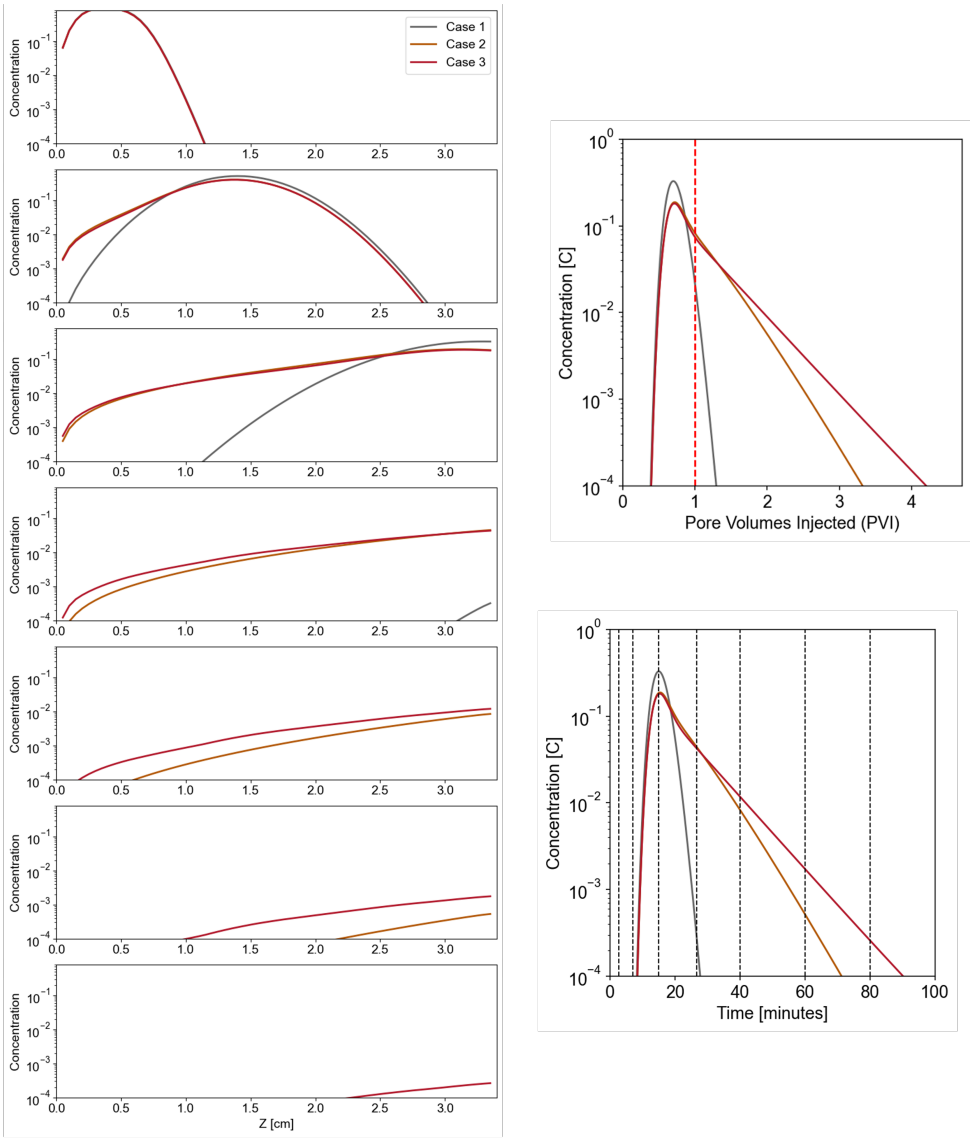


Figure 7.6: Internal concentration profiles and breakthrough curves (C vs. PVI and C vs. time) for cases 1-3. The red vertical dashed line indicates 1 pore volume injected (PVI), while the black vertical dashed lines mark the time points at which internal profiles are extracted and shown.

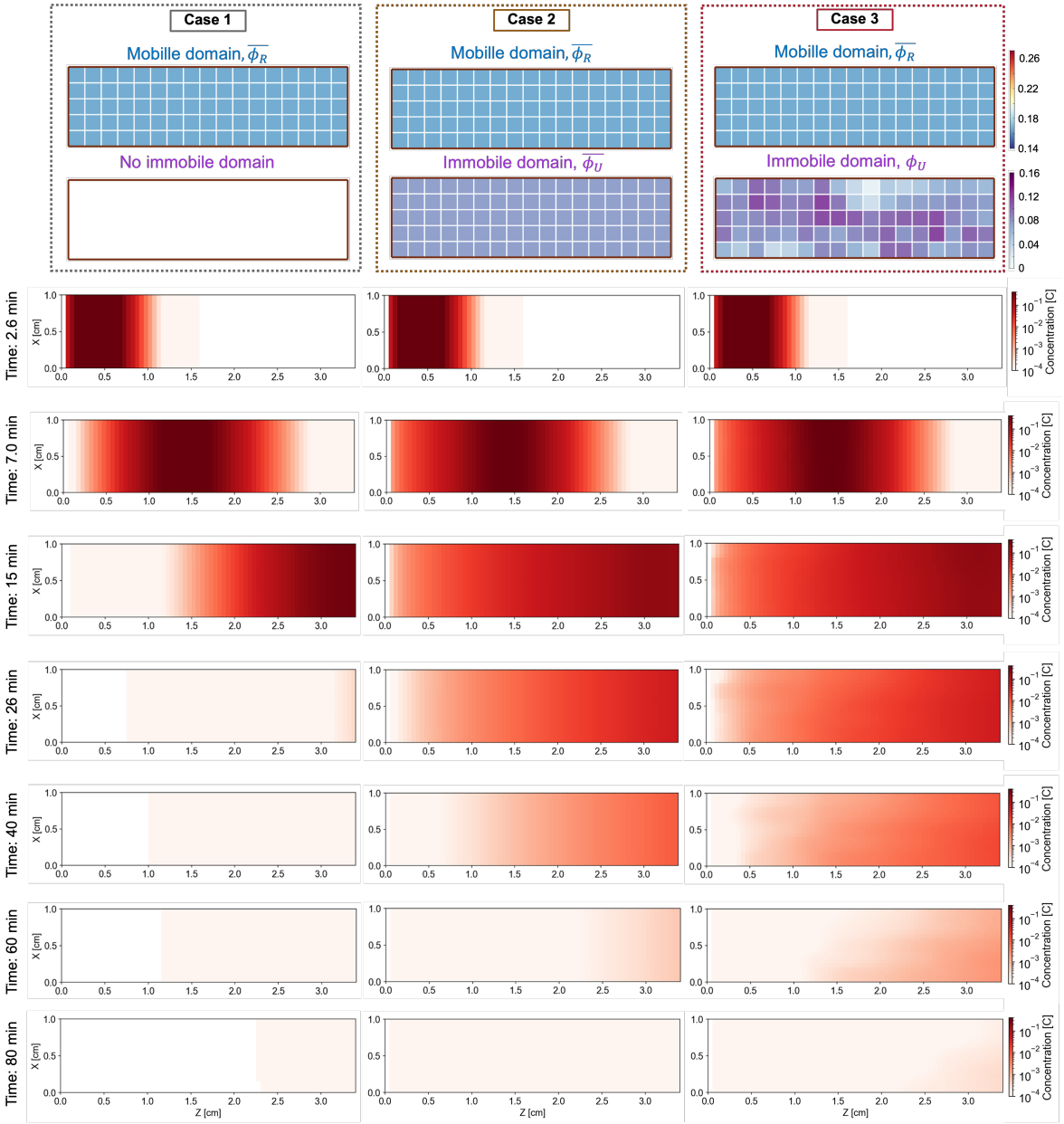


Figure 7.7: Snapshots of the flow simulation results showing the plume evolution at selected times (t=2.6, 7.0, 15.0, 26.0, 40.0, 60.0, and 80.0 minutes) for the first three proposed cases, displayed in the XZ cross sections.

The breakthrough curves in Figure 7.6 clearly demonstrate the evolution from simple advective transport to dual-porosity behavior. Case 1 exhibits the expected plug-like transport characteristic of purely advective flow through a homogeneous mobile domain, with a sharp concentration front and minimal tailing. The introduction of a uniform immobile domain in Case 2 fundamentally alters the transport dynamics, creating significant retention effects evidenced by both delayed peak arrival and pronounced

concentration tailing, also visualised from the differences in the internal profiles from the second panel onward. This tailing reflects the gradual release of solute from the immobile domain back into the mobile phase, a signature of dual-porosity transport controlled by the mass transfer coefficient. Case 3 reveals the important role of sub-resolution heterogeneity in the immobile domain. The spatially-variable unresolved porosity field enhances retention effects compared to the uniform immobile domain of Case 2, as demonstrated by the more extended tailing in the breakthrough curve. This enhanced tailing suggests that heterogeneous immobile domain properties create a distribution of mass transfer rates and residence times rather than the single characteristic time scale present in Case 2. Regions with higher immobile porosity likely retain solute longer, while areas with lower immobile porosity release solute faster, resulting in a broader spectrum of exchange timescales. The net effect is increased overall retention and a more gradual concentration decline, highlighting how sub-resolution heterogeneity can significantly influence macroscopic transport behavior even in relatively small core-scale systems.

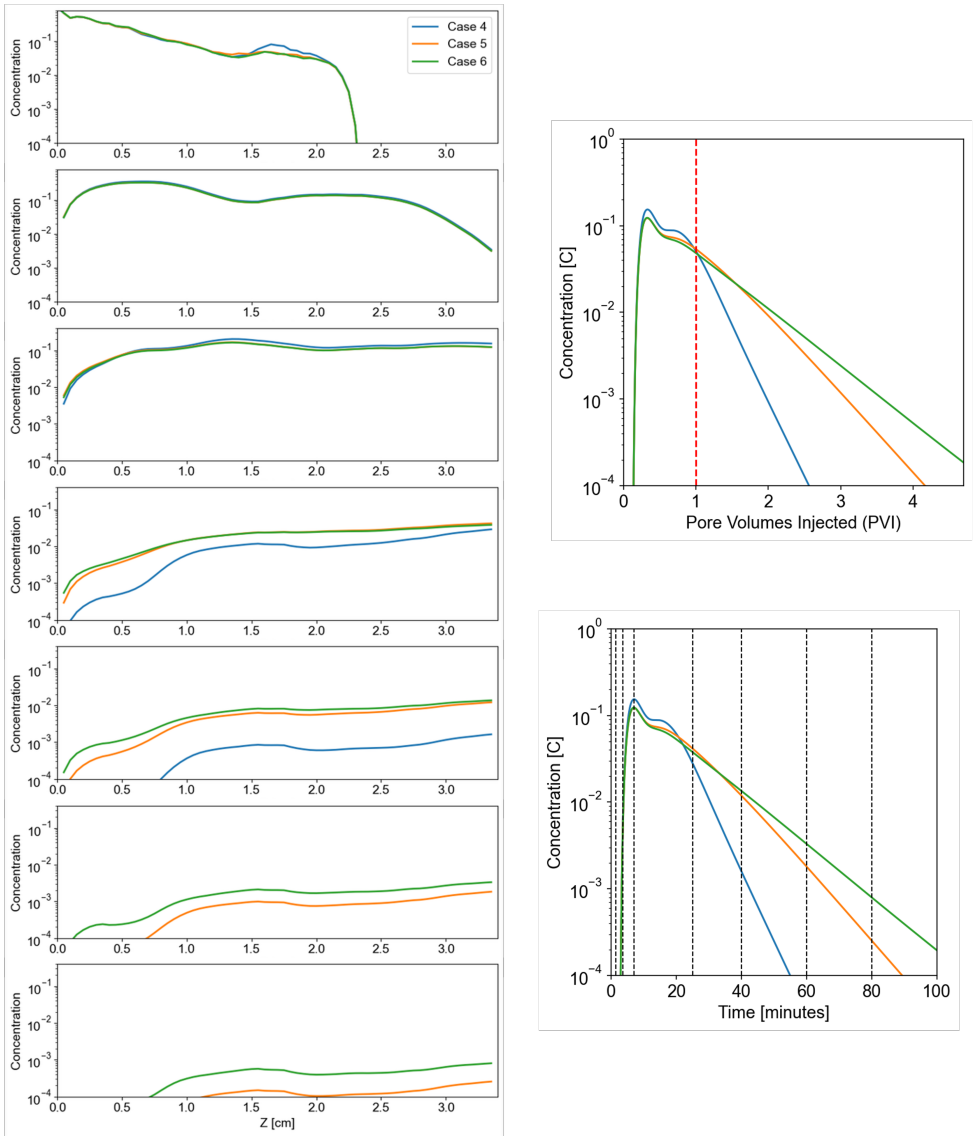
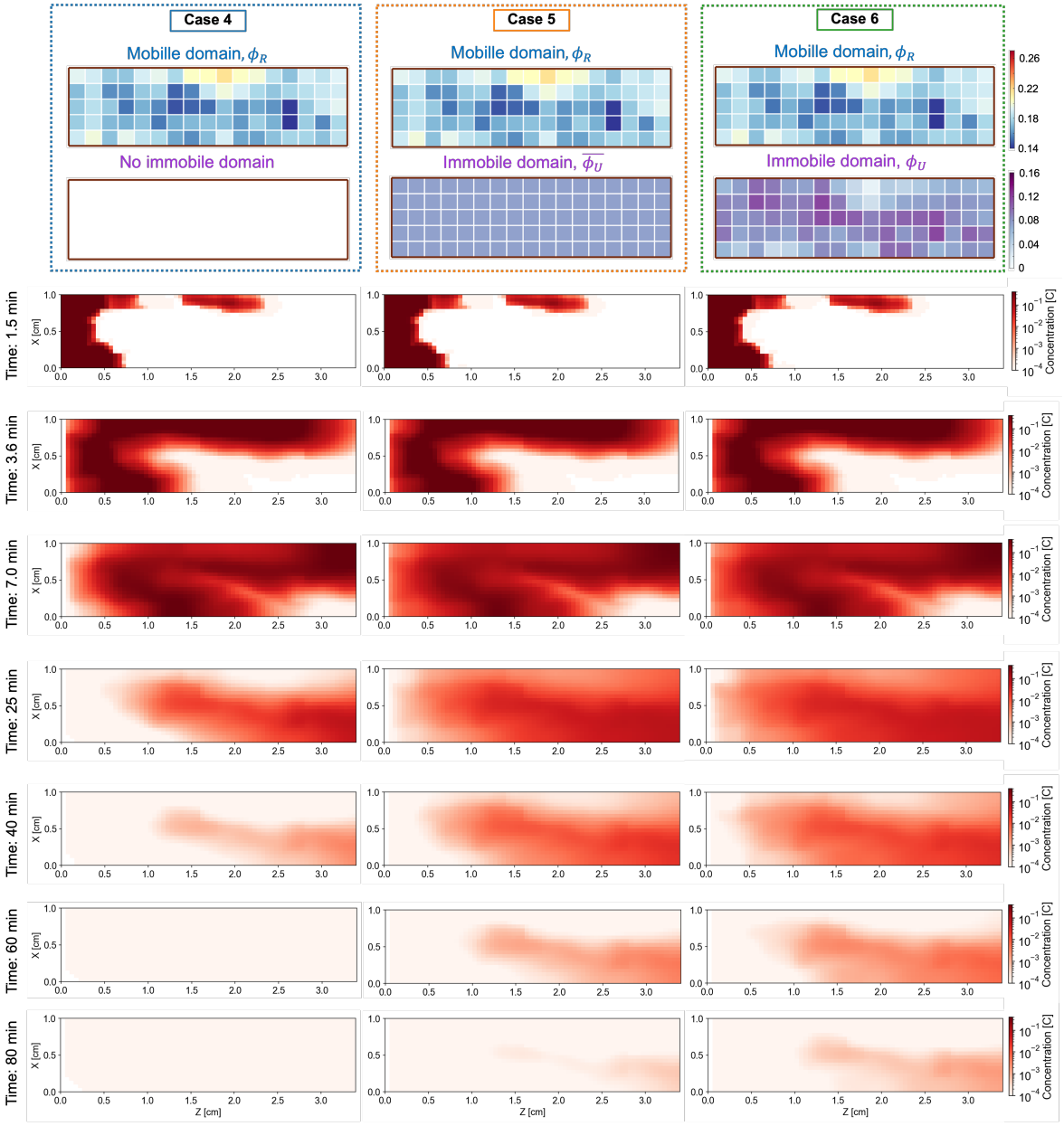


Figure 7.8: Internal concentration profiles and breakthrough curves (C vs. PVI and C vs. time) for cases 4-6. The red vertical dashed line indicates 1 pore volume injected (PVI), while the black vertical dashed lines mark the time points at which internal profiles are extracted and shown.


Case 4
Mobille domain, ϕ_R
No immobile domain
Case 5
Mobille domain, ϕ_R
Immobile domain, $\overline{\phi_U}$
Case 6
Mobille domain, ϕ_R
Immobile domain, ϕ_U
0.26
0.22
0.18
0.14
0.16
0.12
0.08
0.04
0
Time: 1.5 min
Time: 3.6 min
Time: 7.0 min
Time: 25 min
Time: 40 min
Time: 60 min
Time: 80 min
X [cm]
Z [cm]
Concentration [C]

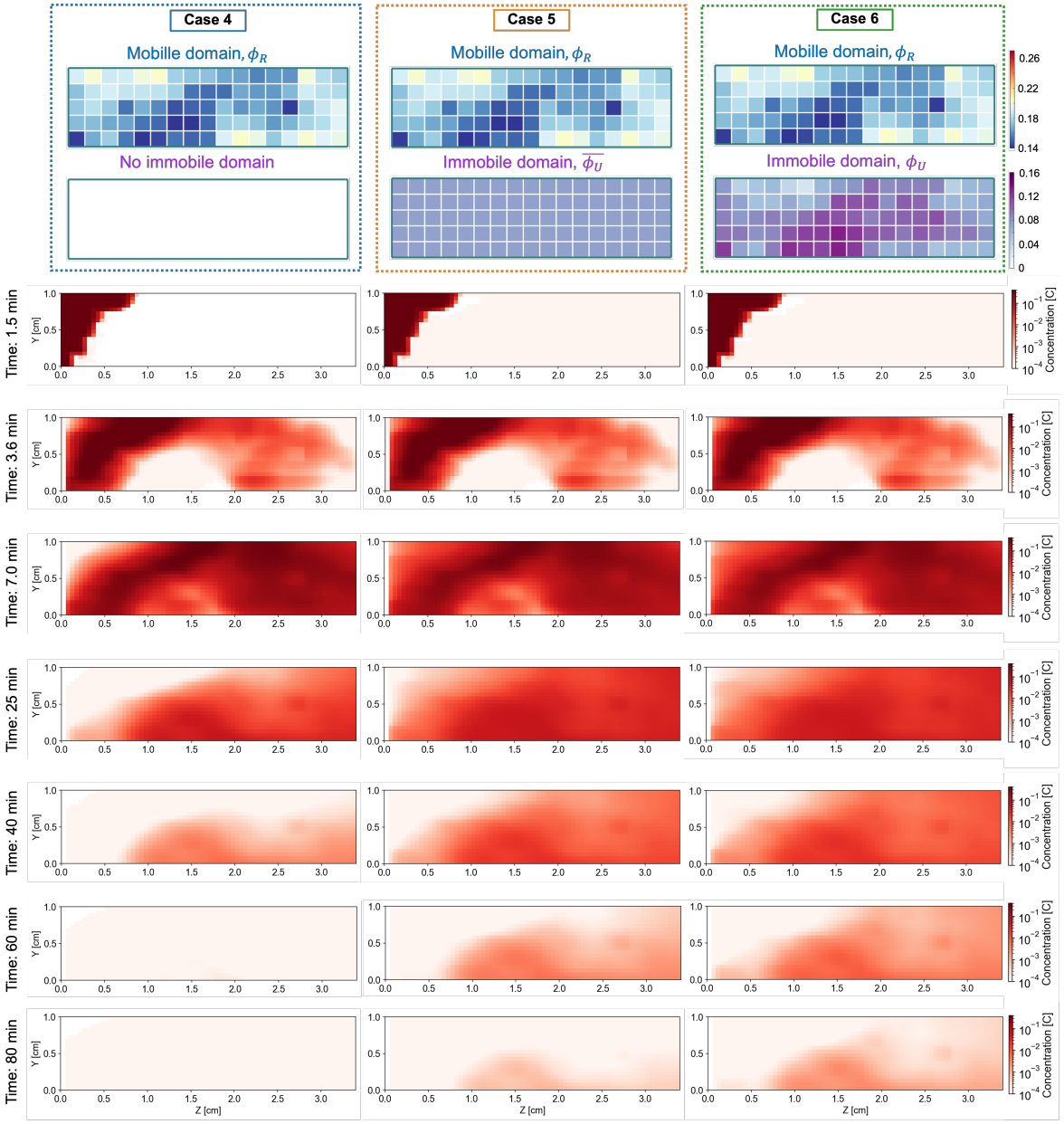


Figure 7.9: Snapshots of the flow simulation results showing the plume evolution at selected times (t=1.5, 3.6, 7.0, 25.0, 40.0, 60.0, and 80.0 minutes) for the last three proposed cases, displayed in cross sections XZ and YZ respectively.

The first notable observation from cases 4-6 compared to cases 1-3 is that the solute plume follows preferential flow paths guided by regions of higher porosity (Figure 7.9). This spatial heterogeneity in the pore structure of the mobile domain creates a spectrum of flow velocities and path lengths altering flow resistance along certain pathways, allowing the solute to bypass lower-permeability zones and move more efficiently through the core. As a result, breakthrough occurs earlier than the homogeneous mobile domain system,

as evidenced by the concentration versus pore volumes injected (PVI) plot, where peak concentrations consistently appear before the ones observed in cases 1-3 (Figure 7.10). Additionally, Cases 2 and 3 exhibit slightly lower peak concentrations, reflecting the early dilution effect as solute begins to partition into the immobile domain during injection.

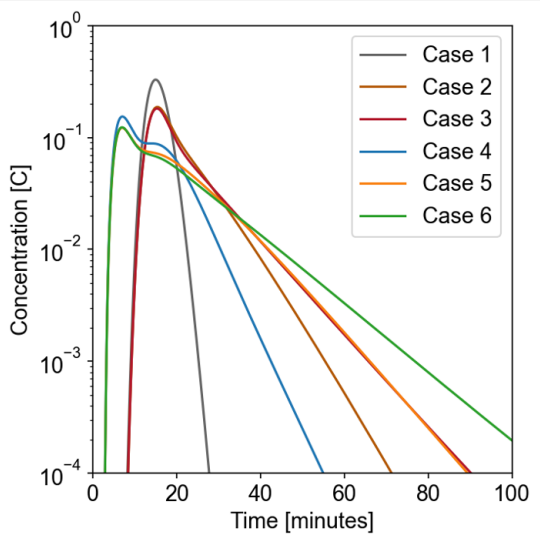


Figure 7.10: Breakthrough curves (C vs. time) for all simulated cases.

The comparison between Cases 1 and 4 isolates the pure effect of mobile domain heterogeneity on advective transport. Case 1, with its homogeneous mobile porosity produces the characteristic sharp breakthrough curve of uniform advective flow. In contrast, Case 4 demonstrates how spatial heterogeneity in the resolved porosity field extends tailing due to slower transport through lower-porosity regions, even in the absence of any immobile domain effects. Heterogeneity in the mobile domain also causes peak broadening and asymmetric tailing in the breakthrough curve, with the peak concentration occurring earlier and at a lower magnitude compared to Case 1.

After breakthrough, solute in Case 4 appears to evacuate the sample faster indicated by the sharpest decline in the BTC compared to Cases 5 and 6. The presence of an immobile domain in Cases 5 and 6 introduces increasing retardation due to mass exchange between the mobile and immobile regions. The impact of immobile domain heterogeneity becomes more evident at later times, particularly in the heterogeneous case (Case 6), where the concentration tail flattens significantly, evidence of a broader distribution of residence

times. in the heterogeneous case (Case 6), a larger solute volume remains stored within the system, reflecting the role of spatial variability in trapping and releasing solute over extended periods. These results underscore the impact of immobile domain structure, highlighting the distinction between using a uniform (averaged) porosity versus a spatially heterogeneous distribution in the immobile domain.

7.5 Concluding Remarks

This chapter presented a numerical investigation of flow and solute transport in a dual-domain porous medium, with a focus on assessing the impact of sub-resolution heterogeneity in the immobile domain. The simulation framework was based on the advection–dispersion equation coupled with first-order mass exchange between mobile and immobile regions. Model implementation was validated through a grid sensitivity analysis, demonstrating that numerical dispersion was minimised with appropriate spatial discretisation, ensuring accurate representation of breakthrough curve (BTC) dynamics.

Model parameterization was guided by dimensionless analysis using the Péclet (Pe) and Damköhler (Da) numbers to identify flow regimes where advection, diffusion, and mass transfer processes occur on comparable timescales. A Pe value of 8.2 and a Da value of 0.18 were selected to establish a balanced regime, which was particularly sensitive to the effects of heterogeneity in the immobile domain.

Simulations were conducted for six configurations: (1) transport in the homogeneous mobile domain only, (2) transport in a homogeneous mobile domain coupled with an averaged immobile domain, (3) homogeneous mobile domain coupled with heterogeneous immobile domain, (4) transport in the heterogeneous mobile domain only, (5) heterogeneous mobile domain coupled with an averaged immobile domain, and (6) heterogeneous mobile domain coupled with a spatially heterogeneous immobile domain.

The results demonstrate that preferential flow paths within the mobile domain, controlled by porosity heterogeneity, drive early solute breakthrough across all heterogeneous cases. The critical role of diffusive transport in overall system behaviour becomes evident when comparing cases with and without immobile domains: the coupling of advective

flow in the mobile domain with diffusion-dominated transport in the immobile domain produces characteristic extended tailing in the breakthrough curves. This tailing effect is particularly pronounced when spatial variability is incorporated into the immobile domain properties. The systematic comparison across cases reveals that simplified or averaged representations of pore-scale properties could significantly underestimate the impact of microstructural heterogeneity on macroscopic solute transport behaviour. These findings highlight the limitations of homogenized dual-porosity models and underscore the necessity of incorporating realistic spatial distributions of both mobile and immobile domain properties to accurately predict solute retention and release in natural porous media.

These findings have important implications for upscaling transport models to the field scale. Significant changes in breakthrough behaviour were observed in a meso-scale core of only 3.4 cm in length, indicating that even sub-centimeter scale heterogeneities can substantially affect transport dynamics. Neglecting such heterogeneity in larger-scale models may result in inaccurate predictions of plume evolution, mass retention, and recovery, especially in diffusion-sensitive systems. The multi-scale X-ray methodology developed in this work, which integrates 3D microporosity and macroporosity maps in meso-scale samples, provides a pathway for bridging the gap between pore-scale observations and continuum-scale representations. By explicitly capturing the spatial distribution and connectivity of both microporous and macroporous domains, these maps enable more physically representative parameterisation of dual-porosity or multi-continuum models commonly employed at reservoir scales. However, upscaling from the centimeter-scale sample volumes investigated here to meter- or field-scale domains introduces several challenges. The representativeness of sample volumes relative to larger-scale heterogeneity structures (such as bedding, fracture networks, or diagenetic zones) must be carefully evaluated to determine appropriate Representative Elementary Volumes (REVs) for different transport properties. These results demonstrate that microporosity distributions can exhibit significant spatial variability even within individual samples, suggesting that traditional upscaling approaches based on arithmetic or harmonic averaging may inadequately capture the impact of preferential flow pathways and diffusive exchange between porosity scales. Furthermore, the computational cost of explicitly resolving microporosity distributions in field-scale numerical models remains

prohibitive, needing the development of effective medium approximations or sub-grid parameterisations that preserve the essential physics of multi-scale transport while remaining manageable for large-domain simulations. The methodology presented here provides quantitative constraints on these parameterisations by directly linking pore-scale architecture to observed breakthrough behavior, thereby reducing uncertainties inherent in purely empirical upscaling relationships. Future work should focus on analysing multiple samples from different stratigraphic intervals and diagenetic facies to assess the statistical variability of microporosity distributions and establish robust upscaling frameworks that account for sub-core scale heterogeneity while maintaining computational efficiency at reservoir scales.

Chapter 8

Conclusions and Future Work

8.1 Conclusions

This thesis has successfully addressed the fundamental challenge of multi-scale porosity quantification in sedimentary rocks through the development of a novel dual-resolution X-ray CT methodology. The approach addresses a critical gap in the characterisation of three-dimensional architecture of complex porous media systems and enables improved prediction of flow and transport behaviour. The validation across multiple rock types and the demonstration of successful integration with numerical modelling frameworks establish this methodology as a valuable tool for both fundamental research and practical applications in subsurface engineering, making significant contributions to the field of petrophysics and digital rock analysis.

The primary contribution of this work is the development of a dual-resolution approach that combines medical CT and micro CT imaging to provide complete porosity characterisation across multiple scales. This methodology successfully addresses the fundamental challenge of capturing both spatial macro-scale effective porosity and micro-scale resolved porosity within a single analytical framework. The integration of these two imaging modalities enables the quantification of previously unresolved porosity components that are critical for understanding flow and transport behaviour in geological materials.

The introduction of radio-opaque gases, specifically krypton, as a saturating fluid represents a significant advancement in the analysis of low permeability samples. This application overcomes traditional limitations in differential imaging techniques and

extends the applicability of the dual-resolution method to tight rock systems that are increasingly important in subsurface applications.

The thesis demonstrates the successful generation of 3D porosity maps that distinguish between effective, resolved, and unresolved porosity components. This capability provides unprecedented spatial resolution of pore system heterogeneity and enables detailed analysis of porosity distribution patterns in both simple and complex geological systems.

The dual-resolution methodology has been rigorously validated against established bulk porosity measurement techniques, including helium pycnometry, mercury intrusion capillary pressure (MICP), and Archimedes' method measurements. The results demonstrate excellent agreement across diverse rock types, including Bentheimer sandstone, Ketton limestone, Nugget sandstone, and Silurian dolomite, confirming the accuracy and reliability of the proposed approach.

The detailed porosity maps enable improved parametrization of numerical models, particularly in capturing the effects of sub-resolution porosity on bulk transport properties. This capability is essential for upscaling applications and represents a significant advancement over traditional parameter averaging approaches.

8.2 Suggested Future Work

Several opportunities exist for extending this work:

Tracer-Based Validation of Dual-Resolution Porosity Characterisation: Tracer-based experiments are proposed to confirm that the dual-resolution methodology produces porosity characterisations of sufficient quality and to validate the predictive modelling applications. These experiments would involve the injection of contrast agents or chemical tracers into rock samples during imaging, under controlled flow conditions and a range of flow rates, as explored by (Kurotori, Zahasky, Hejazi, et al. 2019), where PET imaging was applied during radio-tracer injection allowing to evaluate the spatial and temporal degree of the tracer plume mixing and spreading, these observations could be describe by the modelling approach described in Chapter 7, having a better

informed sub-resolution domain. Ideally, the same samples used in this study should be employed given that the developed methodology in this thesis is non-destructive and samples remained intact for further use in experimental campaigns. Additionally, these experiments could provide the means to establish calibration for key parameters affecting flow and transport that were assumed during the exploratory modelling exercise, including the porosity–permeability relationship, the mass transfer coefficient, and the longitudinal dispersion coefficient. By fitting breakthrough curves (BTCs) and plume behaviour from experiments to numerical simulations, a more robust understanding of the role of sub-resolution porosity in controlling transport processes can be achieved.

Tracking Temporal Porosity Evolution in Geological Systems: Extending the methodology to time-lapse imaging offers opportunities to monitor porosity evolution during chemical reactions, mechanical deformation, and fluid–rock interactions, using the porosity characterisation developed in this thesis as an initial reference that can be repeated after such changes to track porosity development and provide insights into dynamic processes in geological systems. These studies would require the development of specialised sample holders and control systems that allow for imaging while subjecting samples to controlled stress, temperature, and chemical conditions representative of subsurface environments. The temporal resolution requirements would vary significantly depending on the process being studied, from rapid mechanical deformation to long-term chemical alteration studies spanning weeks or months with daily or weekly imaging schedules. Advanced image registration and analysis algorithms would be essential for accurately tracking porosity changes over time, particularly in cases where sample deformation complicates direct comparison between time steps. The methodology should also incorporate uncertainty quantification approaches to distinguish genuine porosity evolution from measurement noise and imaging artifacts. Applications could include monitoring hydraulic fracturing processes (Tatone and Grasselli 2015), studying diagenetic changes under varying temperature and pressure conditions, investigating reactive processes in enhanced oil recovery scenarios, and characterising porosity evolution during acidic brine-CO_2-rock interactions (Hao et al. 2025). Such studies would provide insights into the temporal aspects of pore network evolution and could significantly improve predictive models for reservoir behaviour and geological storage applications.

Protocol Enhancement by Automated Machine Learning Segmentation: Integration of artificial intelligence approaches for automated image segmentation and porosity classification, particularly for complex heterogeneous systems, represents an opportunity for advancing the efficiency and objectivity of porosity characterisation workflows. Deep learning architectures could help for automating the traditionally labour-intensive process of image segmentation in CT datasets. The development of comprehensive training datasets encompassing diverse rock types, porosity ranges, and imaging conditions would be crucial for creating robust AI models capable of generalising across different geological materials and imaging parameters (Arganda-Carreras et al. 2017; Purswani et al. 2020). These machine learning systems should be designed to handle multi-resolution datasets effectively, potentially using hierarchical approaches that leverage information from both high-resolution local regions and lower-resolution global context. Beyond basic segmentation, AI approaches could enable sophisticated porosity classification schemes that automatically identify different pore types and predict their likely contributions to fluid transport properties.

Field-Scale Applications of Dual-Resolution Porosity Characterisation: Development of upscaling techniques to apply laboratory-derived porosity characterisations to field-scale reservoir models constitutes one of the most challenging yet potentially impactful extensions of this work. The fundamental challenge lies in bridging the scale gap between millimetre-scale laboratory samples and kilometre-scale reservoir domains while preserving the essential connectivity and heterogeneity characteristics that control fluid flow behaviour. Effective upscaling methodologies must address both the statistical representation of porosity heterogeneity and the preservation of critical flow pathways that may be under-represented in conventional geostatistical approaches. The proposed methodology could be implemented to characterise the representative rock types during the exploration and development of a reservoir, assessing flow patterns, plume migration and rock sealing capabilities. Integration with reservoir simulation workflows would require the development of efficient computational approaches for handling the increased complexity of porosity models while maintaining acceptable simulation run times for field development decisions. The methodology should also incorporate uncertainty quantification frameworks that properly propagate the uncertainties associated with upscaling from laboratory samples to field-scale

applications. Validation of these upscaling approaches would need comparison with field performance data, production history matching, and tracer test interpretations to demonstrate that laboratory-derived insights translate meaningfully to reservoir-scale behaviour. Furthermore, the development of adaptive upscaling strategies that can incorporate new data as it becomes available during field development would provide a framework for continuously improving reservoir models throughout the reservoir lifecycle.

Bibliography

Alatrash, Hasan and Felicitász Velledits (2024). "Comparing petrophysical properties and pore network characteristics of carbonate reservoir rocks using micro X-ray tomography imaging and microfacies analyses". In: *GEM-International Journal on Geomathematics* 15.1, p. 1.

Alpak, Faruk, Aleksandar Samardžić, and Florian Frank (2018). "A distributed parallel direct simulator for pore-scale two-phase flow on digital rock images using a finite difference implementation of the phase-field method". In: *Journal of Petroleum Science and Engineering* 166, pp. 806–824.

Alyafei, Nayef, Thomas J Mckay, and Theis I Solling (2016). "Characterization of petrophysical properties using pore-network and lattice-Boltzmann modelling: Choice of method and image sub-volume size". In: *Journal of Petroleum Science and Engineering* 145, pp. 256–265.

Andersson, L et al. (2013). "High-resolution x-ray tomography imaging of supercritical CO2: Investigating capillary trapping under reservoir conditions and addressing wettability alteration". In: *AGU Fall Meeting Abstracts*. Vol. 2013, H41P–03.

Andrä, Heiko et al. (2013a). "Digital rock physics benchmarks—Part I: Imaging and segmentation". In: *Computers & Geosciences* 50, pp. 25–32.

– (2013b). "Digital rock physics benchmarks—Part II: Computing effective properties". In: *Computers & Geosciences* 50, pp. 33–43.

Andrew, Matthew, Branko Bijeljic, and Martin J Blunt (2014). "Pore-scale imaging of trapped supercritical carbon dioxide in sandstones and carbonates". In: *International Journal of Greenhouse Gas Control* 22, pp. 1–14.

API (1998). “Recommended Practices for Core Analysis”. In: *American Petroleum Institute*.

Arganda-Carreras, Ignacio et al. (2017). “Trainable Weka Segmentation: a machine learning tool for microscopy pixel classification”. In: *Bioinformatics* 33.15, pp. 2424–2426.

Bear, Jacob (2013). *Dynamics of fluids in porous media*. Courier Corporation.

Berg, Carl Fredrik, Olivier Lopez, and Håvard Berland (2017). “Industrial applications of digital rock technology”. In: *Journal of Petroleum Science and Engineering* 157, pp. 131–147.

Berg, Steffen et al. (2018). “Generation of ground truth images to validate micro-CT image-processing pipelines”. In: *The Leading Edge* 37.6, pp. 412–420.

Bijeljic, Branko, Peyman Mostaghimi, and Martin J Blunt (2013). “Insights into non-Fickian solute transport in carbonates”. In: *Water resources research* 49.5, pp. 2714–2728.

Bijeljic, Branko, Ali Q Raeini, et al. (2018). “Multimodal functions as flow signatures in complex porous media”. In: *arXiv preprint arXiv:1807.07611*.

Blunt, Martin J et al. (2013). “Pore-scale imaging and modelling”. In: *Advances in Water resources* 51, pp. 197–216.

Boas, F Edward, Dominik Fleischmann, et al. (2012). “CT artifacts: causes and reduction techniques”. In: *Imaging Med* 4.2, pp. 229–240.

Boggs Jr, Sam (2009). *Petrology of sedimentary rocks*. Cambridge university press.

Bultreys, Tom, Marijn A Boone, et al. (2016). “Fast laboratory-based micro-computed tomography for pore-scale research: Illustrative experiments and perspectives on the future”. In: *Advances in water resources* 95, pp. 341–351.

Bultreys, Tom, Luc Van Hoorebeke, and Veerle Cnudde (2015). "Multi-scale, micro-computed tomography-based pore network models to simulate drainage in heterogeneous rocks". In: *Advances in Water Resources* 78, pp. 36–49.

Choquette, P. and LL. Pray (1970). "Geologic Nomenclature and Classification of Porosity in Sedimentary Carbonates". In: *The American Association of Petroleum Geologists Bulletin*.

Cnudde, Veerle and Matthieu Nicolaas Boone (2013). "High-resolution X-ray computed tomography in geosciences: A review of the current technology and applications". In: *Earth-Science Reviews* 123, pp. 1–17.

Dalton, Laura E, Dustin Crandall, and Angela Goodman (2020). "Characterizing the evolution of trapped scCO2 curvature in Bentheimer and Nugget sandstone pore geometry". In: *Geofluids* 2020.1, p. 3016595.

Darling, Toby (2005). "CHAPTER 10 - PRODUCTION GEOLOGY ISSUES". In: *Well Logging and Formation Evaluation*. Ed. by Toby Darling. Burlington: Gulf Professional Publishing, pp. 137–154.

Dvorkin, Jack et al. (2011). "Relevance of computational rock physics". In: *Geophysics* 76.5, E141–E153.

Flügel, Erik and Axel Munnecke (2010). *Microfacies of carbonate rocks: analysis, interpretation and application*. Vol. 976. Springer.

Frippiat, Christophe C and Alain E Holeyman (2008). "A comparative review of upscaling methods for solute transport in heterogeneous porous media". In: *Journal of Hydrology* 362.1-2, pp. 150–176.

Fusseis, Florian et al. (2014). "A brief guide to synchrotron radiation-based microtomography in (structural) geology and rock mechanics". In: *Journal of Structural Geology* 65, pp. 1–16.

Ganguli, Shib Sankar and Vijay Prasad Dimri (2023). "Reservoir characterization: State-of-the-art, key challenges and ways forward". In: *Developments in structural geology and tectonics*. Vol. 6. Elsevier, pp. 1–35.

Gao, Ying et al. (2019). "Pore occupancy, relative permeability and flow intermittency measurements using X-ray micro-tomography in a complex carbonate". In: *Advances in Water Resources* 129, pp. 56–69.

Ghadami, Nader et al. (2015). "Consistent porosity–permeability modeling, reservoir rock typing and hydraulic flow unitization in a giant carbonate reservoir". In: *Journal of Petroleum Science and Engineering* 131, pp. 58–69.

Grader, Abraham S et al. (2010). "Multi-scale imaging process for computations of porosity and permeability from carbonate rocks". In: *Geo 2010 Conference, The European Association of Geoscientists and Engineers (EAGE) Publication*.

Haggerty, Roy and Steven M Gorelick (1995). "Multiple-rate mass transfer for modeling diffusion and surface reactions in media with pore-scale heterogeneity". In: *Water Resources Research* 31.10, pp. 2383–2400.

Hao, Jingyue et al. (2025). "Time-lapse 3D imaging and modelling of acid-rock interactions within a mudstone: Implications for cap-rock behaviour during carbon storage". In: *Fuel* 381, p. 133629.

Harbaugh, Arlen W et al. (2000). "MODFLOW-2000, the US Geological Survey modular ground-water model: User guide to modularization concepts and the ground-water flow process". In.

Herring, AL et al. (2021). "Evolution of bentheimer sandstone wettability during cyclic scCO2-brine injections". In: *Water resources research* 57.11, e2021WR030891.

Herring, Anna L et al. (2014). "Pore-scale observations of supercritical CO2 drainage in Bentheimer sandstone by synchrotron x-ray imaging". In: *International Journal of Greenhouse Gas Control* 25, pp. 93–101.

Iassonov, Pavel, Thomas Gebrenegus, and Markus Tuller (2009). "Segmentation of X-ray computed tomography images of porous materials: A crucial step for characterization and quantitative analysis of pore structures". In: *Water resources research* 45.9.

Iscan, AG and MV Kok (2009). "Porosity and permeability determinations in sandstone and limestone rocks using thin section analysis approach". In: *Energy Sources, Part A: Recovery, Utilization, and Environmental Effects* 31.7, pp. 568–575.

Jeandey, C et al. (1990). "Comparative Imaging of Liquids in Rocks by NMR and Differential X Ray CT". In: *MRS Online Proceedings Library (OPL)* 217, p. 175.

Kantzas, Apostolos, Jonathan Bryan, and Saeed Taheri (2012). "Fundamentals of fluid flow in porous media". In: *Pore size distribution*.

Karlsons, K et al. (2022). "Integrating pore-scale flow MRI and X-ray μCT for validation of numerical flow simulations in porous sedimentary rocks". In: *Transport in Porous Media* 143.2, pp. 373–396.

Kashif, Muhammad et al. (2019). "Pore size distribution, their geometry and connectivity in deeply buried Paleogene Es1 sandstone reservoir, Nanpu Sag, East China". In: *Petroleum Science* 16.5, pp. 981–1000.

Keelan, Dare K and David M Marschall (1979). "The Fundamentals of Core Analysis". In: *Core Laboratories, Ver* 3, pp. 1–2.

Keele, Dustin and James Evans (2008). "Analysis of Reservoir Properties of Faulted and Fractured Eolian Thrust-Belt Reservoirs (OFR-529) 2008". In: *Utah Geological Survey*.

Konikow, Leonard F (2011). "The secret to successful solute-transport modeling". In: *Groundwater* 49.2, pp. 144–159.

Krause, M, J-C-C Perrin, and SM M Benson (2011). "Modeling permeability distributions in a sandstone core for history matching coreflood experiments". In: *Spe Journal* 16.04, pp. 768–777.

Kurotori, Takeshi, Christopher Zahasky, Sally M Benson, et al. (2020). "Description of chemical transport in laboratory rock cores using the continuous random walk formalism". In: *Water Resources Research* 56.9, e2020WR027511.

Kurotori, Takeshi, Christopher Zahasky, Sayed Alireza Hosseinzadeh Hejazi, et al. (2019). "Measuring, imaging and modelling solute transport in a microporous limestone". In: *Chemical Engineering Science* 196, pp. 366–383.

Lai, Peter, Kevin Moulton, and Samuel Krevor (2015). "Pore-scale heterogeneity in the mineral distribution and reactive surface area of porous rocks". In: *Chemical Geology* 411, pp. 260–273.

Liao, Ping-Sung, Tse-Sheng Chen, Pau-Choo Chung, et al. (2001). "A fast algorithm for multilevel thresholding". In: *J. Inf. Sci. Eng.* 17.5, pp. 713–727.

Liao, Qinzhuo et al. (2023). "Convergence analysis of Lattice Boltzmann method for Stokes flow in digital rock characterization". In: *Geoenergy Science and Engineering* 230, p. 212161.

Lin, Qingyang et al. (2016). "Quantification of sub-resolution porosity in carbonate rocks by applying high-salinity contrast brine using X-ray microtomography differential imaging". In: *Advances in water resources* 96, pp. 306–322.

Lindquist, Sandra J (1988). "Practical characterization of eolian reservoirs for development: Nugget Sandstone, Utah—Wyoming thrust belt". In: *Sedimentary Geology* 56.1-4, pp. 315–339.

Luna, José Leão de et al. (2016). "Petrophysical rock typing of Coquinas from the Morro do Chaves Formation, Sergipe-Alagoas Basin (Northeast Brazil)". In: *Brazilian Journal of Geophysics* 34.4, pp. 509–521.

Ma, Lin et al. (2019). "A novel upscaling procedure for characterising heterogeneous shale porosity from nanometer-to millimetre-scale in 3D". In: *Energy* 181, pp. 1285–1297.

Maire, Eric and Philip John Withers (2014). "Quantitative X-ray tomography". In: *International materials reviews* 59.1, pp. 1–43.

Mayo, Sheridan et al. (2015). "Quantitative micro-porosity characterization using synchrotron micro-CT and xenon K-edge subtraction in sandstones, carbonates, shales and coal". In: *Fuel* 154, pp. 167–173.

Mazzullo, S. (2004). "Overview of Porosity Evolution in Carbonate Reservoirs". In: *Kansas Geological Society Bulletin*.

Al-Menhali, Ali et al. (2014). "Advanced reservoir characterization for CO2 storage". In: *IPTC 2014: International Petroleum Technology Conference*. European Association of Geoscientists & Engineers, cp–395.

Menke, Hannah P, Ying Gao, et al. (2022). "Using nano-XRM and high-contrast imaging to inform micro-porosity permeability during Stokes–Brinkman single and two-phase flow simulations on micro-CT images". In: *Frontiers in Water* 4, p. 935035.

Menke, Hannah P, Julien Maes, and Sebastian Geiger (2021). "Upscaling the porosity–permeability relationship of a microporous carbonate for Darcy-scale flow with machine learning". In: *Scientific reports* 11.1, p. 2625.

Moslemipour, Abolfazl and Saeid Sadeghnejad (2021). "Dual-scale pore network reconstruction of vugular carbonates using multi-scale imaging techniques". In: *Advances in Water Resources* 147, p. 103795.

Nimmo, J. (2013). "Porosity and Pore Size Distribution". In: *Earth Systems and Environmental Sciences*.

NIST Chemistry WebBook, NIST Standard Reference Database (2025). National Institute of Standards and Technology, https://webbook.nist.gov.

Otsu, Nobuyuki (1979). "A threshold selection method from gray-level histograms". In: *IEEE transactions on systems, man, and cybernetics* 9.1, pp. 62–66.

Pape, Hansgeorg, Christoph Clauser, and Joachim Iffland (1999). "Permeability prediction based on fractal pore-space geometry". In: *Geophysics* 64.5, pp. 1447–1460.

Patmonoaji, Aninditya et al. (2025). "Differential Imaging-Based Porous Plate Measurements of Fluid Distribution and Capillary Pressure During Drainage in a Multiscale Oolitic Limestone". In: *Transport in Porous Media* 152.5, pp. 1–18.

Peksa, Anna E, Karl-Heinz AA Wolf, and Pacelli LJ Zitha (2015). "Bentheimer sandstone revisited for experimental purposes". In: *Marine and Petroleum Geology* 67, pp. 701–719.

Peters, Kenneth, D. Curry, and M. Kacewicz (2012). *An overview of basin and petroleum system modeling: Definitions and concepts*. AAPG Hedberg Series no. 4. Basin modeling: New horizons in research and applications.

Pini, Ronny and Claudio Madonna (2016). "Moving across scales: a quantitative assessment of X-ray CT to measure the porosity of rocks". In: *Journal of Porous Materials* 23.2, pp. 325–338.

Prior, David J et al. (1999). "The application of electron backscatter diffraction and orientation contrast imaging in the SEM to textural problems in rocks". In: *American Mineralogist* 84.11-12, pp. 1741–1759.

Prodanović, Maša, Ayaz Mehmani, and Adrian P Sheppard (2015). "Imaged-based multiscale network modelling of microporosity in carbonates". In.

Purswani, Prakash et al. (2020). "Evaluation of image segmentation techniques for image-based rock property estimation". In: *Journal of Petroleum Science and Engineering* 195, p. 107890.

Qajar, Jafar, Maryam Mohammadi, and Hamed Aghaei (2021). "An investigation on the robustness and accuracy of permeability estimation from 3D μ-CT images of rock samples based on the solution of Laplace's equation for pressure". In: *Computers & Geosciences* 155, p. 104857.

Rejeki, Sri, Julfi Hadi, and Ilan Suhayati (2005). "Porosity study for detail reservoir characterization in Darajat geothermal field, West Java, Indonesia". In: *Proceedings, World Geothermal Congress, Antalya, Turkey*, pp. 24–29.

Rücker, Maja et al. (2020). "Workflow for upscaling wettability from the nanoscale to core scale". In: *Petrophysics* 61.02, pp. 189–205.

Sadeghnejad, Saeid, Frieder Enzmann, and Michael Kersten (2021). "Digital rock physics, chemistry, and biology: challenges and prospects of pore-scale modelling approach". In: *Applied Geochemistry* 131, p. 105028.

Schlüter, Steffen et al. (2014). "Image processing of multiphase images obtained via X-ray microtomography: a review". In: *Water Resources Research* 50.4, pp. 3615–3639.

Shah, SM et al. (2016). "Micro-computed tomography pore-scale study of flow in porous media: Effect of voxel resolution". In: *Advances in water resources* 95, pp. 276–287.

Silva, Marly Terezinha Quadri Simões da et al. (2023). "Porosity: Some characterization techniques". In: *Materials Today: Proceedings*.

Singh, Kamaljit et al. (2017). "Dynamics of snap-off and pore-filling events during two-phase fluid flow in permeable media". In: *Scientific reports* 7.1, p. 5192.

RS-Systems (2021). *Core Holder User Manual*. RS-Systems.

Tang, Qianhao and Ivan Gratchev (2023). "Estimation of sedimentary rock porosity using a digital image analysis". In: *Applied Sciences* 13.4, p. 2066.

Tanino, Yukie and Martin J Blunt (2012). "Capillary trapping in sandstones and carbonates: Dependence on pore structure". In: *Water Resources Research* 48.8.

Tatone, Bryan SA and Giovanni Grasselli (2015). "Characterization of the effect of normal load on the discontinuity morphology in direct shear specimens using X-ray micro-CT". In: *Acta Geotechnica* 10.1, pp. 31–54.

Vafai, Kambiz (2015). *Handbook of porous media*. Crc Press.

Van Sciver, Steven W, KD Timmerhaus, and Alan F Clark (2012). *Helium cryogenics*. Vol. 470. Springer.

Vega, Bolivia, Abhishek Dutta, and Anthony R Kovscek (2014). "CT imaging of low-permeability, dual-porosity systems using high X-ray contrast gas". In: *Transport in porous media* 101.1, pp. 81–97.

Wetzel, Maria, Thomas Kempka, and Michael Kühn (2020). "Digital rock physics approach to simulate hydraulic effects of anhydrite cement in Bentheim sandstone". In: *Advances in Geosciences* 54, pp. 33–39.

Wildenschild, Dorthe and Adrian P Sheppard (2013). "X-ray imaging and analysis techniques for quantifying pore-scale structure and processes in subsurface porous medium systems". In: *Advances in Water resources* 51, pp. 217–246.

Withers, Philip J et al. (2021). "X-ray computed tomography". In: *Nature Reviews Methods Primers* 1.1, p. 18.

Xiao, Yitian, Tianfu Xu, and Karsten Pruess (2009). "The effects of gas-fluid-rock interactions on CO2 injection and storage: insights from reactive transport modeling". In: *Energy Procedia* 1.1, pp. 1783–1790.

Xu, Wen-jie, Zhong-qi Yue, and Rui-lin Hu (2008). "Study on the mesostructure and mesomechanical characteristics of the soil–rock mixture using digital image processing based finite element method". In: *International Journal of Rock Mechanics and Mining Sciences* 45.5, pp. 749–762.

Yang, Yong-Fei et al. (2021). "Flow simulation considering adsorption boundary layer based on digital rock and finite element method". In: *Petroleum Science* 18.1, pp. 183–194.

Yang, Yongfei et al. (2018). "Flow simulation of artificially induced microfractures using digital rock and lattice Boltzmann methods". In: *Energies* 11.8, p. 2145.

Zahid, Fizza and Jeffrey A Cunningham (2025). "Review of the color gradient lattice Boltzmann method for simulating multi-phase flow in porous media: Viscosity, gradient calculation, and fluid acceleration". In: *Fluids* 10.5, p. 128.

Zhang, Daren et al. (2025). “Stable physical property estimation across resolutions for digital rock utilizing texture and intensity features”. In: *Rock Mechanics and Rock Engineering* 58.3, pp. 3175–3195.

Zhang, Haiyang et al. (2021). “Pore-scale characterization and pnm simulations of multiphase flow in carbonate rocks”. In: *Energies* 14.21, p. 6897.

Zhang, Na et al. (2021). “Characterization of the pore structure and fluid movability of coal-measure sedimentary rocks by nuclear magnetic resonance (NMR)”. In: *ACS omega* 6.35, pp. 22831–22839.

Zheng, C et al. (2012). “MT3DMS: Model use, calibration, and validation”. In: *Transactions of the ASABE* 55.4, pp. 1549–1559.

Zheng, Chunmiao, Gordon D Bennett, et al. (2002). *Applied contaminant transport modeling*. Vol. 2. Wiley-Interscience New York.

Zhuang, Li et al. (2022). “A novel method for estimating subresolution porosity from CT images and its application to homogeneity evaluation of porous media”. In: *Scientific reports* 12.1, p. 16229.